Non-linear Control of the Plasma Vertical Position in a Tokamak

Luigi Scibile

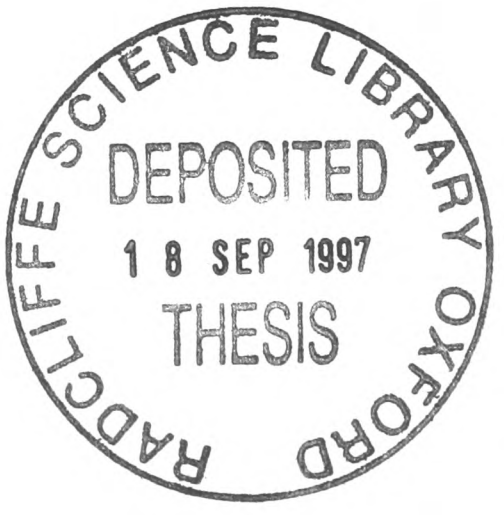
A thesis submitted in partial fulfilment of the requirements for the degree of Doctor of Philosophy at the University of Oxford.

JET Joint Undertaking
Abingdon, OX14 3EA, UK

Oriel College
Oxford

Dept. Engineering Science
University of Oxford

Hilary Term 1997



Non-linear Control of the Plasma Vertical Position in a Tokamak

Luigi Scibile

D.Phil Thesis Abstract

JET Joint Undertaking Oriel College Dept. Engineering Science
Abingdon, OX14 3EA, UK Oxford University of Oxford

The thesis describes the design of a novel non-linear controller for the plasma vertical position in a Tokamak that maximizes the stability region and is robust to certain disturbances and measurement noise.

The plasma vertical position in a Tokamak can be open loop unstable with time-varying dynamics. The limitation in the output power of the control amplifier makes the time varying unstable system particularly difficult to control. Fixed-coefficient linear controllers usually fail to maintain control in the presence of large disturbances, like Edge Localized Modes (ELMs), which saturate the amplifier output. During the saturation period the vertical position of the plasma will grow exponentially with the unstable eigenvalue and may reach values that cannot be controlled by the energy provided by the control amplifier which is limited by economic restraints. The primary sources of disturbances and measurement noise that effect the vertical position are the ELMs and the $600Hz$ noise from the thyristor power supplies. The former are present during high energy confinement plasma configurations in the form pulses.

A simple model structure is derived for the vertical position which includes the effect of the disturbances and the measurement noise and the control amplifier. The model is validated against experimental data from the JET and the COMPASS-D Tokamaks. A method to measure the maximum obtainable stability region of unstable systems subject to control limitations is derived and used to determine the conditions for a maximum stabilizer controller. A novel technique to determine the existence, the stability and the period of possible limit cycles for relay controlled systems is derived and used to determine the stability region of unstable systems incorporating relay controllers with and without time delays.

A novel non-linear controller for the vertical position based on a discrete time adaptive near-minimum time algorithm (DANTOC) is designed to stabilize the system, to maximize the stability region and to be robust to the aforementioned sources of disturbances and measurement noise. The controller is tested in simulation for the JET Tokamak and the results demonstrate its feasibility in controlling the vertical position for different plasma configurations. The controller is also tested on the COMPASS-D Tokamak and the results demonstrate the improvement with respect to a simple linear $P + D$ controller in the presence of the aforementioned sources of disturbances and measurement noise.

The proposed controller represents a much better solution than existing conventional controllers for the control of the plasma vertical position for the new generation of Tokamaks.

Acknowledgements

It is a great pleasure to acknowledge the support and the guidance of those people who supported and encouraged the development of this thesis. I wish to thank Dr. P. Noll and Dr. V. Marchese for their support and guidance which has been encouraging and stimulating throughout the years I have been at the JET project. My thanks are due to my academic supervisors at Oxford: to Dr. D. Mustafa for his guidance and many useful suggestions during the initial part of the project, and to Dr. A. L. Dexter for his invaluable help and stimulating comments during the latter part of this work.

During my stay at the JET project I had many valuable discussions for these I would like to thank Dr. T. Raimondi, E. de Marchi, M. Buzio, Dr. M. Garribba, Dr. S. Puppin, F. Sartori, Dr. A. W. Paynter, J. J. Howie, Dr. S. Ali-Arshad, Dr. D. Chiron, Dr. T. Bonnicelli and Dr. M. L. Browne. A special thanks is due to Dr. J. G. Jacquinot for his encouragements.

I would like to express my gratitude to Dr. W. Morris for giving me the opportunity to carry out the experiments on COMPASS-D. Many thanks go to Dr. P. Vyas for his assistance during the experiments and the valuable discussions I had with him. I would also like to thank G. McArdle for having been my COMPASS-D operator during the whole experimental campaign.

A special thanks goes to Prof. F. Garofalo of Naples University who has always been present with his useful advice.

I am grateful for financial support to the JET Joint Undertaking and especially Dr. M. Keilhacker and Dr. E. Bertolini for giving me the opportunity to carry out this thesis working in the JET team.

This thesis would not even have started without the support and the encouragement of my beloved wife Adriana and a special thanks is due to her. A final, but not least, thank you is due to my parents: *grazie per tutto.*

List of Symbols

A''_{pp} is the vertical force produced by the equilibrium field on a plasma subject to a unit vertical displacement

B_{equ} is the equilibrium magnetic field

B_n is the normal magnetic field components

B_R^{equ} is the radial component of the equilibrium magnetic field

B_R^{iron} is the radial component of the virtual field generated by an image current

B_t is the tangential magnetic field components

c_j is the $j-th$ value of T for which $|\lambda_i(T)| = 1$

$d = F_p$ is the external force disturbance

$\mathbf{D}_d$ is the coupling matrix between the divertor pick-up coils and the divertor busbars

d_{600} is the disturbance due to the characteristics of the thyristor power supplies

$\bar{d}_{600}$ is the maximum observed RMS values due to the characteristics of the thyristor power supplies

d_{ELM} is the disturbance due to the plasma Edge Localized Modes

$\bar{d}_{ELM}$ is the ELM's observed maximum amplitude

F_{dest} is the total destabilizing force acting on a filamentary massless plasma

F_{equ} is the equilibrium magnetic field

F_p is an external vertical force normalized to the plasma current I_p acting on the plasma as a disturbance

$g(\mathbf{K}, \mathbf{T}) = \rho \left\| \mathbf{K}^T \right\| \|\mathbf{T}\|$

J is the Jordan canonical form

K is a stabilizing state feedback gain matrix

K_a is the control amplifier gain

h is the sampling period

H_α is the signal of the H_α emission

I is the vector of the currents flowing in the stabilizing circuit (active coils and passive coils)

I_a is the current flowing in the active coils

I_{CA1} is the CA1 current

I_{D_i} is the $i-th$ divertod current

I_{FAx} is the FAx current

I_p is the plasma current

I_v is the current flowing in the passive coils

I_Φ is the total toroidal current flowing in the closed path l

L is the inductance matrix of the stabilizing coils

$\mathbf{L_{mod}}$ is the modified inductance matrix

$\acute{\mathbf{L}}_p$ is the mutual change inductance vector

m is the measurement noise

m_{600} is the measurement noise due to the characteristics of the thyristor power supplies

$\bar{m}_{600}$ is the maximum observed RMS values due to the characteristics of the thyristor power supplies

m_{ELM} is the measurement noise due to the plasma Edge Localized Modes

$m_{n=1}$ is the measurement noise due to errors induced by the plasma non-axisymmetric modes with $n = 1$

m_{z_p} is the measurement noise due to the approximations and errors in equation (??)

n_{ion} is the plasma ion density

N_r is the number of iterations from the initial value to the maximum expected value of q_r

N_s is the number of iterations from the initial value to the maximum expected value of q_s

P_i is the proportional gain of the proportional+integral controller on the current loop in the JET Tokamak

P_{IAE} is the Integral Absolute Error (IAE) performance index

P_T is the Total Average Power Dissipation (TAPD)

$q_r(k)$ is the parameters that identifies the rotating hyperplane

$q_r^{\max}$ is the value for which the rotating hyperplane $s_r(\mathbf{x})$ crosses the intersection between Σ_r and Ω_{in}

$q_s(k)$ is the parameters that identifies the shifting hyperplane

$q_s^{\max}$ as the maximum value for which the shifting hyperplane $s_s(\mathbf{x})$ does not exceed the region $\Omega_{\max}^{\tau}$

$\mathbf{R}$ is the resistance matrix of the stabilizing coils

R_p is the plasma major radius

$s(\mathbf{x})$ is a stabilizing relay-type sliding controller

$s_c(x)$ is a central hyperplane

$s_r[\mathbf{x}(k)]$ is a rotating hyperplane

$s_s[\mathbf{x}(k)]$ is a shifting hyperplane

$\mathbf{T}$ is a diagonal definite positive scaling matrix

T_i is the integrator time constant gain of the proportional+integral controller on the current loop in the JET Tokamak

T_{ion} is the ion temperature

$\mathbf{V}$ is the vector of the external applied voltages

V_a is the power supply of the active coils

V_{CA1} is the CA1 voltage

V_{FAx} is the FAx voltage

$V_{p_i}^{\dot{z}_p}$ is the $i-th$ analogue weighted sum of the signals measured by the pick-up coils

V_{ref} is the reference input to the control amplifier

$V_{s_i}^{\dot{z}_p}$ is the $i-th$ analogue weighted sum of the signals measured by the saddle loops

$\mathbf{u}$ is the input vector

$u = V_a$ is the external input

u_o is a constant value

$\mathbf{u}_o$ is a constant vector

$\mathbf{v}_p$ is the left eigenvector associated with the unstable eigenvalue

$\mathbf{x}$ is the state vector

$\mathbf{x}_{equ}$ is the equilibrium state

$\mathbf{x}_{ELM}$ is the state displacement caused by an ELM

$\mathbf{x}_s$ is the intersection between the stable/unstable directions

$\mathbf{W}$ is the matrix of the generalized eigenvectors

$Z_c I_\Phi$ is the current moment centroid

z_{D_i} is the $i-th$ divertor coil current centroid

z_p is the plasma vertical position with repect to the middle plane

$z_p^c = z_p I_p$ is the vertical current moment of the plasma current centroid

z_p^e is the deviation from the equilibrium position

$\dot{z}_p^m$ is the measured plasma vertical velocity

z_p^m is the measured plasma vertical position

z_p^{ref} is the vertical position reference signal

$\partial\Omega$ is the boundary of Ω

$\partial\Omega_{\max}$ is the boundary of $\Omega_{\max}$

γ_n is a negative eigenvalue (associated to the stabilizing passive structure of the plasma vertical position)

γ_p is a positive eigenvalue (associated to the instability growth rate of the plasma vertical position)

Σ is a pseudo-sliding boundary locus

Σ_r is the pseudo-sliding boundary loci associated respectively with $s_r\left[\mathbf{x}\left(k\right)\right]$

Σ_s is the pseudo-sliding boundary loci associated respectively with $s_s\left[\mathbf{x}\left(k\right)\right]$

ϵ_s is the rate of increase of the shifting hyperplane

ϵ_r is the rate of increase of the rotating hyperplane

$\mathbf{\Phi}_c\left(T_k\right)$ is the transition matrix of the unconstrained closed loop system

$\mathbf{\Phi}_r\left(T_k\right)$ is the transition matrix of the system restricted to the switching surface $\mathbf{v}^T\mathbf{x}=0$

λ_i is the $i-th$ eigenvalue

$\boldsymbol{\mu}$ is a vector of normalizing parameters

$\rho = \max_{k>0}\left\|\left(\mathbf{\Phi}+\mathbf{\Gamma}\mathbf{K}^T\right)^k\right\|$

$\boldsymbol{\sigma}$ is the vector of the saturation thresholds

$\mathbf{\Theta}$ is a diagonal gain matrix

τ_{ad} is the average time delay of the control amplifier

τ_E is the energy confinement time

$\bar{\tau}_{ELM}$ is the observed average duration of an ELM

$\tau_{ELM}^{\max}$ is the longest observed ELM's duration

τ_{GTO} is the maximum time delay expected from a GTO

τ_{opt} is the minimum time for the states to re-enter Ω_{in}

$\bar{\tau}_{rep}$ is the observed average ELMs' repetition rate

τ_s is the adaptation delay

$\bar{\tau}_v$ is the average measured delay from when the voltage is applied to the active coils to when the plasma starts moving

Ω_K is the domain within which the feedback control is not saturated

Ω_{in}, is the Inner control region

$\Omega_{\max}$ is the maximum obtainable stability region

$\Omega_{\max}^{\tau}$ is the maximum stability region for systems with a time delay τ on the control input

Ω_{sl} is the stability region under linear saturated controllers

Ω_{out} is the Outer control region

Contents

1 Introduction 1

2 Models for the Plasma vertical position system 4

2.1 Introduction 4

2.2 A simple model of the Plasma vertical position 6

2.3 A model of the measurement system 18

2.4 Deriving models for the disturbances 22

2.4.1 ELM disturbances 22

2.4.2 Thyristor power supplies disturbances 25

2.5 Deriving a model for the actuators 30

2.6 Experimental model validation 35

2.6.1 Comparison of the experimental data with open loop simulations . . . 37

2.6.2 Comparison of the experimental data with closed loop simulations . . 41

2.6.3 Experimental validation of the disturbance model 45

2.7 Concluding Remarks 47

3 Control of unstable LTI systems with constrained inputs 48

3.1 Introduction 49

3.2 Maximum obtainable stability region for Unstable LTI systems with a constrained input 50

3.2.1 Optimum controllers for Unstable LTI systems with a constrained input 56

3.3 Stability region for single input LTI systems under state feedback control with constrained input 61

3.3.1 Relay control law 62

3.3.2 Relay control law with a time delay 73

3.3.3 Stability region under linear saturated continuous time and discrete time controllers 79
3.3.4 Stability regions under continuous time and discrete time variable structure relay control 84
3.4 Concluding remarks 84

4 Vertical stabilization control system design **86**
4.1 Introduction 86
4.1.1 Aim of the Chapter 87
4.1.2 Review of earlier work 88
4.2 Discrete Adaptive Near-Time Optimum Control with time-varying hyperplanes for unstable systems 91
4.2.1 The DANTOC control law 94
4.2.2 The basic adaptive controller 97
4.2.3 Modifications to the basic adaptive controller to improve the robustness to external disturbances 107
4.3 Selection of controller parameters 109
4.3.1 Inner region control scheme 109
4.3.2 Outer region control scheme 111
4.4 Does the controller achieve the predefined objectives? 113

5 Testing of the control algorithm on a simulation of the JET Tokamak **115**
5.1 Introduction 115
5.2 Setup of the controller for the JET Tokamak 116
5.3 Closed loop simulations using the proposed controller 118
5.3.1 Response to generic initial conditions 118
5.3.2 Response to large disturbances (ELMs) and measurement noise (ELMs and $600Hz$) - Comparison with the JET present controller 121
5.3.3 Effect of the current limit constraint 127
5.3.4 Effect of asymmetric plasma configurations having different up/down growth rates 129
5.4 Concluding remarks 129

6 Experimental testing of the controller on the COMPASS-D tokamak **131**

6.1 Introduction 131

6.2 Experimental setup of the COMPASS-D control system 133

6.3 Tests to assess the sensitivity of the closed loop behaviour to the choice of the DANTOC parameters. 137

6.3.1 Varying the adaptation rates 137

6.3.2 Reducing the size of the inner control region 140

6.3.3 Removing the resetting conditions 141

6.4 Tests to investigate the effect of ELMs on the plasma vertical position when using the DANTOC. 145

6.4.1 The DANTOC behaviour in the presence of ELMs. 145

6.4.2 Effect of increasing the adaptation delay 146

6.4.3 Effect of decreasing the adaptation delay 148

6.4.4 Fixing the switching hyperplanes 149

6.5 Tests to examine the sensitivity to measurement noise. 151

6.6 Tests to validate the predicted stability region 153

6.7 Concluding remarks 160

7 Conclusions and future work **161**

A A brief introduction to Nuclear Fusion and Tokamaks **164**

A.1 Principles of Nuclear Fusion 164

A.2 The Tokamak 166

A.3 The JET Tokamak 169

A.3.1 Vertical position control system 173

A.4 The COMPASS-D Tokamak 176

A.4.1 Vertical position control system 176

B A brief introduction to Variable Structure Control and Minimum Time Control **178**

B.1 Variable Structure Control review 178

B.2 Minimum Time Control review 181

List of Figures

2.1 (a) Quadrupolar shaping field - (b) Image currents in the iron 8

2.2 Forces on the plasma in the vertical direction 10

2.3 The lumped-element electrical circuit 10

2.4 Eigenvalues deriving from equation (2.26) versus A''_{pp} 16

2.5 Example of a model having two different growth rates and similarities with the plasma in the vessel. 17

2.6 Magnetic sensors - Pick-up coils and Saddle loops 19

2.7 Description of plasma modes 21

2.8 ELMs in JET and in COMPASS-D. 23

2.9 The effect of an ELM on the $\dot{z}_p$ when the equalizing filters are used (JET experiment #29914). 24

2.10 Comparison between a real ELM (JET experiment #40452) and the function $d_{ELM}(t) = 6.5 \cdot \left(e^{-\frac{t}{6 \cdot 10^{-4}}} - e^{-\frac{t}{1.7 \cdot 10^{-4}}}\right)$. 25

2.11 The frequency spectrum of the feedback signal for JET and COMPASS-D. . . 26

2.12 Comparison between the measured value of $\dot{z}_p$ with and without equalizing filters (JET experiment #29279). 28

2.13 Comparison between the measured value of $\dot{z}_p$ with and without equalizing filters (JET experiment #29327). 29

2.14 A schematic diagram of the plasma vertical position model including the disturbances, d_{ELM} and d_{600}, and measurement noise $m_{ELM} + m_{600}$. 30

2.15 Schematic diagram of an H-bridge inverter 31

2.16 FRFA operational modes 32

2.17 System identification setup. 32

2.18 The Real FRFA compared to the Simulated FRFA 33

2.19 Model validation of unstable systems: (a)-open loop validation (b)-closed loop validation 36
2.20 Comparison of the experimental data with open loop simulations (JET experiment #36376) 38
2.21 Comparison of the experimental data with open loop simulations (COMPASS-D experiment #18135) 39
2.22 COMPASS-D experiment 40
2.23 Comparison between the vertical position and the current flowing into the active coils 41
2.24 Comparison of the experimental data with closed loop simulations (JET experiment #36376). 43
2.25 Comparison of the experimental data with closed loop simulations (COMPASS-D experiment #18135). 44
2.26 Comparison between a real and a simulated ELM (JET experiment #40452). 46

3.1 Stability region for a 2^{nd} order unstable system ($\gamma_p = 2$, $\gamma_n = 1$). 56
3.2 Time-optimum switching lines. 61
3.3 2^{nd} order unstable system trajectories under saturated state feedback ($\gamma_p = 2$, $\gamma_n = 1$). 68
3.4 $\lambda_{\max}(T)$ of the matrix $\Phi_r(T)$ for different values of q ($\gamma_p = 2$, $\gamma_n = 1$). 69
3.5 Stability regions of 2^{nd} order unstable system under relay feedback control ($\gamma_p = 2$, $\gamma_n = 1$). 70
3.6 $\lambda_{\max}(T)$ of the matrix $\Phi_r(T)$ for a 3^{rd} order system. 71
3.7 (a) Initial conditions inside the asymptotic stability region, (b) Initial conditions inside the stability region and the limit cycle, (c) Initial conditions inside the stability region but outside the limit cycle, (d) Initial conditions outside the stability region. 72
3.8 Limit cycle in the phase-plane. 73
3.9 $\lambda_{\max}(T)$ of the matrix $\Phi_r(T)$ ($\tau_1 = 0$, $\tau_2 = 0.05\,[s]$, $\tau_3 = 0.1\,[s]$). 76
3.10 (a) Initial conditions inside the stability region and the limit cycle, (b) Initial conditions inside the stability region but outside the limit cycle, (c) Initial conditions on the limit cycle, (d) Initial conditions outside the stability region. 77

3.11 (a) Initial conditions inside the stability region and the limit cycle, (b) Initial conditions inside the stability region but outside the limit cycle, (c) Initial conditions on the limit cycle, (d) Initial conditions outside the stability region. 78
3.12 The $|\lambda_i(\mathbf{x}_o)|$ or the values of x_o which are of interest: Case (a) and Case (b). 81
3.13 Stability regions: Case (a). 82
3.14 Stability regions: Case (b). 83

4.1 Control characteristic in the phase plane. 95
4.2 Example using a fixed $s[x(k)]$. 96
4.3 Mimimum time switching curves for different values of γ_p. 97
4.4 Outer region control scheme. 98
4.5 An example of the basic adaptive controller. 99
4.6 Stabilty region varying $q_r(k)$. 103
4.7 Pseudo-sliding boundary locus compared to the time-optimum switching line. 104
4.8 Example of the DANTOC performances when γ_p changes from 200 $[s^{-1}]$ to 1000 $[s^{-1}]$ starting from the same initial conditions. 105
4.9 Pseudo-sliding detector flowchart. 106
4.10 Comparison between typcal stability regions obtained using a saturating linear controller and the DANTOC. 114

5.1 Proposed control scheme for JET tokamak. 116
5.2 Simulation of the JET Tokamak vertical stabilization system using the DANTOC: phase-plane diagram of the response to arbitrary initial conditions. . . 119
5.3 Simulation of the JET Tokamak vertical stabilization system using the DANTOC: time evolution of the response to generic initial conditions. 120
5.4 Comparison between the simulations of the JET vertical stabilization system using the DANTOC and using the present JET vertical stabilization controller (vertical position and speed): Response to large disturbances (ELMs). . . . 122
5.5 Comparison between the simulations of the JET vertical stabilization system using the DANTOC and using the present JET vertical stabilization controller (FRFA voltage and current): Response to large disturbances (ELMs). 123

5.6 Comparison between the simulations of the JET vertical stabilization system using the DANTOC and using the present JET vertical stabilization controller (Phase-plane diagram): Response to measurement noise. 124
5.7 Comparison between the simulations of the JET vertical stabilization system using the DANTOC and using the present JET vertical stabilization controller (Vertical position and speed): Response to measurement noise. 125
5.8 Comparison between the simulations of the JET vertical stabilization system using the DANTOC and using the present JET vertical stabilization controller (FRFA voltage and current): Response to measurement noise. 126
5.9 Simulation of the JET Tokamak vertical stabilization system using the DANTOC: phase-plane diagram of the response to initial conditions close to the FRFA current limit. 127
5.10 Simulation of the JET Tokamak vertical stabilization system using the DANTOC: time evolution of the response to initial conditions close to the FRFA current limit. 128
5.11 Example of the DANTOC with an up/down asymmetric plasma. A different up/down growth rate is used: $\gamma_p = 200s^{-1}$ for a downward movement and $\gamma_p = 1000s^{-1}$ for an upward movement. 130

6.1 Schematic diagram of the COMPASS-D modified vertical position control system. 133
6.2 FAx - CA1 decoupling shot 134
6.3 Comparison between the simulation results and the experiment #18135. . . . 135
6.4 Experiments executed varying the adaptation rates: CA1 output voltage. . . 138
6.5 Experiments executed varying the adaptation rates: plasma vertical position z_p. 139
6.6 Phase-plane plot of the control response: a) using the correct estimate of $\bar{m}_{600}$, b) decreasing the estimate of $\bar{m}_{600}$ below the measurement noise level. 140
6.7 CA1 output voltage: a) using the correct estimate of $\bar{m}_{600}$, b) decreasing the estimate of $\bar{m}_{600}$ below the measurement noise level. 141
6.8 Experiment with no resetting conditions. Comparing the COMPASS-D experiments #18136 and #18511. 142
6.9 COMPASS-D experiment #18509 with no resetting conditions. 143
6.10 Plasma boundary reconstructions for experiment #18509 144
6.11 The effect of ELMs when the set of tuned DANTOC parameters is used. . . . 146

6.12 Effect of increasing the adaptation delay. 147
6.13 Effect of decreasing the adaptation delay. 149
6.14 Experiment fixing the switching hyperplane. 150
6.15 Comparison between the DANTOC (#17496) and the COMPASS-D's linear analogue controller (#17479). 152
6.16 Comparison between the DANTOC (#17497) and the COMPASS-D's linear analogue controller (#17480). 154
6.17 The expected stability region of experiment #17480 is displayed on the phase-plane diagram when using the P+D controller. 155
6.18 Phase-plane diagram when using the DANTOC (pulse #17497) also showing the stability region. 156
6.19 COMPASS-D experiment #18524 showing the control response during a gradual increase to the elongation of the plasma: time evolution. 158
6.20 COMPASS-D experiment #18524 showing the control response during a gradual increase to the elongation of the plasma: phase-plane diagram. 159

A.1 The Deuterium (D) - Tritium (T) fusion reaction. 165
A.2 The tokamak concept. 166
A.3 Magnetic flux surfaces forming a set of nested toroids 167
A.4 Plasma operating modes. 168
A.5 The JET Machine. 169
A.6 JET tokamak vessel and mechanical structure 171
A.7 TF coil system 172
A.8 PF coil system 172
A.9 Cross section of the PF System 174
A.10 Schematic diagram of the JET vertical stabilization system. 175
A.11 Schematic diagram of the present COMPASS-D vertical stabilization system. 177

B.1 Typical variable structure system with relay control law. 179
B.2 Typical phase state trajectories. 180

Chapter 1

Introduction

In the search for new sources of energy, nuclear fusion offers great possibilities for the future with virtually inexhaustible reserves and a negligible basic fuel cost. On the other hand, the conditions for thermonuclear reaction are difficult and complex to implement mainly because of the temperature of $\approx 10^8\,[^oC]$ ($\approx 10{\cdot}10^3\,[eV]$) necessary to initiate nuclear combustion. One approach to controlled fusion is the magnetic confinement scheme where magnetic fields are used to contain a fully ionized gas called plasma. Among the various possible configurations the most promising approach has been demonstrated to be the Tokamak (see Appendix A).

The largest experimental Tokamak device in the world is the Joint European Torus (JET). JET is the leading project supported by Euratom in the framework of the European research on the non-military exploitation of the controlled thermonuclear fusion [Keen93][Duchs92]. A much larger tokamak (the International Thermonuclear Experiment Reactor (ITER) [Tomabechi91]) is being developed by the EC, USA, Japan and Russia with the aim of providing sufficient knowledge to build a working demonstration power-plant. Part of the JET programme includes experiments that are relevant for ITER. The COMPASS-D tokamak is a small tokamak which is being used as a testbed for studying new ideas before they are implemented on JET or considered for ITER.

In a Tokamak the plasma is kept away from the vacuum vessel walls by a magnetic field which also determines the shape of the plasma. The vertical position of a vertically elongated plasma is open loop unstable [Wesson87]. Thus, an essential requirement in the operation of a Tokamak fusion reactor is the active vertical stabilization of the plasma. The plasma vertical position is controlled by a magnetic field generated by a pair of poloidal conducting coils. The current flowing in such coils is regulated by a power amplifier. The limitation in

the output power of a real amplifier causes the stability region to be limited. A robust control algorithm for the stabilization of the vertical position of the plasma in a Tokamak is of crucial interest for fusion research. The loss of vertical stability results in vertical disruptions which are particularly dangerous because they can generate severe stresses on the vacuum vessel wall and its support structure that, in the past, have damaged the JET tokamak [Noll90].

The aim of this thesis is to design a controller that maximizes the stability region of the plasma vertical position, independently of the plasma operating configuration, and minimizes the effect of disturbances and measurement noise. In order to do that the **first objective** is to derive a simple model that approximates the plasma vertical position for different plasma configurations. This must also include a characterization of the disturbances, the measurement noise and the power amplifiers. The **second objective** is to determine the maximum obtainable stability region of an unstable system with control limitations in order to design a controller that increases the closed loop stability region. The **third objective** is to design an adaptive controller that maximizes the stability region and guarantees the same performance for different plasma configurations. The **fourth objective** is to tune the control parameters for the JET Tokamak and test the control system by simulation. The **fifth objective** is to test the feasibility of real-time implementation on the COMPASS-D Tokamak.

An outline of the thesis is given below.

- In **Chapter 2** a simple model between the control input and the plasma vertical position is derived and validated with experimental data. Disturbances are included in the plasma vertical position model as additional inputs and are characterized from experimental observations. The measurement system is analysed and possible sources of measurement noise are identified. Finally a model for the power amplifier is derived and validated.

- In **Chapter 3** the maximum obtainable stability region of an unstable Linear Time Invariant (herein LTI) system with a constrained input under feedback control is determined. The sufficient stability conditions are given in the case of a relay control with and without a time delay. The necessary and sufficient stability conditions are given in the case of one unstable eigenvalue. A novel technique to determine the existence, the stability and the period of possible limit cycles is also derived.

- In **Chapter 4** a novel technique for vertical stabilization control is presented. The technique aims to achieve Time Optimal Control for unstable systems by using a pseudo-sliding controller with time varying hyperplanes. The resulting control algorithm has been named Discrete Adaptive Near-Time Optimum Control (herein DANTOC). The DANTOC maximizes the stability region and recovers from any displacement that lies within the maximum obtainable stability region in a short time and in a reliable way. Elements of Variable Structure System theory, Minimum Time Control and the stability regions derived in Chapter 3 are used for the design of the DANTOC which takes into account the presence of the saturation in the actuators to improve the performance while maintaining acceptable stability margins.

- To tune the control parameters for the JET Tokamak and test the control system a series of tests of the DANTOC on a simulation of the JET tokamak have been carried out and the results are presented in **Chapter 5.**

- To demonstrate the feasibility of the DANTOC a series of experiments have been carried out on the COMPASS-D tokamak and the results are presented in **Chapter 6.**

Chapter 2

Models for the Plasma vertical position system

The vertical position of a vertically elongated plasma is unstable. In order to design a stabilising control system knowledge of the plasma dynamics, the associated measurement system and the power control actuators is required. The derivation of a global model and its associated parameters has proved to be very complicated and usually these models are not suitable for the control design. Simple Linear Time Invariant (LTI) models have been used in the past for the control design but the real system is neither time invariant nor linear. The aims of this chapter are to:

1. Derive a simple model structure.
2. Assess its validity via experimental data.
3. Characterize the disturbances based on the observation of the experimental data.
4. Derive parameters required for the control design described in Chapter 4.

2.1 Introduction

Every controller design method requires a certain degree of knowledge of the plant. For example, methods based on the Nyquist diagram need the frequency response of the plant while fuzzy logic controllers can be designed on a more qualitative basis.

Although the controller design technique proposed in Chapter 4 does not require a precise quantitative description of the dynamic behaviour; i.e. eigenvalues, saturation limits, time

delays and the range of these parameters, some knowledge of the disturbances can be used to enhance the robustness.

Ideally the controller design would require a simple model that captures the dominant modes including non-linearities and the effect of the disturbances.

Simple models for the plasma vertical position are based on the assumption of a rigid massless plasma [Jardin82], [Albanese84], [Lazarus90] and [Noll91a]. The difference between a rigid ideal Magnetic Hydro Dynamic (MHD) (§ Section 2.2) shift and a rigid constant current shift was studied in [Hutchinson89] where it is shown that the latter method gives more conservative results.

[Albanese89] proposed a variation of the rigid displacement model consisting of a simple, MHD consistent, non-rigid model. This model includes the plasma dynamics and allows a simpler calculation of the model parameters. However the model structure remains unchanged from the rigid displacement model.

The assumption of rigid motion of the plasma was also studied in [Ward92]. It was found that the magnetic measurements based on this assumption can lead to incorrect results and, in particular, do not describe some of the plasma movements.

More complex models are used for the full simulation of plasma evolution; these models include complete solution of the MHD equations and, in some cases, the 3D eddy current effect induced by the vacuum vessel and the surrounding supporting structures [MAXFEA] and [PROTEUS]. The high order ($\sim$ 100 states) LTI models derived by these simulations are often simplified to low order (from 2 to 7 states) by means of model reduction techniques [Al-Husari91], [Tinios93], [Portone92].

Black box system identification of a stationary plasma have produced simple (from 2 to 3 states) LTI models whose parameters depend on the plasma configurations [Lister90], [Vyas96].

In all the aforementioned work and in [Ambrosino88] and [Noll89], the simplified models used for control design were described by a transfer function

$$G(s) = \frac{1}{s - \gamma_p} G_s(s) \tag{2.1}$$

where γ_p is an unstable pole and $G_s(s)$ represents the passive structure dynamics (between the 2^{nd} and the 5^{th} order). It has been observed that it is possible to represent the passive

structure dynamics with a single stable pole γ_n without losing the basic characteristic dynamic behaviour [Noll91a], [Lister90], [Lazarus90], [Browne90].

However these models do not include any non-linearities like the magnetic field penetration through the vacuum vessel walls and the effect of the mechanical shell. Some analysis on the effect of the vacuum vessel penetration and mechanical shell was carried out in [Core88], [Noll95b], [Noll91b].

From all the previous work it appears that a simple model is quite sufficient for controller design purposes. In section 2.2 it will be shown by means of experimental evidence that it is possible to represent the model for the plasma vertical position by one unstable pole, one stable pole and a time delay.

Disturbances on the plasma vertical position can lead to a vertical disruption [Wesson89], [Noll90]. Particularly important is the effect of the Edge Localized Modes (ELM), whose physical effect on the plasma vertical position is still not clear [Zohm96], and the $600Hz$ ripple produced by the thyristor power supplies [Garribba94], [Vyas96]. A new model including these two effects is proposed in section 2.4.

Saturation of the actuators has never been included in the controller design. The power supply limits are usually checked *a posteriori* [Humphreys93] or, in simulations, by measuring the voltage/current needed for the recovery of the plasma position for a given initial condition [Ambrosino84], [Portone92], [Zama92], [Noll95a]. Section 2.5 gives a simplified model for the actuators which is suitable for the controller design technique in Chapter 4.

2.2 A simple model of the Plasma vertical position

In general, a model describing the plasma position can be derived by the Magneto Hydro Dynamic (MHD) theory. In this model the plasma is represented as a fluid of charged particles, ions and electrons, coupled to an electromagnetic field. An elegant derivation of the MHD equilibrium equations can be found in [Wesson87].

The basic condition for equilibrium is that the magnetic forces on the plasma balance the force due to the plasma pressure. If the current density is $\mathbf{J}$, the magnetic field is $\mathbf{B}$ and the plasma pressure is p then the condition is expressed by

$$\mathbf{J} \times \mathbf{B} = \nabla p. \tag{2.2}$$

To satisfy this condition both the magnetic field and the current must lie on nested toroidal surfaces (§ Figure A.3). In an axisymmetric geometry, using the cylindrical coordinates (r, z, ϕ) and defining the auxiliary scalar functions

$$\psi(r,z) = \int_0^r B_z(\rho,z)\, 2\pi\rho d\rho, \tag{2.3}$$

$$I(r,z) = \int_0^r J_z(\rho,z)\, 2\pi\rho d\rho, \tag{2.4}$$

the poloidal magnetic is described by

$$B_z = \frac{1}{2\pi r}\frac{\partial\psi}{\partial r} \tag{2.5}$$

$$B_r = -\frac{1}{2\pi r}\frac{\partial\psi}{\partial z} \tag{2.6}$$

and the poloidal current density by

$$J_z = \frac{1}{2\pi r}\frac{\partial I}{\partial r} \tag{2.7}$$

$$J_r = -\frac{1}{2\pi r}\frac{\partial I}{\partial z}. \tag{2.8}$$

Substituting (2.5) (2.6) (2.7) (2.8) into equation (2.2) and eliminating all the fields lead to the Grad-Shafranov equation

$$\frac{\partial^2\psi}{\partial r^2} - \frac{1}{r}\frac{\partial\psi}{\partial r} + \frac{\partial^2\psi}{\partial z^2} = -2\pi r\mu_0\left(2\pi r\frac{dp}{d\psi} + \frac{\mu_0}{4\pi r}\frac{dI^2}{d\psi^2}\right). \tag{2.9}$$

This equation, once the source of the equilibrium magnetic field is defined, gives the value of the magnetic flux surfaces confining the plasma. Using this equation it is possible to calculate the boundary and the position of the plasma. The equation will be used later when the plasma position is derived from a set of magnetic measurements (§ Section 2.3).

In all of the previous work mentioned in Section 2.1 the simplified models have the same structure, indeed the only difference between the various derivations concerns the definition of the plasma behaviour. For a better understanding of the rest of the work the plasma model based on a rigid constant current vertical shift will be described. In this approach it is assumed that the plasma current is constant and the plasma shape does not change (rigid movement) during a vertical shift. The same approach was used, for example by

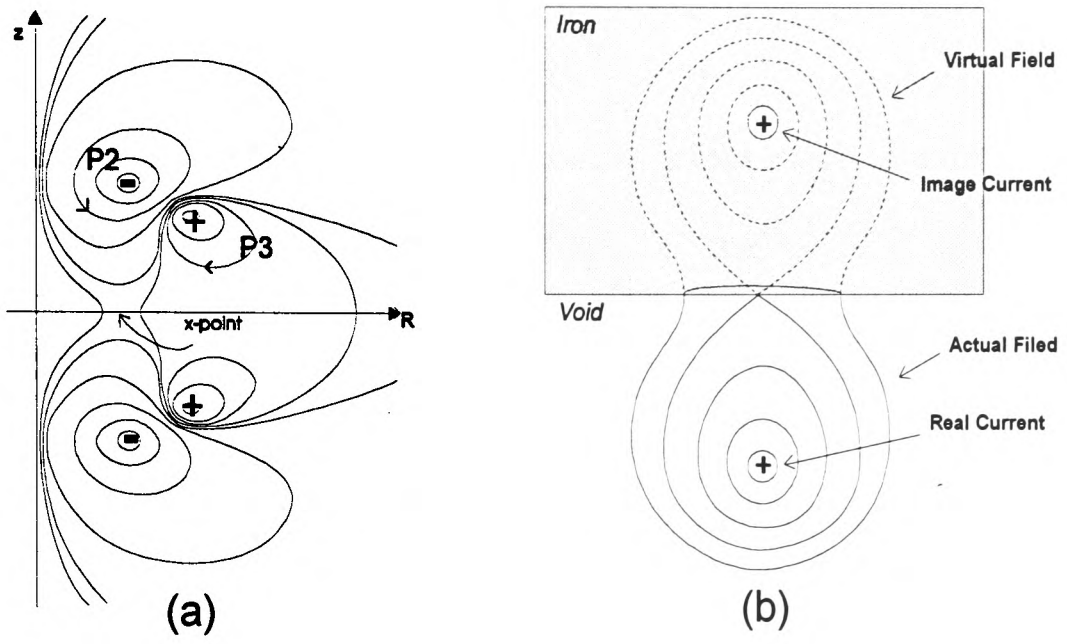


Figure 2.1: (a) Quadrupolar shaping field - (b) Image currents in the iron

[Noll90], [Lazarus90], [Albanese89], [Hoffmann86] and [Humphreys93]. The basic concept of this simplified model is that the plasma is considered as a set of toroidal filaments carrying a constant current which is magnetically coupled with external conducting circuits. In the case of a vertically elongated plasma the vertical position is open loop unstable because of the destabilizing effects of the equilibrium magnetic field required to produce an elongated plasma shape (the quadrupolar field and the iron contribution) and of the iron magnetic circuit.

The equilibrium magnetic field B^{equ} consists of the static field produced by the currents flowing in the external conductors (excluding the plasma current) and the static iron image current field produced by the currents flowing in the external conductors and the plasma at its equilibrium position. The destabilizing effect of the equilibrium magnetic field arises from the electromagnetic interaction between its radial component B_R^{equ} and the plasma current. Figure 2.1(a) shows the quadrupolar component of B^{equ}. When the plasma is moved into the equilibrium magnetic field by z_p it is subject to a force F_{equ} given by

$$F_{equ} \simeq -2\pi R_p I_p \frac{\partial B_R^{equ}}{\partial z} z_p. \tag{2.10}$$

where R_p is the plasma major radius.

The destabilizing effect of the iron magnetic circuit arises from the electromagnetic in-

teraction between plasma current and the transformer iron magnetic circuit. The effect can be explained by means of the concept of the image current. As shown in Figure 2.1(b), this is a virtual current, of the same sign as the real one, symmetrically located (assuming an ideal geometry) with respect to the interface. The resulting effect is to introduce a vertical instability because an attractive force, F_{iron}, arises between the two currents flowing in the same direction. F_{iron} can be described in terms of B_R^{iron}, the virtual field generated by an image current, and the plasma current I_p. The variation of B_R^{iron} with a displacement δz_p generates a force acting on the plasma which can be approximated by

$$F_{iron} \simeq -2\pi R_p I_p \frac{\delta B_R^{iron}}{\delta z_p} z_p \tag{2.11}$$

where z_p is the distance between the plasma current centroid vertical position and the torus middle plane.

Summing the effects just described, the total destabilizing force F_{dest} acting on a filamentary massless plasma can therefore be summarized as follows:

$$F_{dest} \simeq -2\pi R_p I_p \left[\frac{\partial B_R^{equ}}{\partial z} + \frac{\delta B_R^{iron}}{\delta z_p} \right] z_p. \tag{2.12}$$

It is convenient to define the parameter A''_{pp} as

$$A''_{pp} = -\frac{2\pi R_p}{I_p^2} \left[\frac{\partial B_R^{equ}}{\partial z} + \frac{\delta B_R^{iron}}{\delta z_p} \right]. \tag{2.13}$$

A passive and an active action can be taken to counteract the vertical instability.

The passive action is performed by the mechanical structure surrounding the plasma (first wall, blanket, shield, vacuum vessel) and by the poloidal coils in which the response time of the current is slow compared to the vertical instability (they are considered flux conserving). Limits to the passive stabilization can be found in [Lazarus90] and [Leuer89].

The active action is performed by a feedback-driven current and forced into two toroidal conductors, which produces the radial field necessary to push back the plasma into its equilibrium position. In Figure 2.2 the various vertical forces on the plasma are shown.

In general, by integrating the MHD equations, it is possible to derive a lumped model described by a system of linearized equations. A lumped-element electrical circuit diagram is given in Figure 2.3; this consists of the active coils, the plasma filamentary model and the

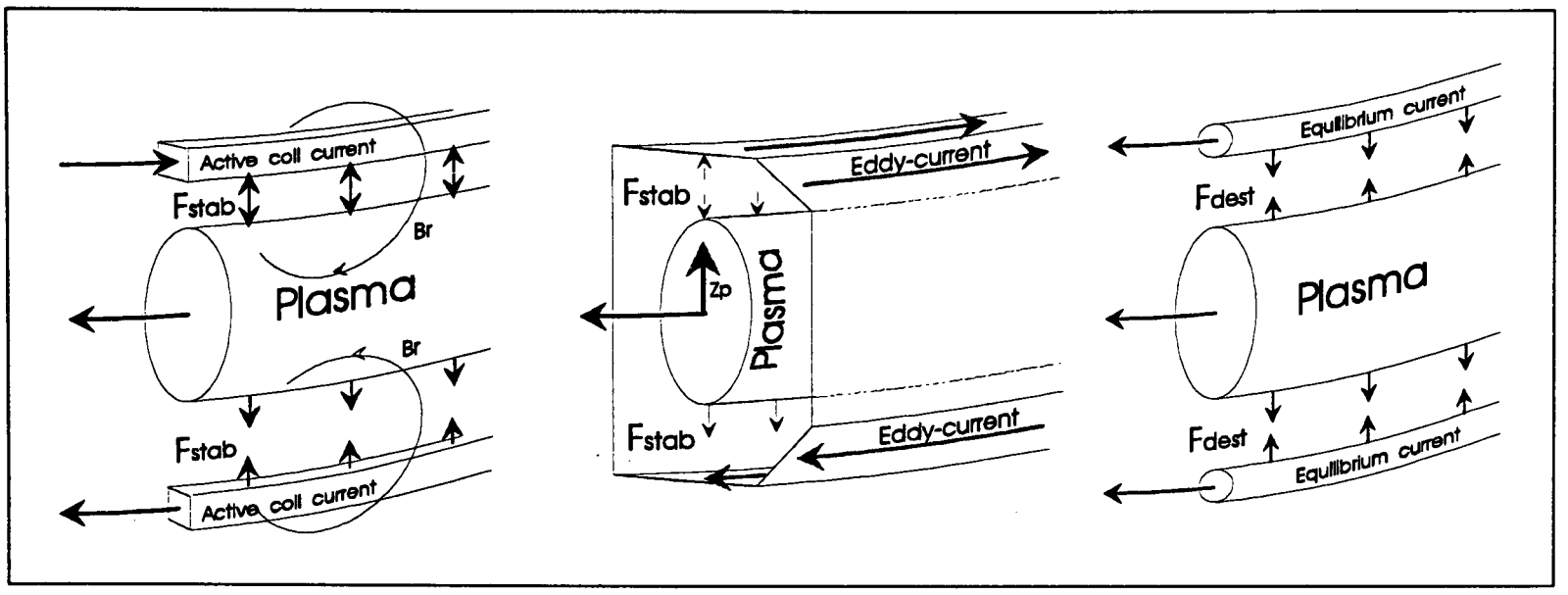


Figure 2.2: Forces on the plasma in the vertical direction

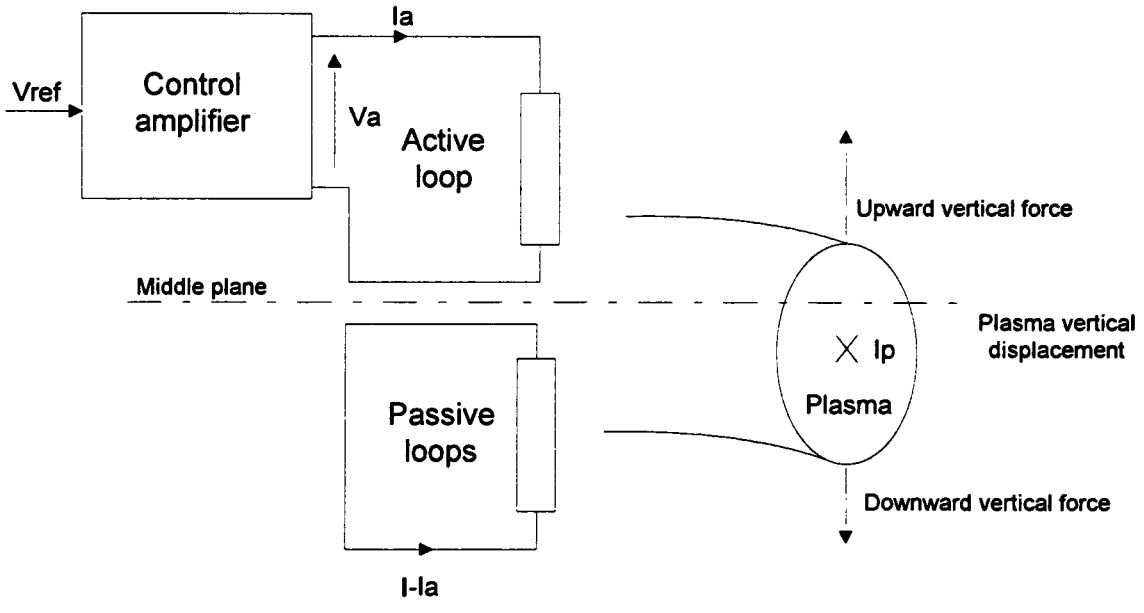


Figure 2.3: The lumped-element electrical circuit

The equations describing the simplified model are the force balance equation and Kirchoff's equations.

The force balance equation is derived from the integration of equation (2.2) over the plasma volume when a passive stabilization is used and the inertial term is negligible [Al-Husari91], and it can be expressed by

$$\acute{\mathbf{L}}_p^T \mathbf{I} + A''_{pp} z_p I_p = F_p \tag{2.14}$$

where

- $\mathbf{I}$ is the vector of the currents flowing in the stabilizing circuit (active coils and passive coils).

- z_p is the vertical plasma displacement.

- $\acute{\mathbf{L}}_p$ is the mutual change inductance vector. The $i-th$ element of $\acute{\mathbf{L}}_p$, $\acute{L}_{ip}$, represents the contribution to the fluxes ψ_i linked with the $i-th$ circuit induced by a unit displacement of the plasma

$$\frac{\partial \psi_i}{\partial z_p} = \frac{\partial L_{ip}}{\partial z_p} I_p$$

or it can be seen as a force acting on the plasma produced by a unit current flowing in the $i-th$ circuit.

- F_p is an external vertical force normalized to the plasma current I_p acting on the plasma as a disturbance.

- A''_{pp} is the normalized destabilizing force. i.e. the vertical force produced by the equilibrium field on a plasma subject to a unit vertical displacement z_p for a unit plasma current (as defined in (2.13)).

- I_p is the plasma current.

Kirchoff's equations describe the dynamics of the currents flowing in the stabilizing circuit taking into account the coupling with the plasma vertical movement. They are expressed by

$$\mathbf{L}\dot{\mathbf{I}} + \mathbf{R}\mathbf{I} + \acute{\mathbf{L}}_p \dot{z}_p I_p = \mathbf{\Gamma}\mathbf{V} \tag{2.15}$$

where

- $\mathbf{V}$ is the vector of the external applied voltages

- $\mathbf{\Gamma}$ is the incident matrix describing the connection of the external voltages to the different circuits.

- $\mathbf{L}$ is the inductance matrix of the stabilizing coils.

- $\mathbf{R}$ is the resistance matrix of the stabilizing coils.

Typical parameters for JET and COMPASS-D are reported in the Section A.3 and Section A.4 of Appendix A.

The equation (2.14) is the plasma momentum balance while equation (2.15) describes the dynamics of the eddy and control currents. Differentiating equation (2.14) with respect to time and substituting into equation (2.15) leads to

$$\mathbf{L}_{\text{mod}}\dot{\mathbf{I}} + \mathbf{R}\mathbf{I} + \acute{\mathbf{L}}_p A''^{-1}_{pp}\dot{F}_p = \mathbf{\Gamma}\mathbf{V} \tag{2.16}$$

where

$$\mathbf{L}_{\text{mod}} = \mathbf{L} - \acute{\mathbf{L}}_p \acute{\mathbf{L}}_p^T A''^{-1}_{pp} \tag{2.17}$$

is defined as the modified inductance matrix [Albanese89].

A state-space representation of the system that includes the external force disturbance, is derived from the equations (2.14) and (2.16)

$$\begin{cases} \dot{\mathbf{x}} = \mathbf{A}\mathbf{x} + \mathbf{B}\mathbf{u} \\ z_p^c = \mathbf{C}\mathbf{x} + \mathbf{D}\mathbf{u} + m \end{cases} \tag{2.18}$$

where $z_p^c = z_p I_p$ is the vertical current moment of the plasma current centroid,

$$\begin{aligned} \mathbf{A} &= -\mathbf{L}_{\text{mod}}^{-1}\mathbf{R} \\ \mathbf{B} &= \begin{bmatrix} \mathbf{L}_{\text{mod}}^{-1}\mathbf{\Gamma} & -\mathbf{L}_{\text{mod}}^{-1}\acute{\mathbf{L}}_p A''^{-1}_{pp} & \mathbf{0}_{n\times 1} \end{bmatrix} \\ \mathbf{C} &= \begin{bmatrix} -\acute{\mathbf{L}}_p^T A''^{-1}_{pp} \end{bmatrix} \\ \mathbf{D} &= \begin{bmatrix} \mathbf{0}_{1\times m} & 0 & A''^{-1}_{pp} \end{bmatrix}. \end{aligned} \tag{2.19}$$

$\mathbf{x}$ is the state vector and, in the given format, the state variables are the currents flowing in the magnetic circuits. $\mathbf{u}$ is the input vector and using the equations (2.14) and (2.15)

$$\mathbf{u} = \begin{bmatrix} \mathbf{V}^T & \dot{F}_p & F_p \end{bmatrix}^T \tag{2.20}$$

and m is the measurement noise.

To derive a simple model the stabilizing circuit can be divided into two sets of coils: active coils and passive coils. Let us assume that there is only one external applied voltage V_a to supply the active coils (as there is in every operating tokamak) and that the vector of the currents flowing in the stabilizing circuit is composed of two currents: I_a for the active coils and I_v for the passive coils (the same assumption was used in [Noll89], [Noll91a], [Lister90], [Lazarus90], [Browne90]). With this simplification the matrices of equations (2.14) and (2.15) become

$$\mathbf{L} = \begin{bmatrix} L_{aa} & L_{av} \\ L_{va} & L_{vv} \end{bmatrix}$$

$$\mathbf{R} = \begin{bmatrix} R_{aa} & 0 \\ 0 & R_{vv} \end{bmatrix} \tag{2.21}$$

$$\acute{\mathbf{L}}_p = \begin{bmatrix} \acute{L}_{ap} & \acute{L}_{vp} \end{bmatrix}.$$

The vacuum vessel acts as a screen for the plasma to fast changes in the external applied voltage V_a. To include this screening effect the following condition must be satisfied

$$L_{av}\acute{L}_{vp} = L_{vv}\acute{L}_{ap}. \tag{2.22}$$

Defining

$$k_{av} = \frac{L_{av}^2}{L_{aa}L_{vv}}$$

$$M_{vp} = \frac{A_{pp}^{''}L_{vv}}{\left(L_{vp}^{'}\right)^2}$$

$$M_{ap} = \frac{A_{pp}^{''}L_{aa}}{\left(L_{ap}^{'}\right)^2} \tag{2.23}$$

$$K_a = \frac{1}{L_{aa}\left(1 - k_{av}\right)},$$

using the model structure (2.18) and substituting the matrices (2.21) into the matrices (2.19),

applying the condition (2.22), the simplified model equations are expressed by

$$\begin{cases} \begin{bmatrix} \dot{I}_a \\ \dot{I}_v \end{bmatrix} = \mathbf{A}^s \begin{bmatrix} I_a \\ I_v \end{bmatrix} + \mathbf{B}^s \begin{bmatrix} V_a \\ \dot{F}_p \\ F_p \end{bmatrix} \\ z_p^c = \mathbf{C}^s \begin{bmatrix} I_a \\ I_v \end{bmatrix} + \mathbf{D}^s \begin{bmatrix} V_a \\ \dot{F}_p \\ F_p \end{bmatrix} + m \end{cases} \tag{2.24}$$

where

$$\mathbf{A}^s = \frac{1}{1-k_{av}} \begin{bmatrix} -\dfrac{R_{aa}}{L_{aa}} & \dfrac{R_{vv}}{L_{av}} k_{av} \\ \dfrac{R_{aa}}{L_{av}} k_{av} & -\dfrac{R_{vv}}{L_{vv}} \dfrac{k_{av} - M_{vp}}{1 - M_{vp}} \end{bmatrix}$$

$$\mathbf{B}^s = \begin{bmatrix} K_a & 0 & 0 \\ -\dfrac{k_{av}}{L_{av}(1-k_{av})} & \dfrac{1}{\acute{L}_{vp}(1-M_{vp})} & 0 \end{bmatrix} \tag{2.25}$$

$$\mathbf{C}^s = \begin{bmatrix} -\dfrac{\acute{L}_{ap}}{A''_{pp}} & -\dfrac{\acute{L}_{vp}}{A''_{pp}} \end{bmatrix}$$

$$\mathbf{D}^s = \begin{bmatrix} 0 & 0 & A''^{-1}_{pp} \end{bmatrix}.$$

Defining

$$T_v = L_{vv} \frac{1 - k_{av}}{R_{vv}}$$

$$a_0 = \frac{1}{T_v} \frac{M_{vp} - k_{av}}{1 - M_{vp}} \tag{2.26}$$

$$a_1 = \frac{R_{aa}}{L_{aa}(1 - k_{av})}$$

$$\alpha = a_0 + \frac{k_{av}}{T_v}$$

the characteristic polynomial of A^s is

$$\gamma^2 - (a_0 - a_1)\gamma - \alpha a_1 = 0. \tag{2.27}$$

For an elongated plasma in a resistive vacuum vessel the conditions

$$\begin{aligned} k_{av} &< 1 \\ M_{vp} &< 1 \\ \frac{R_{aa}}{R_{vv}} &< \frac{A''_{pp}A_{aa} - \acute{L}^2_{ap}}{\acute{L}^2_{vp} - A''_{pp}A_{vv}} \end{aligned} \tag{2.28}$$

are true ([Noll86] and [Noll91a]). Therefore

$$\begin{aligned} (a_0 - a_1) &> 0 \\ (a_0 - a_1) &> 0 \\ (a_0 - a_1)^2 + 4\alpha a_1 &> 0 \end{aligned}$$

and equation (2.27) has two real roots of which one is positive and one negative:

$$\gamma_{1,2} = \frac{1}{2}\left[a_0 - a_1 \pm \sqrt{(a_0 - a_1)^2 + 4\alpha a_1}\right]. \tag{2.29}$$

Therefore the matrix A^s has one unstable pole $\gamma_p = \gamma_1$ and one stable pole $\gamma_n = -\gamma_2$. The roots (2.29) depend on the value of A''_{pp}. In Figure 2.4 the solution of equation (2.27) for different values of A''_{pp} is shown using the parameters of the JET tokamak (see Table A.2 in Section A.3 of Appendix A). A solution for z^c_p can be readily found by using the Laplace transform of equations (2.24)

$$z^c_p(s) = \frac{K_1}{(s-\gamma_p)(s+\gamma_n)} V_a(s) + \frac{K_2\left(s^2 + b_1 s + b_o\right)}{(s-\gamma_p)(s+\gamma_n)} F_p(s) + m(s) \tag{2.30}$$

where

$$\begin{aligned} K_1 &= \frac{\acute{L}_{vp} L_{av}}{L_{vv} A''_{pp}} K_a \alpha \\ K_2 &= \frac{1}{A''_{pp}} \frac{M_{vp} - 2}{M_{vp} - 1} \\ b_1 &= \frac{(M_{vp} - 2)(a_1 - a_0) - \alpha}{M_{vp} - 2} \end{aligned}$$

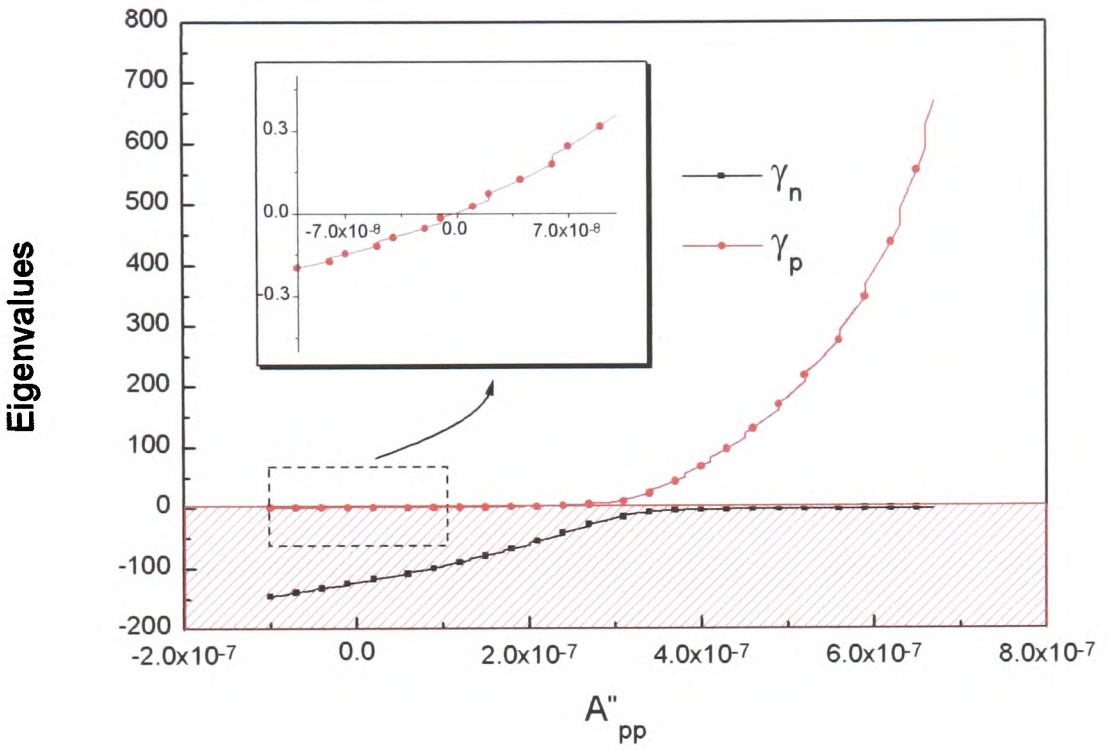


Figure 2.4: Eigenvalues deriving from equation (2.26) versus A''_{pp}

$$b_0 = a_1 \alpha \frac{1 - M_{vp}}{M_{vp} - 2}$$

In addition to the simplified model described above it is necessary to include the effect of the field penetration through the vacuum vessel and the mechanical shell. Given the complexity of the structure, see Figure A.6 in Section A.3 of Appendix A, it is very difficult to give exact analytical formulas. An attempt was made in [Core88] but the predicted time constants are very long compared to the one measured and reported below. The basic effect of the field penetration is that the magnetic field generated by the active coils, typically located outside the vacuum vessel and the supporting mechanical shell, is delayed. The average values of the measured delay τ_v from when the voltage is applied to the active coils to when the plasma starts moving for JET and for COMPASS-D are

$$\bar{\tau}_v|_{JET} \simeq 200 \cdot 10^{-6}\,[s] \text{ and } \bar{\tau}_v|_{COMPASS-D} \simeq 100 \cdot 10^{-6}\,[s]\,.$$

The values are estimated by taking the average of the time delays measured for several experiments. Equation (2.20) is then modified to include the effect of the field penetration

through the vacuum vessel and the mechanical shell

$$\mathbf{u}(t) = \left[\; V_a(t - \bar{\tau}_v) \quad \frac{dF_p(t)}{dt} \quad F_p(t) \; \right]^T . \tag{2.31}$$

By substituting the Laplace transform of equation (2.31) into equation (2.30) the vertical position can be estimated using the model

$$z_p^c(s) = \frac{K_1 e^{-s\bar{\tau}_v}}{(s-\gamma_p)(s+\gamma_n)} V_a(s) + \frac{K_2 (s^2 + b_1 s + b_o)}{(s-\gamma_p)(s+\gamma_n)} F_p(s) + m(s) . \tag{2.32}$$

When the assumption of up/down symmetric plasma does not hold, for example, in divertor plasma configurations, it can be observed from experiments that with an x-point in the lower part of the vacuum vessel upward movements have a faster dynamic than downward ones. This effect can be explained by the fact that the percentage of plasma volume in the upper part of the vacuum vessel is greater and therefore, when moving upwards the amount of current interacting with the radial magnetic field is higher. For example it is like having a ball which can fall from the edge of a hill with two different slopes as shown in Figure 2.5. This additional non-linear effect is included in the simple model given in equation (2.32) by allowing γ_p to have a different value for upward and downward movements.

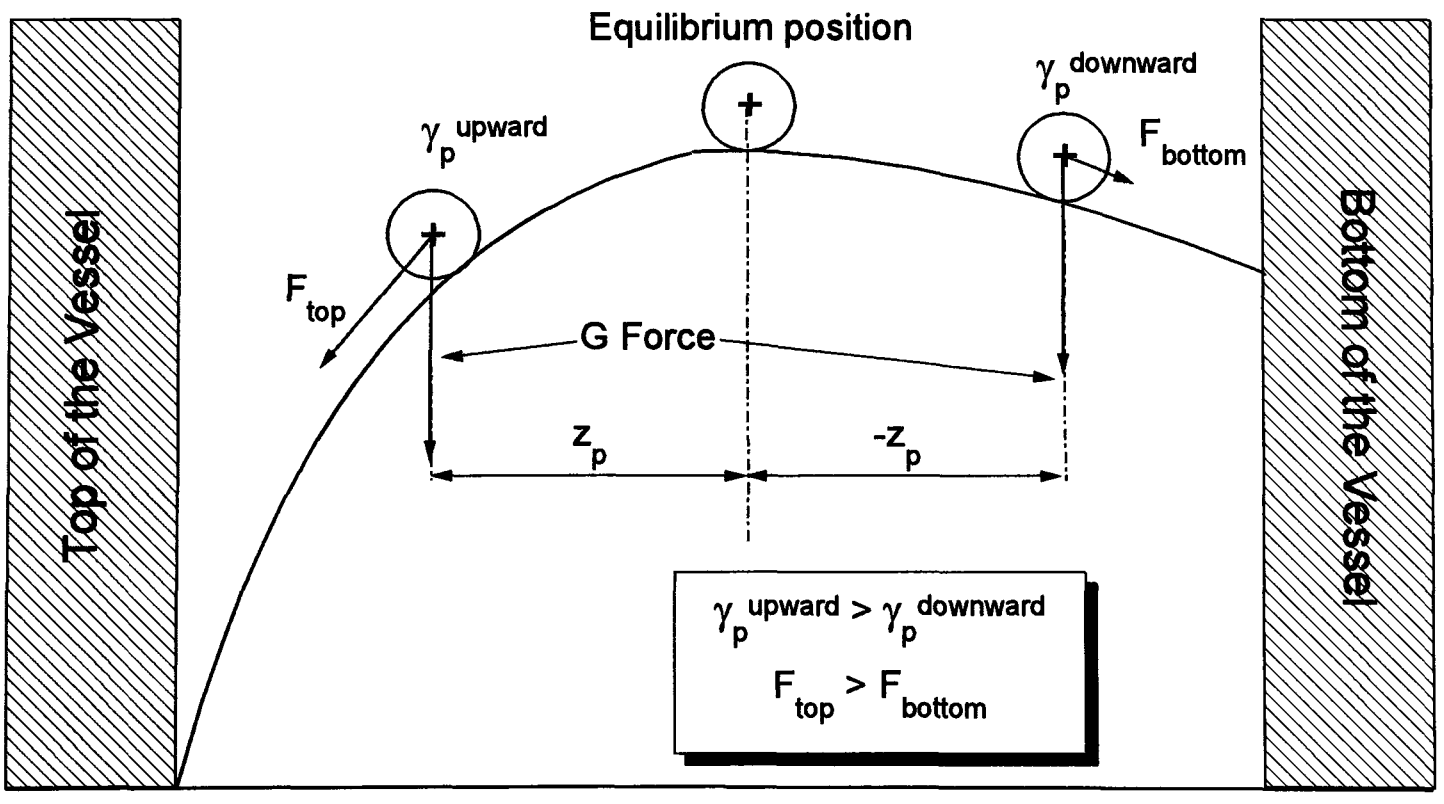


Figure 2.5: Example of a model having two different growth rates and similarities with the plasma in the vessel.

It can be concluded that a simplified relationship between a control amplifier, an external force disturbance and a measurement noise and the plasma vertical position can be expressed as

$$z_p^c(s) = \frac{K_1 e^{-s\tau_v}}{(s-\gamma_p)(s+\gamma_n)} u(s) + \frac{K_2 (s^2 + b_1 s + b_o)}{(s-\gamma_p)(s+\gamma_n)} d(s) + m(s) \tag{2.33}$$

where $u = V_a$ is the external input, $d = F_p$ is the external force disturbance and m is the measurement noise, τ_v is a pure time delay. For the A''_{pp} of interest ($A''_{pp} > 4 \cdot 10^{-7}\,[Hm^{-2}]$) a variation of γ_n has no significant effect on the open loop response because $|\gamma_n| << |\gamma_p|$. Figure 2.4 shows that for any significantly elongated plasma ($\gamma_p > 100\,[s^{-1}]$) $|\gamma_n| << |\gamma_p|$. Therefore it is assumed that the only plasma parameter that can vary is the growth rate γ_p which depends on the plasma configuration and can change during an experiment.

2.3 A model of the measurement system

The plasma vertical position is typically derived from magnetic sensors distributed inside or outside the vacuum vessel.

On the JET Tokamak the vertical position is derived from the tangential and normal magnetic field components, B_t and B_n respectively, measured by the pick-up coils and the saddle loops located as shown in Figure 2.6. In particular, the pick-up coils, which are located around two opposite poloidal sections (octants 3 and 7, see Section A.3 of Appendix A), measure the time derivative of B_t, and the saddle loops, which have the same spacial distribution, measure the time derivative of B_n. The method to estimate the vertical position from the magnetic signals, named the current moment method, is based on the multipole moment theory first introduced in [Zakharov73] and revisited in [Aikawa76] and [Ogata77]. The current moment centroid $Z_c I_\Phi$ is related to B_n and B_t as follows:

$$Z_c I_\Phi = \frac{1}{\mu} \oint_l \left[B_t Z - R \log\left(\frac{R}{R_0}\right) B_n \right] dl \tag{2.34}$$

where I_Φ is the total toroidal current flowing in the closed path l, namely the sum of the plasma current I_p and the four divertor currents I_{D_i}. $Z_c I_\Phi$ is related to I_p and to I_{D_i} as follows:

$$Z_c I_\Phi = z_p I_p + \sum_{i=1}^{4} z_{D_i} I_{D_i} \tag{2.35}$$

where z_{D_i} is the $i-th$ divertor coil current centroid. The derivative of equations (2.34) and

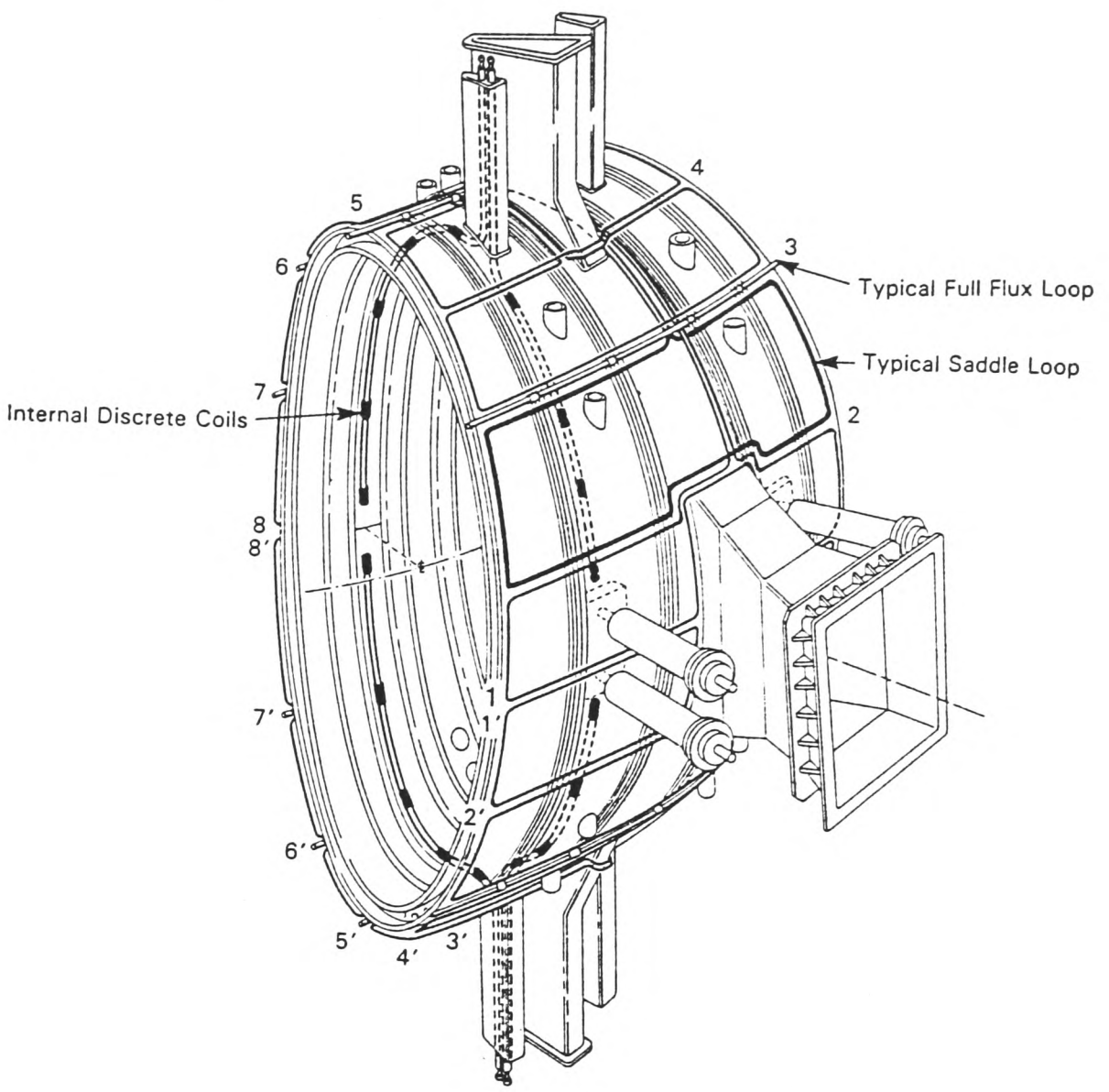


Figure 2.6: Magnetic sensors - Pick-up coils and Saddle loops

(2.35) are given by:

$$\frac{d}{dt}\left(Z_c I_\Phi\right) = \frac{1}{\mu}\oint_l \left[Z\frac{dB_t}{dt} - R\log\left(\frac{R}{R_0}\right)\frac{dB_n}{dt}\right] dl \tag{2.36}$$

$$\frac{d}{dt}\left(Z_c I_\Phi\right) = I_p\frac{dz_p}{dt} + z_p\frac{dI_p}{dt} + \sum_{i=1}^{4} z_{D_i}\frac{dI_{D_i}}{dt} + \sum_{i=1}^{4} I_{D_i}\frac{dz_{D_i}}{dt} \tag{2.37}$$

The last term in equation (2.37) is identically zero because the divertor coils are fixed. Substituting (2.37) into (2.36) we can obtain $\frac{dz_p}{dt}$:

$$I_p\frac{dz_p}{dt} = \left\{\frac{1}{\mu}\oint_l \left[Z\frac{dB_t}{dt} - R\log\left(\frac{R}{R_0}\right)\frac{dB_n}{dt}\right] dl - z_p\frac{dI_p}{dt} - \sum_{i=1}^{4} z_{D_i}\frac{dI_{D_i}}{dt}\right\} \tag{2.38}$$

By substituting a discretization of the line integral and adopting the notation $\frac{dx}{dt} = \dot{x}$ equation (2.38) becomes:

$$I_p \dot{z}_p^m = \left\{ \sum_{i=1}^{4} a_i V_{p_i}^{\dot{z}_p} + \sum_{i=1}^{4} b_i V_{s_i}^{\dot{z}_p} - z_p \dot{I}_p - \sum_{i=1}^{4} \gamma_i \dot{I}_{D_i} \right\} \tag{2.39}$$

where

- $\dot{z}_p^m$ is the measured plasma vertical velocity.
- $V_{p_i}^{\dot{z}_p}$ is the $i-th$ analogue weighted sum of the signals measured by the pick-up coils as in [Milani92].
- $V_{s_i}^{\dot{z}_p}$ is the $i-th$ analogue weighted sum of the signals measured by the saddle loops as in [Milani92].

A measurement of the plasma vertical position z_p^m is obtained by integrating equation (2.39). The divertor current derivatives are not measured but derived from the divertor pick-up coils signals ($V_{p_i}^{\dot{I}_D}$). These transducers are located at the divertor coils busbars outside the torus and detect the magnetic flux variations due to the divertor current derivatives. The relation between the magnetic flux and the divertor current can be expressed as

$$\dot{I}_{D_i} = \mathbf{D}_d^{-1} V_{p_i}^{\dot{I}_D} \tag{2.40}$$

where $\mathbf{D}_d$ is the coupling matrix between the divertor pick-up coils and the divertor busbars. The plasma current derivative itself is not directly measured but obtained from the weighted sum of the magnetic pick-up coils and compensation for the divertor current derivatives. If $V_{p_i}^{\dot{I}_p}$ are the voltages measured after the analogue signal conditioning, the plasma current derivative $\dot{I}_p$ can be calculated from

$$\dot{I}_p = \sum_{i=1}^{4} c_i V_{p_i}^{\dot{I}_p} - \sum_{i=1}^{4} \beta_i \dot{I}_{D_i} \tag{2.41}$$

The parameters a_i b_i and c_i have been tuned during operations [Garribba94]. The measurement of the plasma vertical position is related to the actual vertical position by the equation

$$z_p^m = z_p + m_{z_p} + m_{ELM} + m_{600} + m_{n=1} \tag{2.42}$$

where

- m_{z_p} is the measurement noise due to the approximations and errors in equation (2.39). The effect of m_{z_p} can be evaluated experimentally. It also depends on the accuracy of the magnetic transducer positioning.

- m_{ELM} is due to the plasma Edge Localized Modes and m_{600} to the characteristics of the thyristor power supplies. The effect of m_{ELM} and m_{600} is described in Section 2.4.

- $m_{n=1}$ is the measurement noise due to errors induced by the plasma non-axisymmetric modes with $n = 1$. To eliminate the pick-up from the $n = 1$ mode the measurements are taken at two opposite octants. However errors in the cancellations of the $n = 1$ mode can be seen on the measurement even if it has a minimal impact of the stabilization. The modes with $n > 1$ are either highly unstable or very difficult to quantify (see Figure 2.7). In both cases they cannot be controlled. This noise component is normally negligible when compared to the other measurement noises.

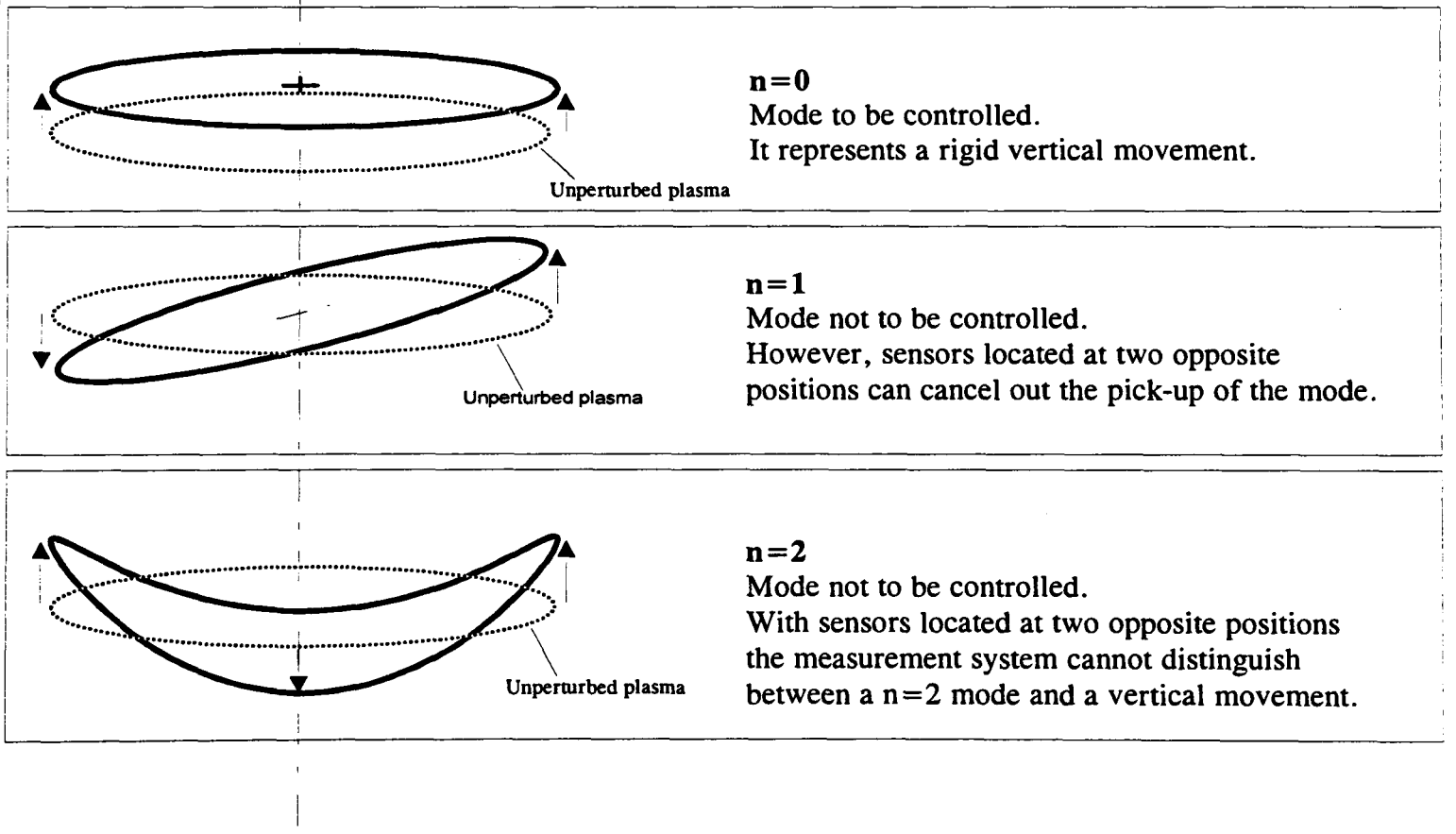


Figure 2.7: Description of plasma modes

On the COMPASS-D tokamak the vertical position is derived from four toroidally continuous flux loops (FL) outside the vacuum vessel. By integrating the difference between the

voltage signals induced in the upper FLs and those induced in the lower FLs, a signal closely proportional to the vertical position is obtained. The plasma vertical velocity is derived from eight Internal Partial Rogowski (IPR) coils located inside the vacuum vessel. The difference between the voltage signals induced in the upper IPRs and those induced in the lower IPRs is proportional to the vertical velocity (more details can be found in [Vyas96]).

Overall the performance of the JET and COMPASS-D measurement systems are very similar. The measurement of the plasma vertical position on COMPASS-D is still related to the actual vertical position by equation (2.42) however the term $m_{n=1}$ can be quite substantial because the magnetic sensors are located at only one toroidal position.

2.4 Deriving models for the disturbances

In a confined plasma there is a complex activity [Wesson87]. Internal plasma events or modes can be considered as disturbances in the simplified plasma position model. Sometimes these modes have no effect on the plasma position itself but can be sensed by the magnetic sensors, resulting in measurement noise.

There are two major sources of disturbances to be considered for the vertical position model:

1. The Edge Localized Mode (ELM)

2. The Thyristor power supplies

2.4.1 ELM disturbances

The ELMs are MHD instabilities occurring at the edge of H-mode plasmas (see Section A.2 of Appendix A). They lead to a loss of energy and particles from the plasma edge in a time scale of milliseconds. ELMs can be revealed from the intensity of the H_α emission (H_α signals) and appear as spikes separated in time as shown in Figure 2.8 (JET experiment #40452 and COMPASS-D experiment #17724).

There are various hypotheses in the literature on the effect of ELMs on the vertical position [Ali-Arshad96] [Lingertat95] [Fielding96]. The hypothesis that best fits the experimental observations and can be repeated by means of simulations is that the plasma current density and the pressure profile assume a new equilibrium configuration during the energy dissipation

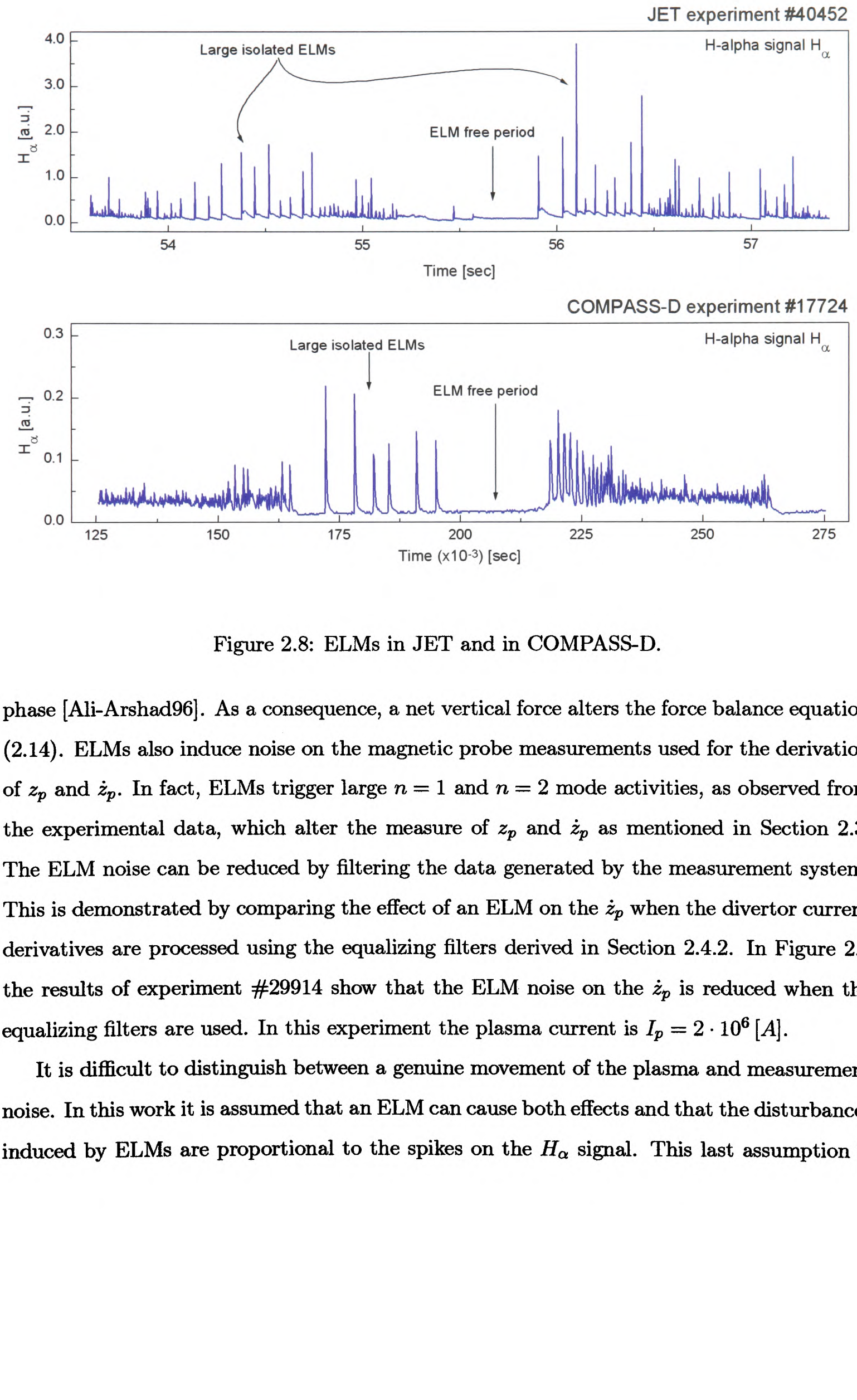


Figure 2.8: ELMs in JET and in COMPASS-D.

phase [Ali-Arshad96]. As a consequence, a net vertical force alters the force balance equation (2.14). ELMs also induce noise on the magnetic probe measurements used for the derivation of z_p and $\dot{z}_p$. In fact, ELMs trigger large $n = 1$ and $n = 2$ mode activities, as observed from the experimental data, which alter the measure of z_p and $\dot{z}_p$ as mentioned in Section 2.3. The ELM noise can be reduced by filtering the data generated by the measurement system. This is demonstrated by comparing the effect of an ELM on the $\dot{z}_p$ when the divertor current derivatives are processed using the equalizing filters derived in Section 2.4.2. In Figure 2.9 the results of experiment #29914 show that the ELM noise on the $\dot{z}_p$ is reduced when the equalizing filters are used. In this experiment the plasma current is $I_p = 2 \cdot 10^6\,[A]$.

It is difficult to distinguish between a genuine movement of the plasma and measurement noise. In this work it is assumed that an ELM can cause both effects and that the disturbances induced by ELMs are proportional to the spikes on the H_α signal. This last assumption is

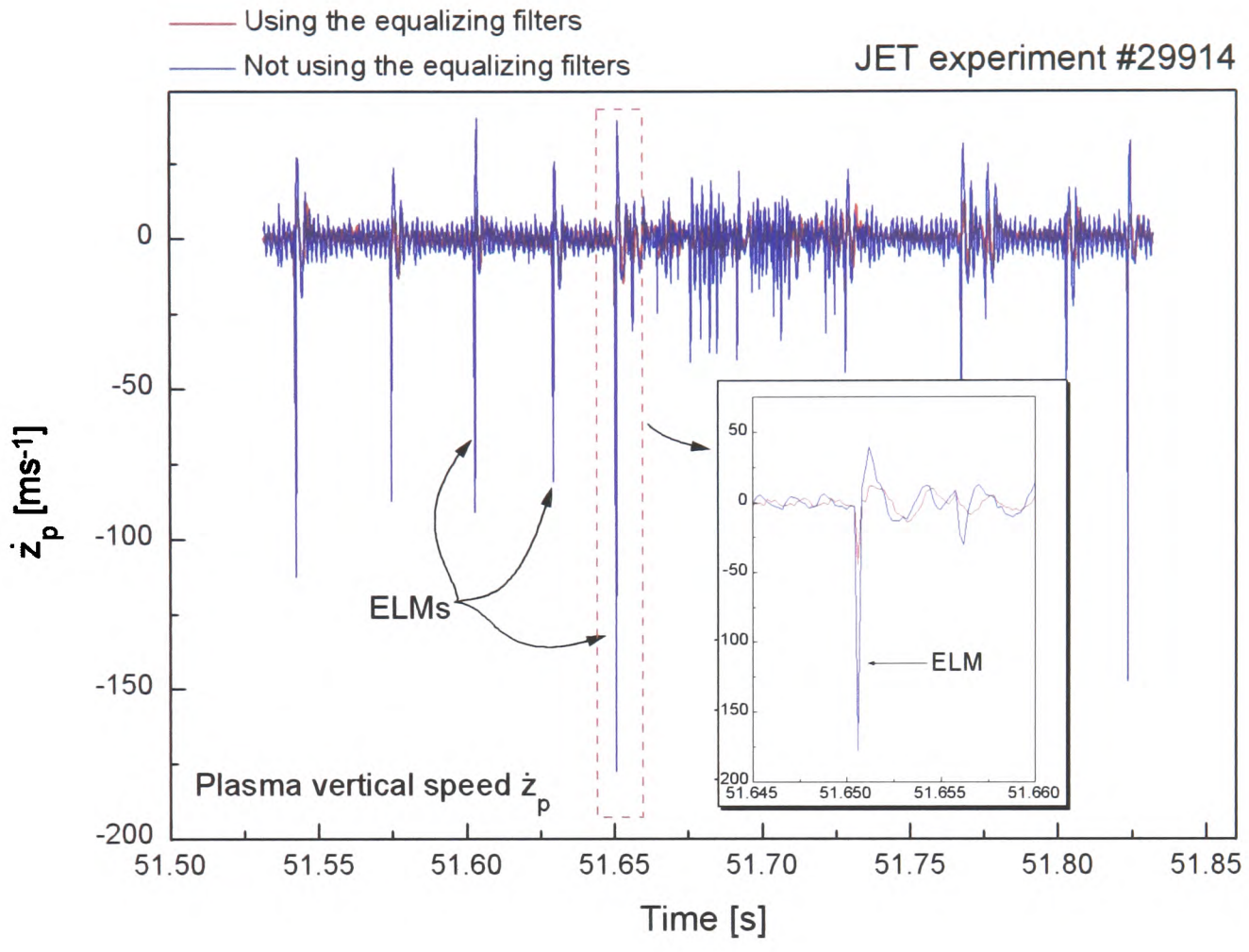


Figure 2.9: The effect of an ELM on the $\dot{z}_p$ when the equalizing filters are used (JET experiment #29914).

verified in Section 2.6. The spikes that characterize the ELMs can be represented by

$$d_{ELM}(t) = \bar{d}_{ELM} \underset{\tau_3}{rep} \left[f(t, \tau_1, \tau_2) \right] \text{ with } (\tau_1 - \tau_2) \leq \bar{\tau}_{ELM} \text{ and } \tau_3 \geq \bar{\tau}_{rep} \tag{2.43}$$

where the $rep(\cdot)$ function is the repetition function of period τ_3, $\bar{\tau}_{ELM}$ is the observed average duration of an ELM, $\bar{\tau}_{rep}$ is the observed average ELMs' repetition rate, $f(t, \tau_1, \tau_2)$ is the function

$$f(t, \tau_1, \tau_2) = e^{-\frac{t}{\tau_1}} - e^{-\frac{t}{\tau_2}} \text{ where } \tau_1 > \tau_2 \tag{2.44}$$

and $\bar{d}_{ELM}$ is the ELM's observed maximum amplitude. For example, in Figure 2.10, a real ELM is compared to $d_{ELM}(t)$. It is also assumed that the ELMs' effect on the measurements can be characterized in the same way:

$$m_{ELM}(t) = \bar{m}_{ELM} \underset{\tau_3}{rep} \left[f(t, \tau_1, \tau_2) \right] \text{ with } (\tau_1 - \tau_2) \leq \bar{\tau}_{ELM} \text{ and } \tau_3 \geq \bar{\tau}_{rep} \tag{2.45}$$

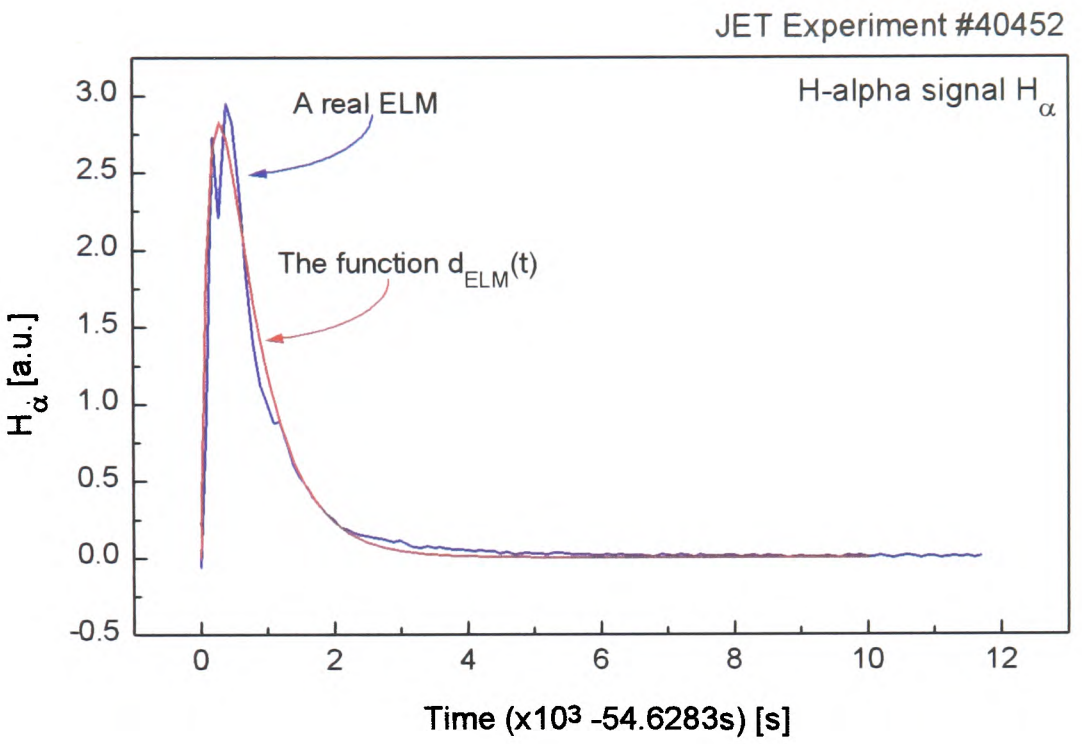


Figure 2.10: Comparison between a real ELM (JET experiment #40452) and the function $d_{ELM}(t) = 6.5 \cdot \left(e^{-\frac{t}{6 \cdot 10^{-4}}} - e^{-\frac{t}{1.7 \cdot 10^{-4}}}\right)$.

where, from the observation of the experimental data, usually $\bar{m}_{ELM} < d_{ELM}$.

2.4.2 Thyristor power supplies disturbances

The thyristor power supplies are typically *12 pulse* thyristor rectifiers. Since the firing pulses are synchronized with the AC frequency of $50\,[Hz]$, a large $600\,[Hz]$ component with its multiple harmonics is picked up by the magnetic sensors at the divertor coils busbars. The $600Hz$ ripple in the power supply's voltages also moves the actual vertical position in up/down asymmetric plasma scenarios. In fact in these scenarios the ripple's effect is not cancelled out by the symmetric configuration. The frequency spectra of the control signals to the amplifiers for the JET and the COMPASS-D Tokamak are shown in Figure 2.11.

In JET the problem of the $600Hz$ ripple is even more severe because of the presence of the divertor coils inside the vacuum vessel. In fact, as it appears from the experiment results, the divertor current derivative measurements $\dot{I}_{D_i}$ need some corrections. In experiment #29279 the values I_p, z_p and $\dot{z}_p$ are zero. The equations (2.39) and (2.41) in this case should become

$$0 = \sum_{i=1}^{4} V_{p_i}^{\dot{z}_p} + \sum_{i=1}^{4} V_{s_i}^{\dot{z}_p} - \sum_{i=1}^{4} \gamma_i \dot{I}_{D_i} \tag{2.46}$$

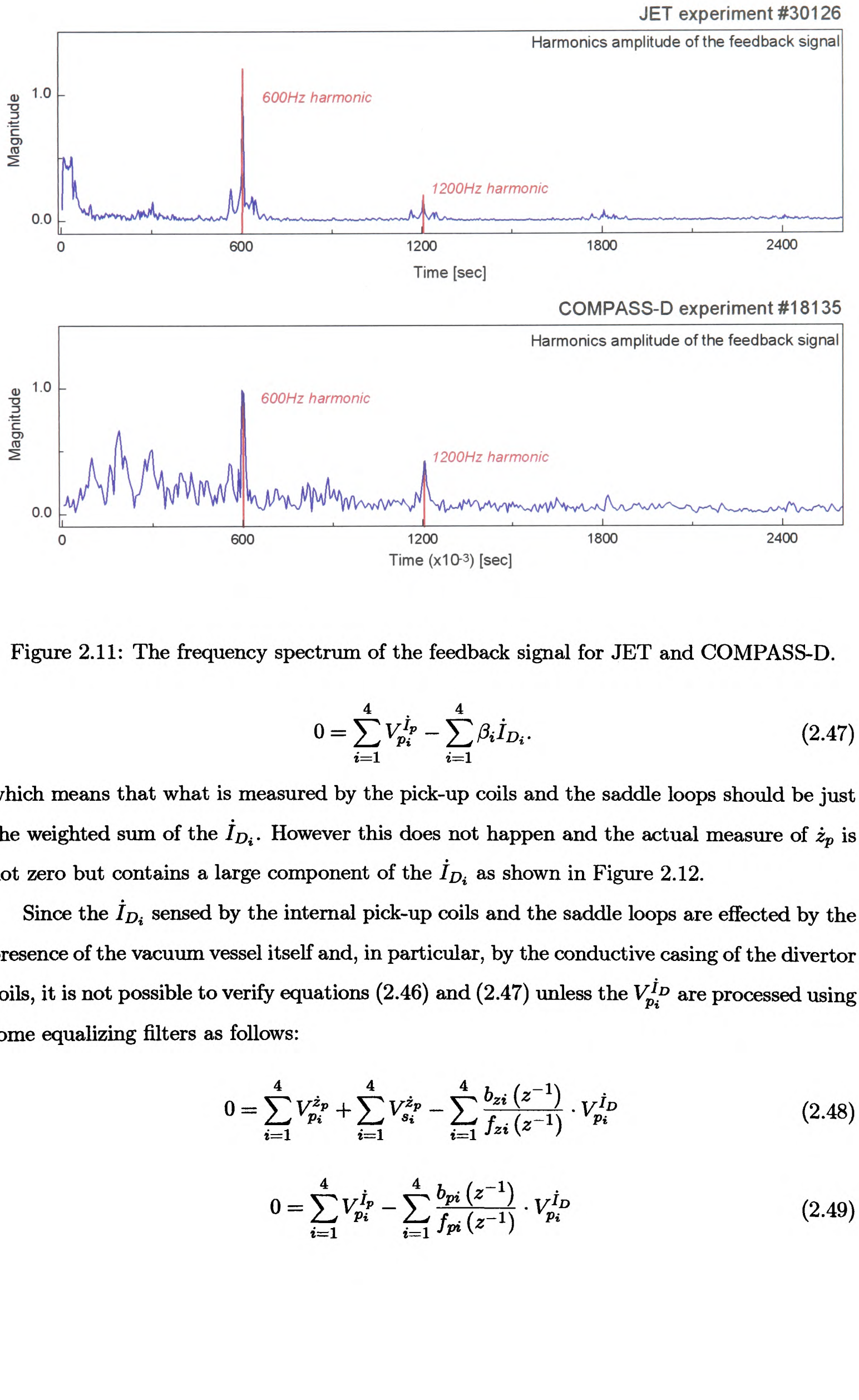


Figure 2.11: The frequency spectrum of the feedback signal for JET and COMPASS-D.

$$0 = \sum_{i=1}^{4} V_{p_i}^{\dot{I}_p} - \sum_{i=1}^{4} \beta_i \dot{I}_{D_i}. \tag{2.47}$$

which means that what is measured by the pick-up coils and the saddle loops should be just the weighted sum of the $\dot{I}_{D_i}$. However this does not happen and the actual measure of $\dot{z}_p$ is not zero but contains a large component of the $\dot{I}_{D_i}$ as shown in Figure 2.12.

Since the $\dot{I}_{D_i}$ sensed by the internal pick-up coils and the saddle loops are effected by the presence of the vacuum vessel itself and, in particular, by the conductive casing of the divertor coils, it is not possible to verify equations (2.46) and (2.47) unless the $V_{p_i}^{\dot{I}_D}$ are processed using some equalizing filters as follows:

$$0 = \sum_{i=1}^{4} V_{p_i}^{\dot{z}_p} + \sum_{i=1}^{4} V_{s_i}^{\dot{z}_p} - \sum_{i=1}^{4} \frac{b_{zi}\left(z^{-1}\right)}{f_{zi}\left(z^{-1}\right)} \cdot V_{p_i}^{\dot{I}_D} \tag{2.48}$$

$$0 = \sum_{i=1}^{4} V_{p_i}^{\dot{I}_p} - \sum_{i=1}^{4} \frac{b_{pi}\left(z^{-1}\right)}{f_{pi}\left(z^{-1}\right)} \cdot V_{p_i}^{\dot{I}_D} \tag{2.49}$$

Essentially the constants γ_i and β_i are replaced by transfer functions. The so called Box-Jenkins model structure is used to identify the filters [Ljung87]:

$$y(t) = \frac{B_1(z^{-1})}{F_1(z^{-1})}u(t-nk_1) + \ldots + \frac{B_{nu}(z^{-1})}{F_{nu}(z^{-1})}u(t-nk_{nu}) + \frac{C(z^{-1})}{D(z^{-1})}e(t) \tag{2.50}$$

The effect of the vacuum vessel and of the casing of the divertor coils can be modelled by 2^{nd} order transfer functions. This can be explained by observing that $\dot{I}_{D_i}$ inside the vacuum vessel are screened and therefore the magnetic field measured by the internal pick-up coils and the saddle loops is affected by induced currents which can be modelled by a 2^{nd} order system. The transfer functions are estimated from data collected over a 0.1 seconds time interval for experiment #29279 and then they are applied to the same experiment over a different time interval. The results are presented in Figure 2.12. Under the given experiment conditions, an ideal measurement system would measure a $\dot{z}_p = 0$. This is clearly not the case when the equalizing filter are not used. Applying the filters the effect is reduced by about the 90% showing that the equalizing filters are very efficient. The effect of the filters during a standard plasma experiment (during JET experiment #29327 the plasma current is $I_p = 2 \cdot 10^6\,[A]$) is shown in Figure 2.13. The results show a net reduction of the $600Hz$ noise.The transfer functions, identified using MATLAB and the System Identification toolbox, are listed below:

$$\frac{b_{z1}(z^{-1})}{f_{z1}(z^{-1})} = \frac{0.0615}{(1-0.9499z^{-1})(1-0.1967z^{-1})}$$

$$\frac{b_{z2}(z^{-1})}{f_{z2}(z^{-1})} = \frac{0.0474}{[1-(0.6263+0.2704i)z^{-1}][1-(0.6263-0.2704i)z^{-1}]}$$

$$\frac{b_{z3}(z^{-1})}{f_{z3}(z^{-1})} = \frac{0.1697}{[1-(0.4493+0.5771i)z^{-1}][1-(0.4493-0.5771i)z^{-1}]}$$

$$\frac{b_{z4}(z^{-1})}{f_{z4}(z^{-1})} = \frac{0.1538}{[1-(0.6541+0.3592i)z^{-1}][1-(0.6541-0.3592i)z^{-1}]}$$

$$\frac{b_{p1}(z^{-1})}{f_{p1}(z^{-1})} = \frac{0.0145}{(1+0.8707z^{-1})(1+0.1723z^{-1})}$$

$$\frac{b_{p2}(z^{-1})}{f_{p2}(z^{-1})} = \frac{-0.0023}{(1-0.7741z^{-1})(1-0.4959z^{-1})}$$

$$\frac{b_{p3}(z^{-1})}{f_{p3}(z^{-1})} = \frac{-0.0045}{[1-(0.6173+0.5061i)z^{-1}][1-(0.6173-0.5061i)z^{-1}]}$$

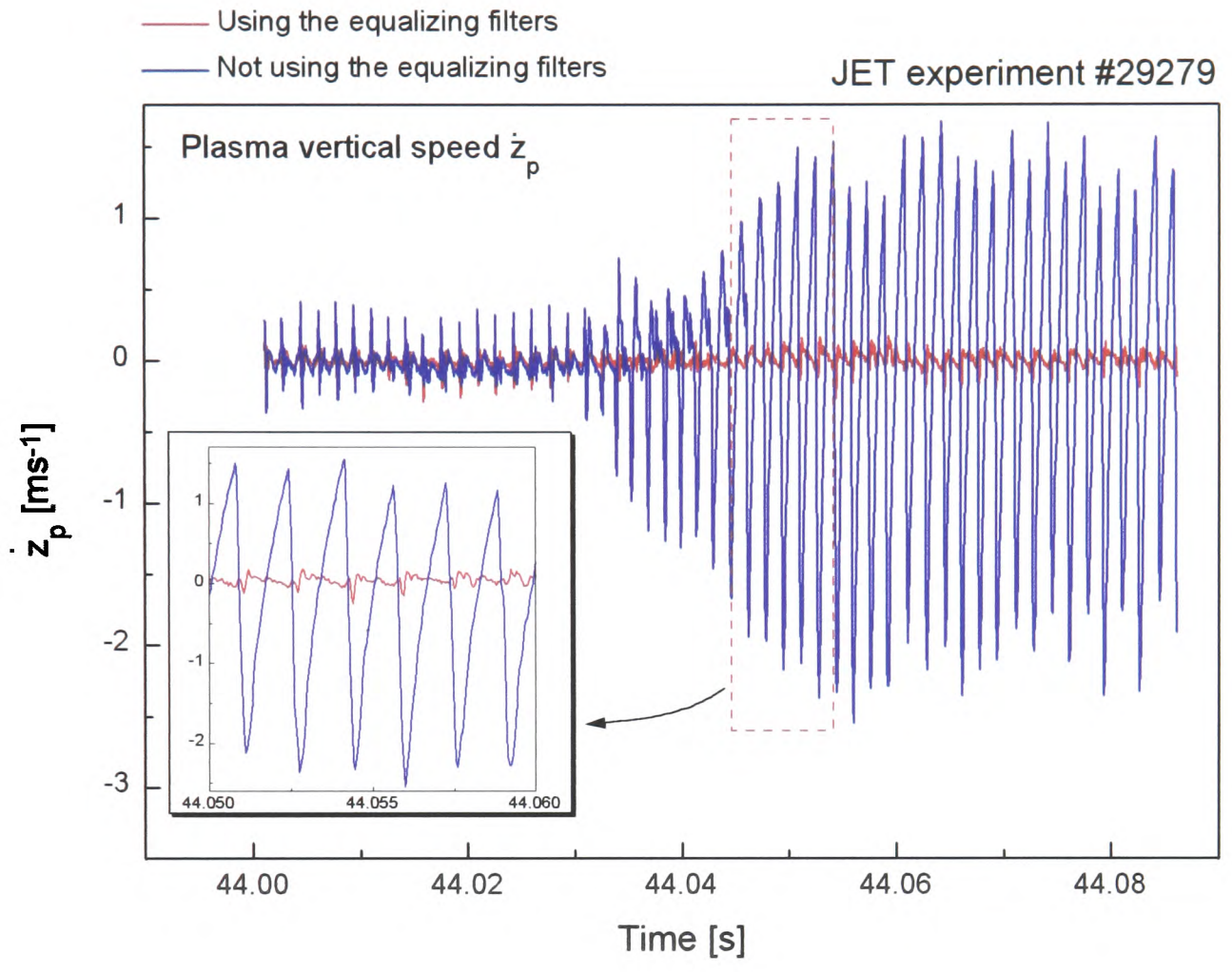


Figure 2.12: Comparison between the measured value of $\dot{z}_p$ with and without equalizing filters (JET experiment #29279).

$$\frac{b_{p4}\left(z^{-1}\right)}{f_{p4}\left(z^{-1}\right)} = \frac{-0.0080}{\left[1-\left(0.7811+0.2632i\right)z^{-1}\right]\left[1-\left(0.7811-0.2632i\right)z^{-1}\right]}$$

In each case, the sampling frequency is $20 \cdot 10^3\,[Hz]$.

In this work it is assumed that the $600Hz$ ripple can cause both noise on the measurements and a movement of the plasma vertical position. Both the effects are assumed to be RMS bounded

$$\|d_{600}(t)\|_{RMS} < \bar{d}_{600} \tag{2.51}$$

$$\|m_{600}(t)\|_{RMS} < \bar{m}_{600} \tag{2.52}$$

where the $\|\cdot\|_{RMS}$ is the RMS norm operator and $\bar{d}_{600}$ and $\bar{m}_{600}$ are the maximum observed RMS values. From the experimental data, it can be observed that $\bar{m}_{600} >> \bar{d}_{600}$.

After characterizing the disturbance/noise behaviour it is necessary to model how their

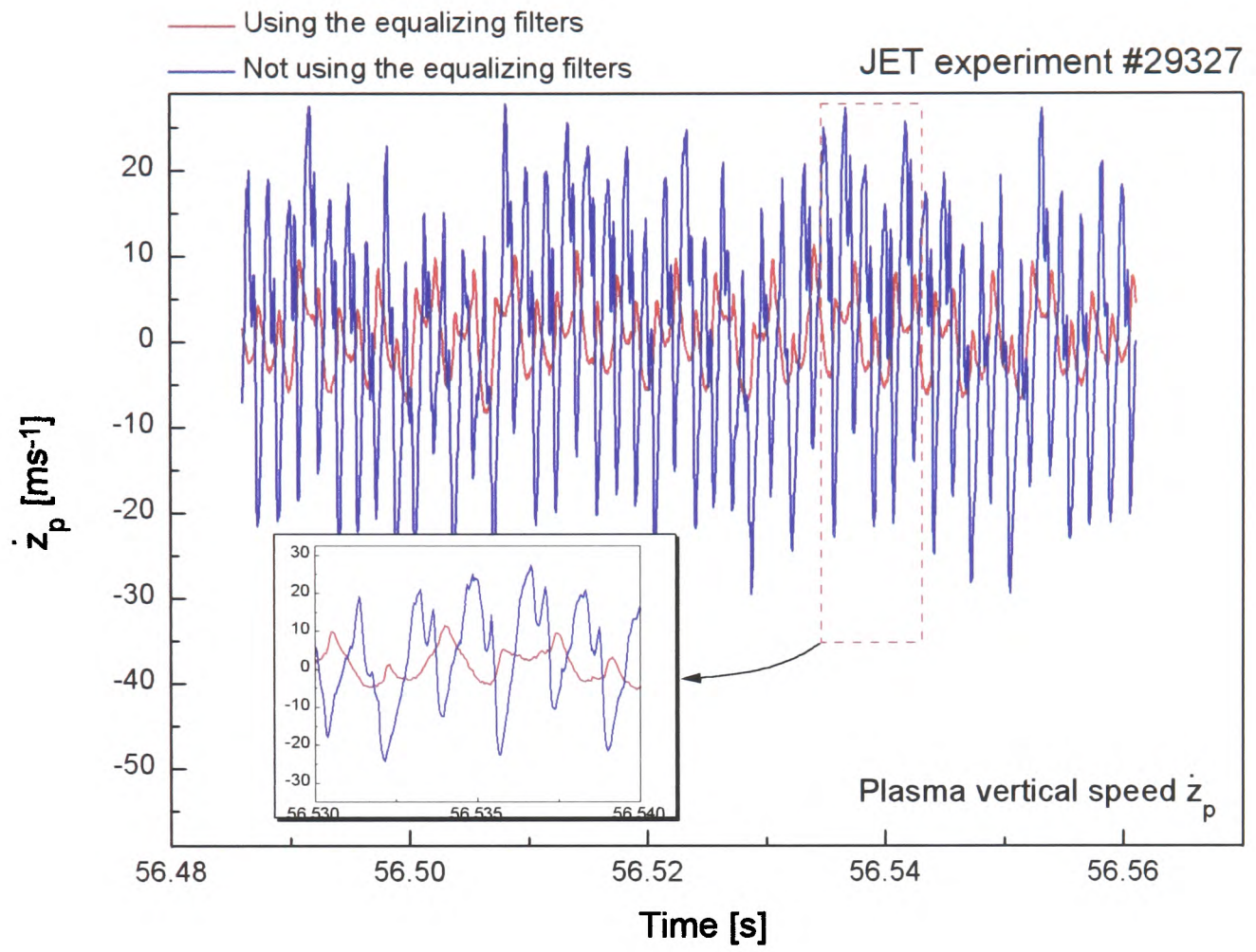


Figure 2.13: Comparison between the measured value of $\dot{z}_p$ with and without equalizing filters (JET experiment #29327).

effects enter the vertical position model described by equation (2.33). As mentioned before, the disturbances induced by an ELM enter directly as an additional net vertical force in the force balance equilibrium equation (2.14). In a similar way, the disturbances generated by the $600Hz$ ripple modify the force balance equilibrium. Hence it may be assumed that

$$d(t) = F_p(t) = d_{ELM}(t) + d_{600}(t - \bar{\tau}_v) \tag{2.53}$$

The measurement noise is simply

$$m(t) = m_{ELM}(t) + m_{600}(t). \tag{2.54}$$

A schematic diagram of the plasma vertical position model described by equation (2.33) including the disturbances and measurement noise is shown in Figure 2.14.

The values of the parameters $\bar{\tau}_{ELM}$, $\bar{\tau}_{rep}$, $\bar{d}_{ELM}$, $\bar{d}_{600}$, $\bar{m}_{ELM}$ and $\bar{m}_{600}$ will be used for

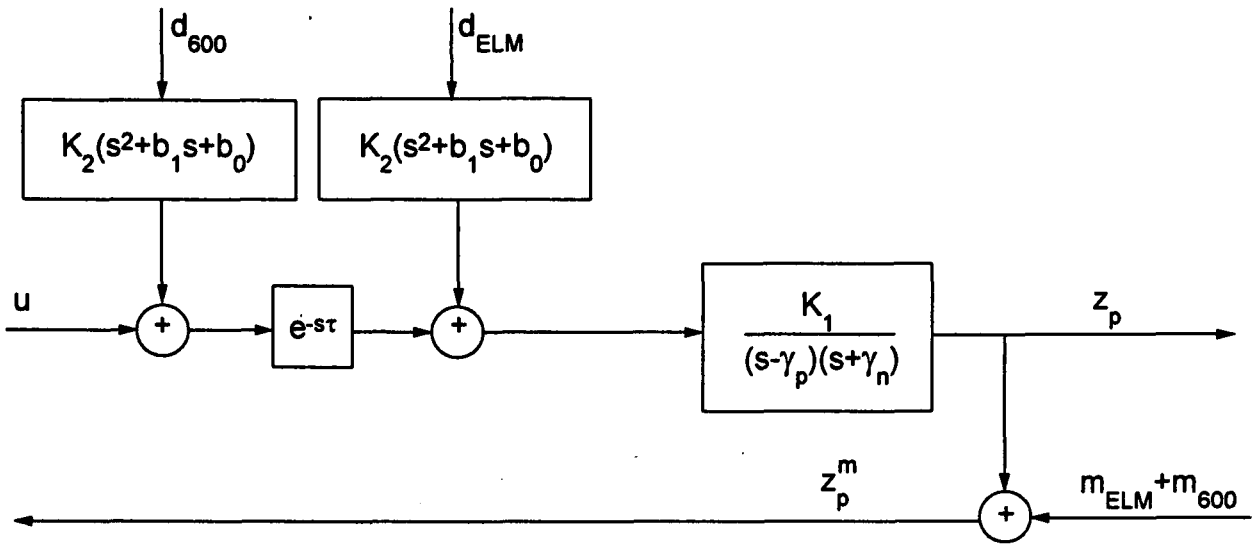


Figure 2.14: A schematic diagram of the plasma vertical position model including the disturbances, d_{ELM} and d_{600}, and measurement noise $m_{ELM} + m_{600}$.

the controller design in Chapter 4.

2.5 Deriving a model for the actuators

The actuators for the control of the vertical position are the power supplies that drive the currents into the poloidal conductors (§ Figure 2.2) to generate the radial magnetic field needed to control the vertical position of the plasma. The power supplies are limited both in current and voltage and this poses the problem of the unstable systems with constrained input studied in Chapter 3. In order to maximize the stability margins it is necessary to minimize the response time (defined as the maximum time delay between the request and the actual implementation of a control signal output level). Gate Turn-Off-thyristor (GTO) based power supplies are being used in tokamaks [Mondino92] and [Hay92], and have been proposed for ITER [Zama92] because of their power handling capability and fast response time of a few hundreds of microseconds. The maximum slew rate dV/dt is limited to $< 2 \cdot 10^9\ [Vs^{-1}]$ but it is negligible compared to the response time. The model for the GTO-thyristor based power supplies depends on the I/O characteristic, which is non-linear and has a finite time delay due to the GTO. Typically the I/O characteristic can be seen as a state machine whose states are the voltage levels, and whose transitions depend on the reference input V_{ref} and timing constraints introduced by the GTOs. If τ_{GTO} is the maximum time delay expected from a GTO and $f\left(V_{ref}\left(\cdot\right), t\right)$ is a non continuous function then an expression for the power

supply model can be

$$V_a(t) = K_a f(V_{ref}(t - \tau_{GTO}), t) \tag{2.55}$$

where K_a is the amplifier gain. Sometimes an inductor is connected to the amplifier output to limit the voltage ramp on the coils. This implies that the model must also include some dynamics.

In JET the power supply for the control of the vertical position is named Fast Radial Field Amplifier (FRFA). It was procured and installed during 1991-1993 [Mondino92] because the previous amplifier, named Poloidal Radial Field Amplifier, would have not been capable of stabilizing the increased unstable plasmas resulting from new operating scenarios.

Fast Radial Field Amplifier: FRFA The FRFA is essentially a high power GTO, four quadrant, H-bridge inverter fed by a DC power supply as shown in Figure 2.15. The amplifier

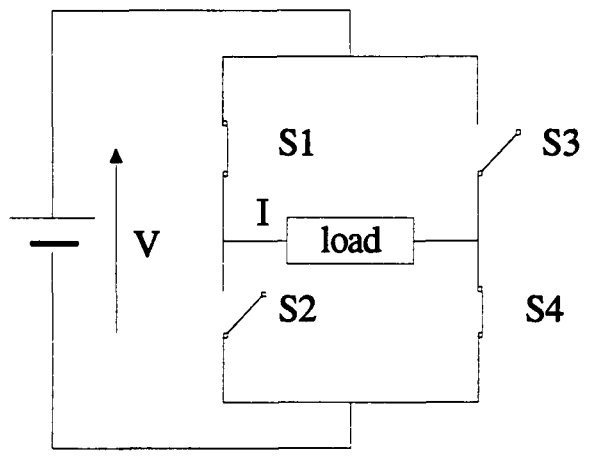


Figure 2.15: Schematic diagram of an H-bridge inverter

is composed of four identical subunits with an output rating of $\pm 2.5 \cdot 10^3\,[V]$ at $\pm 2.5 \cdot 10^3\,[A]$ each. The four units can be connected in two configurations:

Configuration A: the output of the system is $\pm 5 \cdot 10^3\,[V]$ at $\pm 5 \cdot 10^3\,[A]$ ($K_a = 5 \cdot 10^3\,[V]$).

Configuration B: the output of the system is $\pm 10 \cdot 10^3\,[V]$ at $\pm 2.5 \cdot 10^3\,[A]$ ($K_a = 10 \cdot 10^3\,[V]$).

The measured response time varies between $50 \cdot 10^{-6}\,[s]$ and $200 \cdot 10^{-6}\,[s]$. It is therefore assumed an average time delay of $\tau_{ad} \simeq 100 \cdot 10^{-6}\,[s]$. The FRFA can operate in different modes described in Figure 2.16.

1. 9/5 level Hysteresis mode

2. 9/5 level Quantized mode

3. Pulse Width Modulation (PWM) 9/5 multi-level mode

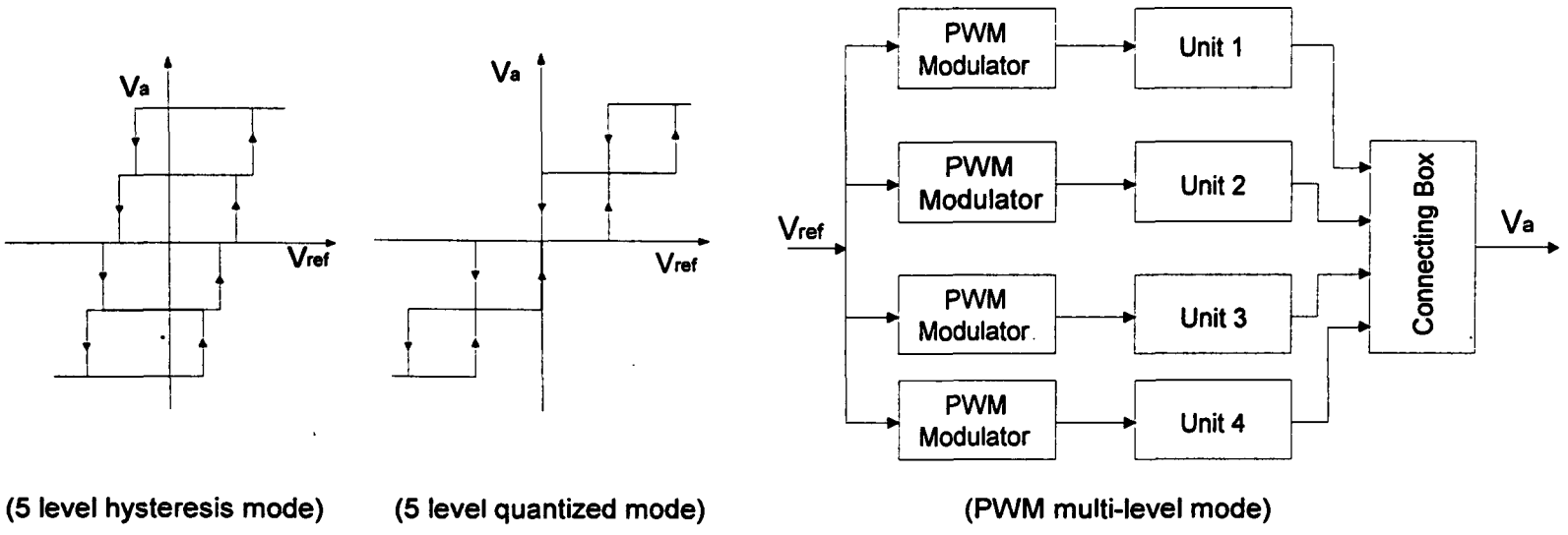


Figure 2.16: FRFA operational modes

The first two modes have been in operation while the use of the third mode is still under consideration.

A model of the amplifier has been developed in a MATLAB/SIMULINK environment (§ Section 2.6) in order to evaluate the performances of the overall system in the different modes of operation. A schematic diagram of the model is shown in Figure 2.17.

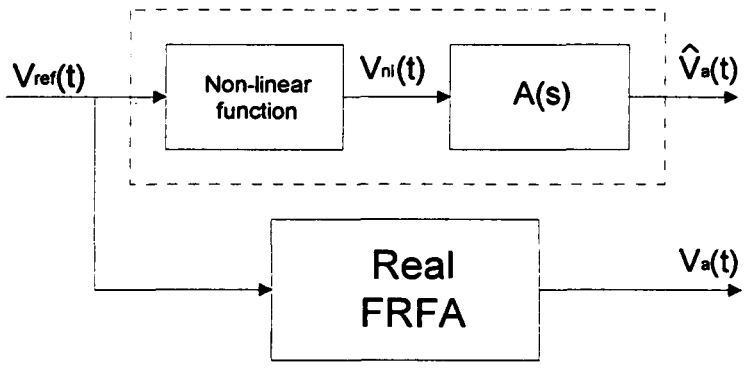


Figure 2.17: System identification setup.

To simulate the true behaviour of the system, a non-linear static algorithm for the different modes is used. This includes the function $V_{nl}(t) = K_a f(V_{ref}(t - \tau_{ad}), t)$ approximating the response time of the amplifier by a finite time delay. In JET there is a limiting inductor and the transfer function between the input reference and the output voltage on the coils

$$A(s) = \frac{V_a(s)}{V_{nl}(s)} \tag{2.56}$$

is identified via the experimental data. A simple ARX model is used to identify the above transfer function using a Least Square Identification algorithm implemented in MATLAB [Ljung87]. The identified transfer function is given below

$$A(s) = \frac{p_1 p_2 \bar{p}_2}{z_1 \bar{z}_1} \frac{(s+z_1)(s+\bar{z}_1)}{(s+p_1)(s+p_2)(s+\bar{p}_2)} \tag{2.57}$$

where $z_1 = 3.7146 \cdot 10^4 + 3.9307 \cdot 10^4 j \, [s^{-1}]$, $p_1 = 9.5892 \cdot 10^4 \, [s^{-1}]$, $p_2 = 2.1157 \cdot 10^4 + 4.9311 \cdot 10^3 j \, [s^{-1}]$ and overbar denotes complex conjugation. The results of this identification fit very well with the experimental data as it can be seen in Figure 2.18. However these additional dynamics, represented by equation (2.57), are negligible given the approximations made in the derivation of the plasma model. Therefore a pure time delay model will be used in the controller design.

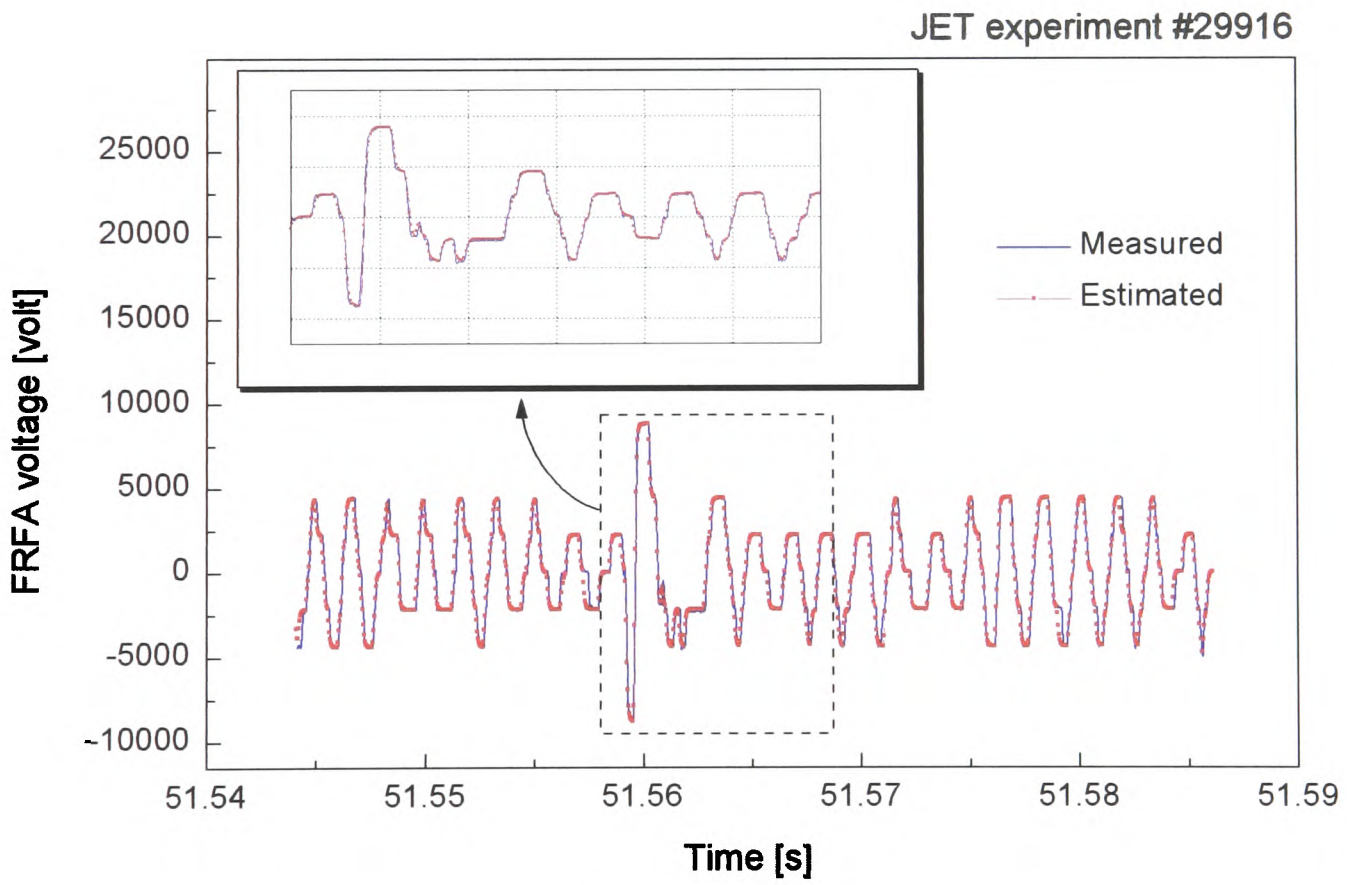


Figure 2.18: The Real FRFA compared to the Simulated FRFA

In COMPASS-D the standard actuators for the control of the vertical position are composed of one or two series connected linear amplifiers (FAx). An additional power supply, a chopper amplifier (CA1), was added to the vertical position circuit [Hay92] in order to

emulate the JET control system for the experiments reported in Chapter 6.

Linear Amplifier: FAx The FAx power supply is a transistor amplifier rated at $\pm 5 \cdot 10^3\,[A]$, $\pm 50\,[V]$ and $16 \cdot 10^3\,[Hz]$ bandwidth. [Vyas96] derived an FAx model including the protection logic and a $6 \cdot 10^3\,[Hz]$ output low pass filter:

$$G_a(s) = e^{-s\tau_{ad}} K_a \frac{p_a \bar{p}_a}{(s+p_a)(s+\bar{p}_a)} \tag{2.58}$$

where $\tau_{ad} = 31 \cdot 10^{-6}\,[s]$, $K_a = 57.6\,[V]$, $p_a = 26657 + 26657j\,[s^{-1}]$ and overbar denotes complex conjugation.

Chopper Amplifier: CA1 The new power supply is similar to one FRFA subunit and it is rated at $\pm 10 \cdot 10^3\,[A]$ and $\pm 2 \cdot 10^3\,[V]$. The measured response time varies between $100 \cdot 10^{-6}\,[s]$ and $400 \cdot 10^{-6}\,[s]$. It is therefore assumed an average time delay of $\tau_{ad} \simeq 200 \cdot 10^{-6}\,[s]$. CA1 is modelled in the same way as the FRFA subunit.

The controllers and the amplifiers are connected via optical links to galvanically isolate the circuit and to immunize from electromagnetic fields. The optical links usually have a high bandwidth compared to the controlled system and they can be represented by a pure time delay

$$G_l(s) = e^{-s\tau_{ld}}. \tag{2.59}$$

For JET the measured values of $\tau_{ld} \simeq 10 \cdot 10^{-6}\,[s]$ and for COMPASS-D $\tau_{ld} \simeq 32 \cdot 10^{-6}\,[s]$.

In conclusion, given the uncertainties on the plasma model, an approximate model of the GTO-based power supplies includes the static non-linear characteristic and a time delay due to the GTOs and the optical link

$$V_a(t) = K_a f\left(V_{ref}\left(t - \tau_{psd}\right), t\right) \tag{2.60}$$

with $\tau_{psd} = \tau_{ad} + \tau_{ld}$. By adding τ_{psd} to the $\bar{\tau}_v$ equation (2.32) also approximates the presence of a power supply.

2.6 Experimental model validation

From the previous Sections it has been found that a simple relationship between the control signal to the power amplifiers, the disturbances, the measurement noise and the plasma vertical position can be expressed as

$$z_p(s) = \frac{1}{I_p}\left[\frac{Ke^{-s\tau_{tot}}}{(s-\gamma_p)(s+\gamma_n)}V_{ref}(s) + \frac{K_2(s^2+b_1s+b_o)}{(s-\gamma_p)(s+\gamma_n)}d(s) + m(s)\right] \tag{2.61}$$

where $\tau_{tot} = \tau_v + \tau_{da} + \tau_{dl}$, $K = K_aK_1$ and all the other variables have been defined in the previous sections. The aim of this section is to prove the consistency of the model described in equation (2.61) with the experimental data from the COMPASS-D and the JET Tokamak. The section is divided into two parts:

1. A comparison of the experimental data with open loop simulations (§ Figure 2.19$-a$)
2. A comparison of the experimental data with closed loop simulations (§ Figure 2.19$-b$).

In the schematic diagram in Figure 2.19 $G_u(s)$ is an unstable system and $C(s)$ is a stabilising controller. Let suppose that $G_e(s)$ is an approximate version of $G_u(s)$ then, to compare the two systems, it may be necessary to use the closed loop validation otherwise $y_e(t)$ will diverge whatever the control signal $u(t)$. This method is not suitable when the exact values of the parameters need to be estimated because the closed loop system will be less sensitive to parameter variations. However the aim is just to show that the model structure is consistent with the experimental data and therefore even the closed loop simulation can increase confidence in the use of the model.

In the following Sections the results of the JET experiment #36376 and the COMPASS-D experiments #18135 and #18509 are compared to the simulation results. The JET plasma parameters for experiment #36376 are:

- $I_p = 1.5 \cdot 10^6\,[A]$
- $\gamma_p = 115\,[s^{-1}]$, obtained by measuring the exponential growth during a switch-off test

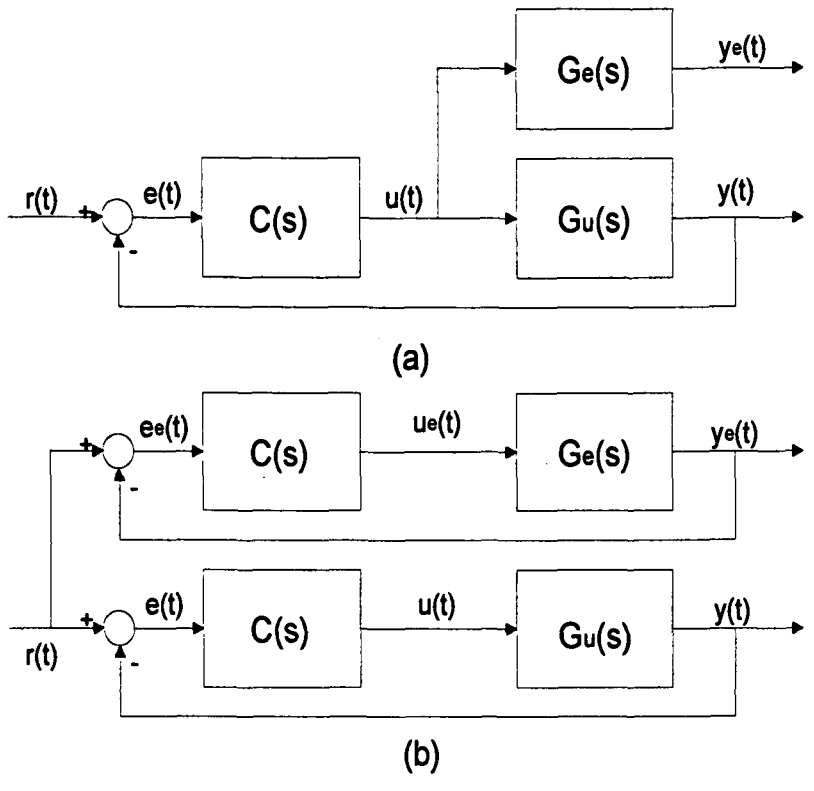


Figure 2.19: Model validation of unstable systems: (a)-open loop validation (b)-closed loop validation

- $\gamma_n = 2.67\,[s^{-1}]$, $K_1 = 2.6\,[m]$, $K_2 = 2.23\,[m]$, $b_1 = -114.46$ and $b_0 = -570.01$, calculated using the parameters given in Table A.2 in the Section A.3 of Appendix A

- $\tau_v = \bar{\tau}_v|_{JET} = 200 \cdot 10^{-6}\,[s]$, $\tau_{da} = 100 \cdot 10^{-6}\,[s]$, $\tau_{dl} = 10 \cdot 10^{-6}\,[s]$

The COMPASS-D plasma parameters for experiment #18135 are:

- $I_p = 143 \cdot 10^3\,[A]$

- $\gamma_p = 1000\,[s^{-1}]$, $\gamma_n = 100\,[s^{-1}]$ and $K_1 = 135\,[m]$ derived from [Vyas96]

- $\tau_v = \bar{\tau}_v|_{COMPASS-D} = 100 \cdot 10^{-6}\,[s]$, $\tau_{da} = 200 \cdot 10^{-6}\,[s]$, $\tau_{dl} = 32 \cdot 10^{-6}\,[s]$

while for experiment #18509

- $I_p = 143 \cdot 10^3\,[A]$

- γ_p varies during the experiment from $1000\,[s^{-1}]$ to $80\,[s^{-1}]$, $\gamma_n = 100\,[s^{-1}]$ and $K_1 = 135\,[m]$ derived from [Vyas96]

- $\tau_v = \bar{\tau}_v|_{COMPASS-D}$ ·

The simulations are executed using the package SIMULINK® [MATLAB].

Note that z_p^e shown in all the following diagrams is the deviation from the equilibrium position.

2.6.1 Comparison of the experimental data with open loop simulations

In these simulations the output voltages of the amplifiers are used as input to the model described by equation (2.61). The model results are compared to the observed values $\dot{z}_p$ and z_p. Since the system is unstable and the simulations are in open loop, small parameter differences result in diverging solutions. However it is possible to make the comparison over small time intervals. The simulations are stopped before the open loop model diverges.

In the JET experiment #36376 (see Figure 2.20) the controller output was intentionally zeroed between the time $59.502\,[s]$ and $59.517\,[s]$. As expected a vertical instability is triggered. The position and speed start diverging from their equilibrium state, and, when the controller is reinstated, the equilibrium state is recovered. This experiment is the ideal case to compare to the model because there is a large excursion of the state variables. Figure 2.20 shows the input voltage and the observed plasma vertical speed and position compared to the simulated ones. The results show a very good agreement between the experimental and the simulation data which indicates that the selected model structure represents well the real system.

In the COMPASS-D experiment #18135 a pulse is added to the position reference so as to cause a large excursion of the state variables. In Figure 2.21 the observed plasma vertical position and speed are compared to the simulated ones. Even in this experiment the results show a very good agreement between the experiment and the simulation data.

The COMPASS-D experiment #18509 is analysed in order to demonstrate that the model can follow the real system even when large parameter changes occur. During this experiment the plasma is moved very far from its equilibrium position. As a consequence the parameters change over a relatively short time. The instability growth rate γ_p is calculated at various times and the values of γ_p are used to simulate the fact that the model changes in time. As it can be seen in Figure 2.22, the simulation results are still consistent with the experimental data.

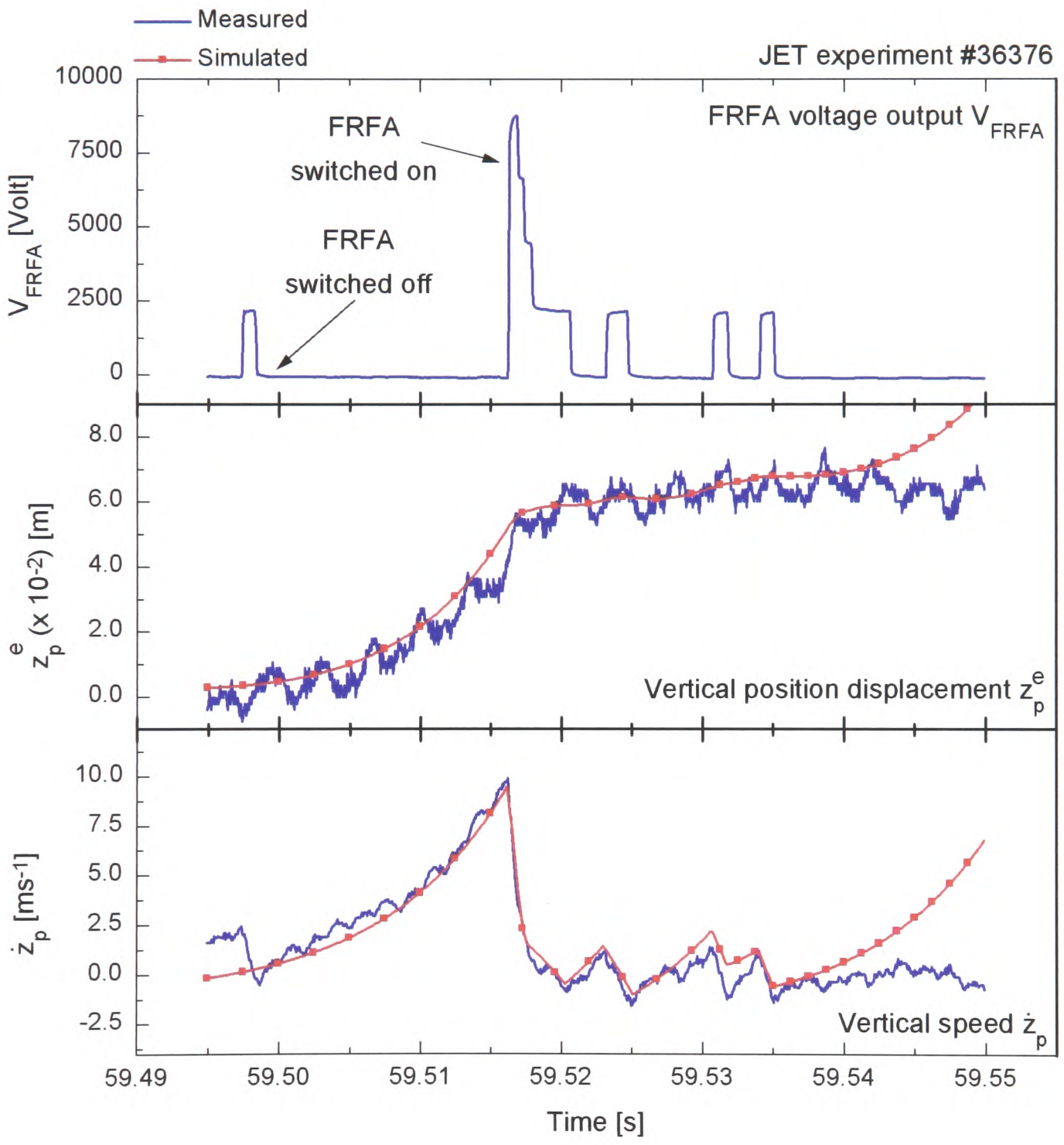


Figure 2.20: Comparison of the experimental data with open loop simulations (JET experiment #36376)

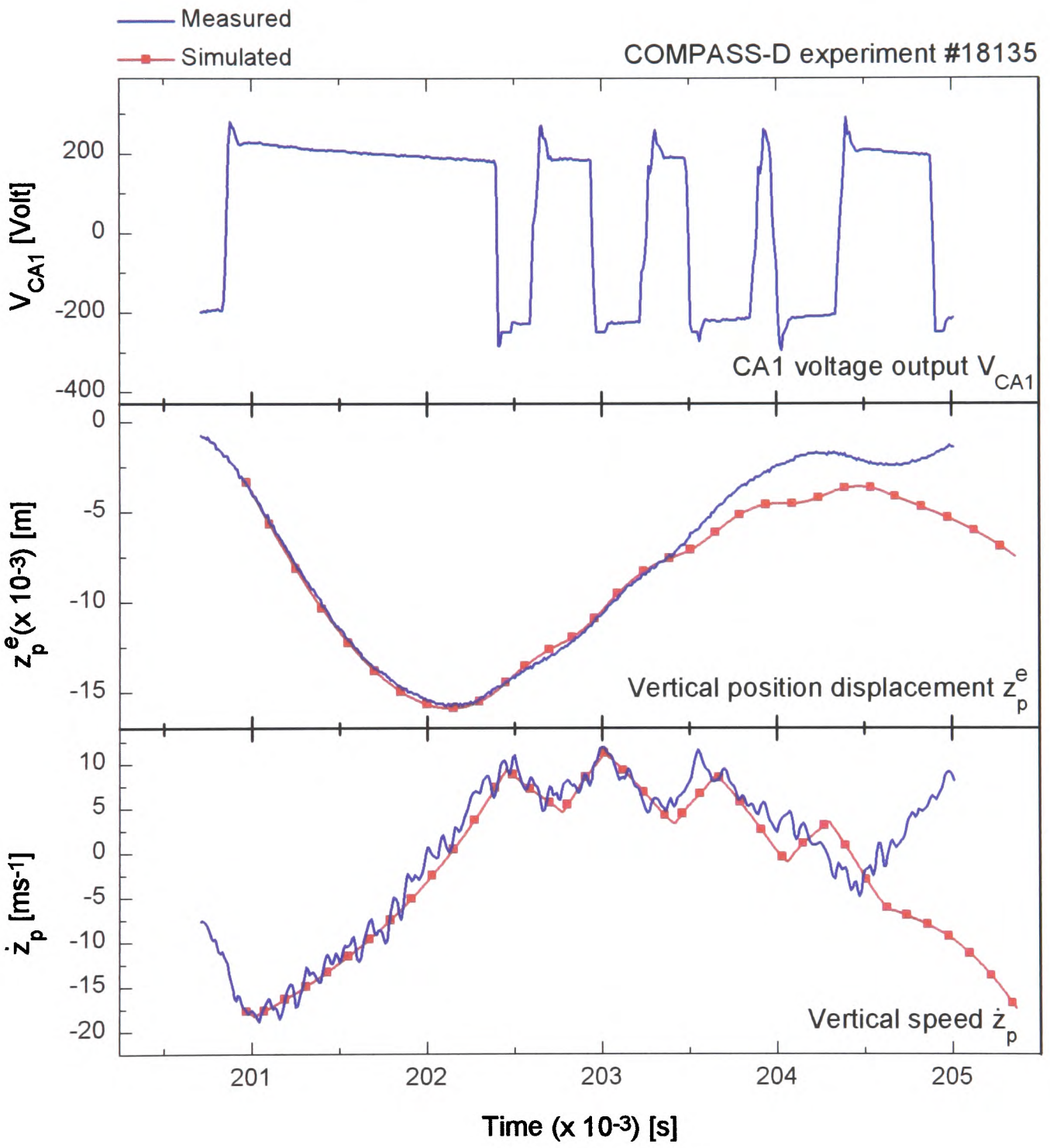


Figure 2.21: Comparison of the experimental data with open loop simulations (COMPASS-D experiment #18135)

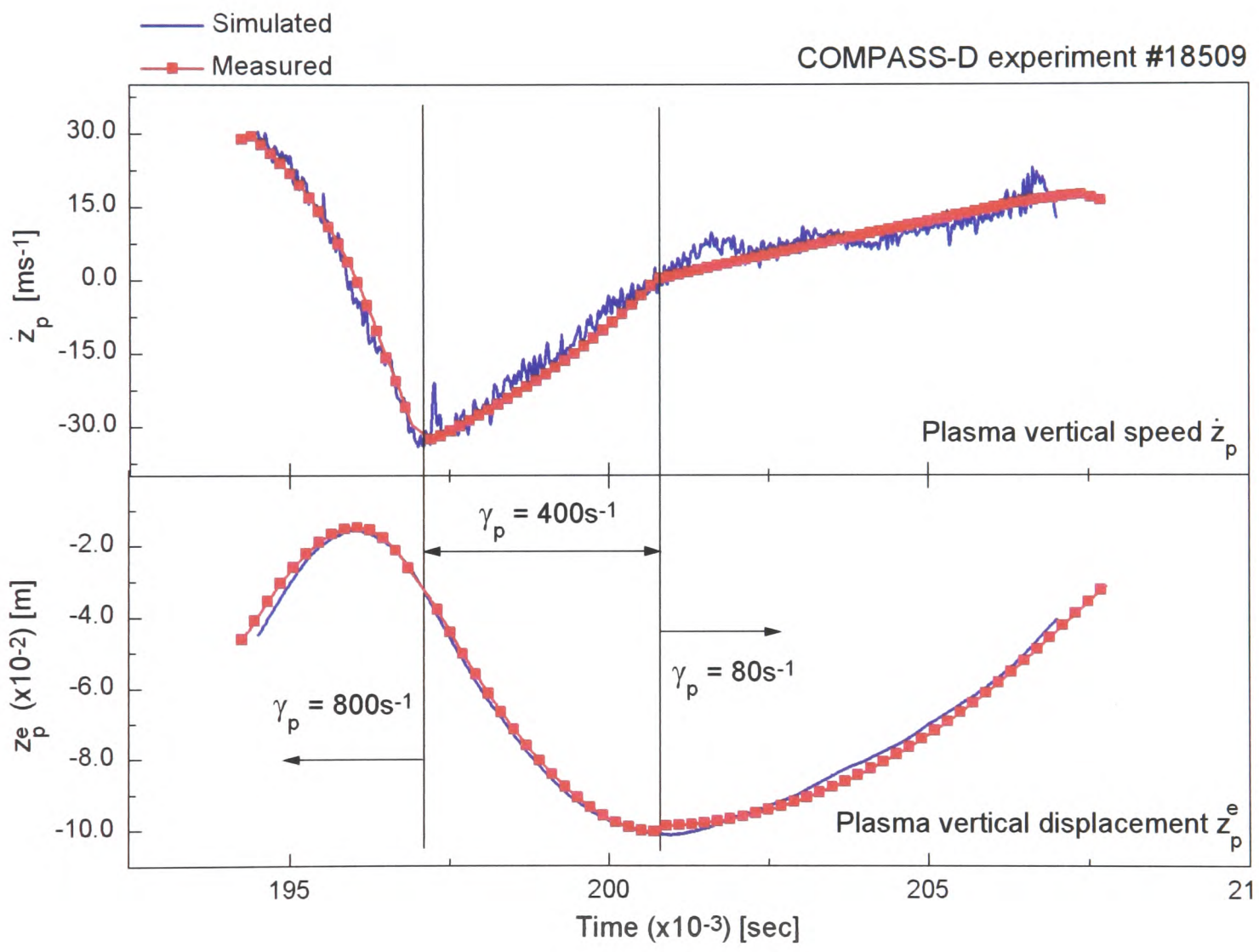


Figure 2.22: COMPASS-D experiment

2.6.2 Comparison of the experimental data with closed loop simulations

In this Section the complete vertical stabilization system is simulated. The plant model is described by equation (2.61). An emulation of the actual feedback controller and a detailed model of the power supplies is used with the same parameters as were used in the JET experiment #36376 and the COMPASS-D experiment #18135 (see Section 2.6). The simulation results are compared to the observed $\dot{z}_p$ and z_p. The measurements are assumed not to be affected by noise. Note that, as shown in Figure A.10, at JET the current flowing into the active coils (FRFA current) is used instead of the vertical position as position feedback. Indeed, when the plasma is in equilibrium, after the passive stabilizing current has decayed, the vertical position is proportional to the FRFA current (see equation (2.14)). This can also be seen in Figure 2.23.

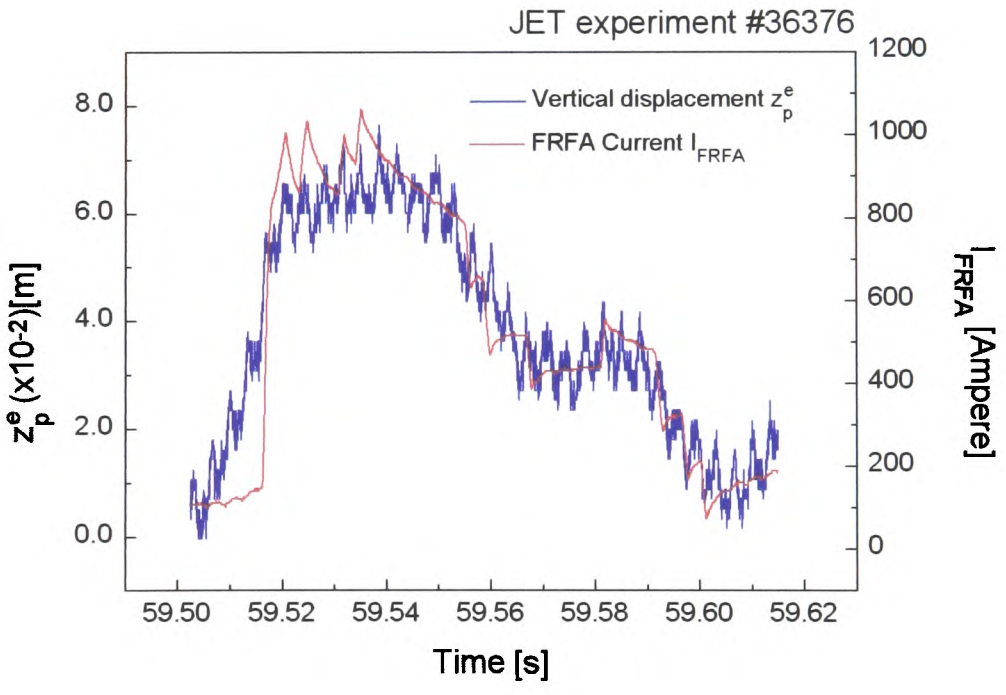


Figure 2.23: Comparison between the vertical position and the current flowing into the active coils

The JET feedback controller consists of a proportional controller (P_d) on the plasma velocity loop and a proportional+integral controller (P_i, T_i) on the FRFA current loop. In the JET experiment #36376 the controller parameters are: $P_d = 0.68\,[ms^{-1}]$, $P_i = 2{\cdot}10^{-3}\,[A]$ and $T_i = 0.5{\cdot}10^{-3}\,[A^{-1}s^{-1}]$. The initial conditions for the simulation are set at time $59.52\,[s]$

when,

$$z_p = 4.0 \cdot 10^{-2}\,[m] \text{ and } \dot{z}_p = 10.03\left[ms^{-1}\right]. \tag{2.62}$$

Figure 2.24 shows the observed plasma vertical speed and position compared to the simulated ones. The output of the simulated amplifier and the current flowing into the active coil are also compared to the observed ones. The results show that the overall behaviour of the model follows the experiment. This indicates that the selected models for the plasma, the controller and the power amplifier are a reasonable representation of the real system.

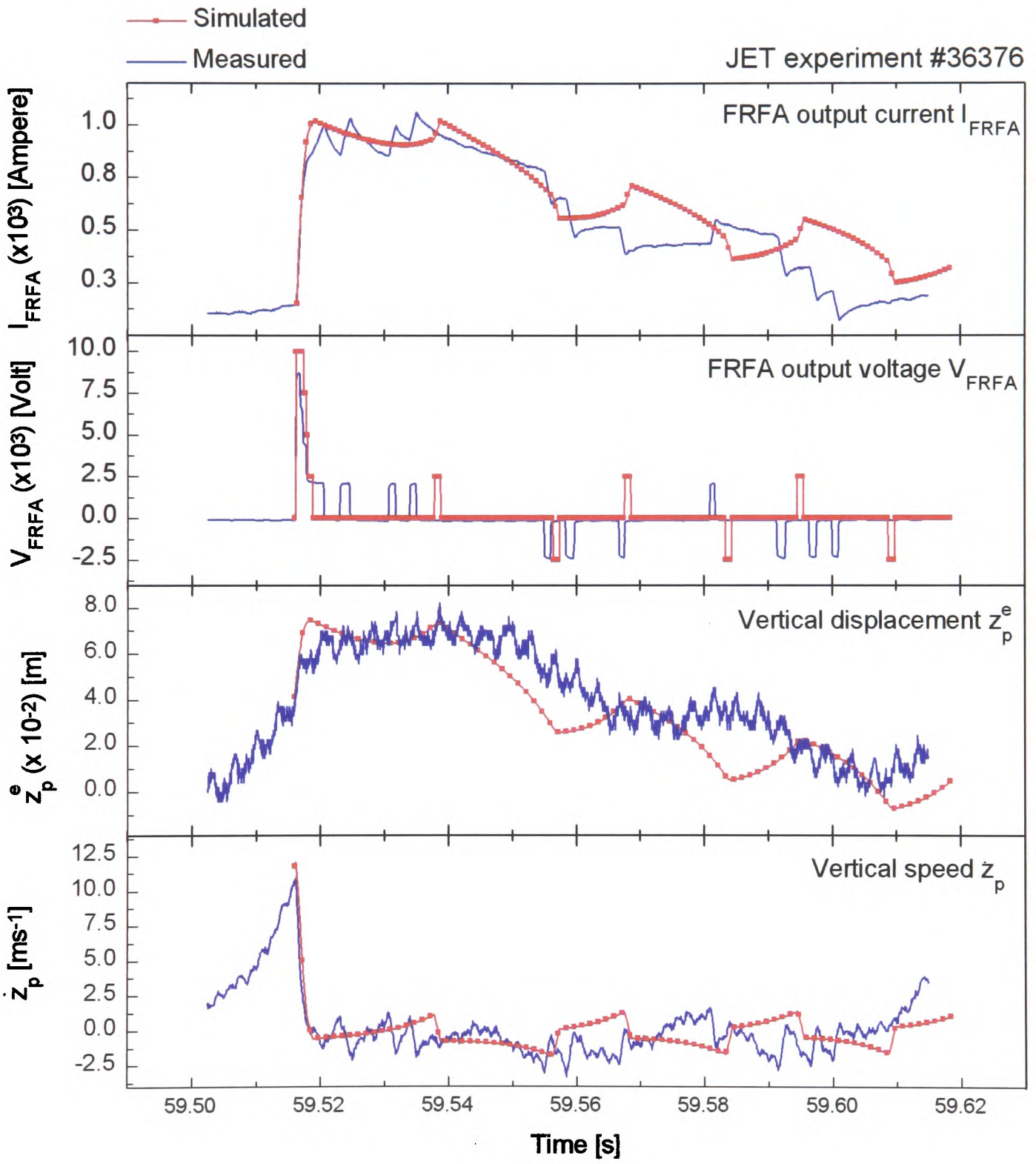


Figure 2.24: Comparison of the experimental data with closed loop simulations (JET experiment #36376).

Experiment #18135 is used to compare the COMPASS-D experimental and simulated data. The COMPASS-D feedback controller for this experiment is the Discrete Adaptive Near-Time Optimum Controller (details of the controller and the parameters used in this experiment are given in Chapter 6). The initial conditions for the simulation are set at time 0.200 $[s]$ when,

$$z_p = 3.36 \cdot 10^{-3}\,[m] \text{ and } \dot{z}_p = -17.62\left[ms^{-1}\right]. \tag{2.63}$$

In Figure 2.25 the comparison between the measured and simulated plasma vertical speed and position is presented. The results show a good agreement between the experiment and the simulation data.

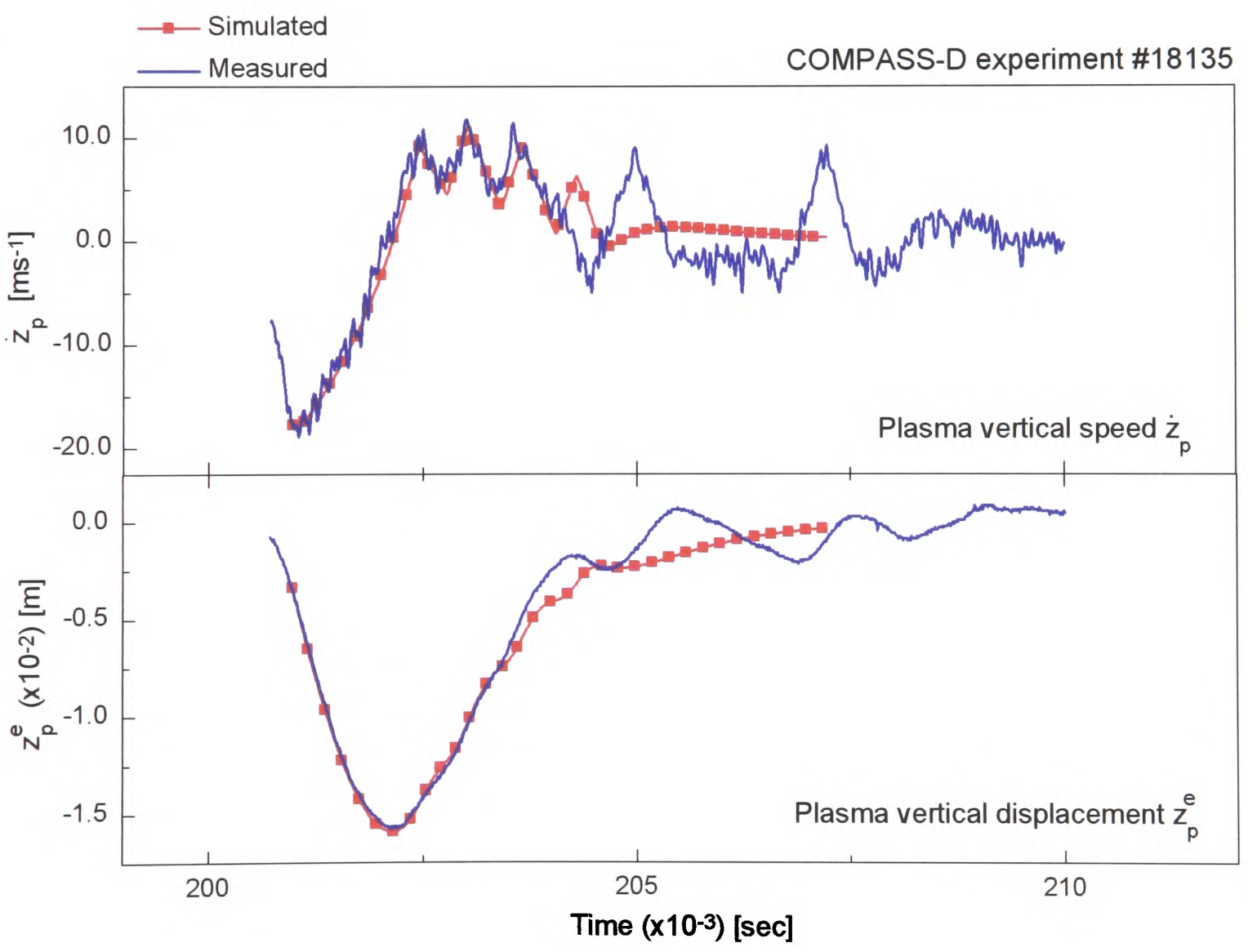


Figure 2.25: Comparison of the experimental data with closed loop simulations (COMPASS-D experiment #18135).

2.6.3 Experimental validation of the disturbance model

To verify the assumptions made in the derivation of the disturbance model in Section 2.4 the simulation data are compared to the JET experiment #40452. The plasma parameters for this experiment are the same as in Section 2.6 but the plasma current is $I_p = 2 \cdot 10^6\,[A]$. The disturbance input d_{ELM} is set as $d_{ELM}(t) = 6.5 H_\alpha(t)$ in equation (2.53) (§ Section 2.4.1). The value of $d_{600}(t)$ is set to zero. To include the measurement noise, $m(t) = 1 \cdot 10^{-4} \sin(2\pi 600)\,[m]$ is added to the measurement of the z_p to emulate the $600Hz$ noise $m_{600}(t)$. The value of $m_{ELM}(t)$ is set to zero. In Figure 2.26 it can be seen that the plasma model responds to the effect of an ELM as in the real plasma. The effect of the first ELM is equivalent to a destabilizing force of about $14 \cdot 10^3\,[N]$. The results verify the assumption that the disturbances induced by ELMs are proportional to the spikes on the H_α signal. The differences between the model and the measurement of $\dot{z}_p$ can be identified as measurement noise m_{ELM} induced by the ELM. The ELM's effect on the vertical position is very small because the amplitude and duration of these particular ELMs are not large. On the other hand the effect of the measurement noise m_{600} is clearly predominant.

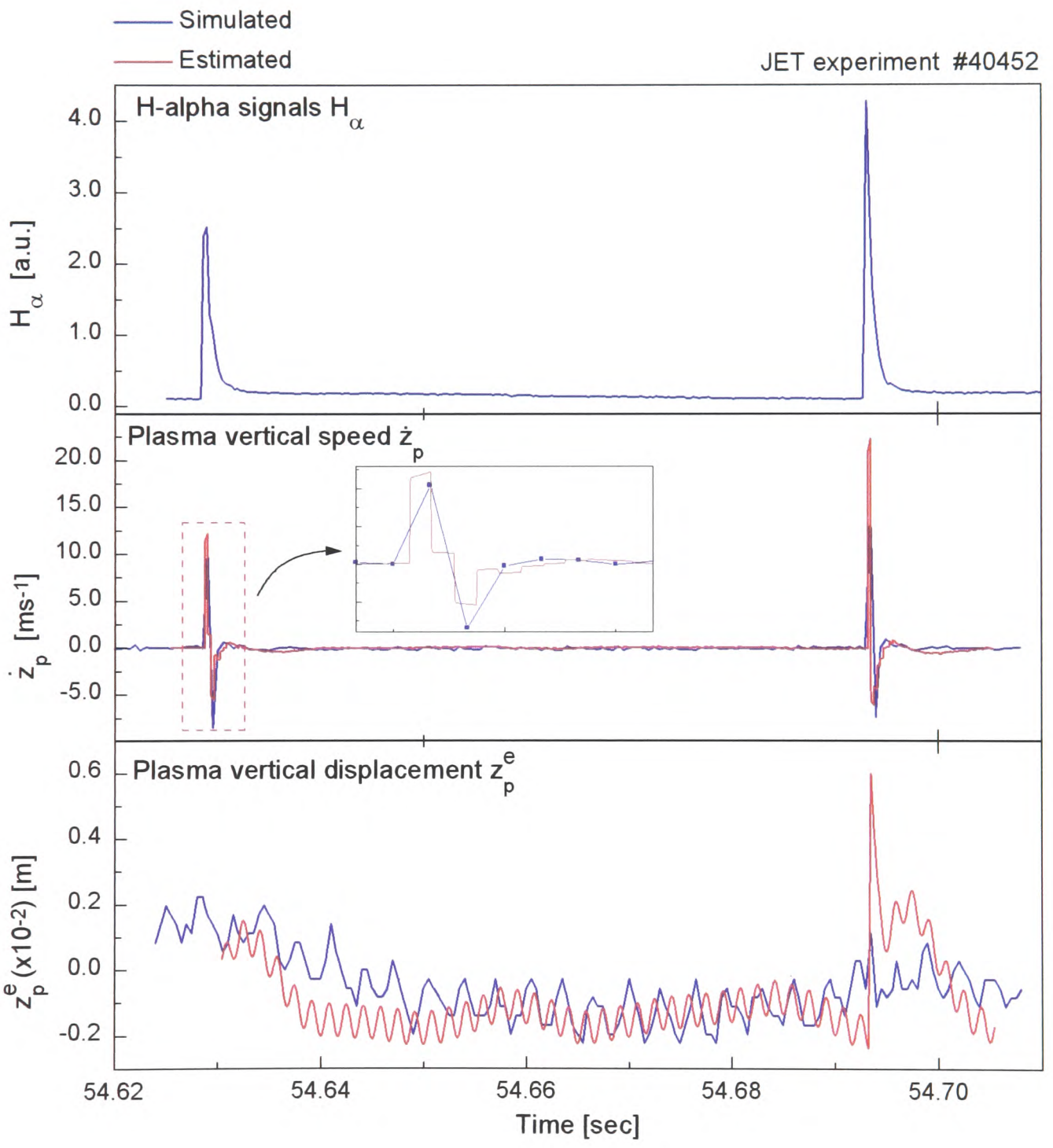


Figure 2.26: Comparison between a real and a simulated ELM (JET experiment #40452).

2.7 Concluding Remarks

In this chapter a simple model structure for the plasma vertical position has been derived and validated with experimental data from the JET and the COMPASS-D Tokamaks. The main sources of measurement noise and disturbances that most affect the vertical position have been identified and characterized on the basis of the experimental evidence. A model for the switched power supplies has been developed taking into account the saturation and the I/O non-linear characteristics. It is observed that the dynamics can be approximated by a pure time delay without significantly reducing the overall model accuracy.

The comparison between the experimental data and the simulation results (§ Section 2.6) increases the confidence that simple model structures can provide information on the dynamic behaviour and that simulations can be used to test new control algorithms before the on-line implementation.

Chapter 3

Control of unstable LTI systems with constrained inputs

Saturation of the control inputs to an open loop unstable plant may cause the closed loop to become unstable. During the saturation period the system states will grow exponentially with the unstable eigenvalues and may reach levels that cannot be controlled with the limited energy provided by the inputs. For example, large disturbances can saturate the control input. Therefore the knowledge of the stability region is necessary to determine the maximum allowable disturbances before the system is driven into an uncontrollable state. It is of primary importance to predict the stability region to avoid dangerous operating regimes. In Tokamaks a loss of vertical control results in a disruption with associated Vertical Displacement Events which can be extremely dangerous for the integrity of the machine (see [Gruber93], [Bertolini95] and [Noll96]). Even if in theory it is possible to overcome this problem by increasing the input capabilities, in practice the associated costs are very high.

It is possible to design a controller with reduced gains so as not to reach the saturation limits. However, this reduces its performance. To overcome this problem the knowledge of the stability region can be incorporated in the controller to improve the performance.

The aim of this chapter is to determine the stability region of an unstable LTI system with a constrained input under feedback control. The measure of the stability region will be used in Chapter 4 for the control design.

3.1 Introduction

The problem of determining the Stability Region (SR) of an open loop unstable system under a bounded feedback control has been solved in discrete time by [Kouvaritakis96]. [Zhao95] and [Lee95] formally showed that an open loop unstable system cannot be globally stabilized by a bounded control input. Sometimes this problem is addressed so as to determine the area of semiglobal stability [Lee95], [Lin95], [Lin93], [Megretski96]. Estimations of the SR have been obtained in different ways. In [Zhao95], [Lee95], [Corless93] and [Megretski96] the SR is estimated by finding a region in the state space where the actuators are not-saturated and the system is stable. Others, [Blanchini90], [Blanchini95], [Bitsoris95], [Gutman87] and [Vassilaki88], fix a region in the state space and find a controller that stabilizes the initial conditions belonging to that region. [Bugart94] and [Kamenetskiy96] extended the estimate of the stability region when the control is saturated by using Lyapunov functions. [Madani-Esfahani90], [Choi94a], [Glazos95], [Gutman86], [Hui93] and [Lin95] estimated the region of asymptotic stability of variable structure systems with bounded control inputs. Finally, in [Flugge-Lotz68], the stability region for a 2^{nd} order system with bounded input is determined graphically. |Methods to calculate the existence and the period of limit cycles in relay controlled systems can be found in [Atherton75] and [Atherton82]. Necessary and sufficient conditions stability limit cycles in relay controlled systems are given in [Balasubramanian81].

In this chapter an alternative method to measure the maximum obtainable SR is given for the case of one unstable eigenvalue. Necessary stability conditions are found in **Section 3.2** for the case of $n - order$ systems with one input. Optimum controllers for unstable LTI systems with a constrained input are given in **Section 3.2.1**.

In **section 3.3** the result of the Section 3.2 is extended to a generalized state feedback control with a constrained input. Sufficient stability conditions are given in the case of a relay control law with and without a time delay. Necessary and sufficient stability conditions are given in the case of one unstable eigenvalue. A novel result on the existence, the stability and the period of limit cycles is also derived in this section.

In this Chapter some elements of Variable Structure System and Minimum Time Control theory are used: a short review is given in Section B.1 and Section B.2 of Appendix B.

3.2 Maximum obtainable stability region for Unstable LTI systems with a constrained input

In this section the problem of finding the maximum obtainable stability region for Unstable LTI systems with constrained inputs is addressed in the case of one unstable eigenvalue.

Let us consider an LTI system in general state space form:

$$\dot{\mathbf{x}} = \mathbf{A}\mathbf{x} + \mathbf{b}u \tag{3.1}$$

where $\mathbf{A} \in R^{n\times n}$, $\mathbf{b} \in R^{n\times 1}$, $\mathbf{x} \in R^n$, $u \in R$. It is assumed that $\mathbf{b}$ is of rank 1 and the pair $(\mathbf{A}, \mathbf{b})$ is completely controllable. It is assumed that the unforced system has one unstable eigenvalue γ_p and the inputs are subject to a saturation

$$|u| < u_o. \tag{3.2}$$

where $u_o > 0$ is a constant. When the system is saturated at $+u_o$ $(-u_o)$ the equilibrium state is:

$$\mathbf{x}_{equ} = -\mathbf{A}^{-1}\mathbf{b}u_o \qquad (\mathbf{x}_{equ} = \mathbf{A}^{-1}\mathbf{b}u_o). \tag{3.3}$$

The matrix $\mathbf{A}$ can always be written as [Pease65]

$$\mathbf{A} = \mathbf{W}\mathbf{J}\mathbf{W}^{-1} \tag{3.4}$$

where $\mathbf{J}$ is the Jordan canonical form of $\mathbf{A}$ and $\mathbf{W}$ is the matrix of the generalized eigenvectors. The matrix J for the system (3.1) can be written as

$$\mathbf{J} = \begin{bmatrix} \mathbf{J}_1 & \mathbf{0} & \mathbf{0} & \cdots & \mathbf{0} \\ \mathbf{0} & \mathbf{J}_2 & \mathbf{0} & \cdots & \mathbf{0} \\ \mathbf{0} & \mathbf{0} & \ddots & & \vdots \\ \vdots & \vdots & & \mathbf{J}_s & \mathbf{0} \\ \mathbf{0} & \mathbf{0} & \cdots & \mathbf{0} & \gamma_p \end{bmatrix} \tag{3.5}$$

where the element $\mathbf{J}_i$ is the Jordan block associated with the k_i times repeated eigenvalue λ_i such that $\sum_{i=1}^{s} k_i = n - 1$.

For a given initial condition $\mathbf{x}_o$ the solution of equation (3.1) is

$$\mathbf{x}(t) = \mathbf{W}e^{\mathbf{J}t}\mathbf{W}^{-1}\mathbf{x}_o + \int_0^t \mathbf{W}e^{\mathbf{J}(t-\tau)}\mathbf{W}^{-1}\mathbf{b}u(\tau)\,d\tau \tag{3.6}$$

and when the inputs are saturated the solution is

$$\mathbf{x}(t) = \mathbf{W}e^{\mathbf{J}t}\mathbf{W}^{-1}(\mathbf{x}_o \pm \mathbf{A}^{-1}\mathbf{b}u_o) \mp \mathbf{A}^{-1}\mathbf{b}u_o; \tag{3.7}$$

since the product $\mathbf{W}e^{\mathbf{J}t}\mathbf{W}^{-1}$ can be written as

$$\mathbf{W}e^{\mathbf{J}t}\mathbf{W}^{-1} = \sum_{i=1}^{n-1} u_i e^{\mathbf{J}_i t}\mathbf{v}_i^T + e^{\gamma_p t}u_p\mathbf{v}_p^T \tag{3.8}$$

equation (3.7) becomes

$$\mathbf{x}(t) = \sum_{i=1}^{n-1} u_i e^{\mathbf{J}_i t}\mathbf{v}_i^T(\mathbf{x}_o \pm \mathbf{A}^{-1}\mathbf{b}u_o) + e^{\gamma_p t}u_p\mathbf{v}_p^T(\mathbf{x}_o \pm \mathbf{A}^{-1}\mathbf{b}u_o) \mp \mathbf{A}^{-1}\mathbf{b}u_o \tag{3.9}$$

where u_i and $\mathbf{v}_i$ are, respectively, the right and the left generalized eigenvectors associated with the k_i times repeated eigenvalue λ_i and u_p and $\mathbf{v}_p$ are the right and the left eigenvector associated with the unstable eigenvalue γ_p.

Definition 3.2.1 *Let $\mathbf{v}_p$ be the left eigenvector associated with the unstable eigenvalue of the system (3.1). $s_c(x)$ is a central hyperplane if*

$$s_c(x) \equiv \mathbf{v}_p^T\mathbf{x}. \tag{3.10}$$

Lemma 3.2.1 *A central hyperplane yields asymptotic stable motion in the sliding mode.*

Proof: Consider the system (3.1) and the discontinuous control

$$u = -u_o sgn(s_c(\mathbf{x})) \tag{3.11}$$

where $s_c(\mathbf{x}) = \mathbf{v}_p^T\mathbf{x}$ is the associated central hyperplane and $\mathbf{v}_p^T\mathbf{b}u_o > 0$. During sliding mode, assuming that the switching logic works infinitely fast and that the non-unique control u has been suitably chosen [Elghezawi83], the state is constrained to remain on the switching hyperplane $s_c(\mathbf{x}) = 0$ (in the null space of $\mathbf{v}_p^T$). From equation (3.9) it is clear, that, during

sliding, the mode associated with the unstable eigenvalue is null yielding asymptotic stable motion.□

It was demonstrated by [Zhao95] and [Lee95] that an unstable LTI system cannot be globally stabilised in the presence of control saturations. The problem of finding the maximum obtainable stability region can be solved, in the case of discrete time, using the results in [Kouvaritakis96]. In the case of continuous time, an alternative method to derive the necessary conditions for the stabilization of an unstable LTI system with bounded control inputs in the case of one unstable eigenvalue is given in the following theorem 3.2.2.

Theorem 3.2.2 *Let us consider the system (3.1). It is assumed that* $\mathbf{b}$ *is of rank* 1 *and the pair* $(\mathbf{A}, \mathbf{b})$ *is completely controllable. It is also assumed that the unforced system has one unstable eigenvalue* γ_p *and the input is subject to a saturation*

$$|u| \leq u_o \tag{3.12}$$

where $u_o > 0$ *is a constant. Let* $\mathbf{v}_p$ *be the left eigenvector associated with the unstable eigenvalue* γ_p *such that* $\mathbf{v}_p^T \mathbf{b} u_o > 0$. *Then the maximum obtainable stability region is*

$$\Omega_{\max} = \left\{ \mathbf{x}_o \in R^n ; \gamma_p \left| \mathbf{v}_p^T \mathbf{x}_o \right| - \mathbf{v}_p^T \mathbf{b} u_o < 0 \right\} \tag{3.13}$$

Proof: Let us define a domain Ω

$$\Omega = \left\{ \mathbf{x}_o \in R^n ; \gamma_p \left| \mathbf{v}_p^T \mathbf{x}_o \right| - \mathbf{v}_p^T \mathbf{b} u_o < 0 \right\}. \tag{3.14}$$

The proof is divided into two steps: any initial state inside Ω can be stabilized and any initial state outside Ω is non stabilizable.

Step 1: Let us consider the system (3.1) and the control function (3.11). This is clearly a Variable Structure Control scheme characterized by a discontinuous control law. Asymptotic stability of the system is guaranteed if the following two conditions are satisfied [Utkin77], [Hung93]:

1. The switching hyperplane is chosen so as to give asymptotic stability during ideal switching.

2. The control is selected to ensure that the states reach the given hyperplane in a finite time.

The first point is satisfied if the switching hyperplane is chosen to be the central hyperplane associated with the system (3.1). As demonstrated in the lemma 3.2.1, this hyperplane is given by equation (3.10).

The second point is satisfied if the reaching condition

$$\mathbf{s}(\mathbf{x})\,\dot{\mathbf{s}}(\mathbf{x}) < 0 \tag{3.15}$$

holds [Hung93]. Substituting equations (3.1), (3.10) and (3.11) into equation (3.15) and assuming an initial state $\mathbf{x}_o$ gives

$$\left(\mathbf{v}_p^T\mathbf{x}_o\right)\left[\mathbf{v}_p^T\left(\mathbf{A}\mathbf{x}_o - \mathbf{b}u_o sgn\left(\mathbf{v}_p^T\mathbf{x}_o\right)\right)\right] < 0. \tag{3.16}$$

The initial states that satisfy equation (3.16) describe the stability region of the controlled system.

Now it will be shown that equation (3.16) is satisfied in Ω.

The conditions for a $\mathbf{x}_o$ to belong to Ω can be written as

$$\begin{cases} \mathbf{v}_p^T\mathbf{A}\mathbf{x}_o - \mathbf{v}_p^T\mathbf{b}u_o < 0 & if \;\; \mathbf{v}_p^T\mathbf{x}_o > 0 \\ \mathbf{v}_p^T\mathbf{A}\mathbf{x}_o + \mathbf{v}_p^T\mathbf{b}u_o > 0 & if \;\; \mathbf{v}_p^T\mathbf{x}_o < 0 \end{cases} \tag{3.17}$$

which is equivalent to

$$\left|\mathbf{v}_p^T\mathbf{A}\mathbf{x}_o\right| - \mathbf{v}_p^T\mathbf{b}u_o < 0. \tag{3.18}$$

Substituting equation (3.4) into equation (3.18)

$$\left|\mathbf{v}_p^T\mathbf{W}\mathbf{J}\mathbf{W}^{-1}\mathbf{x}_o\right| - \mathbf{v}_p^T\mathbf{b}u_o < 0 \tag{3.19}$$

and, since W represents a base of generalized eigenvectors for the system (3.1), equation (3.19) becomes

$$\gamma_p\left|\mathbf{v}_p^T\mathbf{x}_o\right| - \mathbf{v}_p^T\mathbf{b}u_o < 0 \tag{3.20}$$

which shows that equation (3.15) is identical to the constraint in equation (3.14), i.e. the initial states inside Ω satisfy the two conditions for asymptotic stability and therefore any

initial state inside Ω can be stabilized.

Step 2: As the control input is subject to saturation, there will be some initial conditions for which the system cannot be stabilized [Zhao95]. It will be shown that equation (3.15) is a necessary condition for the stability.

To demonstrate that any $\mathbf{x}_o \notin \Omega$ cannot be stabilized it is sufficient to show that the state trajectory starting from $\mathbf{x}_o \notin \Omega$ will never cross the boundary of Ω. Let $\partial\Omega$ be defined as the boundary of Ω. Let us assume that the control is saturated and therefore the maximum input is applied $\pm u_o$. If the $\mathbf{x}(t)$ enters Ω then it has been already shown that, using equation (3.11), $\mathbf{x}(t)$ will reach the switching hyperplane (3.10) in finite time. Therefore $\mathbf{x}(t)$ starting from $\mathbf{x}_o \notin \Omega$ will cross $\partial\Omega$ if and only if there exists a $\tau \in R$ such that $s_c(\tau) = 0$. From equation (3.7), the time domain evolution of the $s_c(t)$ starting from an initial condition x_o is

$$s_c(t) = \mathbf{v}_p^T \left[\mathbf{W} e^{\mathbf{J}t} \mathbf{W}^{-1} (\mathbf{x}_o \pm \mathbf{A}^{-1}\mathbf{b}u_o) \mp \mathbf{A}^{-1}\mathbf{b}u_o \right] \tag{3.21}$$

and, since $\mathbf{W}$ represents a base of generalized eigenvectors for the system (3.1), equation (3.21) becomes

$$s_c(t) = e^{\gamma_p t} \left(\mathbf{v}_p^T \mathbf{x}_o \pm \frac{\mathbf{v}_p^T \mathbf{b}u_o}{\gamma_p} \right) \mp \frac{\mathbf{v}_p^T \mathbf{b}u_o}{\gamma_p}. \tag{3.22}$$

The state trajectory will reach the switching hyperplane $s_c = \mathbf{v}_p^T \mathbf{x}$ in a finite time ($s_c(t) = 0$) only if the following condition is verified

$$\frac{\pm \mathbf{v}_p^T \mathbf{b}u_o}{\gamma_p \mathbf{v}_p^T \mathbf{x}_o \pm \mathbf{v}_p^T \mathbf{b}u_o} > 0. \tag{3.23}$$

There are only two cases to analyse

$$\mathbf{v}_p^T \mathbf{x}_o > 0 \rightarrow \begin{cases} \mathbf{v}_p^T \mathbf{b}u_o > 0 \\ \gamma_p \mathbf{v}_p^T \mathbf{x}_o - \mathbf{v}_p^T \mathbf{b}u_o < 0 \end{cases} \tag{3.24}$$

$$\mathbf{v}_p^T \mathbf{x}_o < 0 \rightarrow \begin{cases} \mathbf{v}_p^T \mathbf{b}u_o > 0 \\ \gamma_p \mathbf{v}_p^T \mathbf{x}_o + \mathbf{v}_p^T \mathbf{b}u_o > 0 \end{cases}. \tag{3.25}$$

Since equations (3.24) and (3.25) are the same as equation (3.20) only the state trajectories starting at $\mathbf{x}_o \in \Omega$ will reach the switching hyperplane $s_c(t)$ in a finite time. If a $u(t) < u_o$ is used instead of the maximum input u_o then the time domain evolution of the $s_c(t)$ starting

from an initial condition $\mathbf{x}_o$ is

$$s_c(t) = e^{\gamma_p t}\mathbf{v}_p^T\mathbf{x}_o + \int_o^t e^{\gamma_p(t-\xi)}\mathbf{v}_p^T\mathbf{b}u(\xi)\,d\xi. \tag{3.26}$$

To decrease $s_c(t)$ the condition

$$\gamma_p\mathbf{v}_p^T\mathbf{x}_o < \mathbf{v}_p^T\mathbf{b}\,|u(\tau)| \tag{3.27}$$

has to be satisfied. But if $\mathbf{x}_o \notin \Omega$ then $\gamma_p\left|\mathbf{v}_p^T\mathbf{x}_o\right| > \mathbf{v}_p^T\mathbf{b}u_o$, as from definition (3.14). Therefore condition (3.27) clearly cannot be satisfied since $|u(\tau)| \leq u_o$. This proves that even if we apply an input different from u_o the system will still be unstable. Therefore any initial state outside Ω is non-stabilizable. Having shown that any initial state outside Ω is non-stabilizable and that there exists a controller that stabilizes any initial state inside Ω it is proved that $\Omega = \Omega_{\max}$.□

Definition 3.2.2 *A controller for the systems (3.1) subject to (3.2) is defined as a maximum stabilizer controller if it guarantees for each* $t \in R$ *and* $\mathbf{x}_o \in \Omega_{\max}$ *that the states* $\mathbf{x}(t) \in \Omega_{\max}$*; where* x_o *are the states at a certain time* t_o*.*

Corollary 3.2.3 *The controller defined by equation (3.11) is a maximum stabilizer controller for the systems (3.1) subject to (3.2).*

Proof: The proof is derived from Definition 3.2.2 and Theorem 3.2.2.□

Example 3.1 *Let a* 2^{nd} *order unstable system be described by*

$$\begin{cases} \dot{x}_1(t) = x_2(t) \\ \dot{x}_2(t) = \gamma_p\gamma_n x_1(t) + (\gamma_p - \gamma_n)\,x_2(t) + u(t) \end{cases} \tag{3.28}$$

with $\gamma_p > \gamma_n > 0$ ***and the allowed*** *control input to be constrained* $|u(t)| \leq u_o$*. The left eigenvector* ***associated*** *with the unstable eigenvalue* γ_p *is*

$$\mathbf{v}_p = \begin{bmatrix} \dfrac{\gamma_n}{\gamma_p + \gamma_n} \\ \dfrac{1}{\gamma_p + \gamma_n} \end{bmatrix}; \tag{3.29}$$

the region $\Omega_{\max}$ *is calculated applying the theorem 3.2.2*

$$\Omega_{\max} = \left\{(x_1, x_2) \in R^2; |\gamma_n \gamma_p x_1 + \gamma_p x_2| < u_o\right\}. \tag{3.30}$$

Equation (3.30) describes a strip in the phase plane inside which the system can be stabilized (see Figure 3.1). The same result was obtained graphically by [Flugge-Lotz68] and, applying Theorem 2 in [Glazos95]. However in the latter case the conditions are only sufficient. Outside the region $\Omega_{\max}$ *no control action can stabilize the system. In other work the estimated stability region is described by ellipsoids in [Corless93] and [Choi94a], by polytopes in [Madani-Esfahani90] and by balls and polytopes in [Zhao95]. In Figure 3.1, a typical ball, calculated using the technique in [Zhao95], describing the estimated stability region* Ω_e *is shown.*

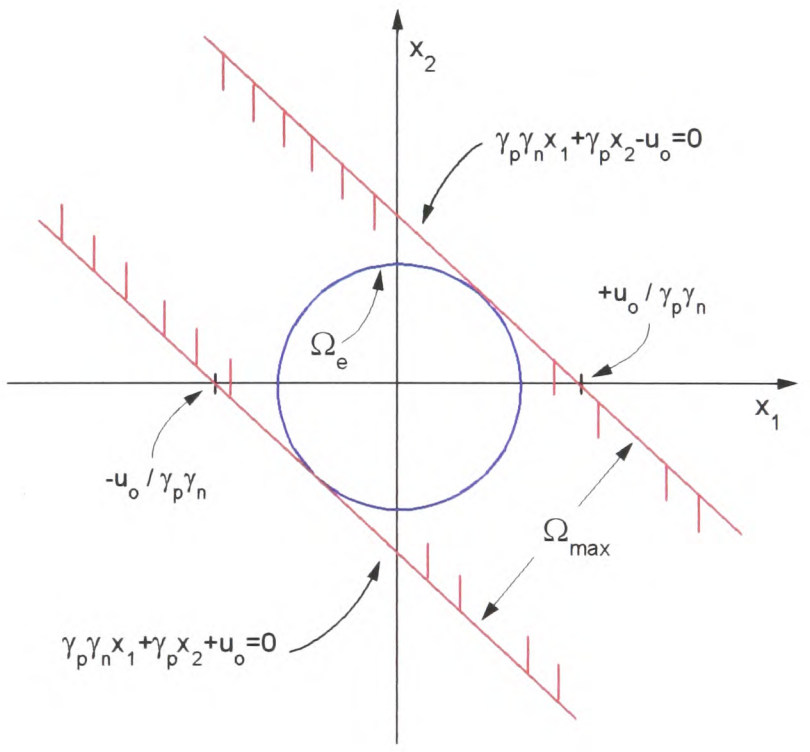


Figure 3.1: Stability region for a 2^{nd} *order unstable system* ($\gamma_p = 2$, $\gamma_n = 1$).

3.2.1 Optimum controllers for Unstable LTI systems with a constrained input

In this Section it will be demonstrated that, given an unstable LTI system with a constrained input, it is possible to find controllers that maximize the stability region. These controllers

can be categorized into linear and non-linear controllers.

3.2.1.1 Linear saturating controllers

Let us consider a LTI system as defined in Section 3.2. Let the controller be

$$u = sat\left(-\mathbf{K}^T\mathbf{x}\right), \tag{3.31}$$

where $sat(\cdot)$ is defined as

$$sat(\xi) = \begin{cases} \xi & \text{if } |\xi| < \sigma \\ u_o sgn(\xi) & \text{if } |\xi| \geq \sigma \end{cases} \tag{3.32}$$

σ is the saturation threshold. $\mathbf{K}^T \in R^{1\times n}$ is the controller vector. The linear feedback controller that maximizes the stability region is derived in the following theorem.

Theorem 3.2.4 *Given an LTI system as defined in Section 3.2 with feedback controller given by equations (3.31) and (3.32) the feedback gain that maximizes the stability region is*

$$\mathbf{K}^T = \theta\mu\mathbf{v}_p^T \tag{3.33}$$

where $\mathbf{v}_p \in R^{n\times 1}$ *is the left eigenvector associated with the unstable eigenvalue* γ_p, $\mu \in R$ *is a normalizing parameter defined as*

$$\mu = \sigma\frac{\gamma_p}{\mathbf{v}_p^T\mathbf{b}u_o}, \tag{3.34}$$

$\theta > 1$ *and* $\mathbf{v}_p^T\mathbf{b}u_o > 0$.

Proof: Let $\theta \to \infty$, then equations (3.31) and (3.32) are equivalent to equation (3.11) and the system will be stable according to the theorem 3.2.2. In the limit case that $\theta = 1$, the control will saturate on the boundary of $\Omega_{\max}$ ($\partial\Omega_{\max}$).

To find a μ that makes the control saturate on $\partial\Omega_{\max}$ let fix $\theta = 1$ and consider the state feedback controller

$$u = -\mu\mathbf{v}_p^T\mathbf{x}. \tag{3.35}$$

If the controller is saturated then

$$\mu\left|\mathbf{v}_p^T\mathbf{x}\right| = \sigma \tag{3.36}$$

and it is on $\partial\Omega_{\max}$ for the same value of $\mathbf{x}$ if

$$\gamma_p \left|\mathbf{v}_p^T \mathbf{x}\right| - \mathbf{v}_p^T \mathbf{b} u_o = 0. \tag{3.37}$$

Therefore, substituting equation (3.36) into equation (3.37)

$$\mu = \sigma \frac{\gamma_p}{\mathbf{v}_p^T \mathbf{b} u_o}.$$

Thus ensuring that

$$\theta > 1$$

also guarantees that the system will be asymptotically stable.□

The same result can be obtained by assigning the region $\Omega_{\max}$, the control constraints (3.2) and using the methods described in [Blanchini90] and [Bitsoris95].

From Theorem 3.2.4 it can be observed that a linear maximum stabilizer controller is such that it saturates only on the boundary of $\Omega_{\max}$.

3.2.1.2 Non-linear saturating controllers

Definition 3.2.3 *Let us consider an LTI system as defined in Section 3.2. Let the controller*

$$u = f(\mathbf{x}, \dot{\mathbf{x}}, t) \tag{3.38}$$

be a generic non continuous function of the states and the time. The controller defined by equation (3.38) is a maximum stabilizer controller if for each $t \in R$ and $\mathbf{x}_o \in \Omega_{\max}$ the state trajectory $\mathbf{x}(t) \in \Omega_{\max}$; where $\mathbf{x}_o$ are the states at a certain time t_o.

Potentially there can be non-linear controllers designed to be maximum stabilizers. For example a minimum time controller is a maximum stabilizer (see Section B.2 of Appendix B). Another clear example is given by the design of constrained *LQR* by [Ledwich95] where the gains are modified according to the position in the phase-plane.

Corollary 3.2.5 *A negative feedback bang-bang controller for an LTI system as defined in Section 3.2 is a maximum stabilizer controller if and only if the input-output characteristic lies in the region $\Omega_{\max}$.*

Proof: Let us assume that there exists a static bang-bang controller for the system (3.38) such that the closed loop system is stable. The input-output characteristic of a static bang-bang controller can be seen as a switching hyperplane defined by the equation $f(\mathbf{x}) = 0$. If the controller is such as to direct the state trajectory onto the hyperplane $f(\mathbf{x}) = 0$, then the system (3.38) will be closed loop stable for each $\mathbf{x} \in \Omega_{\max}$ and, according to Proposition 3.2.3, it will also be a maximum stabilizer controller. If the input-output characteristic does not lie in the region $\Omega_{\max}$ then there can be a trajectory that trying to reach the hyperplane $f(\mathbf{x}) = 0$ crosses the boundary of $\Omega_{\max}$.□

Corollary 3.2.6 *A negative feedback bang-bang controller for an LTI system as defined in Section 3.2 with a time delay τ on the control input is a maximum stabilizer controller if the input-output characteristic lies in the region*

$$\Omega_{\max}^{\tau} = \left\{ \mathbf{x} \in R^n; \left| \mathbf{v}_p^T \mathbf{x} \right| - \frac{2e^{-\gamma_p \tau} - 1}{\gamma_p} \mathbf{v}_p^T \mathbf{b} u_o < 0 \right\} \tag{3.39}$$

where the time delay τ must satisfy the condition

$$0 \leq \tau \leq \frac{1}{\gamma_p} \ln 2. \tag{3.40}$$

Proof: The proof is similar to Corollary 3.2.5 with the only difference that the input-output characteristic must lie in the region $\Omega_{\max}^{\tau}$. It is therefore sufficient to show that the state inside $\Omega_{\max}^{\tau}$ will not exceed the boundary of $\Omega_{\max}$ in a time τ. When the control is saturated the state is governed by equation (3.7). By substituting equation (3.7) in equation (3.13), and considering that $\mathbf{W}$ represents a base of generalized eigenvectors, the following two conditions must be verified

$$\left| \gamma_p e^{\gamma_p \tau} \mathbf{v}_p^T \mathbf{x} + (1 - e^{\gamma_p \tau}) \mathbf{v}_p^T \mathbf{b} u_o \right| < \mathbf{v}_p^T \mathbf{b} u_o \tag{3.41}$$

$$\left| \gamma_p e^{\gamma_p \tau} \mathbf{v}_p^T \mathbf{x} - (1 - e^{\gamma_p \tau}) \mathbf{v}_p^T \mathbf{b} u_o \right| < \mathbf{v}_p^T \mathbf{b} u_o, \tag{3.42}$$

and the state satisfying these conditions belongs to the following regions

$$\Omega_1 = \left\{ \mathbf{x} \in R^n; \gamma_p \left| \mathbf{v}_p^T \mathbf{x} \right| - \mathbf{v}_p^T \mathbf{b} u_o < 0 \right\} \tag{3.43}$$

$$\Omega_2 = \left\{ \mathbf{x} \in R^n; \left| \mathbf{v}_p^T \mathbf{x} \right| - \frac{2e^{-\gamma_p \tau} - 1}{\gamma_p} \mathbf{v}_p^T \mathbf{b} u_o < 0 \right\}. \tag{3.44}$$

The region $\Omega_1 \equiv \Omega_{\max}$ while, for the values of τ in the interval

$$0 \leq \tau \leq \frac{1}{\gamma_p} \ln 2,$$

it is verified that $\Omega_2 \subseteq \Omega_1$. If the input-output characteristic lies in the region Ω_2, then the state inside Ω_2 will not exceed the boundary of $\Omega_{\max}$ in a time τ which proves the Corollary.□

Example 3.2 *Let a 2^{nd} order unstable system be described by equation (3.28), let us also assume that there is a time delay τ on the control input. The time-optimum switching line for the case without time delay is given in equation (B.18) in Section B.2 of Appendix B. The time-optimum switching line for the case with a delay τ on the control input is easily computed from equation (B.18) assuming that the switch has to take place a time τ before crossing equation (B.18). A continuous minimum time controller is a maximum stabilizer since the input/output characteristic of the controller lies entirely in the region $\Omega_{\max}$ as shown in Figure 3.2. This is not true in the case of a digital implementation or if there is a time delay in the control action because it is not possible to guarantee the exact switching time which is crucial if the system is unstable. Indeed the nonlinear characteristic of the controller converges to the $\Omega_{\max}$ when the state is far from the origin (see Figure 3.2) and a delay τ can make the system enter the unstable region. However it is possible to determine an optimum controller that takes into account the delay τ. Let us consider the region $\Omega^{\tau}_{\max}$. By comparing equation (3.39) to the expression of $\Omega_{\max}$ it can be noted that an optimum controller designed with a modified maximum control signal*

$$\bar{u}_o = \left(2e^{-\gamma_p \tau} - 1\right) u_o \tag{3.45}$$

guarantees the maximum stability region because it satisfies the conditions of Corollary 3.2.6. The time-optimum switching line in the case of a τ delay is then obtained by substituting equation (3.45) into equation (B.18). The time-optimum switching lines with and without the time delay are given in Figure 3.2.

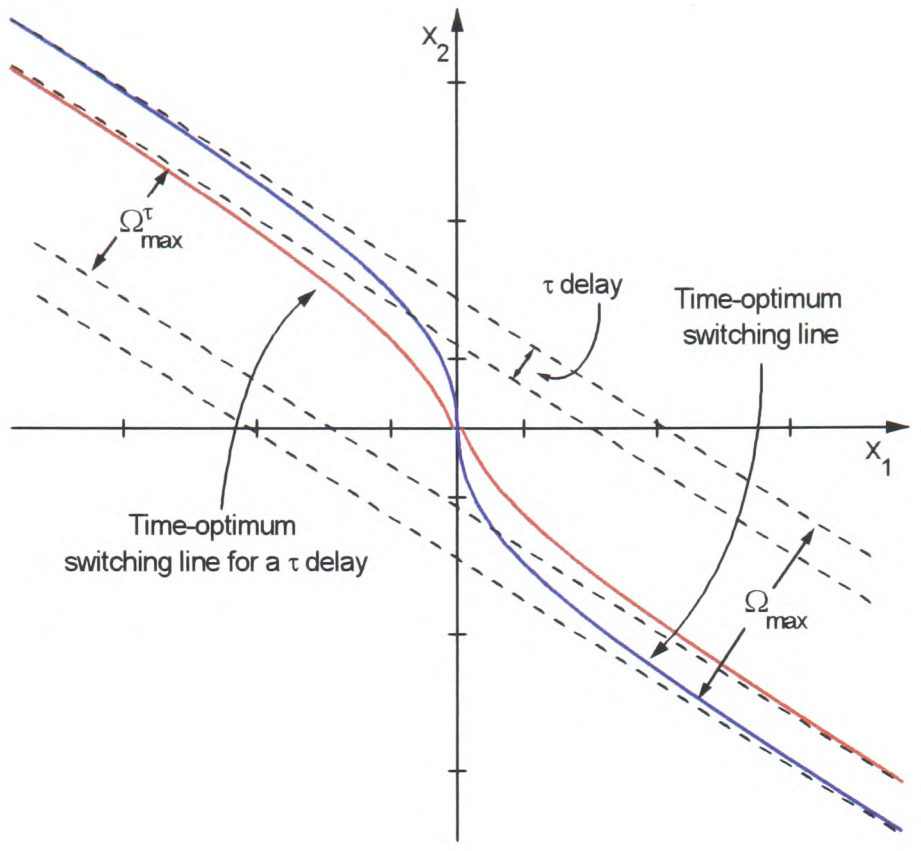


Figure 3.2: Time-optimum switching lines.

3.3 Stability region for single input LTI systems under state feedback control with constrained input

In the previous section the stability region for a generic LTI system with one unstable eigenvalue and a constrained input was considered. It was demonstrated that there exist controllers that maximize the stability region (§ Section 3.2.1). In this section the stability region for single input systems under state feedback control with constrained input that is not a maximum stabilizer is analysed. Let us consider an LTI system in general state space form:

$$\dot{\mathbf{x}} = \mathbf{A}\mathbf{x} + \mathbf{b}u \tag{3.46}$$

where $\mathbf{A} \in R^{n\times n}$, $b \in R^{n\times 1}$, $\mathbf{x} \in R^n$, $u \in R$. It is assumed that b is of rank 1 and the pair $(\mathbf{A}, \mathbf{b})$ is completely controllable. It is also assumed that the input is subject to a saturation

$$|u| \leq u_o. \tag{3.47}$$

where u_o is a constant value. A state feedback control can be linear or nonlinear and in continuous time and discrete time. It is assumed that the nonlinear controllers are memoryless

and have a symmetric characteristic with respect to the origin of the state space. With the above assumptions a constrained state feedback control can be expressed as

$$u = -u_o sat\left(f\left(\mathbf{x}\right)\right). \tag{3.48}$$

In this Section only some cases will be studied which represent the cases mostly found in the control of the vertical position of a plasma. These cases are the relay control law, the relay control law with a time delay and the saturating linear control law. Equation (3.48) takes the following forms

$$\begin{array}{ll} \text{Relay control law:} & f\left(\mathbf{x}\right) = sgn\left(\mathbf{v}^T\mathbf{x}\right) \\ \text{Relay control law with a time delay:} & f\left(\mathbf{x}\right) = sgn\left[\mathbf{v}^T\mathbf{x}\left(t-\tau\right)\right] \\ \text{Saturating linear control law:} & f\left(\mathbf{x}\right) = \sigma\mathbf{k}^T\mathbf{x} \end{array}.$$

The basic idea to calculate the stability region is to discretize the controlled system and determine the conditions for which the stability of the discrete time system holds. The discretization time is given when the state crosses a given hyperplane, describing the control function, and is therefore not constant. Applying this criteria, it is also possible to determine the existence, the stability and the period of possible limit cycles.

3.3.1 Relay control law

The following Theorem give necessary conditions for stability of the system (3.46) under control (3.48) in the case of a relay control law.

Theorem 3.3.1 *Let us consider a LTI system as defined above and assume that the constrained state feedback control is*

$$u = -u_o sgn\left(\mathbf{v}^T\mathbf{x}\right) = -u_o \frac{\mathbf{v}^T\mathbf{x}\left(t_k^+\right)}{\left|\mathbf{v}^T\mathbf{x}\left(t_k^+\right)\right|} \tag{3.49}$$

where $\mathbf{v}^T\mathbf{b}$ *is nonsingular and* $\mathbf{v}^T\mathbf{b}u_o > 0$. $\mathbf{v}^T$ *is selected as to generate a stabilizing control [Elghezawi83] and* $\mathbf{x}\left(t_k^+\right)$ *are the states just after the crossing of the hyperplane. A sufficient condition for stability is that the trajectory* $\mathbf{x}\left(t\right)$ *reaches the switching hyperplane and, when the* $\mathbf{x}\left(t\right)$ *crosses the hyperplane at the times* $t_o, t_1, \ldots, t_{k-1}, t_k, t_{k+1}, \ldots t_\infty$, *the eigenvalues*

of the matrix $\Phi_r(T_k)$ *are inside the unit circle. Where* $T_k = t_k - t_{k-1}$ *and* $\Phi_r(T_k)$ *is the transition matrix of the system restricted to the switching surface* $\mathbf{v}^T\mathbf{x} = 0$.

Proof: The control is described by the hyperplane $\mathbf{v}^T\mathbf{x} = 0$. When the state trajectory crosses the hyperplane at the times $t_o, t_1, \ldots, t_{k-1}, t_k, t_{k+1}$, the

$$\mathbf{v}^T\mathbf{x}(t_o) = \mathbf{v}^T\mathbf{x}(t_1) = \ldots = \mathbf{v}^T\mathbf{x}(t_{k-1}) = \mathbf{v}^T\mathbf{x}(t_k) = \mathbf{v}^T\mathbf{x}(t_{k+1}). \tag{3.50}$$

is true. The states at the time t_{k+1} can be expressed in terms of $\mathbf{x}(t_k)$ as

$$\mathbf{x}(t_{k+1}) = \mathbf{e}^{\mathbf{A}T_k}\mathbf{x}(t_k) + \left(\mathbf{I} - \mathbf{e}^{\mathbf{A}T_k}\right)\mathbf{A}^{-1}\mathbf{b}u_o\frac{\mathbf{v}^T\mathbf{x}\left(t_k^+\right)}{\left|\mathbf{v}^T\mathbf{x}\left(t_k^+\right)\right|}. \tag{3.51}$$

Since from equation (3.50) $\mathbf{v}^T\mathbf{x}(t_k) = \mathbf{v}^T\mathbf{x}(t_{k+1})$ then from equation (3.51)

$$\frac{\mathbf{v}^T\mathbf{x}\left(t_k^+\right)}{\left|\mathbf{v}^T\mathbf{x}\left(t_k^+\right)\right|} = \frac{\mathbf{v}^T\left(I - \mathbf{e}^{\mathbf{A}T_k}\right)}{\mathbf{v}^T\left(I - \mathbf{e}^{\mathbf{A}T_k}\right)\mathbf{A}^{-1}\mathbf{b}u_o}\mathbf{x}(t_k). \tag{3.52}$$

Hence backsubstituting in equation (3.51) it can be shown that

$$\mathbf{x}(t_{k+1}) = \Phi(T_k)\,\mathbf{x}(t_k) \tag{3.53}$$

where

$$\Phi(T_k) = \left[\mathbf{e}^{\mathbf{A}T_k} + \left(\mathbf{I} - \mathbf{e}^{\mathbf{A}T_k}\right)\mathbf{A}^{-1}\mathbf{b}\frac{\mathbf{v}^T\left(I - \mathbf{e}^{\mathbf{A}T_k}\right)}{\mathbf{v}^T\left(I - \mathbf{e}^{\mathbf{A}T_k}\right)\mathbf{A}^{-1}\mathbf{b}}\right]. \tag{3.54}$$

The equations describing the system motion restricted to the switching hyperplane $\mathbf{v}^T\mathbf{x} = 0$ can be written as

$$\begin{cases} \mathbf{x}(t_{k+1}) = \Phi(T_k)\,\mathbf{x}(t_k) \\ \mathbf{v}^T\mathbf{x}(t_k) = 0 \end{cases}. \tag{3.55}$$

This is reflected in a reduction of the system dynamics from a n^{th}-order to a $(n-1)^{th}$-order. To obtain a solution of the reduced order dynamics, the $\mathbf{v}^T\mathbf{x} = 0$ is solved for one of the state variables in terms of the other $n-1$ states and it is substituted in the remaining $n-1$ equations of (3.53). The resultant $(n-1)^{th}$-order can be represented by the system equation

$$\mathbf{z}(t_{k+1}) = \Phi_r(T_k)\,\mathbf{z}(t_k) \tag{3.56}$$

which describes the system motion restricted to the switching surface $\mathbf{v}^T\mathbf{x} = 0$. The system (3.56) is stable if, and only if, the eigenvalues of the matrix $\mathbf{\Phi}_r(T_k)$ are inside the unit circle. Therefore for those values of T_k such that the eigenvalues of the matrix $\mathbf{\Phi}_r(T_k)$ are inside the unit circle the system is stable.□

Necessary and sufficient stability conditions are derived in the following Corollary for the case of one unstable pole.

Corollary 3.3.2 *In the case the system has one unstable pole a necessary and sufficient condition for a given initial condition x_o to be stabilized is that $x_o \in \Omega_{\max}$, the trajectory $x(t)$ generating from x_o reaches the switching hyperplane within the region $\Omega_{\max}$ and that the conditions of Theorem 3.3.1 are satisfied.*

Proof: If the conditions of Theorem 3.3.1 are satisfied it is sufficient to find the locus of the initial conditions $\mathbf{x}_o$ that reach the hyperplane within the region $\Omega_{\max}$. From Theorem 3.2.2, this is given by

$$\Omega = \left\{\forall \mathbf{x}_o \in \Omega_{\max} : \exists t_r \in R;\ \mathbf{v}^T\mathbf{x}(t_r) = 0;\ \gamma_p \left|\mathbf{v}_p^T\mathbf{x}(t_r)\right| - \mathbf{v}_p^T\mathbf{b}u_o < 0\right\} \tag{3.57}$$

where t_r is the time when the state crosses the hyperplane.□

It should be mentioned that the above results include the sufficient condition for sliding mode [Hung93]. Indeed, given a generic stabilizing $s(\mathbf{x}) = \mathbf{v}^T\mathbf{x}$ and a control law (3.49) if the condition $s(\mathbf{x})\,\dot{s}(\mathbf{x}) < 0$ is satisfied then the system will slide along the switching hyperplane and the eigenvalues of the matrix $\mathbf{\Phi}_r(T_k)$ will be inside the unit circle.

From the discrete time sliding mode theory the following important result is derived.

Lemma 3.3.3 *If the system considered in Theorem 3.3.1 uses a stabilizing controller then, if the initial conditions are inside the* ***stability*** *region, the time between switching decreases.*

Proof: Let us consider an initial state on the hyperplane at time t and assume that

$$\mathbf{v}^T\mathbf{x}(t^+) > 0. \tag{3.58}$$

If the system is stable the state will cross the hyperplane at a time $t+T$. Let us fix the sampling time at T. The state at the time $t+T$ is given by

$$\begin{cases} \mathbf{x}(t+T) = \mathbf{\Phi}(T)\,\mathbf{x}(t) \\ \mathbf{v}^T\mathbf{x}(t+T) = 0 \end{cases} \tag{3.59}$$

At the successive sample the state will be $\mathbf{x}(t+2T)$ and if the system is stable the following condition is true [Sarpturk87]

$$\left|\mathbf{v}^T\mathbf{x}(t+2T)\right| \leq \left|\mathbf{v}^T\mathbf{x}(t+T)\right| \tag{3.60}$$

which can be decomposed in

$$\left[\mathbf{v}^T\mathbf{x}(t+2T) - \mathbf{v}^T\mathbf{x}(t+T)\right] sgn\left[\mathbf{v}^T\mathbf{x}(t+T)\right] \leq 0 \tag{3.61}$$

$$\left[\mathbf{v}^T\mathbf{x}(t+2T) + \mathbf{v}^T\mathbf{x}(t+T)\right] sgn\left[\mathbf{v}^T\mathbf{x}(t+T)\right] \geq 0. \tag{3.62}$$

By observing that the control changes sign crossing the hyperplane and that at time t equation (3.58) is true it follows that at time $t+T$ the opposite sign will be used therefore the condition (3.61) can be written as

$$\mathbf{v}^T\mathbf{x}(t+2T) \geq \mathbf{v}^T\mathbf{x}(t+T) \tag{3.63}$$

and, from the second equation in (3.59),

$$\mathbf{v}^T\mathbf{x}(t+2T) \geq \mathbf{0}. \tag{3.64}$$

Equation (3.64) expresses the fact that the time taken to cross the hyperplane from $\mathbf{x}(t+T)$ is less or equal than T therefore the time between switching decreases. Similarly, if the initial state are outside the stability region then, according to equation (3.60), the time between switching increases.□

Let $\lambda_i(T)$ be the $i-th$ eigenvalue of $\mathbf{\Phi}_r(T)$, where $\lambda_i(T)$ can also be a multiple eigenvalue. Let $\boldsymbol{\lambda_{max}(T)}$ be defined as

$$\lambda_{\max}(T) = \max_i \left[|\lambda_i(T)|\right]. \tag{3.65}$$

Let c_j be the $j-th$ solution of the equation $\lambda_{\max}(T) = 1$ such that $c_1 < c_2 < \ldots < c_j < c_{j+1}$. Using the result in Lemma 3.3.3 the two following remarks can be derived. In the first Remark the region describing the boundary of the asymptotic stability region is derived. In the second Remark the existence, the stability and the period of eventual limit cycle are derived.

Remark 3.3.1 *If, for the system in Theorem 3.3.1,* $\exists c_1$ *such that* $\forall T \in]0; c_1] \rightarrow \lambda_{\max}(T) < 1$ *then the state that satisfies*

$$\begin{cases} \mathbf{x} < e^{\mathbf{A}t}\mathbf{x}_l + \left(\mathbf{I} - \mathbf{e}^{\mathbf{A}t}\right)\mathbf{A}^{-1}\mathbf{b}u_o, & \text{for } \mathbf{v}^T\mathbf{x} < \mathbf{0}\,\forall t > 0 \\ \mathbf{x} > -e^{\mathbf{A}t}\mathbf{x}_l - \left(\mathbf{I} - \mathbf{e}^{\mathbf{A}t}\right)\mathbf{A}^{-1}\mathbf{b}u_o, & \text{for } \mathbf{v}^T\mathbf{x} > \mathbf{0}\,\forall t > 0 \end{cases} \tag{3.66}$$

where $\mathbf{x}_l$ is defined by

$$\mathbf{x}_l = \left(\mathbf{I} - \mathbf{e}^{\mathbf{A}c_1}\right)^{-1}\left(2\mathbf{e}^{\mathbf{A}\frac{c_1}{2}} - \mathbf{e}^{\mathbf{A}c_1} - \mathbf{I}\right)\mathbf{A}^{-1}\mathbf{b}u_o, \tag{3.67}$$

can be asymptotically stabilized to the origin.

Proof: The proof is derived from Theorem 3.3.1 and Lemma 3.3.3.□

Remark 3.3.2 *Given a transition matrix* $\mathbf{\Phi}_r(T)$*, by varying* T *the following criteria applies:*

1. *For a stable plant there is a stable limit cycle of period* c_j *if*

$$\dot{\lambda}_{\max}(T)\Big|_{T=c_j} > 0.$$

If the plant is unstable then the stability is restricted to the state that does not exceed the stability region. In other words, for a given c_j*, that gives* $\lambda_{\max}(c_j) > 1$*, the state at time* c_{j+1} *may have exceeded the stability region.*

2. *There is an unstable limit cycle of period* c_j *if*

$$\dot{\lambda}_{\max}(T)\Big|_{T=c_j} > 0.$$

3. *There are no limit cycles* ***if***

$$\lambda_{\max}(T) \neq 1\ \forall T > 0.$$

Proof: The proof is derived from Theorem 3.3.1 and Lemma 3.3.3.□

Remark 3.3.2 allows to determine the existence, the stability and the period of a limit cycle. It differs from other methods, like the describing function, because there is no approximation on the system dynamics and the limit cycle is not supposed to be a sinusoid (see Figure 3.7 in Example 3.4). It also differs from methods found in [Atherton75] and [Atherton82] because it also includes the stability results.

The following two examples (Example 3.3 and Example 3.4) show how to calculate the stability region and determine the existence, the stability and the period of a limit cycle.

Example 3.3 *Consider a 2^{nd} order unstable system as in the example 3.1. Let the control function be*

$$u = -u_o sgn\left(\mathbf{v}^T \mathbf{x}\right). \tag{3.68}$$

The three cases shown in Figure 3.3 must be considered:

case 1: The conditions of Theorem 3.3.1 are satisfied.

case 2: The conditions of Theorem 3.3.1 are not satisfied but the initial conditions are inside the region $\Omega_{\max}$.

case 3: The initial conditions are outside the region $\Omega_{\max}$.

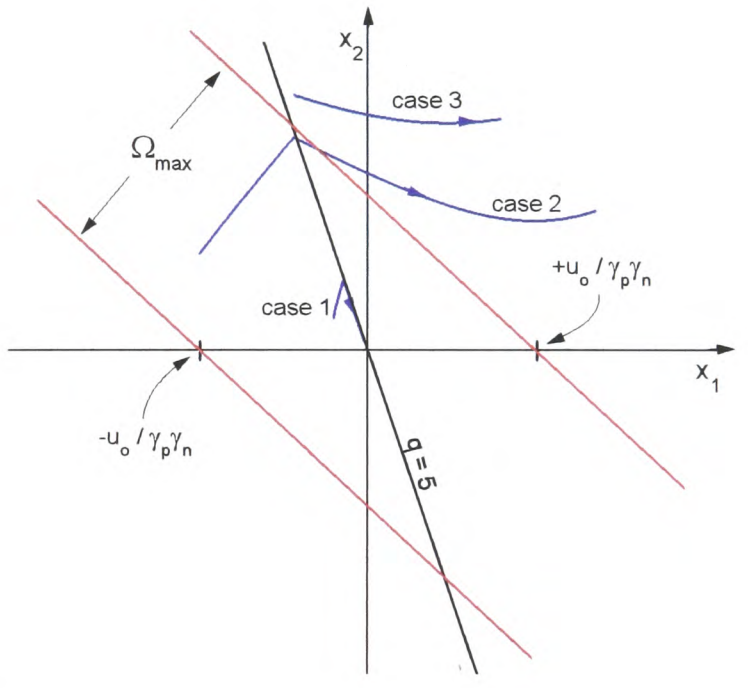


Figure 3.3: 2^{nd} order unstable system trajectories under saturated state feedback ($\gamma_p = 2$, $\gamma_n = 1$).

In the case 1 the system is asymptotically stable while in the cases 2 and 3 the state trajectory diverges from the origin. The region Ω of the states for which the trajectory converges to the origin depends on the value of the state feedback gains $v^T = [\ q \quad 1\ ]$ and in particular on the relative position of the switching line v with respect to the intersection between the stable/unstable directions $\mathbf{x}_s^T$, where

$$\mathbf{x}_s^T = \left[\ \frac{(\gamma_p - \gamma_n)}{\gamma_p \gamma_n (\gamma_p + \gamma_n)} u_o \quad -\frac{2}{(\gamma_p + \gamma_n)} u_o\ \right].$$

Deriving $\mathbf{\Phi}_r(T_k)$ as in Theorem 3.3.1, the system restricted to the switching hyperplane is of the 1^{st} order and the values of $\lambda_{\max}(T)$ for different values of q is shown in Figure 3.4.

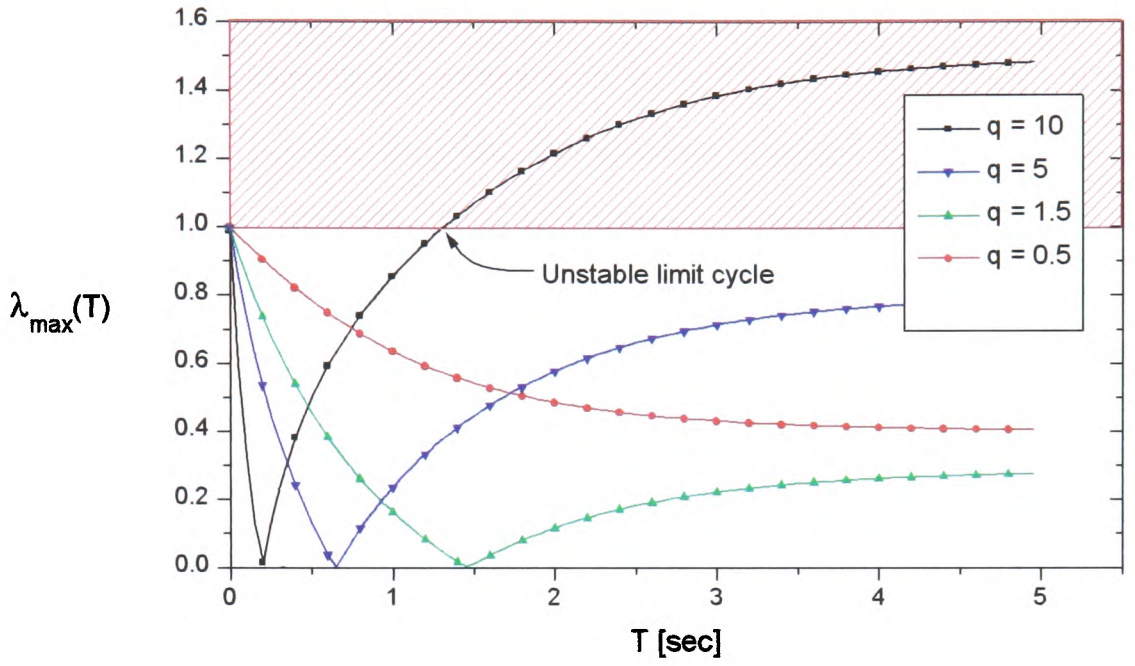


Figure 3.4: $\lambda_{\max}(T)$ of the matrix $\Phi_r(T)$ for different values of q ($\gamma_p = 2$, $\gamma_n = 1$).

From the analysis of this graph it is evident that there are two distinct stability areas. The value of q delimiting the two areas can be calculated analytically. There are two cases:

Case a: if

$$q \leq \frac{2}{\gamma_p \gamma_n (\gamma_p - \gamma_n)}$$

there is no limit cycle and the stability region Ω is given by equation (3.57). This can be calculated using the intersection between the switching line $\mathbf{v}$ and $\Omega_{\max}$

$$\mathbf{x}_{fp}^T = \left[\frac{1}{\gamma_p (q - \gamma_n)} u_o \quad -\frac{q}{\gamma_p (q - \gamma_n)} u_o \right]$$
$$\mathbf{x}_{fn}^T = \left[-\frac{1}{\gamma_p (q - \gamma_n)} u_o \quad \frac{q}{\gamma_p (q - \gamma_n)} u_o \right]$$

and is given by:

$$\begin{cases} \mathbf{x}_o < \mathbf{e}^{-\mathbf{A}t} (\mathbf{x}_{fp} - \mathbf{A}^{-1}\mathbf{b}u_o) + \mathbf{A}^{-1}\mathbf{b}u_o & \text{when } \mathbf{x}_o < \mathbf{x}_{fp}^T \\ \gamma_p \left| \mathbf{v}_p^T \mathbf{x}_s \right| - \mathbf{v}_p^T \mathbf{b} u_o < 0 & \text{when } \mathbf{x}_{fn}^T \leq \mathbf{x}_o \leq \mathbf{x}_{fp}^T \\ \mathbf{x}_o > \mathbf{e}^{-\mathbf{A}t} (\mathbf{x}_{fn} + \mathbf{A}^{-1}\mathbf{b}u_o) - \mathbf{A}^{-1}\mathbf{b}u_o & \text{when } \mathbf{x}_o > \mathbf{x}_{fn}^T \end{cases} \tag{3.69}$$

where $\mathbf{v}_p$ is the left eigenvector associated to the unstable eigenvalue γ_p.

Case b: if

$$q > \frac{2}{\gamma_p \gamma_n (\gamma_p - \gamma_n)}$$

there is a limit cycle and the boundary of the stability region Ω *is calculated using equation (??) and (3.67).* c_1 *is given by the solution of* $\lambda_{\max}(T) = 1$. *The* Ω *for different values of* q *is shown in Figure 3.5. As an example, the stability regions estimated using the methods in [Madani-Esfahani90] and [Choi94a] are also shown. A similar result to [Madani-Esfahani90] and [Choi94a] can be obtained using the methods in [Corless93] and [Glazos95].*

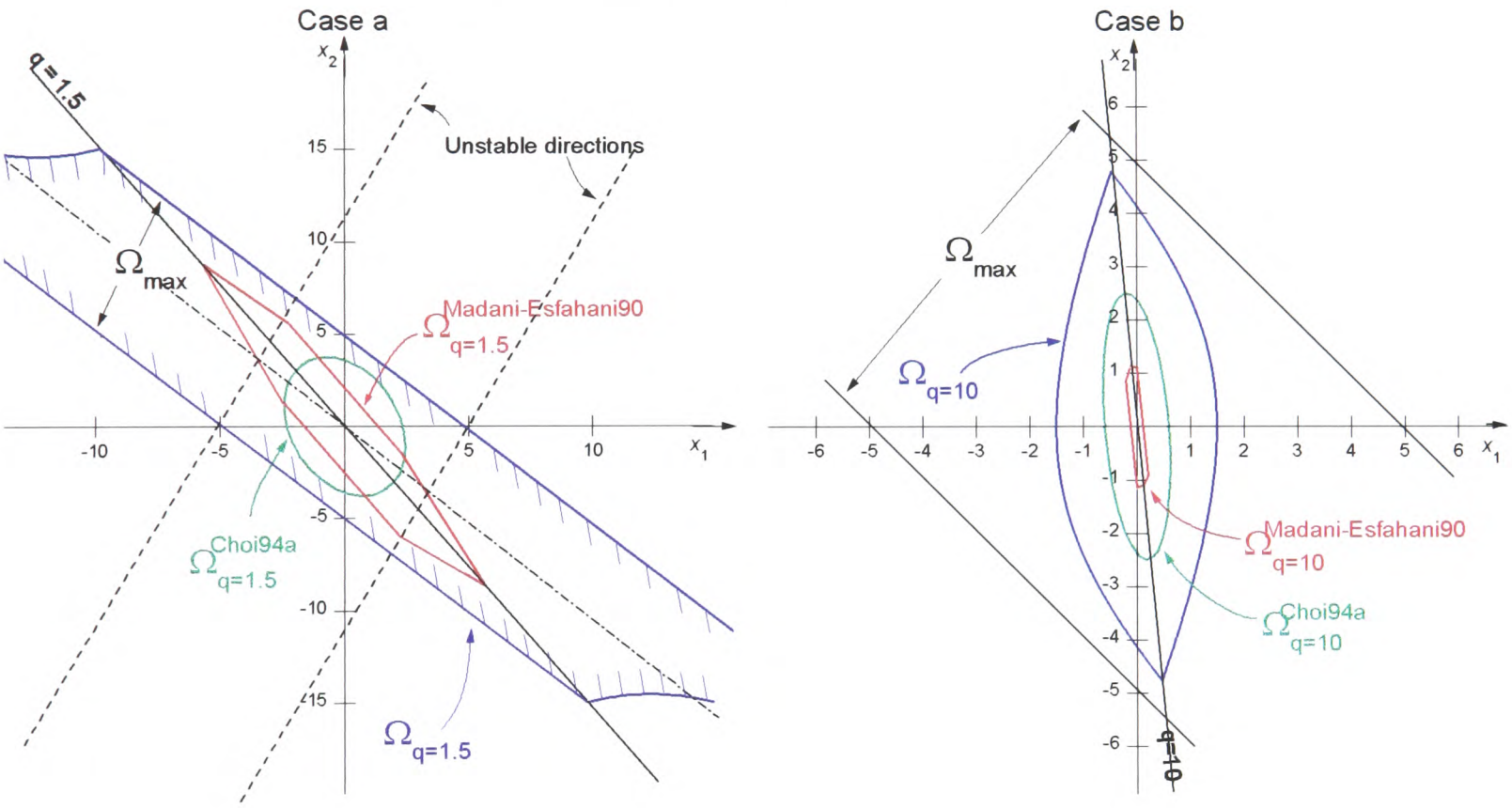


Figure 3.5: Stability regions of 2^{nd} *order unstable system under relay feedback control (*$\gamma_p = 2$, $\gamma_n = 1$*).*

Example 3.4 *Let a 3^{nd} order unstable system in state space form be described by*

$$\mathbf{A} = \begin{pmatrix} 0 & 1 & 0 \\ 0 & 0 & 1 \\ 6 & -1 & -4 \end{pmatrix} \quad \mathbf{b} = \begin{pmatrix} 0 \\ 0 \\ 1 \end{pmatrix}.$$

The open loop eigenvalues are -1, -2 and 3. Let the control function be $u = -u_o sgn\left(\mathbf{v}^T\mathbf{x}\right)$, where $u_o = 1$ and $\mathbf{v}^T = \begin{pmatrix} 70 & 1 & 1 \end{pmatrix}$. The values of $\lambda_{\max}(T)$ of the matrix $\mathbf{\Phi}_r(T)$ are shown in Figure 3.6. There are two values of T for which there is a solution of $\lambda_{\max}(T) = 1$.

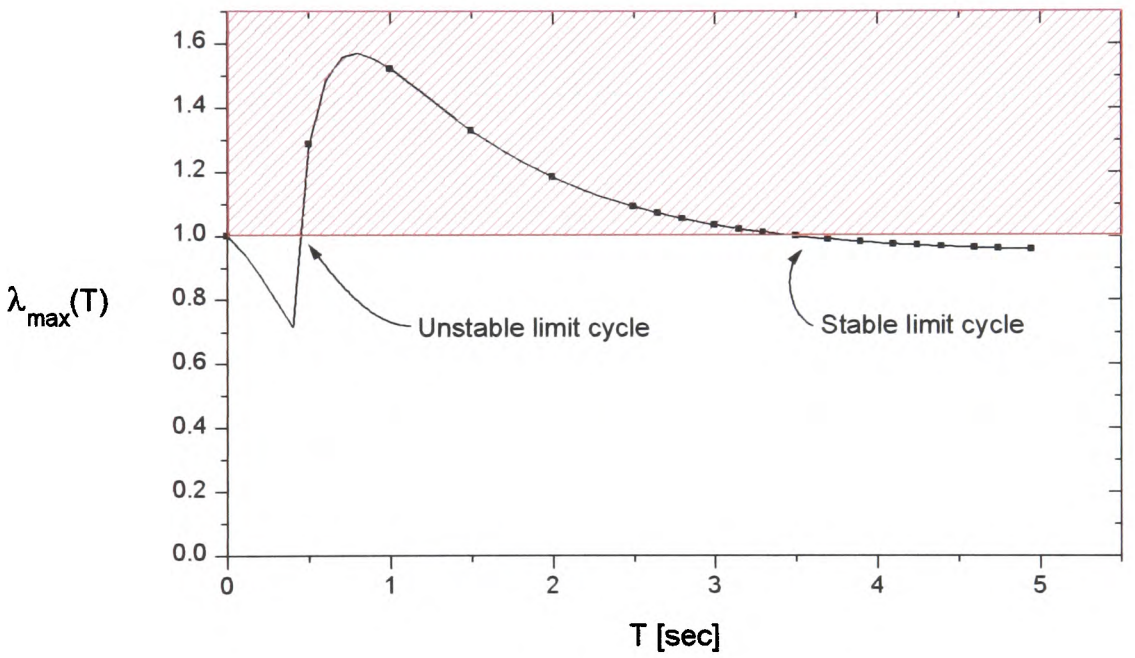


Figure 3.6: $\lambda_{\max}(T)$ of the matrix $\Phi_r(T)$ for a 3^{rd} order system.

The first crossing at c_1 indicates that there is an unstable limit cycle and all the initial conditions starting inside the region defined by equations (??) and (3.67) can be stabilized asymptotically to the origin. The second crossing at c_2 satisfies the conditions for a stable limit cycle. Therefore the stability region is given by equation (3.57). Figure 3.7 shows the trajectories when the initial conditions start inside the asymptotic stability region, in the stability region and outside the stability region.

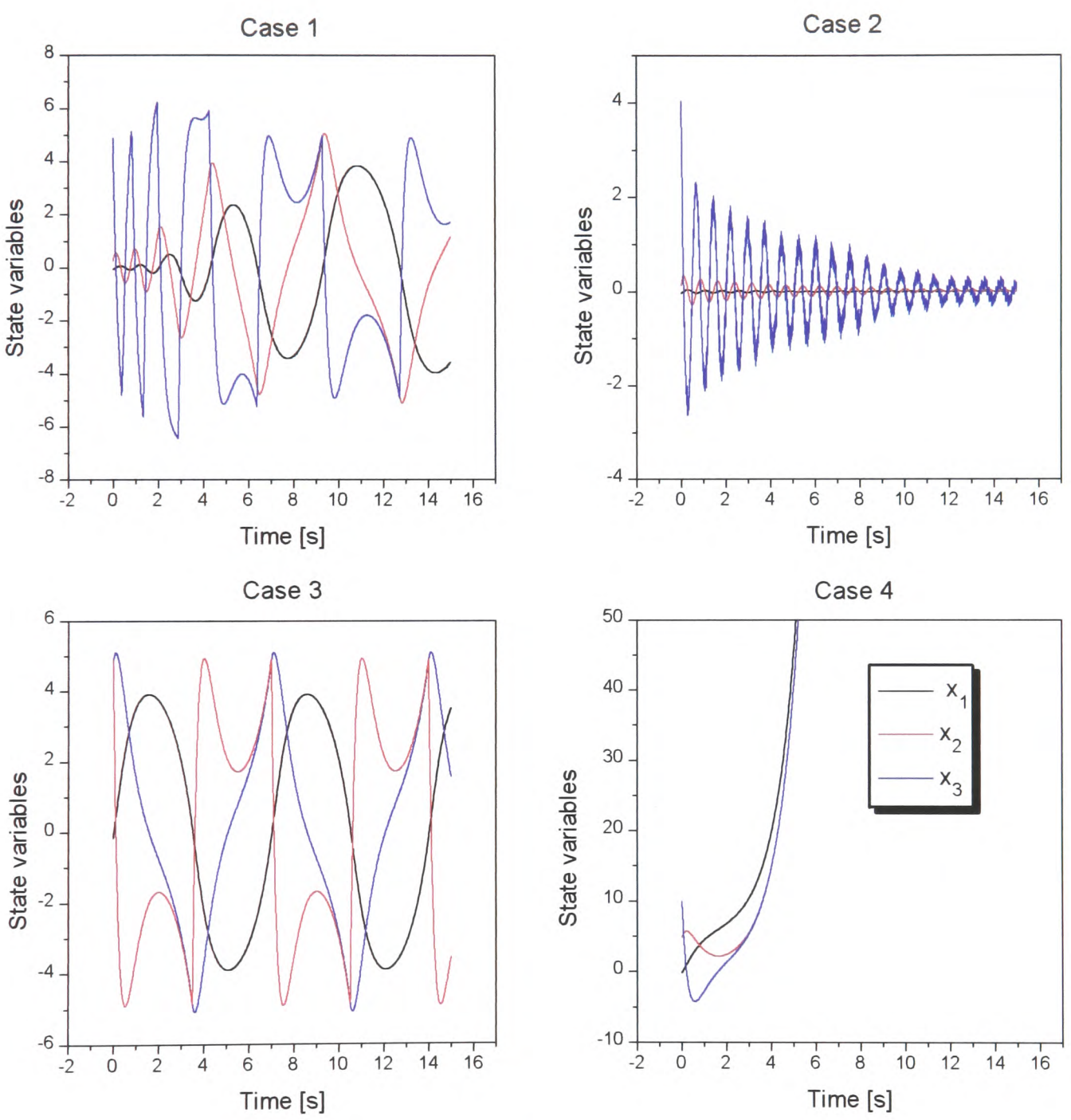


Figure 3.7: (a) Initial conditions inside the asymptotic stability region, (b) Initial conditions inside the stability region and the limit cycle, (c) Initial conditions inside the stability region but outside the limit cycle, (d) Initial conditions outside the stability region.

The three dimensions stable limit cycle is shown in Figure 3.8.

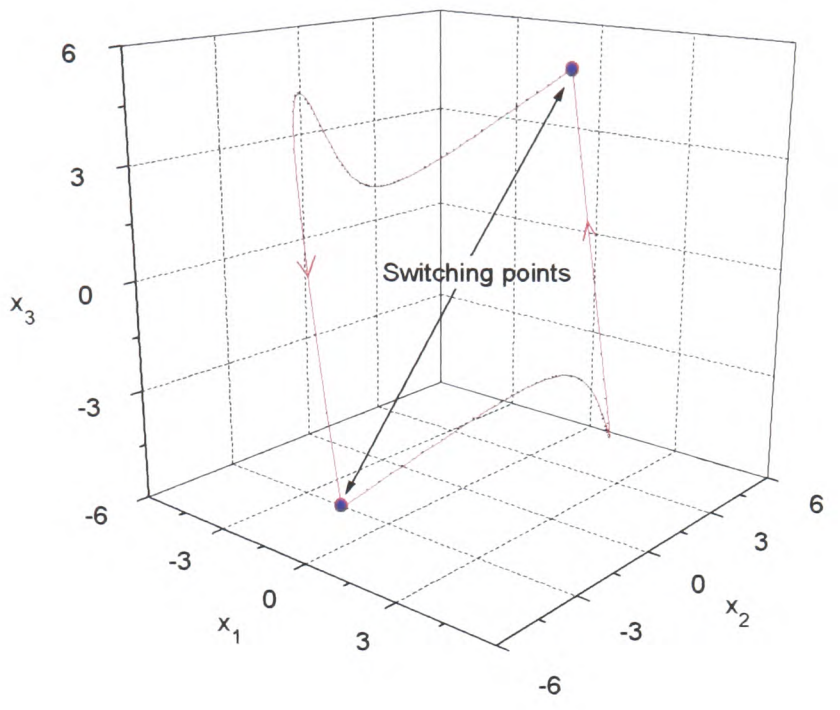


Figure 3.8: Limit cycle in the phase-plane.

3.3.2 Relay control law with a time delay

The results in the previous Section are extended to the case of a relay control law with a time delay in the following Theorem 3.3.4, Corollary 3.3.5 and Remark 3.3.3. The derivations are very similar to the case of a relay control law.

Theorem 3.3.4 *Let us consider a system as defined at the beginning of Section 3.3. Let us assume that the control signal has a delay τ and the constrained state feedback control is*

$$u = \bar{u}(t - \tau) \tag{3.70}$$

where

$$\bar{u} = -u_o sgn\left[\mathbf{v}^T \mathbf{x}(t)\right] = -u_o \frac{\mathbf{v}^T \mathbf{x}(t^+)}{|\mathbf{v}^T \mathbf{x}(t^+)|}, \tag{3.71}$$

$\mathbf{v}^T\mathbf{b}$ *is nonsingular and* $\mathbf{v}^T\mathbf{b}u_o > 0$. $\mathbf{v}^T$ *is selected as to generate a stabilizing control [Elghezawi83] and* $\mathbf{x}\left(t_k^+\right)$ *are the states just after the crossing of the hyperplane. A sufficient condition for a given initial condition* $\mathbf{x}_o$ *to be stabilized is that when the trajectory* $\mathbf{x}(t)$ *generating from* $\mathbf{x}_o$ *crosses the switching hyperplane* $\mathbf{v}^T\mathbf{x}(t) = 0$ *at the times* $t_o, t_1, \ldots, t_{k-1}, t_k$, *the eigenvalues of the matrix* $\mathbf{\Phi}_r(T_k)$ *are inside the unit circle. Where* $T_k = t_k - t_{k-1}$, $x\left(t_k^+\right)$

are the states just after the crossing of the hyperplane and $\mathbf{\Phi}_r(T_k)$ *is the transition matrix of the system restricted to the switching surface* $\mathbf{v}^T\mathbf{x}(t_k) = 0$.

Proof: Let us assume that at the time t_k the system state crosses the switching hyperplane $\mathbf{v}^T\mathbf{x}(t_k) = 0$. After a time τ the control will change sign according to the control function (3.70) and (3.71). At the time $t_k + \tau$ the state will be

$$\mathbf{x}(t_k+\tau) = \mathbf{e}^{\mathbf{A}\tau}\mathbf{x}(t_k) + \left(\mathbf{I} - \mathbf{e}^{\mathbf{A}\tau}\right)\mathbf{A}^{-1}\mathbf{b}u_o\frac{\mathbf{v}^T\mathbf{x}\left(t_k^-\right)}{\left|\mathbf{v}^T\mathbf{x}\left(t_k^-\right)\right|}, \tag{3.72}$$

where $\mathbf{x}(t_k)$ belongs to the hyperplane $\mathbf{v}^T\mathbf{x}(t_k) = 0$ and $\mathbf{x}(t^-)$ are the states just before crossing the hyperplane. Let us assume that at the time t_{k+1} the state crosses again the switching hyperplane

$$\mathbf{v}^T\mathbf{x}(t_k) = \mathbf{v}^T\mathbf{x}(t_{k+1}) = 0. \tag{3.73}$$

The value of the states at the time t_{k+1} starting from $\mathbf{x}(t_k+\tau)$ is given by

$$\mathbf{x}(t_{k+1}) = \mathbf{e}^{\mathbf{A}(T_k-\tau)}\mathbf{x}(t_k+\tau) + \left(\mathbf{I} - \mathbf{e}^{\mathbf{A}(T_k-\tau)}\right)\mathbf{A}^{-1}\mathbf{b}u_o\frac{\mathbf{v}^T\mathbf{x}\left(t_k^+\right)}{\left|\mathbf{v}^T\mathbf{x}\left(t_k^+\right)\right|} \tag{3.74}$$

Substituting equation (3.72) into equation (3.74) and observing from (3.72) that

$$\frac{\mathbf{v}^T\mathbf{x}\left(t_k^+\right)}{\left|\mathbf{v}^T\mathbf{x}\left(t_k^+\right)\right|} = -\frac{\mathbf{v}^T\mathbf{x}\left(t_k^-\right)}{\left|\mathbf{v}^T\mathbf{x}\left(t_k^-\right)\right|}$$

the $\mathbf{x}(t_{k+1})$ can be expressed in terms of $\mathbf{x}(t_k)$ as follows

$$\mathbf{x}(t_{k+1}) = \left[\mathbf{e}^{\mathbf{A}T_k} + \mathbf{d}_1\frac{\mathbf{v}^T\left(\mathbf{I} - \mathbf{e}^{\mathbf{A}T_k}\right)}{\mathbf{v}^T\mathbf{d}_1}\right]\mathbf{x}(t_k) = \mathbf{\Phi}(T_k)\mathbf{x}(t_k). \tag{3.75}$$

where $\mathbf{d}_1 = \left(2\mathbf{e}^{\mathbf{A}T_k}\mathbf{e}^{-\mathbf{A}\tau} - \mathbf{e}^{\mathbf{A}T_k} - \mathbf{I}\right)\mathbf{A}^{-1}b$. The equations describing the system motion restricted to the switching hyperplane $\mathbf{v}^T\mathbf{x}(t_k) = 0$ can be written as

$$\begin{cases} \mathbf{x}(t_{k+1}) = \mathbf{\Phi}(T_k)\mathbf{x}(t_k) \\ \mathbf{v}^T\mathbf{x}(t_k) = 0 \end{cases}. \tag{3.76}$$

Since there is a time delay of τ, except when the state is at the origin and the value of the control signal is zero, the minimum time between switching is τ and the minimum limit cycle period is 2τ. Therefore, deriving $\mathbf{\Phi}_\tau(T_k)$ from equation (3.76) and applying the Theorem 3.3.1 with the condition that $T_k > 2\tau$ the Theorem is demonstrated.□

Necessary and sufficient conditions are derived in the following Corollary for the case of one unstable pole.

Corollary 3.3.5 *In the case that the system has one unstable pole a necessary and sufficient condition for a given initial condition x_o to be stabilized is that $x_o \in \Omega_{\max}$, the trajectory $x(t)$ generating from x_o, reaches the switching hyperplane within the region $\Omega^\tau_{\max}$ and that the conditions of Theorem 3.3.4 are satisfied.*

Proof: If the conditions of Theorem 3.3.4 are satisfied it is sufficient to find the locus of the initial conditions $\mathbf{x}_o$ reaching the hyperplane within the region $\Omega^\tau_{\max}$. From Corollary 3.2.6, this is given by

$$\Omega^\tau = \left\{ \forall \mathbf{x}_o \in \Omega_{\max} : \exists t_r \in R;\ \mathbf{v}^T \mathbf{x}(t_r) = 0;\ \left| \mathbf{v}_p^T \mathbf{x}(t_r) \right| - \frac{2e^{-\gamma_p \tau} - 1}{\gamma_p} \mathbf{v}_p^T \mathbf{b} u_o < 0 \right\} \qquad (3.77)$$

where t_r is the time when the state crosses the hyperplane.□

Remark 3.3.3 *The facts of Remark 3.3.2 are applicable to the above controlled system for $T > 2\tau$.*

Proof: The proof is derived from Theorem 3.3.4.□

In general, calculation of the stability region from the Theorem 3.3.1 or the Theorem 3.3.4 is complex. However in this work the interest is focused on the 2^{nd} order systems for which the stability region can be calculated without difficulty, as shown in the following example.

Example 3.5 *Let us consider a* 2^{nd} *order unstable system as in the Example 3.1. Let the control function be*

$$u = -u_o sgn\left[\mathbf{v}^T \mathbf{x}\left(t-\tau\right)\right] \tag{3.78}$$

with $\gamma_p = 2$, $\gamma_n = 1$, $u_o = 1$ *and* $\mathbf{v}^T = (10\ 1)$. *The values of* $\lambda_{\max}(T)$ *of the matrix* $\Phi_r(T)$ *is shown in Figure 3.9 for the time delays* $\tau_1 = 0$, $\tau_2 = 0.05\,[s]$, $\tau_3 = 0.1\,[s]$. *In the case*

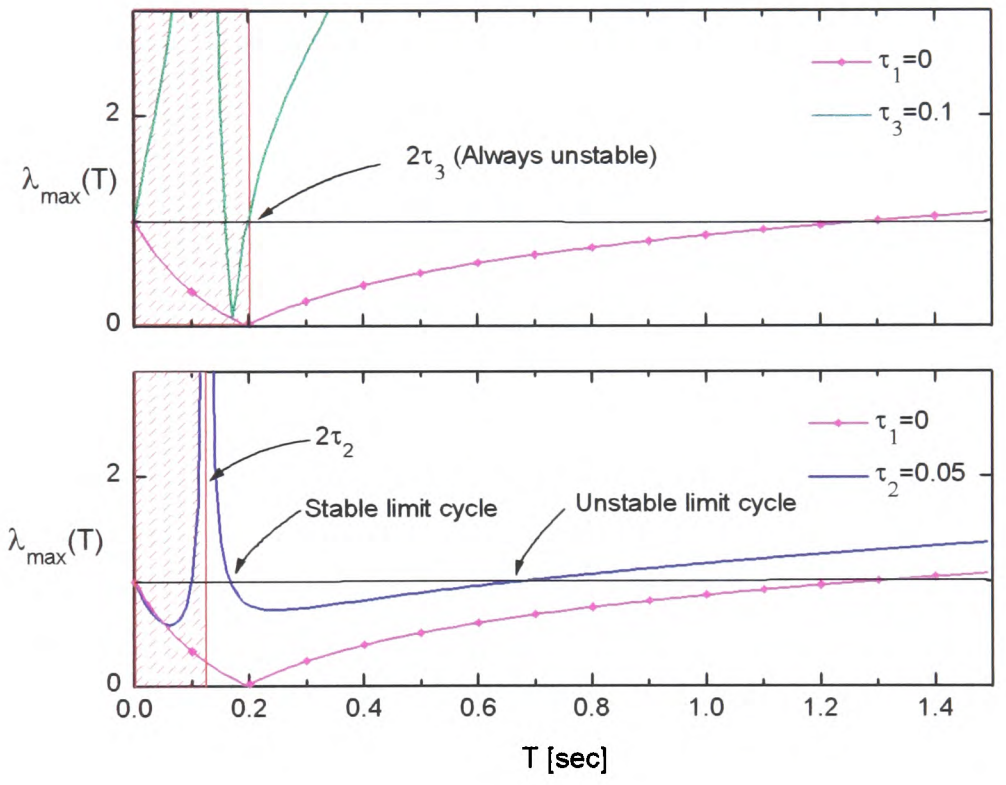


Figure 3.9: $\lambda_{\max}(T)$ *of the matrix* $\Phi_r(T)$ *(*$\tau_1 = 0$, $\tau_2 = 0.05\,[s]$, $\tau_3 = 0.1\,[s]$*).*

of τ_2, *since there are two values of* T *for which the pole exits the unit circle, the stability is determined applying the Remark 3.3.3. The first crossing at* c_1 *indicate that there is a stable limit cycle. The second crossing at* c_2 *satisfies the conditions for an unstable limit cycle and therefore all the initial conditions starting inside the region defined by equations (??) and (3.67) can be stabilized. In the case of* τ_3, *the eigenvalues are outside the unit circle for all the* $T > \tau_3$ *therefore the system is always unstable. In Figure 3.10 and Figure 3.11 the simulations of the case* $\tau_2 = 0.05\,[s]$ *for different initial conditions are displayed. The results show that indeed the two limit cycles predicted by the Remark 3.3.2 exist. The period of the stable limit cycle is* $T_1 = 0.332\ [s]$ *and the period of the unstable limit cycle is* $T_2 = 1.368\,[s]$. *It should be observed that the allowable time delay cannot exceed the limit set in equation (3.40) and, if the controller is not a maximum stabilizer, the closed loop system could become*

unstable for a smaller time delay as for the case of $\tau_3 < \frac{1}{\gamma_p} \ln 2 = 0.346\,[s]$.

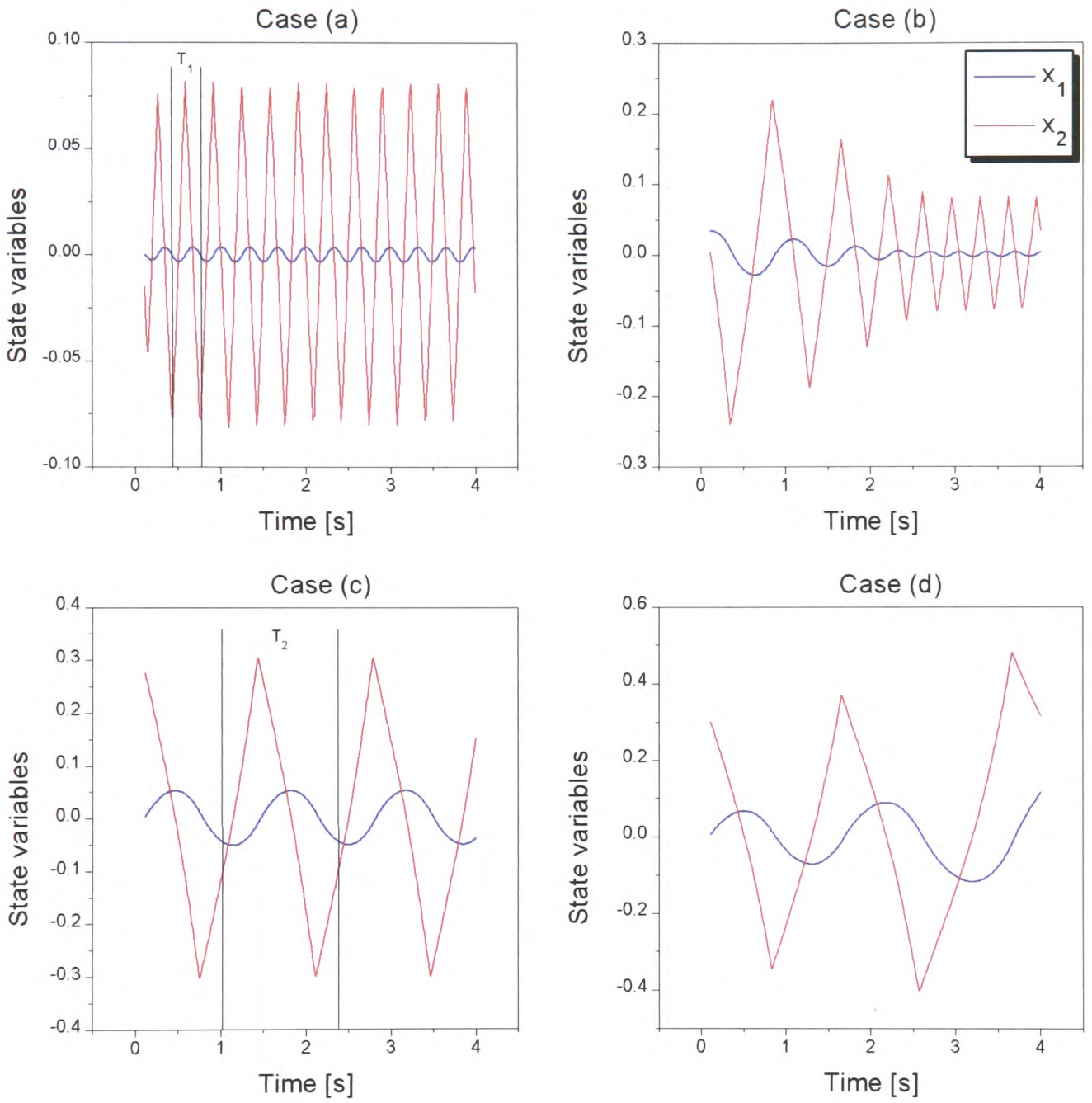


Figure 3.10: (a) Initial conditions inside the stability region and the limit cycle, (b) Initial conditions inside the stability region but outside the limit cycle, (c) Initial conditions on the limit cycle, (d) Initial conditions outside the stability region.

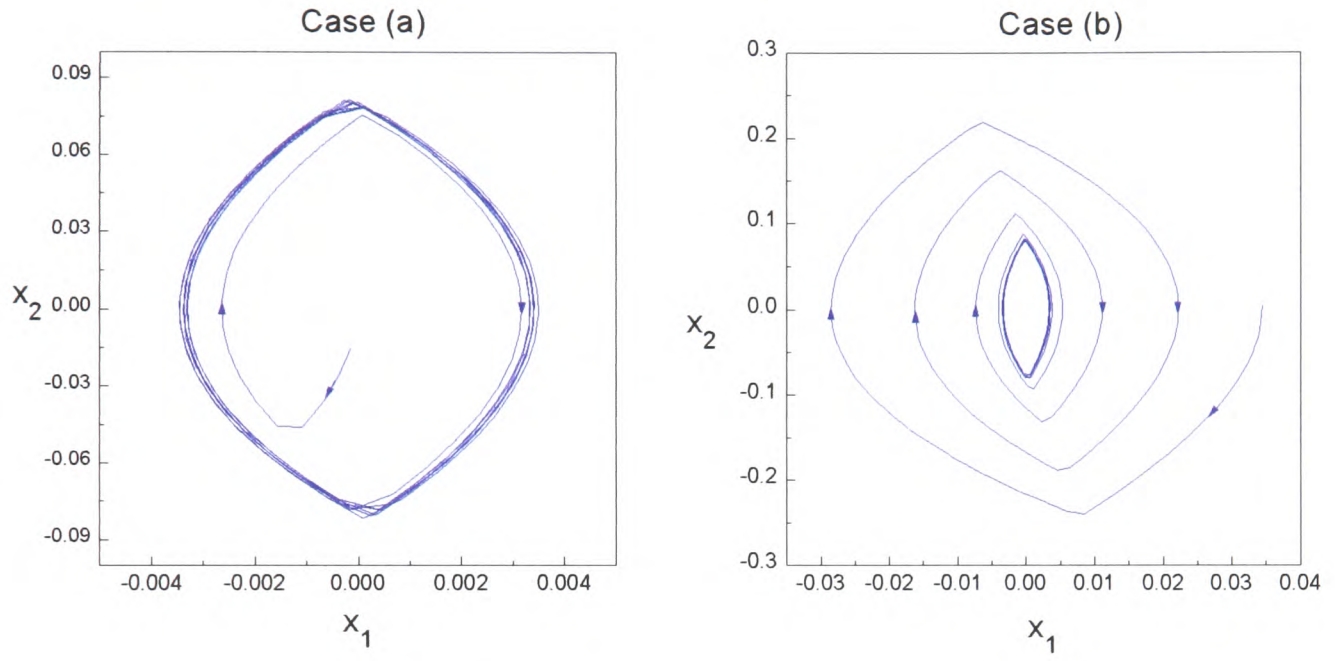


Figure 3.11: (a) Initial conditions inside the stability region and the limit cycle, (b) Initial conditions inside the stability region but outside the limit cycle, (c) Initial conditions on the limit cycle, (d) Initial conditions outside the stability region.

3.3.3 Stability region under linear saturated continuous time and discrete time controllers

The stability region of a single input LTI systems under linear continuous time feedback control with a constrained input can be calculated by applying the same technique as in Theorem 3.3.1. However only the stability region for a 2^{nd} order system with one unstable pole will be analysed in detail using also the results in Theorem 3.2.2. The restriction to a 2^{nd} order system with one unstable pole is justified because the result in this work is needed to compare the performance of linear saturating controllers to non-linear saturating controllers in the problem of the plasma vertical position stabilization (§ Chapter 4).

Let a 2^{nd} order unstable system be described by

$$\begin{cases} \dot{x}_1(t) = x_2(t) \\ \dot{x}_2(t) = \gamma_p \gamma_n x_1(t) + (\gamma_p - \gamma_n) x_2(t) + u(t) \end{cases} \tag{3.79}$$

with $\gamma_p > \gamma_n > 0$ and the allowed control input be constrained $|u(t)| \leq u_o$. The left eigenvector associated with the unstable eigenvalue γ_p is given in equation (3.29). The maximum obtainable stability region $\Omega_{\max}$ was calculated in the example 3.1 and is given in (3.30). Given the system (3.79), let the feedback controller be

$$u = -sat\left(\sigma \mathbf{k}^T \mathbf{x}\right) \tag{3.80}$$

such that the unconstrained closed loop system is stable and $\mathbf{k} \neq \mathbf{v}_p$. The $sat(\cdot)$ function has been defined in equation (3.32). Let the region of non saturation be defined as

$$\Omega_l = \left\{ \mathbf{x} \in R^2 : \sigma \left| \mathbf{k}^T \mathbf{x} \right| < u_o \right\}. \tag{3.81}$$

When the input is always saturated the stability region Ω_s is given by the Corollary 3.3.2 and Remark 3.3.1. If the input is not always saturated then the stability region Ω_{sl} can be calculated by considering the times $t_o, t_1, \ldots, t_{k-1}, t_k$ when $\mathbf{x}(t)$ crosses the hyperplane $\sigma \left| \mathbf{k}^T \mathbf{x}_o \right| - u_o = 0$, and finding the value of $\mathbf{x}_o$ for which the eigenvalues of the matrix $\mathbf{\Phi}_r(T_{k+1})\,\mathbf{\Phi}_c(T_k)$ are inside the unit circle, where $T_{k+1} = t_{k+1} - t_k$, $T_k = t_k - t_{k-1}$, $\mathbf{\Phi}_r(T_{k+1})$ is the transition matrix of the system restricted to the hyperplane $\mathbf{v}^T \mathbf{x} = 0$ and $\mathbf{\Phi}_c(T_k)$ is the transition matrix of the unconstrained closed loop system. Let $\lambda_i(\mathbf{x}_o)$ be the $i-th$

eigenvalue of $\mathbf{\Phi}_r(\mathbf{x}_o)\,\mathbf{\Phi}_c(\mathbf{x}_o)$, where $\lambda_i(\mathbf{x}_o)$ can also be a multiple eigenvalue. Let c_j be the $j-th$ solution of the equation $|\lambda_i(\mathbf{x}_o)| = 1$ such that $c_1 < c_2 < \ldots < c_j < c_{j+1}$. The boundary of Ω_{sl} is calculated solving equation (3.79) using the control function (3.80) with an initial value $\mathbf{x}_o$ such that $|\lambda_i(\mathbf{x}_o)| < 1$. If $|\lambda_i(\mathbf{x}_o)| < 1$ for all the values of $\mathbf{x}_o \in \Omega_{\max} \cap \Omega_l$ then the Ω_{sl} is given by

$$\begin{aligned}\Omega_{sl} = \Big\{ &\forall \mathbf{x}_o \in \Omega_{\max} : \exists t_{r_2} > t_{r_1}; \sigma\left|\mathbf{k}^T\mathbf{x}(t_{r_1})\right| = u_o; \\ &\sigma\left|\mathbf{k}^T\mathbf{x}(t_{r_2})\right| = u_o; \mathbf{x}(t_{r_1}), \mathbf{x}(t_{r_2}) \in \Omega_{\max}\Big\}.\end{aligned} \tag{3.82}$$

This method of calculating the stability region is illustrated in the following Example 3.6.

Example 3.6 *Consider a 2^{nd} order unstable system as (3.79) with control law as (3.80). Let us assume that $\gamma_p = 2$, $\gamma_n = 1$ and the allowed control input $u_o = 10$. Let us consider two cases by choosing the feedback gains and saturation threshold as:*

$$\textit{Case a: } \mathbf{k}_2^T = [10\ \ 1] \textit{ and } \sigma_2 = 2 \rightarrow \Omega_{l_2} = x_1, x_2 \in R : |10x_1 + x_2| < 0.5$$

$$\textit{Case b: } \mathbf{k}_1^T = [1.5\ \ 1] \textit{ and } \sigma_1 = 8 \rightarrow \Omega_{l_1} = \{x_1, x_2 \in R : |1.5x_1 + x_2| < 0.125\}$$

The closed loop eigenvalues of the unsaturated systems are

$$\textit{Case a: } (-0.5000 \pm 4.2131i)$$

$$\textit{Case b: } (-2, -5)$$

The $|\lambda_i(\mathbf{x}_o)|$ are shown in Figure 3.12. The stability region for both cases can be determined by finding the values of $\mathbf{x}_o$ such that $|\lambda_i(\mathbf{x}_o)| < 1$. These are shown in Figure 3.13 and Figure 3.14.

The technique used to calculate the stability region for a continuous controller cannot be used for a discrete controller because it is not possible to give an exact definition of the two systems $\mathbf{\Phi}_r(T_{k+1})$ and $\mathbf{\Phi}_c(T_k)$. Indeed the uncertainty lies in the fact that, sampling at a fixed rate T_s, the region of non saturation Ω_l depends on the initial conditions. However this is beyond the scope of this research and for discrete systems the assumption of a very high sampling frequency compared to the system dynamics will be made. From the result of Theorem 3.3.4, it can be concluded that the stability region of an unstable LTI systems with a constrained input and a saturated linear discrete feedback controller decreases with the sampling frequency. In this respect the sampling frequency should be as high as possible.

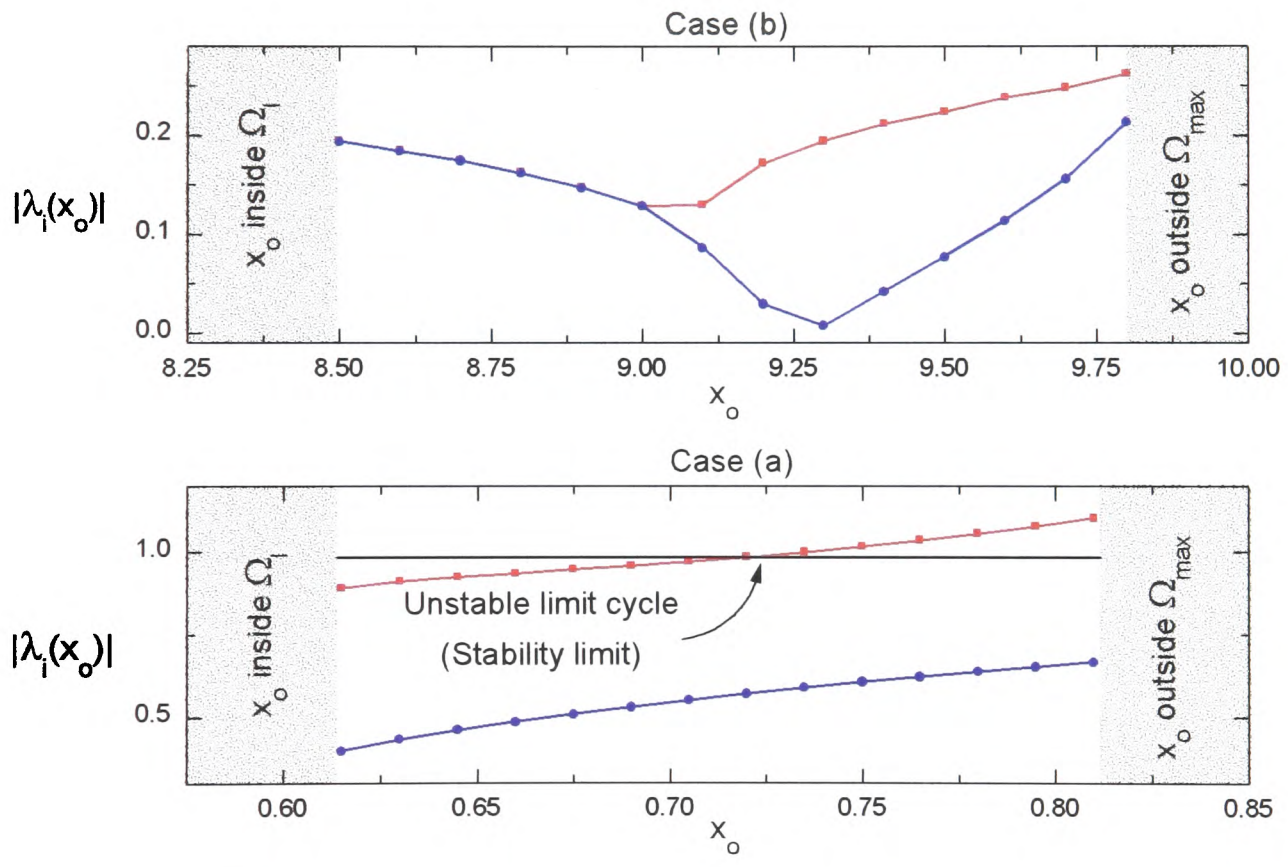


Figure 3.12: The $|\lambda_i(\mathbf{x}_o)|$ or the values of x_o which are of interest: Case (a) and Case (b).

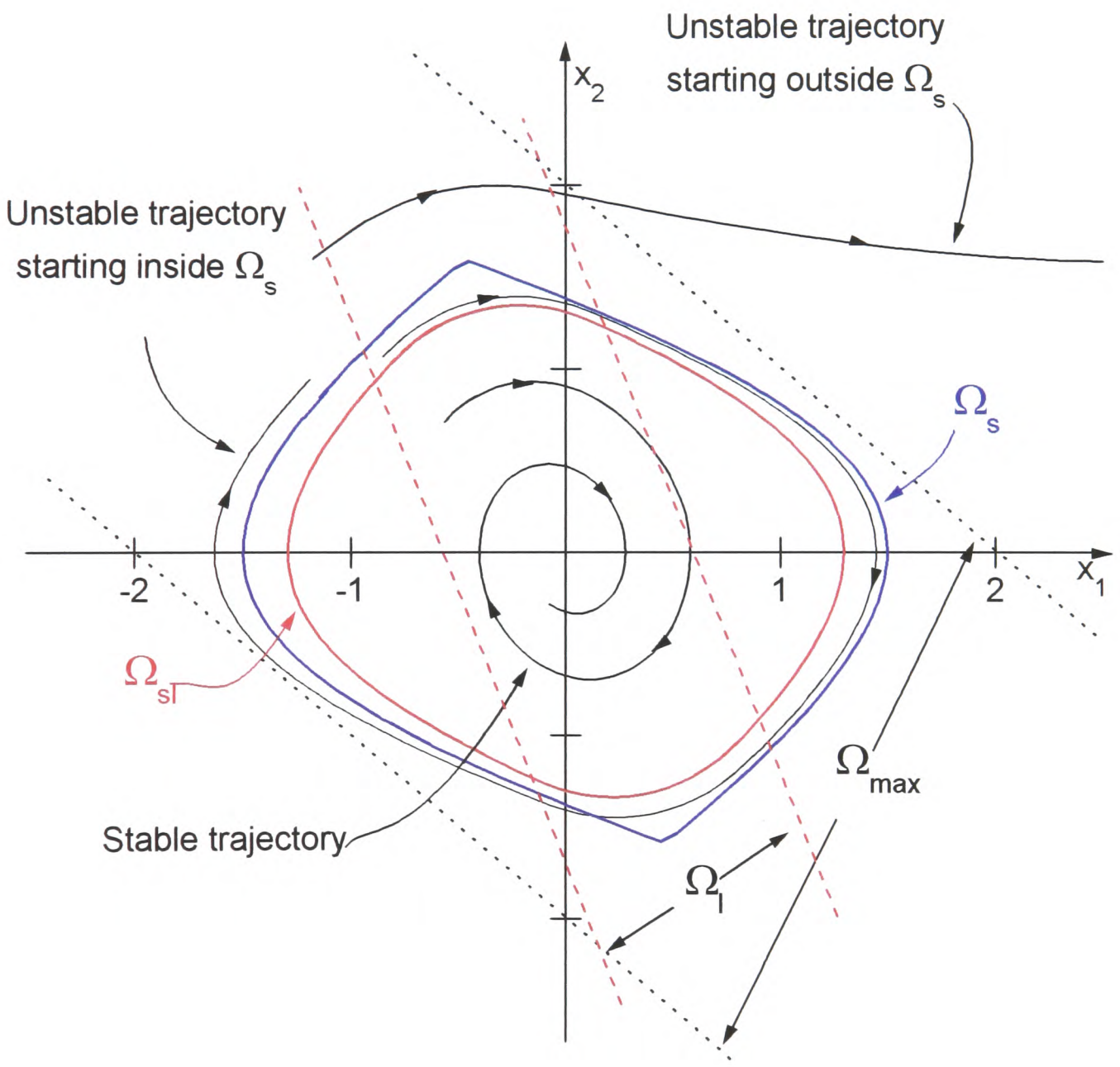


Figure 3.13: Stability regions: Case (a).

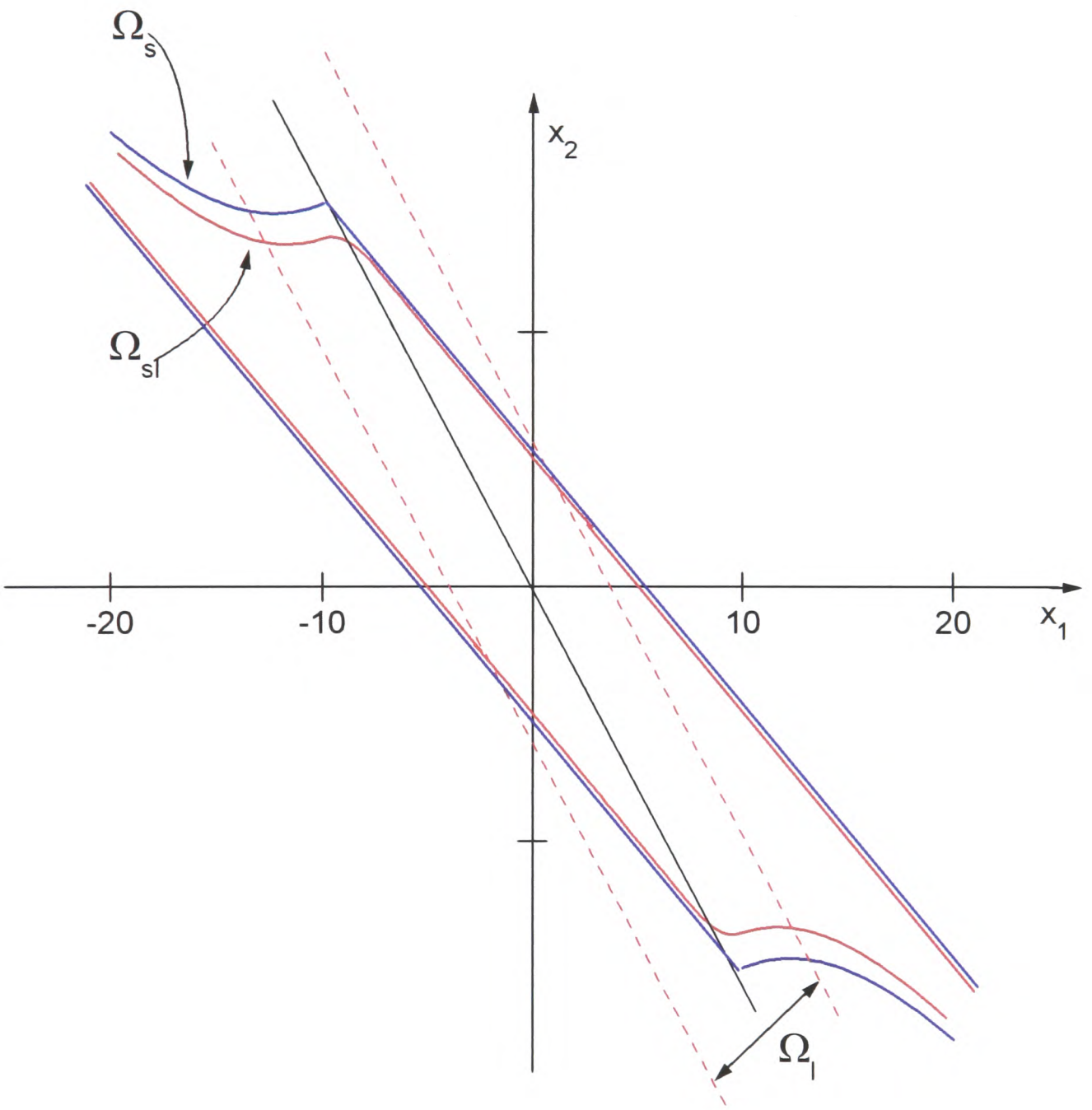


Figure 3.14: Stability regions: Case (b).

3.3.4 Stability regions under continuous time and discrete time variable structure relay control

In Section 3.2 it has been shown that, by choosing the appropriate switching hyperplane, it is possible to obtain the maximum stability region corresponding to given fixed bounded control input.

The condition

$$s(\mathbf{x})\,\dot{s}(\mathbf{x}) < 0$$

guarantees the existence of a sliding motion but not the stability. However if $s(\mathbf{x})$ is a maximum stabilizer then the stability region and the sliding motion region are the same (§ Theorem 3.2.2).

For single input unstable LTI systems with one unstable pole under continuous time variable structure relay control with constrained input, if the switching hyperplane is not the maximum stabilizer, the exact stability region can be calculated using Corollary 3.3.2. Other methods, like the one described in [Madani-Esfahani90], [Choi94a], [Glazos95] and [Hui93], give only an estimation of the stability region. The stability region in the case of a discrete time relay variable structure control can be estimated using corollary 3.3.5 which provides a better approximation than other methods like the one described in [Bartolini95] and [Gutman86].

3.4 Concluding remarks

The key problem for the design of a controller that maximizes the stability region of an unstable system with control bounds is the determination of the maximum obtainable stability region. Theorem 3.2.2 solves this problem for the case of one unstable pole.

In [Zhao95], the question of how to determine a stabilizing controller that would yield the largest domain of attraction for an unstable plant with control bounds was posed: in this work such a controller has been named *maximum stabilizer*. The solution to this problem for one unstable pole is given in Section 3.2.1 where the conditions for a linear or a non-linear controller to be a maximum stabilizer are given.

The stability conditions for the case of a relay control law are presented in Theorem 3.3.1 and Corollary 3.3.2. In particular Remark 3.3.2 shows how to determine the existence, the stability and the exact period of any limit cycles. Similar results are obtained for the case

of a relay control law with a time delay in the Theorem 3.3.4, Corollary 3.3.5 and Remark 3.3.3.

The stability conditions for the case of linear saturated state feedback controller are given in Section 3.3.3. However, the measure of the exact stability region requires the solution of the state trajectory which becomes cumbersome for high order systems.

Chapter 4

Vertical stabilization control system design

A robust control algorithm for the stabilization of the vertical position of the plasma in a Tokamak is of a crucial interest for fusion research. The loss of vertical stability results in a vertical disruption. Vertical disruptions can be particularly dangerous because they generate severe stresses on the vacuum vessel wall and its support structure which, in the past, have damaged the JET Tokamak [Noll90]. For the above reasons the control objective is to obtain a robust controller that maximizes the stability region and recovers any displacements from the equilibrium position caused by a disturbances in a short time and in a reliable way.

4.1 Introduction

A vertical stabilization controller should stabilize the plasma within the vacuum vessel walls in the presence of external disturbances. In case of loss of control, caused by a major disruption, the objective is to ensure stability for as long as possible, ideally until after the plasma current has decayed, to reduce the force eventually generated on the vacuum vessel. The control algorithm should take into account hardware limitations such as analogue to digital conversion, limited computational time and amplifier saturation. It should also make the best use of the non-linear characteristic of amplifiers, in order to optimize the control and at the same time prevent disruptions. The above comments can be summarized in the following control system specifications listed in decreasing order of importance:

1. Stabilize the vertical position

2. Maximize the stability region

3. Reduce the effect of disruptions

4. Reduce the effect of external disturbances

5. Reject measurement noise

6. Be robust to plant parameter variations (γ_p, τ_{tot})

7. Minimize the number of times the amplifiers switch and reduce the energy losses.

In this Chapter a control algorithm which meets all the above objectives is designed.

4.1.1 Aim of the Chapter

The aim of this Chapter is to move forward from the conventional techniques used in the past and develop an algorithm that is potentially applicable to every Tokamak. In addition to the attainments of the stability of the vertical position of the plasma, the control design addresses the robustness to external disturbances and to plasma parameter variations and the optimal control in the presence of saturations or relay-type amplifiers. To meet this objective the proposed controller is designed with an inner and outer control region. In the outer region a relay-type sliding controller reliably and quickly drives the state trajectory towards the inner region regardless of the plasma configuration. The reliability of the controller can be achieved if it is such as to maximize the stability region in all the plasma operating conditions. The recovery time can be minimized by using an adaptive minimum time controller (it is adaptive to be independent of the plasma configuration). In the inner region (small error variations) a linear controller is used. This ensures the local stability of the vertical position and allows the use of a high order controller that can address different objectives in the inner region without reducing the stability limits and performances when the control is saturated. Since in most of the presently operating Tokamaks the controller for the vertical plasma position is linear, this could still be used in the inner region. Elements of Variable Structure System theory, Minimum Time Control and the results in **Chapter 3** are used in the design of the controller which takes into account the presence of the saturation in the actuators to improve the performance while maintaining acceptable stability margins.

In **Section 4.2** a non-linear control algorithm, based on the Variable Structure Control (VSC) theory, Minimum Time Control theory and the stability results, derived in Chapter 3,

is proposed. The control algorithm is provided with an adaptation mechanism that approximates a minimum time controller without prior knowledge of the minimum time trajectories. The VSC is particularly suited to deal with a non-linear and relay-type amplifier like the FRFA (§ Section 2.5). This controller is named: Discrete Adaptive Near-Time Optimum Control (DANTOC) with time-varying hyperplanes for unstable systems. The DANTOC differs from the previous work, mentioned in the next Section 4.1.2, because it is a discrete time controller and the time-varying hyperplanes are designed to maximize the stability region for unstable systems with bounded control (see **Section 4.2.1**). The basic adaptive controller is described in **Section 4.2.2**. The DANTOC uses rotating and shifting hyperplanes to adapt the system trajectory close to the minimum time trajectory. The control algorithm is also designed to be as simple as possible to avoid computational overhead and reduce the commissioning time. In **Section 4.2.3** the robustness of the DANTOC to external disturbances is analysed. The proposed solution is based on the characterization of the external disturbances provided in Section 2.4. In **Section 4.3** the selection of the controller parameters is described which is based on some characteristic parameters (passive structure (γ_n), elongation/growth rate ($\gamma_p^{\max}$), power amplifier limitations ($V_a^{\max}$, $I_a^{\max}$), time delays τ_{tot}) and the external disturbances.

4.1.2 Review of earlier work

Controllers to stabilize an open loop vertically unstable plasma have been designed in the past. The work on this subject can be divided in two categories:

1. Control design based on experiments
2. Control design based on computer models and simulations.

In the works based on experiments the controller structure is usually fixed and the controller parameters are tuned experimentally to yield a plasma which is vertically stable in closed loop. A proportional (P) controller was used in the Cleo-Tokamak [Hugil74] and the TNT-A-Tokamak [Nagayama84]. The control parameters were chosen according to the specific plasma configuration by varying the plasma parameters and the range of stabilizing gains. Proportional + Derivative (PD) control was used in the same fashion on the JFT-2M-Tokamak [Mori87]. [Lazarus90] presented a detailed description of the development of a PD controller based on a reduced order system showing the correlations between some plasma

parameters and the choice of the controller parameters. A PD controller was also used on DIII-D by [Lister90] to obtain a stable closed loop system so that the plasma parameters could be identified. On the JET-Tokamak, [Noll86], using a PD controller, measured the range of stability by changing the controller parameters and identifying the set of parameters that maximized the stability region for a given instability growth rate γ_p. [Garribba88] analysed the application of a Proportional + Integral + Derivative (PID) controller and, more recently, [Scibile92] studied the implementation of a digital PID controller whose parameters were tuned experimentally [Garribba94]. [Scibile92] also developed a Linear Quadratic Gaussian (LQG) controller that addressed the problem of external disturbances and measurement noise observed from the plant. More recently [Vyas96] presented some results on the application of high order linear controllers (namely an H_∞ Controller and a Stable Generalized Predictive Controller) on Compass-D suggesting that alternative control techniques other than PD control are feasible and can lead to improved performance.

In work based on computer models and simulations the designers have tried to include additional control objectives other than maximizing the stability region. [Ambrosino84] presented an optimum PD controller where the controller parameters where chosen to minimize the power requirements while maintaining a fast response time. [Moriyama85] derived a Linear Quadratic (LQ) controller with the same objectives. [Al-Husari91] and [Portone92] designed a H_∞ Controller to stabilize the vertical position of the plasma. They suggested how to select the weighting functions for the control design and presented results based on computer simulations which did not take into account the presence of external disturbances and measurement noise. The application of similar techniques has been used to control the vertical position of the plasma in COMPASS-D [Vyas96] . A self-tuning design procedure was proposed for the JET-Tokamak by [Zheng93]. However his conclusions emphasized the difficulty of studying complex control techniques based on a simplified model without a characterization of the external disturbances and measurement noise from the real plant.

Elements of Variable Structure Control theory and Minimum Time Control theory have never been applied to the control of the plasma vertical position. However they were combined to develop a robust near time-optimal control law but with a fixed controller structure [Newman91] and to design an optimum switching line of a time-invariant plant used in a near time-optimal control of non-linear servo-mechanisms [Danbury94]. The controller designed in this Chapter is an extension of a self-adaptive variable structure controller [Zinober75].

The same self-adaptive principle in [Zinober75] has been applied to the control of a process described by the diffusion equations [Zinober80], using a smoothed variable structure control [Burton88] and, recently, for the stabilization of a power system [Yu94a].

All the above work, which was based on VSC theory, used only one set of linear moving hyperplanes. However, as shown in Chapter 3, it is not possible to achieve the maximum obtainable stability region Ω_{max} with this approach. For example, the application of two sets of moving hyperplanes can be found in [Choi93] and [Choi94b] where rotating and shifting hyperplanes were used to shorten the reaching phase of a variable structure control system.

The digital implementation of controllers based on VSC have an intrinsic limitation to their robustness. This is due to the fact that the intersample behaviour deviates from the sliding manifold and therefore controllers based on discrete-time sliding mode have an inherent limitation in disturbance rejection [Su93]. The problem of robustness in discrete-time sliding mode controllers has been investigated by various authors such as [Furuta90], [Spurgeon92], [Pieper93] and [Chan94]. The main conclusion is that, in discrete time sliding mode controllers, the invariance property, see [Drazenovic69], does not hold and therefore alternative approaches are required to solve the problem of robustness.

4.2 Discrete Adaptive Near-Time Optimum Control with time-varying hyperplanes for unstable systems

The plant to be controlled is defined by the equations (2.61) with the control limitations $|u| \leq u_o$. Using a zero-order hold (ZOH) with a sampling period h the system is discretized as

$$\mathbf{x}(k+1) = \mathbf{\Phi x}(k) + \mathbf{\Gamma} u(k-p) \tag{4.1}$$

where $\mathbf{x}^T = (x_1, x_2) = (z_p, \dot{z}_p)$, p is rounded to the largest integer of the fraction $\left(\frac{\tau_{tot}}{h}\right)$.

The state space is divided into two separate regions called the Inner control region Ω_{in}, which includes the origin, and the Outer control region Ω_{out}. This controller structure is also called *dual-mode control* (see Chapter 10 in [Gibson63]).

When the states belong to Ω_{out} a self-adapting variable structure controller is used to maximize the stability region, to achieve near-time optimum control and the external disturbance rejection.

When the state belongs to Ω_{in} a stabilizing linear feedback controller is used for the following reasons:

- A high order controller can be used to address different objectives in the inner region without reducing the stability limits and performances when the control is saturated.
- The chattering produced by the $sgn(\cdot)$ function, used in the outer region, can be reduced and the closed loop response can be smoother.
- A region Ω_{in} is introduced to use previous linear controllers. This can reduce the commissioning time and increase the stability limits and performances when the control is saturated. In this way the control in the outer region could be added to a present controller when the input saturates without disrupting the present setup.
- Since new control designs, as for ITER [ITER95], are still based on linear controllers these could still be used in the inner control region.

The inner and outer control regions are selected as follows:

- The *inner control region* Ω_{in} represents the domain within which the feedback control is not saturated and such that all the trajectories starting inside Ω_{in} do not saturate the control input. Given a linear feedback controller

$$u(k) = \mathbf{K}^T \mathbf{x}(k) \tag{4.2}$$

where $\mathbf{K} \in R^n$ is a stabilizing state feedback gain matrix, Ω_{in} is defined[1] as

$$\Omega_{in} = \left\{ \mathbf{x} \in R^n; \left\| \mathbf{T}^{-1}\mathbf{x} \right\| \leq \frac{u_o}{g(\mathbf{K}, \mathbf{T})} \right\} \tag{4.3}$$

where $\mathbf{T}$ is a diagonal definite positive scaling matrix that, $\forall \mathbf{x} \in R^n$, satisfies the condition

$$g(\mathbf{K}, \mathbf{T}) \left\| \mathbf{T}^{-1}\mathbf{x} \right\| \leq \left| \mathbf{K}^T \mathbf{x} \right|, \tag{4.4}$$

$g(\mathbf{K}, \mathbf{T}) \geq 1$ is obtained from

$$g(\mathbf{K}, \mathbf{T}) = \rho \left\| \mathbf{K}^T \right\| \|\mathbf{T}\| \tag{4.5}$$

and ρ is given by

$$\rho = \max_{k>0} \left\| \left(\mathbf{\Phi} + \mathbf{\Gamma}\mathbf{K}^T \right)^k \right\| = \max_{k>0} \bar{\sigma} \left[\left(\mathbf{\Phi} + \mathbf{\Gamma}\mathbf{K}^T \right)^k \right] = \left\| \mathbf{\Phi} + \mathbf{\Gamma}\mathbf{K}^T \right\|_\infty . \tag{4.6}$$

---

[1]The operator $\|\cdot\|$ is the Euclidean vector norm (see Chapter 3 in [Maciejowski89]). For a real vector $\mathbf{x}$ this is given by

$$\|\mathbf{x}\| = \sqrt{\mathbf{x}^T\mathbf{x}}.$$

For a real matrix $\mathbf{G}$ the induced matrix norm is the Hilbert or spectral norm given by

$$\|\mathbf{G}\| = \bar{\sigma}$$

where $\bar{\sigma}$ is the square root of the maximum eigenvalue of $\mathbf{G}^T\mathbf{G}$. This is also called the maximum singular value of $\mathbf{G}$. If $\mathbf{G}$ is a function of a variable k then the $\bar{\sigma}$ is also a function of k. The $\infty - norm$ of $\mathbf{G}(k)$ is defined as

$$\|\mathbf{G}\|_\infty = \max_k \{\bar{\sigma}(\mathbf{G}(k))\}.$$

- The *outer control region* Ω_{out} is the remaining state space:

$$\Omega_{out} = R^n - \Omega_{in}. \tag{4.7}$$

To prove that all the trajectories starting inside Ω_{in} do not saturate the control input consider a set of initial conditions $\mathbf{x}(k_o)$ satisfying the condition (4.3). This must not saturate the control input. By denoting the domain within which the feedback control is not saturated as

$$\Omega_K = \left\{ \mathbf{x} \in R^n; \left| \mathbf{K}^T \mathbf{x} \right| < u_o \right\}, \tag{4.8}$$

to guarantee that $\mathbf{x}(k_o)$ belongs to Ω_K, $\mathbf{T}$ must be selected such that the ellipsoid defined by $g(\mathbf{K},\mathbf{T}) \left\| \mathbf{T}^{-1}\mathbf{x} \right\|$ is inside Ω_K which is equivalent to say that the ellipsoid must be tangent to the hyperplanes $\left| \mathbf{K}^T \mathbf{x} \right| = u_o$ and, therefore, that condition (4.4) is satisfied. Let determine the state trajectory starting from $\mathbf{x}(k_o)$. Assuming that the control has not saturated then at the $k-th$ sample the state will be

$$\mathbf{x}(k+1) = \left(\mathbf{\Phi} + \mathbf{\Gamma}\mathbf{K}^T \right)^k \mathbf{x}_o \tag{4.9}$$

and therefore, from equation (4.2) and equation (4.9), the control input at time $k+1$ will be

$$u(k+1) = \mathbf{K}^T \left(\mathbf{\Phi} + \mathbf{\Gamma}\mathbf{K}^T \right)^k \mathbf{x}_o = \mathbf{K}^T \left(\mathbf{\Phi} + \mathbf{\Gamma}\mathbf{K}^T \right)^k \mathbf{T}\mathbf{T}^{-1}\mathbf{x}(k_o). \tag{4.10}$$

Using the definition (4.5), equation (4.10), the condition (4.3) and the Cauchy-Schwartz inequality the following relationship can be derived

$$\begin{aligned}
\left\| u(k+1) \right\| &\leq \left\| \mathbf{K}^T \left(\mathbf{\Phi} + \mathbf{\Gamma}\mathbf{K}^T \right)^k \mathbf{T} \right\| \left\| \mathbf{T}^{-1}\mathbf{x}_o \right\| \\
&\leq \left\| \mathbf{K}^T \right\| \left\| \left(\mathbf{\Phi} + \mathbf{\Gamma}\mathbf{K}^T \right)^k \right\| \left\| \mathbf{T} \right\| \left\| \mathbf{T}^{-1}\mathbf{x}(k_o) \right\| \\
&\leq \max_k \left\{ \left\| \mathbf{K}^T \right\| \left\| \left(\mathbf{\Phi} + \mathbf{\Gamma}\mathbf{K}^T \right)^k \right\| \left\| \mathbf{T} \right\| \right\} \left\| \mathbf{T}^{-1}\mathbf{x}_o \right\| = g(\mathbf{K},\mathbf{T}) \left\| \mathbf{T}^{-1}\mathbf{x}_o \right\|,
\end{aligned}$$

and, in the limit that $\mathbf{x}(k_o)$ is on the boundary of Ω_{in} then $\left\| \mathbf{T}^{-1}\mathbf{x}(k_o) \right\| = \dfrac{u_o}{g(\mathbf{K},\mathbf{T})}$ and

$$\left\| u(k+1) \right\| \leq \frac{u_o}{g(\mathbf{K},\mathbf{T})} \cdot g(\mathbf{K},\mathbf{T}) = u_o.$$

This proves that all the trajectories starting inside Ω_{in} do not saturate the control input.

A similar definition was given for continuous-time linear feedback control [Zhao95]. However in this work the result is not restricted to the case of distinct eigenvalues. Furthermore the introduction of the scaling matrix $\mathbf{T}$ gives an additional degree of freedom when selecting the Ω_{in}.

4.2.1 The DANTOC control law

The combined control law is expressed as:

$$u(k) = \begin{cases} -u_o sgn[s(\mathbf{x})] & \mathbf{x} \in \Omega_{out} \\ \mathbf{K}^T \mathbf{x} & \mathbf{x} \in \Omega_{in} \end{cases} . \tag{4.11}$$

where u_o is the maximum allowable control effort (e.g. maximum FRFA voltage), $\mathbf{K}^T$ is a stabilizing state feedback controller, and $-u_o sgn[s(\mathbf{x})]$ is a stabilizing relay-type sliding controller composed of two switching hyperplanes

$$s[\mathbf{x}(k)] = \begin{bmatrix} s_r[\mathbf{x}(k)] \\ s_s[\mathbf{x}(k)] \end{bmatrix} = \begin{cases} q_r(k) x_1(k) + x_2(k) \\ \gamma_n x_1(k) + x_2(k) + q_s(k) sgn[x_2(k)] \end{cases} \tag{4.12}$$

where the choice of γ_n is derived from Corollary 3.2.6.

By varying $q_r(k)$ and $q_s(k)$, $s_r[\mathbf{x}(k)]$ and $s_s[\mathbf{x}(k)]$ represent respectively a rotating and a shifting hyperplane as shown in Figure 4.1. The parameters q_r and q_s are varied according to the procedure described in Section 4.2.2, Section 4.2.3.1 and Section 4.2.3.2.

The analysis of the stability of the proposed algorithm can be divided into the analysis of the stability of the Inner control region Ω_{in} and the analysis of the stability of the Outer control region Ω_{out}.

When $\mathbf{x}(k)$ is in Ω_{in}, if $\mathbf{K}^T$ is a stabilizing state feedback gain matrix, then $\mathbf{x}(k)$ will remain in the Ω_{in}, according to the definition of Ω_{in}, and the system will be asymptotically stable.

When $\mathbf{x}(k)$ is in Ω_{out}, if $u(k) = -u_o sgn[s(\mathbf{x})]$ is a stabilizing bang-bang feedback controller and the switching hyperplanes $s(\mathbf{x})$ lie entirely in the region $\Omega^{\tau}_{\max}$, then, according to Corollary 3.2.6 every $\mathbf{x}(k)$ starting inside the region $\Omega_{\max}$ can be stabilized. Therefore, by making sure that q_r, q_s and q_n are chosen such that $u(k) = -u_o sgn[s(\mathbf{x})]$ is a stabilizing controller and that $s(\mathbf{x})$ lies entirely in the region $\Omega^{\tau}_{\max}$, the state trajectory will eventually

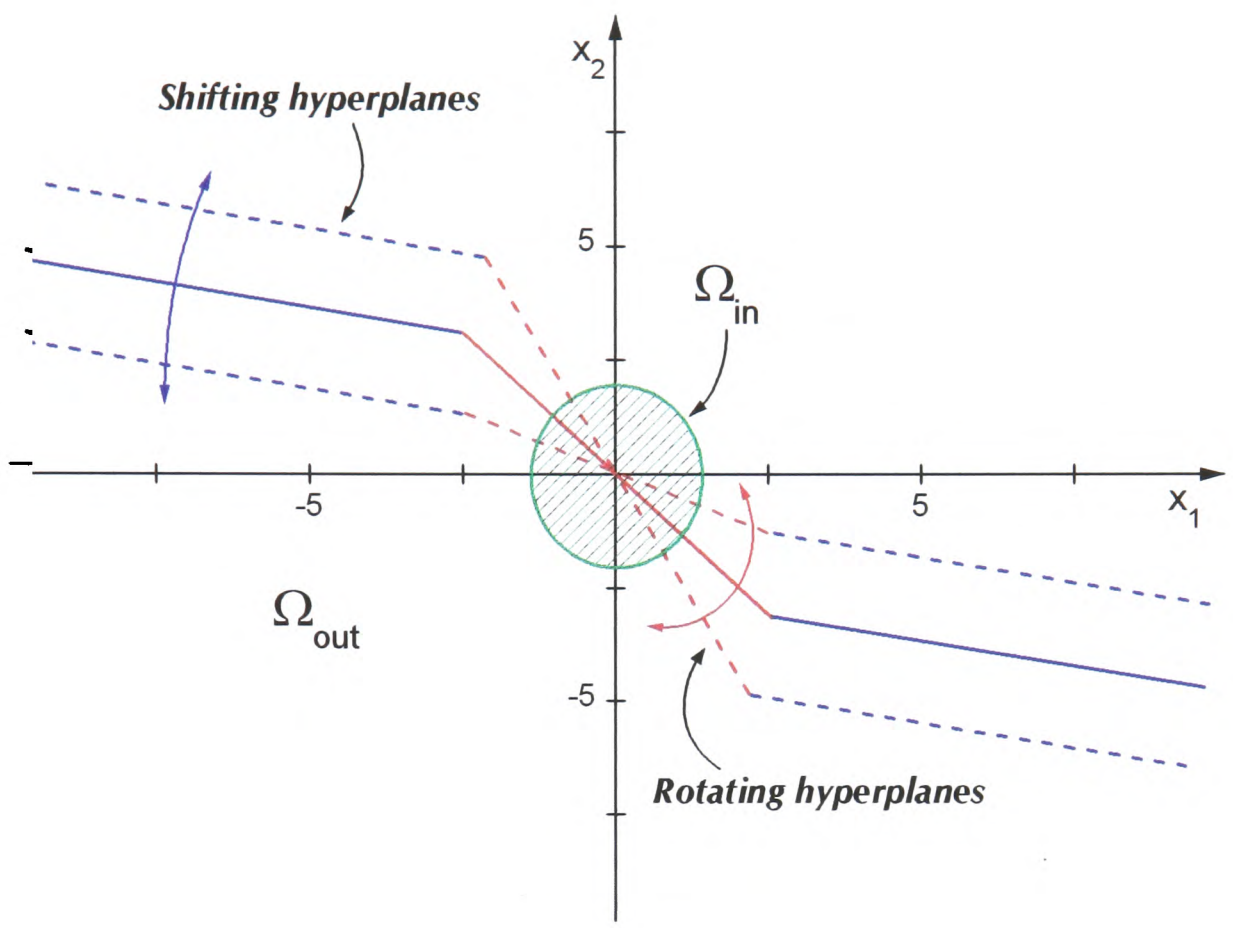


Figure 4.1: Control characteristic in the phase plane.

enter Ω_{in} and the system will be asymptotically stable.

From Corollary 3.2.6, the optimal choice of q_r and q_s, which is independent of the time varying parameters, is $q_r = \gamma_n$ and $q_s = 0$. Indeed the nonlinear characteristic $s(\mathbf{x})$ lies entirely in the region $\Omega^{\tau}_{\max}$. However, since $\gamma_n << \gamma_p$, the dynamics of recovery from an initial condition outside Ω_{in} would be governed by γ_n and therefore it would take a long time. To increase the performances and speed up recovery from an initial condition outside Ω_{in}, q_r and q_s can be chosen to approximate the minimum time switching curve (see Section B.2 of Appendix B) as shown in Figure 4.2.

The need to recover from initial conditions in minimum time is also required for the robustness to external disturbances as explained in the following paragraph. In order to allow the largest stability margin the state should be kept as far as possible from the stability region boundary, which is bounded due to the control limitations, so that a displacement caused by an ELM is contained inside the stability region. Let us assume that the plant parameters are known and the state variables are in Ω_{in}. If an ELM is such as to move the state variables outside Ω_{in}, it will take a minimum time τ_{opt} for the states to re-enter Ω_{in}. The time τ_{opt} depends on the initial conditions and the plant parameters. Assuming the use

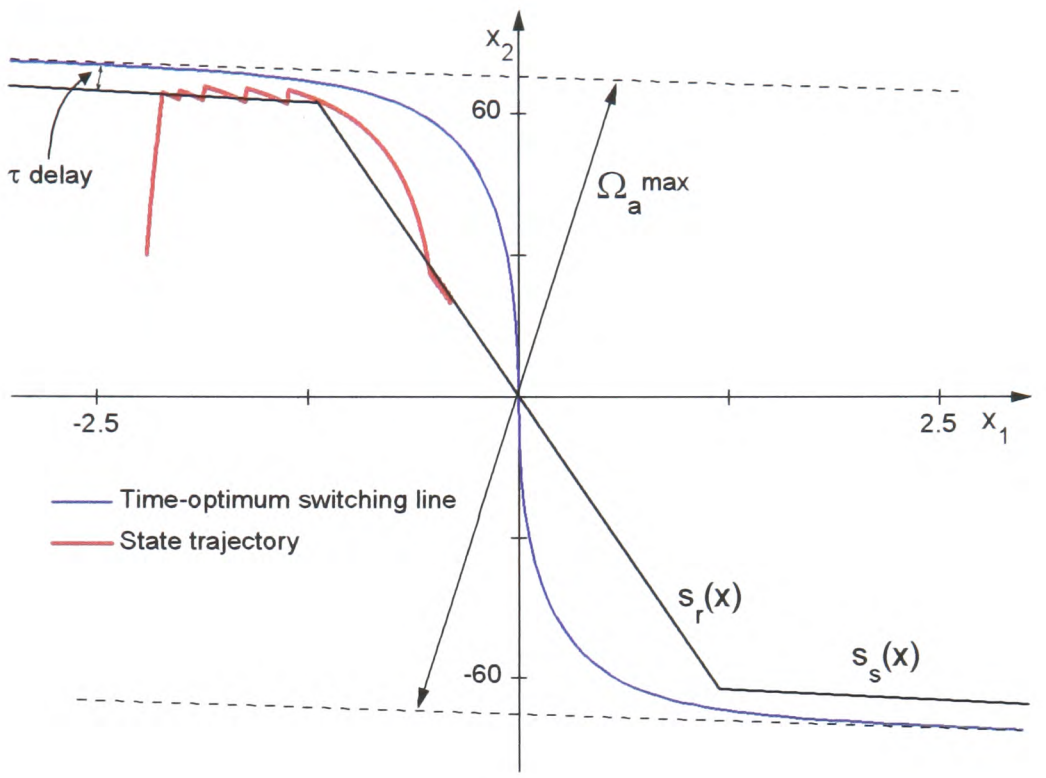


Figure 4.2: Example using a fixed $s[x(k)]$.

of a sub-optimal controller, like the DANTOC, the state will re-enter Ω_{in} in a longer time, say $\tau_r = \alpha\tau_{opt}$ with $\alpha > 1$. Since the ELMs are supposed to have a repetition rate τ_{rep}, by making sure that $\tau_r < \tau_{rep}$, all the ELMs will start from inside Ω_{in} allowing a larger margin for recovery. Let $\mathbf{x}_{ELM}$ be the values of the state variables after an ELM. These depend on the amplitude of an ELM, $\bar{d}_{ELM}$, its duration $\bar{\tau}_{ELM}$ and the closed loop dynamics. The recovery from $\mathbf{x}_{ELM}$ depends on the same parameters. Let us assume that the recovery takes a time τ_r^{ELM}. It is interesting to observe that the allowable repetition rate increases for an ELM of smaller amplitude. Therefore the smaller the recovery time τ_r^{ELM} the higher amplitude or the higher the repetition rate that can be withstood. However, since $\tau_r^{ELM} > \tau_{opt}^{ELM}$, the best that can be done is to approximate the minimum time control.

In the case of time varying parameters the minimum time switching curves will change significantly between the expected variation of $\gamma_p(k)$. The minimum time switching curves are shown in Figure 4.3 assuming that $\gamma_p(k)$ varies between $150\,[s^{-1}]$ to $650\,[s^{-1}]$. Ideally, the value of γ_p would be estimated and used to calculate the optimum switching curve. However there are two major problems associated with this approach. The first problem is that the on-line identification of γ_p has been shown to be very difficult [Munchmeyer95] and the second is that a failure of the identification process could lead to an unstable system. To

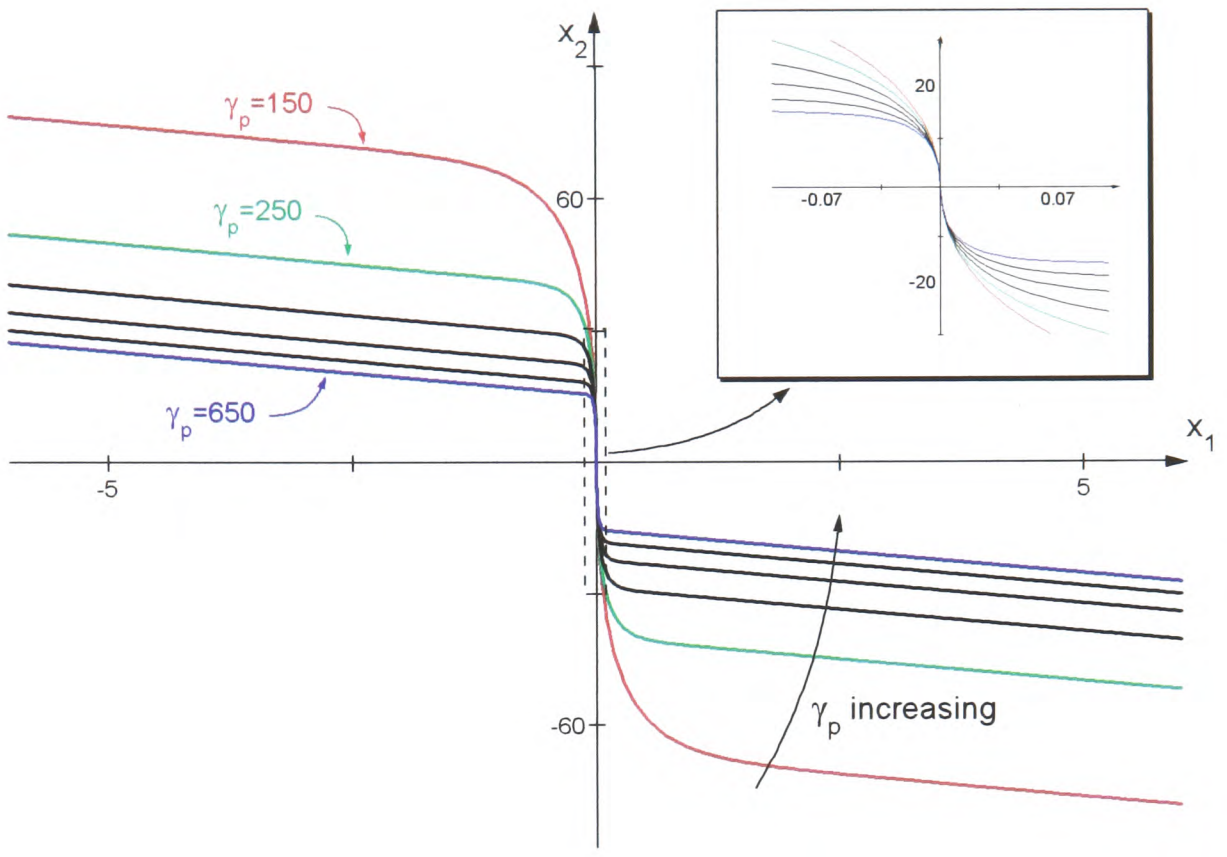


Figure 4.3: Mimimum time switching curves for different values of γ_p.

obtain a response close to minimum time the parameters $q_r(k)$ and $q_s(k)$ need to be adapted to the specific $\gamma_p(k)$.

The adaptive part of the control algorithm will be described in two steps:

1. The basic adaptive controller (§ Section 4.2.2).

2. Modifications to the basic adaptive controller to improve the robustness to external disturbances (§ Section 4.2.3).

In the first step the controlled system is considered not affected by external disturbances. In the second step the robustness of the DANTOC to external disturbances is considered. A schematic diagram of the proposed outer control scheme is shown in Figure 4.4.

4.2.2 The basic adaptive controller

The outer controller is a relay-type sliding controller defined by the first equation in (4.11) where the sliding hyperplane $s(\mathbf{x})$ is composed of two switching hyperplanes defined by the equations (4.12). The hyperplane to be used is chosen with the following rule: if $\mathbf{x}(k)$ reaches

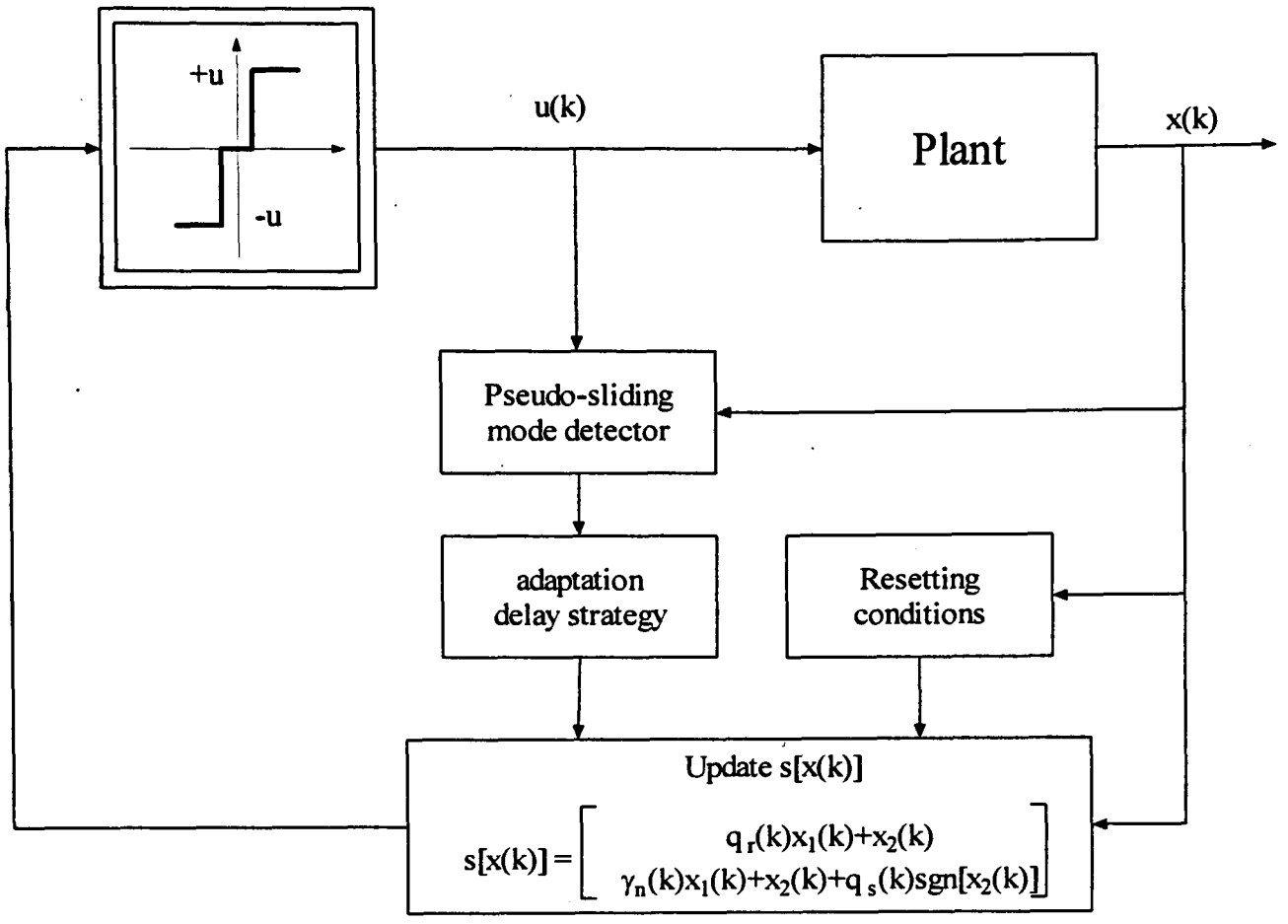


Figure 4.4: Outer region control scheme.

any of the two hyperplanes, this becomes the active hyperplane until $\mathbf{x}(k)$ has returned to it. The hyperplanes are adapted according to the following rules:

1. At time $k = k_o$ the parameters are set to be the maximum stabilizer controller therefore, according to Corollary 3.2.6, $q_r(k_o) = \gamma_n$ and $q_s(k_o) = 0$. With this choice, initially, $s_r[\mathbf{x}(k_o)] = s_s[\mathbf{x}(k_o)]$.

2. When the first pseudo-sliding[2] occurs both $s_r(\mathbf{x})$ and $s_s(\mathbf{x})$ are updated as described below.

3. If pseudo-sliding motion occurs on a shifting hyperplane $s_s(\mathbf{x})$ at the sampling time $k_s > 1$, then $s_s(\mathbf{x})$ is shifted to be ahead of the state point

$$q_s(k + k_s) = q_s(k) + \epsilon_s \quad (\epsilon_s > 0) \tag{4.13}$$

[2](see Section B.1 of Appendix B)

where the amount of increase ϵ_s has to be such that $s[\mathbf{x}(k)]$ is still inside the region $\Omega^{\tau}_{\max}$.

4. If pseudo-sliding motion occurs on a rotating hyperplane $s_r(\mathbf{x})$ at the sampling time $k_r > 1$, then $s_r(\mathbf{x})$ is rotated to be ahead of the state point

$$q_r(k + k_r) = q_r(k) + \epsilon_r \quad (\epsilon_r > 0) \tag{4.14}$$

where the amount of increase ϵ_r has to be such that the state trajectory moves along a locus in the state space associated with a pseudo-sliding motion regime, called the *pseudo-sliding boundary locus*, that is calculated below.

An example of the application of the basic adaptive controller is shown in Figure 4.5. The state trajectory first crosses $s_s(\mathbf{x})$. Since the pseudo-sliding condition is satisfied,

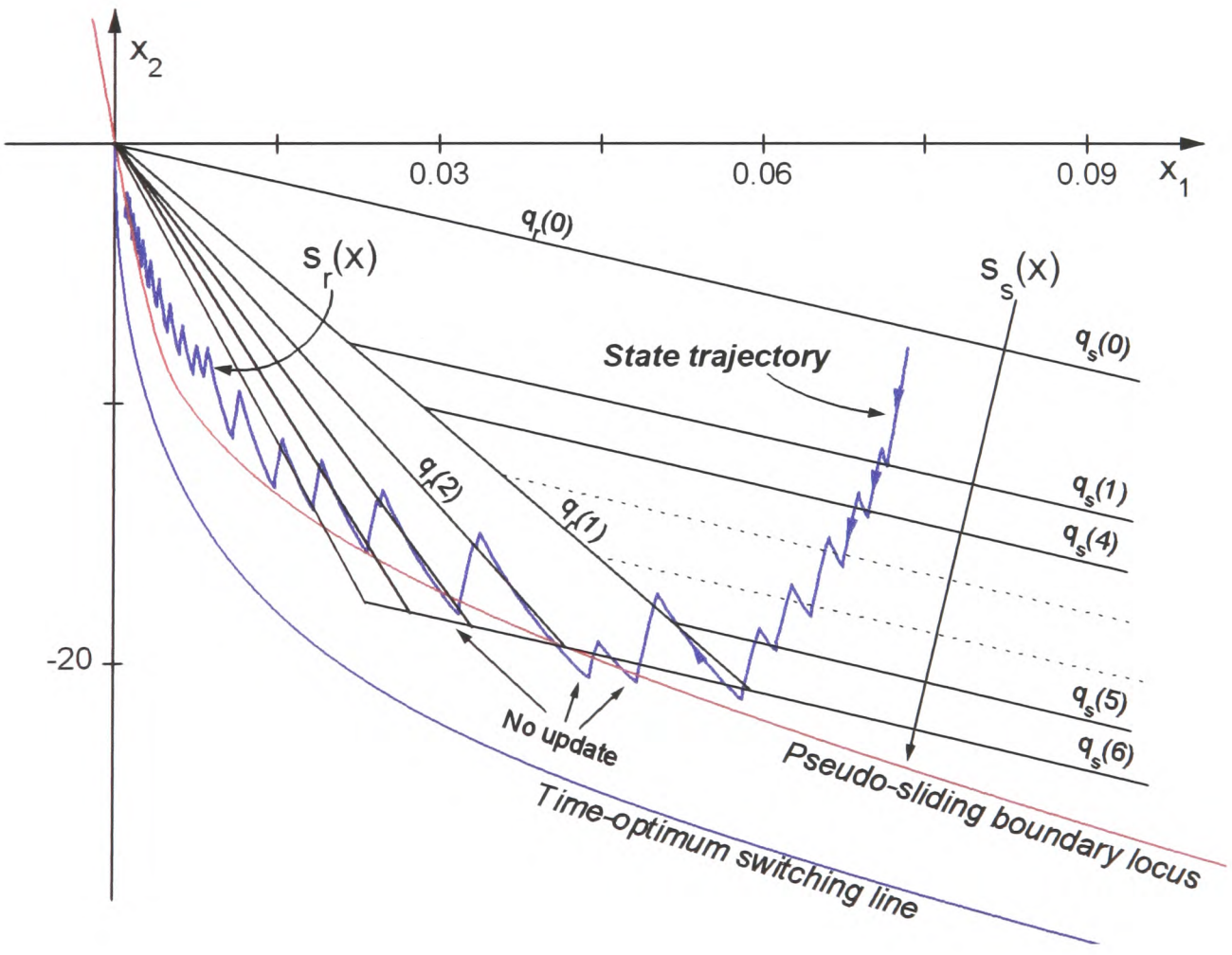


Figure 4.5: An example of the basic adaptive controller.

$s_s(\mathbf{x})$ is updated to be ahead of the state trajectory. This process is repeated until the state trajectory crosses $s_r(\mathbf{x})$ and the pseudo-sliding motion continues on $s_r(\mathbf{x})$. $s_r(\mathbf{x})$ is

subsequently updated when the pseudo-sliding condition is satisfied (note that when the state trajectory exceeds the pseudo-sliding boundary locus there is no adaptation). This strategy of moving the hyperplanes automatically defines the boundary between the rotating and the shifting hyperplanes. It can be seen that the adaptive controller makes the state moves along the pseudo-sliding boundary locus, without any prior knowledge of this locus. Similarly to the result in [Zinober75], this locus is close to the time-optimum switching line and therefore, if $q_r(k)$ and $q_s(k)$ are adapted so that $s[\mathbf{x}(k)]$ approximate this locus, a system response, that is close to minimum time, will result. This control strategy, partially based on [Zinober75], uses an indirect method of adaptation. In fact, it does not require a model identification or a model learning phase but identifies the pseudo-sliding boundary locus.

There exist various possible pseudo-sliding[3] mode definitions. According to the definition of [Yu94b], a pseudo sliding mode occurs if

$$s[\mathbf{x}(k)]\,\nabla s[\mathbf{x}(k)] \leq 0 \tag{4.15}$$

where $\nabla s[\mathbf{x}(k)] = s[\mathbf{x}(k+1)] - s[\mathbf{x}(k)]$. The condition (4.15) is applied to the hyperplane $s_r[\mathbf{x}(k)]$. For $s_r[\mathbf{x}(k)] > 0$ it is required that $\nabla s_r[\mathbf{x}(k)] \leq 0$

$$\begin{bmatrix} q_r(k) & 1 \end{bmatrix} \Phi \begin{bmatrix} x_1(k) \\ x_2(k) \end{bmatrix} + \begin{bmatrix} q_r(k) & 1 \end{bmatrix} \Gamma u_o - \begin{bmatrix} q_r(k) & 1 \end{bmatrix} \begin{bmatrix} x_1(k) \\ x_2(k) \end{bmatrix} \leq 0 \tag{4.16}$$

and for $s_r[\mathbf{x}(k)] < 0$ that $\nabla s_r[\mathbf{x}(k)] \geq 0$

$$\begin{bmatrix} q_r(k) & 1 \end{bmatrix} \Phi \begin{bmatrix} x_1(k) \\ x_2(k) \end{bmatrix} - \begin{bmatrix} q_r(k) & 1 \end{bmatrix} \Gamma u_o - \begin{bmatrix} q_r(k) & 1 \end{bmatrix} \begin{bmatrix} x_1(k) \\ x_2(k) \end{bmatrix} \geq 0, \tag{4.17}$$

which are obtained by substituting the first equation in (4.11) and the undelayed version of equation (4.1) into equations (4.15).

From equations (4.16) and (4.17) the pseudo-sliding region for $s_r[\mathbf{x}(k)]$ consists of the points on the switching line satisfying

$$\left| \begin{bmatrix} q_r(k) & 1 \end{bmatrix} \Phi \begin{bmatrix} x_1(k) \\ x_2(k) \end{bmatrix} - \begin{bmatrix} q_r(k) & 1 \end{bmatrix} \begin{bmatrix} x_1(k) \\ x_2(k) \end{bmatrix} \right| \leq - \begin{bmatrix} q_r(k) & 1 \end{bmatrix} \Gamma u_o. \tag{4.18}$$

[3](see Section B.1 of Appendix B)

Therefore, as long as equation (4.18) is satisfied, the state remains in the pseudo-sliding region. To calculate the boundary of the pseudo-sliding region let us suppose that the state belongs to the switching hyperplane

$$s_r\left[\mathbf{x}\left(k\right)\right] = q_r\left(k\right)x_1\left(k\right) + x_2\left(k\right) = 0 \tag{4.19}$$

and equation (4.18) is evaluated on the limit

$$\left|\left[\begin{array}{cc} q_r\left(k\right) & 1 \end{array}\right]\Phi\left[\begin{array}{c} x_1\left(k\right) \\ x_2\left(k\right) \end{array}\right] - \left[\begin{array}{cc} q_r\left(k\right) & 1 \end{array}\right]\left[\begin{array}{c} x_1\left(k\right) \\ x_2\left(k\right) \end{array}\right]\right| = -\left[\begin{array}{cc} q_r\left(k\right) & 1 \end{array}\right]\Gamma u_o. \tag{4.20}$$

The points satisfying equation (4.19) and equation (4.20) are defined as pseudo-sliding boundary points (see Figure 4.7). If $q_r\left(k\right)$ varies, assuming that $\epsilon_r \rightarrow 0$ and $\epsilon_s \rightarrow 0$, the pseudo-sliding boundary points describe a locus which is defined as a *pseudo-sliding boundary locus* Σ. For continuous systems this locus was named the sliding boundary locus by [Zinober75]. Let us name Σ_r and Σ_s the pseudo-sliding boundary loci associated respectively with $s_r\left[\mathbf{x}\left(k\right)\right]$ and $s_s\left[\mathbf{x}\left(k\right)\right]$. An expression for Σ_r can be derived using equation (4.19) and equation (4.20)

$$\left|\left[\begin{array}{cc} -\dfrac{x_2\left(k\right)}{x_1\left(k\right)} & 1 \end{array}\right]\Phi\left[\begin{array}{c} x_1\left(k\right) \\ x_2\left(k\right) \end{array}\right] - \left[\begin{array}{cc} -\dfrac{x_2\left(k\right)}{x_1\left(k\right)} & 1 \end{array}\right]\left[\begin{array}{c} x_1\left(k\right) \\ x_2\left(k\right) \end{array}\right]\right| = -\left[\begin{array}{cc} -\dfrac{x_2\left(k\right)}{x_1\left(k\right)} & 1 \end{array}\right]\Gamma u_o. \tag{4.21}$$

The same procedure is followed to determine the pseudo-sliding boundary locus associated with $s_s\left[\mathbf{x}\left(k\right)\right]$, Σ_s. Taking into account that $\mathbf{v}_p^T = \left[\begin{array}{cc} \gamma_n & 1 \end{array}\right]$ is the left eigenvector associated with the unstable eigenvalue γ_p, Σ_s is given by

$$\left|\mathbf{v}_p^T\mathbf{x}\right| = \frac{u_o}{\gamma_p}. \tag{4.22}$$

This happens to be the boundary of $\Omega_{\max}$ as calculated in the Example 3.1, which means that, if the value of $q_s\left(k\right)$ is varied in such a way that the pseudo sliding condition (4.15) is satisfied, then the state trajectory will move on the boundary of $\Omega_{\max}$ and this is clearly not possible for an unstable system because any trajectory outside the region $\Omega_{\max}$ will not be stabilizable. Hence for $s_s\left[\mathbf{x}\left(k\right)\right]$ a different pseudo-sliding condition is used. The condition is

$$s_s\left[\mathbf{x}\left(k+1\right)\right]s_s\left[\mathbf{x}\left(k\right)\right] \leq 0. \tag{4.23}$$

This condition requires that for pseudo-sliding the trajectory crosses the hyperplane at each sampling time [Gao95]. This will be shown to guarantee the stability for the case of the control of unstable systems. The condition (4.23) can be expressed by the following set of equations

$$\left.\begin{array}{c} s_s\left[\mathbf{x}\left(k+1\right)\right] > 0 \text{ if } s_s\left[\mathbf{x}\left(k\right)\right] \leq 0 \\ \text{and} \\ s_s\left[\mathbf{x}\left(k+1\right)\right] < 0 \text{ if } s_s\left[\mathbf{x}\left(k\right)\right] \geq 0 \end{array}\right\} \text{for } sgn\left(x_2\right) > 0 \tag{4.24}$$

$$\left.\begin{array}{c} s_s\left[\mathbf{x}\left(k+1\right)\right] > 0 \text{ if } s_s\left[\mathbf{x}\left(k\right)\right] \leq 0 \\ \text{and} \\ s_s\left[\mathbf{x}\left(k+1\right)\right] < 0 \text{ if } s_s\left[\mathbf{x}\left(k\right)\right] \geq 0 \end{array}\right\} \text{for } sgn\left(x_2\right) < 0. \tag{4.25}$$

Substituting the first equation in (4.11) and the undelayed version of equation (4.1) into equations (4.24) and (4.25) and taking into account that $\mathbf{v}_p^T = \begin{bmatrix} \gamma_n & 1 \end{bmatrix}$ is the left eigenvector associated with the unstable eigenvalue γ_p, an expression for Σ_s is given by

$$\left|\mathbf{v}_p^T\mathbf{x}\right| = -\mathbf{v}_p^T \frac{\left(e^{-\gamma_p h}-1\right)}{\gamma_p\left(e^{-\gamma_p h}+1\right)}\mathbf{b}u_o. \tag{4.26}$$

where $\mathbf{b}^T = \begin{bmatrix} 0 & 1 \end{bmatrix}$. The equation of $\Omega_{\max}^{\tau}$ for the system defined by the equations (2.61) is calculated using Corollary 3.2.6 and is given by

$$\left|\mathbf{v}_p^T\mathbf{x}\right| = \mathbf{v}_p^T \frac{\left(2e^{-\gamma_p h}-1\right)}{\gamma_p}\mathbf{b}u_o. \tag{4.27}$$

By comparing equation (4.26) and (4.27) the following fact is derived

$$\forall\gamma_p > 0 \text{ and } \forall h > 0 \rightarrow \Sigma_s \supset \Omega_{\max}^{\tau}.$$

The proposed adaptation mechanism guarantees closed loop stability for $\epsilon_s \rightarrow 0$ as is now demonstrated. By definition $q_s\left(k\right)$ is adapted only when the condition (4.23) is satisfied. This occurs when the state is inside Σ_s given in equation (4.26) which has been demonstrated to be inside the region $\Omega_{\max}^{\tau}$. When the $s_s\left[\mathbf{x}\left(k\right)\right]$ is updated the overshoot over Σ_s becomes negligible as $\epsilon_s \rightarrow 0$ and therefore $s_s\left[\mathbf{x}\left(k\right)\right]$ remains inside the region $\Omega_{\max}^{\tau}$. However, the stability region associated with the rotating hyperplane gets smaller when $q_r\left(k\right)$ increases

(see Figure 4.6). To make sure that the combination of the switching hyperplanes $s_s[\mathbf{x}(k)]$

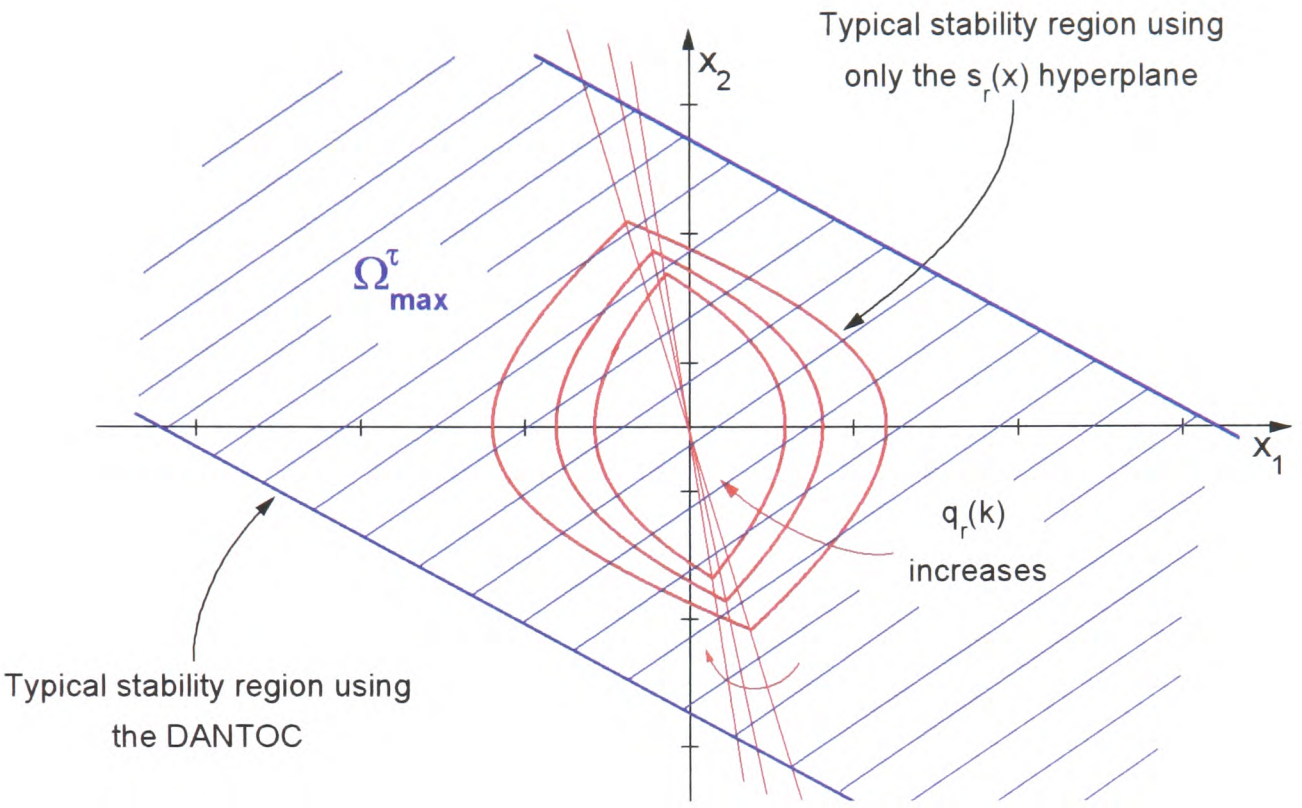


Figure 4.6: Stabilty region varying $q_r(k)$.

and $s_r[\mathbf{x}(k)]$ is always inside the region $\Omega^{\tau}_{\max}$ the mechanism to select the active hyperplane is designed to choose the hyperplane whose corresponding Σ is smaller. Since $\Sigma_s \subset \Omega^{\tau}_{\max}$ the closed loop stability is guaranteed.

The combination of the two switching hyperplanes, considering the adaptation rules (4.13) and (4.14) and the criteria for selecting the active hyperplane, is given by the intersection of Σ_r and Σ_s. Figure 4.7 shows the pseudo-sliding boundary locus using the following parameters: $\gamma_n = 1.5\,[s^{-1}]$, $\gamma_p = 150\,[s^{-1}]$, $u_o = 10000\,[V]$, $h = 50 \cdot 10^{-6}\,[s]$ and $\tau = 300 \cdot 10^{-6}\,[s] \rightarrow p = 6$. In Figure 4.7 a comparison between the pseudo-sliding boundary locus and the minimum time switching curve is also shown. According to equations (4.26) and (4.27) the distance between Σ and the minimum time switching curve can be reduced by increasing the sampling rate.

The adaptation rules (4.13) and (4.14) make the state move along the resulting Σ if

$$q_r(k + k_r) \geq q_r(k)$$

and

$$|q_s(k + k_s)| \geq |q_s(k)|$$

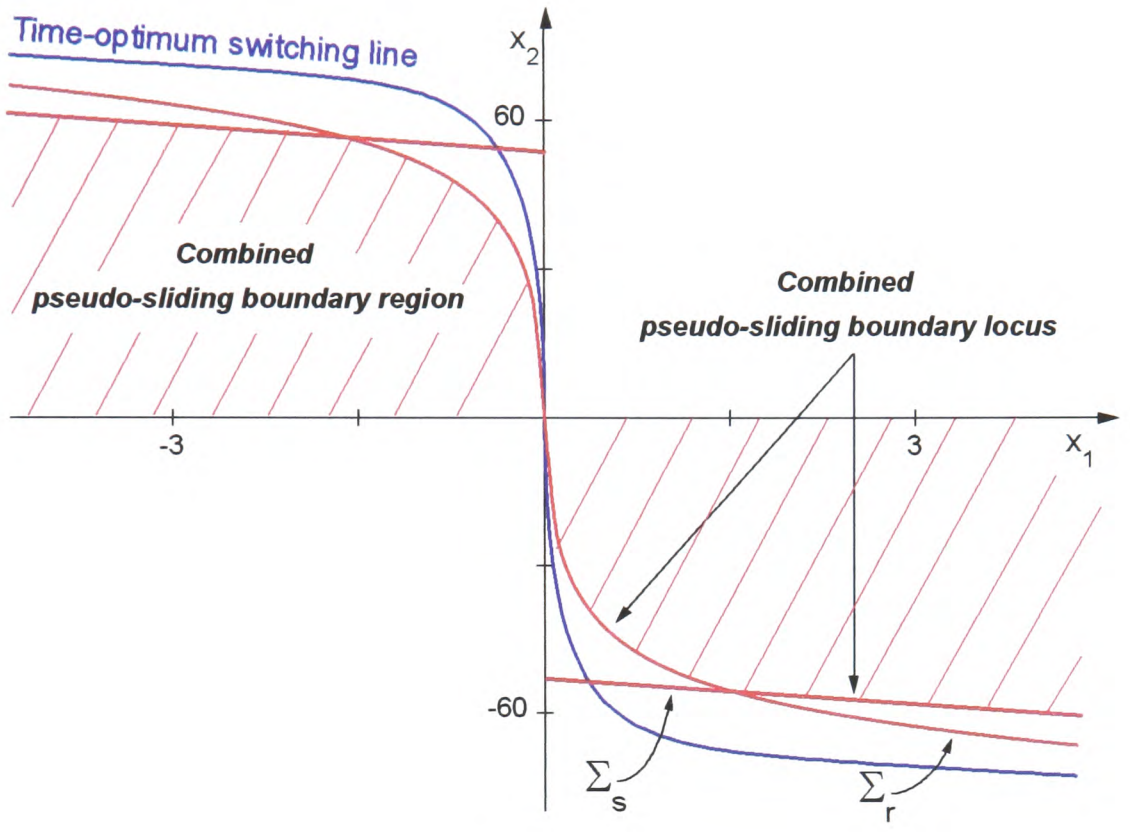


Figure 4.7: Pseudo-sliding boundary locus compared to the time-optimum switching line.

which means that during adaptation the values of $q_r(k)$ and $q_s(k)$ can only increase. This can be verified by inspection in Figure 4.5. As an example, the behaviour of the $\mathbf{x}(t)$ for $\gamma_p = 200\,[s^{-1}]$ and for $\gamma_p = 1000\,[s^{-1}]$ starting from the same initial conditions using the DANTOC is shown in Figure 4.8.

The adaptation only occurs when the closed loop system is in pseudo-sliding mode. A pseudo-sliding mode can be detected by checking that the conditions for pseudo-sliding mode defined in equations (4.15) and (4.23) are satisfied. However if there is a delay in the control action a modified check is needed. Assuming that there is a delay of p samples, then a pseudo sliding motion can be detected by checking that the following conditions hold

$$\{s[\mathbf{x}(k+p+1)] - s[\mathbf{x}(k)]\}\, s[\mathbf{x}(k)] \leq 0. \tag{4.28}$$

$$s[\mathbf{x}(k+p+1)]\, s[\mathbf{x}(k)] \leq 0. \tag{4.29}$$

A pseudo sliding detector detects the presence of a pseudo-sliding motion using the procedure described by the flowchart in Figure 4.9 and indicates to the adaptive algorithm when the rotating or shifting hyperplane must be updated. Therefore, at each time the state crosses

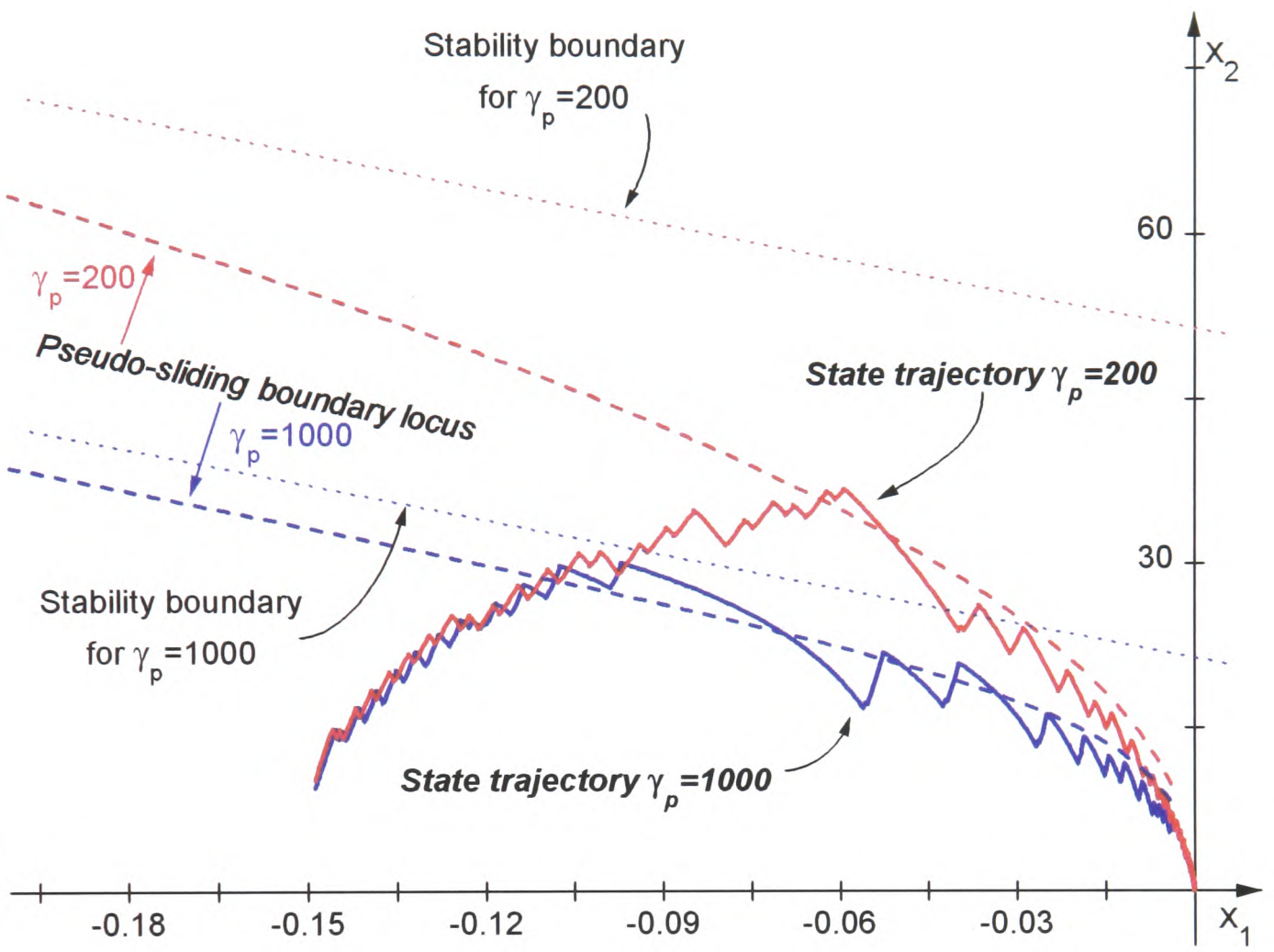


Figure 4.8: Example of the DANTOC performances when γ_p changes from 200 $[s^{-1}]$ to 1000 $[s^{-1}]$ starting from the same initial conditions.

$s[\mathbf{x}(k)]$ from $s[\mathbf{x}(k)]\, x_1(k) > 0$, the adaptive algorithm checks the result of the pseudo sliding detector.

The pseudo-sliding boundary detector is used in the example presented in Figure 4.5 and Figure 4.8.

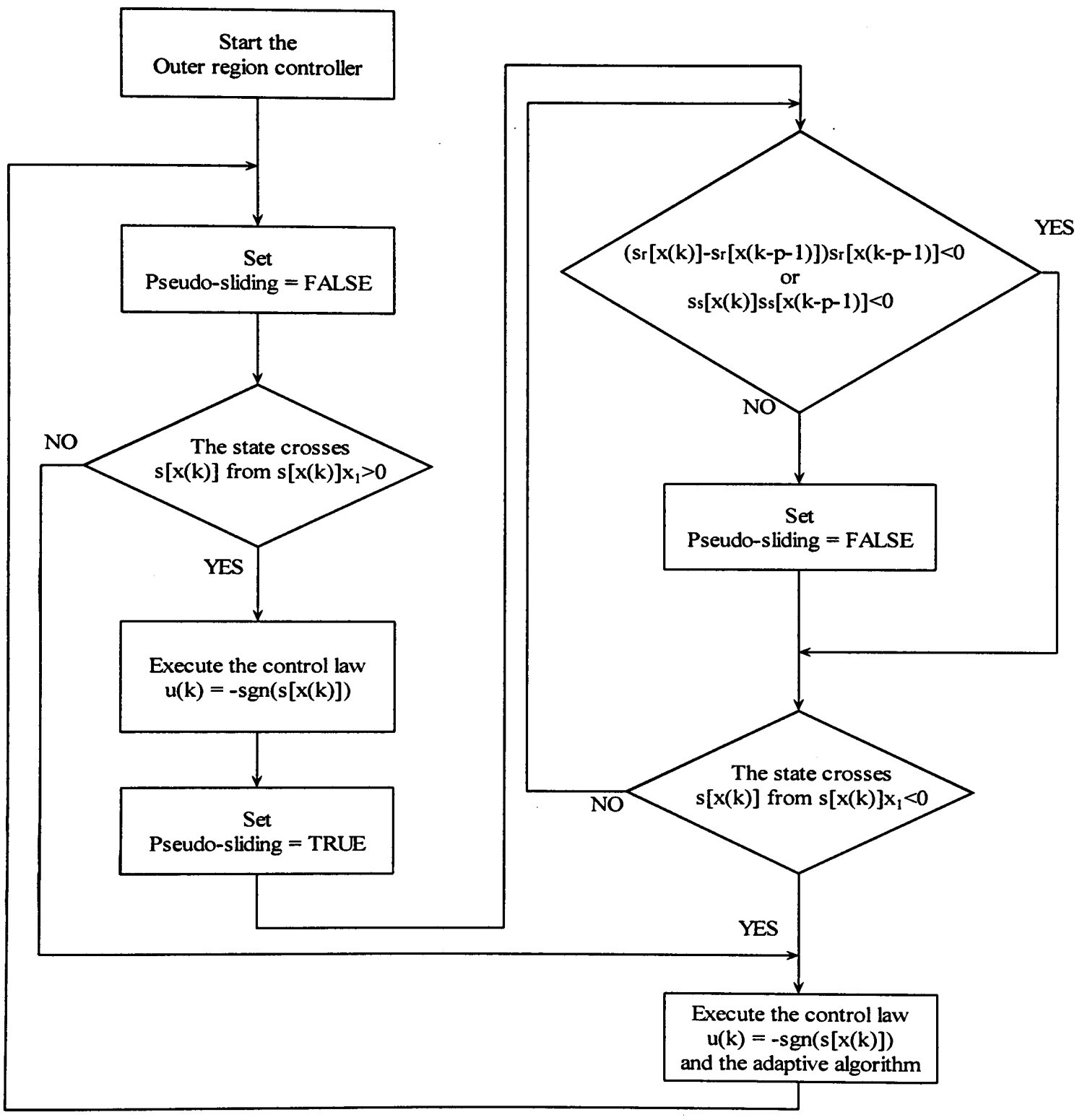


Figure 4.9: Pseudo-sliding detector flowchart.

4.2.3 Modifications to the basic adaptive controller to improve the robustness to external disturbances

As mentioned in Section 4.1.2, in discrete-time sliding mode controllers, the problem of robustness requires an *ad hoc* solution because the invariance property does not hold and therefore alternative approaches are required to solve the problem of robustness.

Some modification to the basic adaptive controller are needed, in the outer control region, to improve the robustness to external disturbances, in particular to ELMs. For the DANTOC's robustness to ELMs the following strategy is proposed:

- The controller is reset if the state crosses the state axes or if there is an unusually large change in either of the states (Section 4.2.3.1).
- Any state displacement caused by an ELM is controlled in minimum time. However the adaptation is started with a delay τ_s bigger than the ELM duration (Section 4.2.3.2)

In the inner control region it would be possible to use high order controllers aimed at the reduction of the $600Hz$ disturbance like in [Vyas96].

4.2.3.1 The resetting conditions

The adaptive control is not always active but it is started every time the state trajectory enters the region Ω_{out}. The initial values of the control parameters are set to be the optimal choice of q_r and q_s independent of the time varying parameters: $q_r(k_o) = \gamma_n$ and $q_s(k_o) = 0$. With this choice, initially, $s_r[\mathbf{x}(k_o)] = s_s[\mathbf{x}(k_o)]$. The resetting of the control parameters to this values is sufficient to guarantee the maximum stability region when entering Ω_{out} regardless of the time varying model parameters according to the Corollary 3.2.6. The control parameters are also reset to their initial values in the following circumstances:

1. The state trajectory crosses the x_1 or the x_2 axes when in Ω_{out}.
2. If there is an unusually large change in either of the states:

$$x_1(k+1) - x_1(k) > \Delta x_1^{\max}$$

$$x_2(k+1) - x_2(k) > \Delta x_2^{\max}$$

where $\Delta x_1^{\max}$ and $\Delta x_2^{\max}$ are calculated using the maximum expected γ_p in the plant model.

The first additional resetting condition is justified when the state trajectory crosses the axes during adaptation and therefore it is preferable to reset the controller rather than to risk exceeding the stability limits.

The second additional resetting condition prevents external disturbances driving the adaptive algorithm. It represents a protection for the main algorithm and it can slow down recovery from state displacements.

4.2.3.2 Adaptation delay strategy

The basic adaptive controller can be modified so as to minimize the state displacement caused by an ELM, $\mathbf{x}_{ELM}$, by using an adaptation delay strategy. This consists of delaying the start of the adaptation mechanism by a time τ_s bigger than the observed ELM's average duration $\bar{\tau}_{ELM}$. If an ELM detector were available, this could have been used to start the adaptation of the switching hyperplanes.

ELMs can have two different effects on the plasma speed and position according to their physical interpretation.

If an ELM only appears as a noise picked up by the magnetic transducers, then the controller should not intervene at all. The proposed strategy delays the start of adaptation by the time of duration of the ELM. In this way the controller will let the $\mathbf{x}(t)$ pseudo-slide about the initial sliding hyperplanes which yield a convergence rate of the order of the passive structure time constant γ_n. After the ELM disappears the measured state will probably be back in the inner region Ω_{in}, but, if it is still in the outer region Ω_{out}, the adaptation mechanism will start and the speed of the closed loop dynamics will be increased such as to recover in near-minimum time. This is considered an acceptable way of controlling this measurement noise because, during the ELM, the initial sliding hyperplanes are used which guarantees the maximum stability region for the plant.

The other possibility is that an ELM is actually moving the plasma and, therefore, action is required. By using the same strategy:

(a) The initial switching hyperplanes are used during the ELM .

(b) After the ELM the state will have been displaced to $\mathbf{x}_{ELM}$, the adaptive mechanism will start and the speed of the closed loop dynamics will be increased so that the plasma will recover in near-minimum time.

This is considered to be acceptable for two reasons. The first is that during the ELM the control action guarantees the maximum stability region and, after the ELM has vanished, the equilibrium position is recovered in minimum time. The second is that if the displaced state is recovered in minimum time, then there is a larger stability margin for the successive ELMs.

4.3 Selection of controller parameters

In the previous sections various controller parameters have been introduced, namely

- The inner control region parameters:
  - The control matrix $\mathbf{K}$.
  - The scaling matrix $\mathbf{T}$
- The outer control region parameters:
  - The rate of increase of the shifting hyperplane ϵ_s.
  - The rate of increase of the rotating hyperplane ϵ_r.
  - The adaptation delay τ_s.

In this section the criteria to choose these parameters are described.

4.3.1 Inner region control scheme

In the inner control region a linear state feedback controller is proposed. The controller matrix $\mathbf{K}$ in use in the past controllers is used in Ω_{in}. This approach allows us to focus on the design of the outer control region. However it is worth mentioning that, the proposed control structure, given by the second equation in (4.11), offers the possibility of using high order controllers of the type studied in [Vyas96]. In this case the total number of states can

increase. Therefore if an inner controller augments the number of states from 2 to n the linear feedback controller has the form of

$$u(t) = \mathbf{K}^T \begin{bmatrix} \mathbf{x} \\ \mathbf{x}^c \end{bmatrix}$$

where $\mathbf{x}^c$ are the states associated to the controller and $\mathbf{K} \in R^n$. When the state variables exit the inner control region the state variables associated with the high order controller are reset to zero and the feedback system is reduced from the $n^{th} - order$ to the $2^{nd} - order$. The use of a high order controller addresses the problem of reducing noise and smoothing the dynamics in the inner region without reducing the stability limits and performances when the control is not saturated. In the experiments on COMPASS-D a discrete version of the P+D analogue linear feedback controller is used to demonstrate how old techniques can be combined with new control designs (§ Section 6.2).

The selection of the scaling matrix $\mathbf{T}$ is based on the level of the $600Hz$ measurement noise. $\mathbf{T}$ can be calculated so that, with the given control limitations and in steady state, the effect of the measurement noise is contained in Ω_{in}. For example, assuming a second order system, Ω_{in} is given by

$$\sqrt{\frac{x_1^2}{t_{11}^2} + \frac{x_2^2}{t_{22}^2}} \leq \frac{u_o}{\rho \max(t_{11}, t_{22}) \sqrt{k_1^2 + k_2^2}}. \tag{4.30}$$

where t_{11} and t_{22} are the diagonal elements of the matrix $\mathbf{T}$. Equation (4.30) represents an ellipse in the phase plane. Assuming that the level of noise on the first and second state variable is $\bar{m}_{600}^{x_1}$ and $\bar{m}_{600}^{x_2}$ respectively, the values of t_{11} and t_{22} are selected according to the following procedure.

Step 1: check if the level of noise is contained in the saturation region Ω_K; if so go to step 2 else the saturation limit must be revised.

Step 2: set the values of t_{11} and t_{22} to one and determine the inner control region Ω_{in}.

Step 3: check if, with the given values of t_{11} and t_{22}, the condition (4.4) is verified; if so go to **step 4** otherwise go to step 6

Step 4: check if, with the given values of t_{11} and t_{22}, the noise levels $\bar{m}_{600}^{x_1}$ and $\bar{m}_{600}^{x_2}$ are contained in Ω_{in}; if so the selection is completed otherwise go to step 5.

Step 5: increase the values of t_{11} and t_{22} and go to step 3

Step 6: decrease the values of t_{11} and t_{22} and go to step 3.

Applications of the selection of Ω_{in} are given in Section 5.2, for the JET Tokamak, and in Section 6.2, for the COMPASS-D Tokamak.

4.3.2 Outer region control scheme

The rate of increase of the shifting and rotating hyperplanes, ϵ_s and ϵ_r respectively, are selected so as to maximize the stability region and minimize the chattering of the amplifier. In order to maximize the stability region it is demonstrated in Section 4.2.2 that the condition $\epsilon_s \to 0$ must be satisfied. Ideally an $\epsilon_r \to 0$ would also be required for the state trajectory to move on the pseudo-sliding boundary locus Σ_r. However if ϵ_s and ϵ_r are small, the chattering increases and the time taken to recover an initial condition increases as well because there is a minimum time of $2\tau_{tot}$ (see Section 2.6) for every increment due to the delay in the action. In addition, frequent switching of the amplifier has been found to be a problem in the JET Tokamak [Garribba94]. Therefore (as usual) ϵ_s and ϵ_r must be selected as a compromise between robustness and performances . Since some of the plant parameters are unknown, a procedure for selecting ϵ_s and ϵ_r based on the higher expected growth rate $\gamma_p^{\max}$ is derived below.

Let us define $q_r^{\max}$ as the value for which the rotating hyperplane $s_r(\mathbf{x})$ crosses the intersection between the pseudo-sliding boundary locus Σ_r, calculated for $\gamma_p^{\max}$ using equation (4.21), and Ω_{in} given in equation (4.3). Since it is rather difficult to give an analytic expression for $q_r^{\max}$ it can be solved graphically. Let us also define $q_s^{\max}$ as the maximum value for which the shifting hyperplane $s_s(\mathbf{x})$ does not exceed the region $\Omega_{\max}^{\tau}$ calculated for $\gamma_p^{\max}$. From equation (4.26), $q_s^{\max}$ is given by

$$q_s^{\max} = \mathbf{v}_p^T \frac{\left(e^{-\gamma_p^{\max}\tau_{tot}} - 1\right)}{\gamma_p^{\max}\left(e^{-\gamma_p^{\max}\tau_{tot}} + 1\right)} \mathbf{b} u_o \tag{4.31}$$

where τ_{tot} is defined in Section 2.6 and $\mathbf{b} = [0 \;\; K_1]^T$. Using $q_s^{\max}$ reduces the risks of exceeding the stability limits. ϵ_r and ϵ_s are calculate as follows:

$$\epsilon_r = \frac{q_r^{\max} - q_r(k_o)}{N_r} \tag{4.32}$$

$$\epsilon_s = \frac{q_s^{\max} - q_s(k_o)}{N_s} \tag{4.33}$$

where $q_s(k_o) = 0$, $q_r(k_o) = \gamma_n$, N_r and N_s represent the number of iterations from the initial value to the maximum expected value. The selection of the ϵ_s and ϵ_r is done indirectly by choosing the values of N_r and N_s. It is more natural to select the number of iteration steps because these are proportional to the number of the amplifier switches. The following properties apply to the selection N_r and N_s:

- The stability region and the chattering is increased by increasing N_r and N_s.
- The stability region is increased and the speed of convergence is decreased by increasing only N_s.
- The number of the amplifier switches is decreased and the convergency speed is increased by decreasing N_r. A disadvantage is that an excessive increase in $q_r(k)$ can put the system trajectory outside the pseudo-sliding region resulting in an overshoot of the reference signal.

The choice of N_r and N_s depends on the specific Tokamak and they can be tuned experimentally, or using simulation, to suit different objectives.

According to the adaptation delay strategy, described in Section 4.2.3.2, the adaptation mechanism must start with a delay τ_s bigger than the observed ELMs' average duration $\bar{\tau}_{ELM}$. The choice of τ_s is therefore straightforward

$$\tau_s \geq \bar{\tau}_{ELM}.$$

A more conservative approach is to select τ_s based on the longest observed ELM's duration $\tau_{ELM}^{\max}$

$$\tau_s \geq \tau_{ELM}^{\max}.$$

A consequence of delaying the adaptation mechanism is that the time taken to recovery from an initial condition is increased. The choice of τ_s depends on the specific Tokamak and it can be tuned experimentally, or using simulation.

The selection of N_r, N_s and τ_s is described in Section 5.2 for the JET Tokamak and in Section 6.2 for the COMPASS-D Tokamak.

4.4 Does the controller achieve the predefined objectives?

Let summarize how the DANTOC satisfies the objectives set in the Section 4.1.

Stabilize the vertical position: The DANTOC guarantees asymptotically stable sliding motion on the moving hyperplanes in Ω_{out} and local asymptotic stability in Ω_{in}. Therefore, given the control bounds the vertical position will be stable as long as the states of the closed loop system are inside the maximum obtainable stability region $\Omega_{\max}$.

Maximize the stability region: The presence of control bounds makes it impossible to globally stabilize the unstable vertical position of the plasma. However the DANTOC maximizes the stability region by adapting the switching hyperplanes. By comparison, the only linear controller that maximizes the stability region was derived in Theorem 3.2.4. However this controller has poor performance since the dynamics are associated with the passive structure time constant γ_n. Any other linear controller with fixed parameters will reduce the stability region. In Figure 4.10 the difference between the stability region of a typical saturating linear controller and the one obtained using the DANTOC is shown.

Reduce the effect of disruptions: The effect of a disruption can only be reduced by counteracting vertical movement of the plasma as long as possible given the power limitations. Typically if an amplifier exceeds a hard limit it will trip causing the control to fail. Holding the controller inside these limits and controlling the vertical position until the plasma current has decreased will minimize the effect of a possible disruption. For example it could avoid exceeding the FRFA current limits and in case of emergency a reduction of the plasma current could be requested and the effect of an imminent disruption reduced.

Reduce the effect of external disturbances and measurement noise: The DANTOC reduces the effect of external disturbances like ELMs by applying the adaptation delay strategy. The measurement noise rejection depends on the region of control:

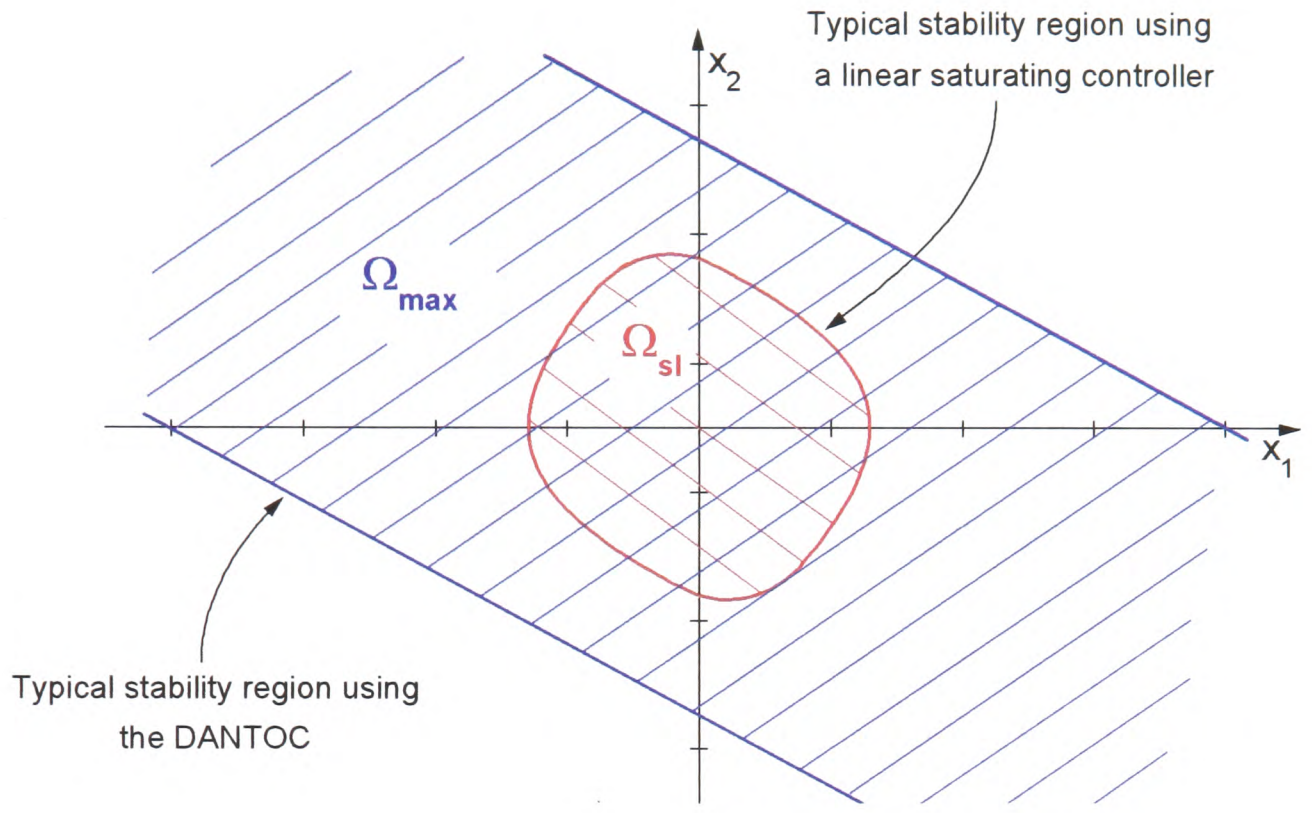


Figure 4.10: Comparison between typcal stability regions obtained using a saturating linear controller and the DANTOC.

- In the outer region, the presence of a pseudo-sliding mode controller avoids destabilization of the system caused by the saturation of the measurement by an ELM and reduces the effect of the $600Hz$ noise.
- In the inner region, a high order linear controller can be designed to reduce the effect of the $600Hz$ noise

Robustness to plant parameter variations: The DANTOC achieves robustness to the plant parameters variations by adaptation. The DANTOC identifies the pseudo-sliding boundary locus without prior knowledge of the plant parameters.

Minimize the number of times the amplifiers switch and reduce the energy losses: The number of times the amplifier switches can be kept relatively small by appropriate selection of the DANTOC's adaptation rates.

It is concluded that the DANTOC satisfies all the control objectives. The use of an adaptive algorithm allows the maximum stability region to be achieved independently of the plasma configuration. The controller also achieves near-time optimal response exploiting all the amplifier capabilities.

Chapter 5

Testing of the control algorithm on a simulation of the JET Tokamak

5.1 Introduction

In this Chapter the application of the DANTOC to the JET Tokamak is presented using a computer simulation of the complete vertical stabilization system which includes the DANTOC, the FRFA, the ELMs, the $600Hz$ noise and the plasma vertical position model. Due to inherent dangers of vertical instabilities in JET and the very limited machine time available it was considered appropriate to test the implementation of the DANTOC on JET using computer simulations for different operating conditions before on-line implementation. The use of computer simulations is also necessary to vary parameters which cannot be easily changed in the real system and to generate situations that can be difficult to repeat experimentally.

As mentioned in Section 2.6.2, the present JET Tokamak vertical stabilization control scheme is based on a P controller on the plasma vertical velocity loop and a PI controller on the FRFA current loop (see Figure A.10 in Section A.3.1 of Appendix A). The $P+PI$ linear control algorithm has fixed parameters. The limitations of the FRFA, namely the maximum voltage $\pm 10 \cdot 10^3\,[V]$ and maximum nominal current $\pm 2.5 \cdot 10^3\,[A]$ (i.e. configuration B, § Section 2.5), are not taken into account by the controller. The present control scheme is susceptible to noise and also suffers from failures during high performance pulses, typically in the presence of large ELMs [Ali-Arshad96]. Large disturbances that saturate the command signal are often observed on JET and typically lead to an overcurrent trip in the FRFA amplifier and, consequently, to a vertical disruption. The DANTOC is proposed to overcome

some of these difficulties. In particular additional logic has been added to the DANTOC algorithm to limit the FRFA current. The effect of this current limiter is examined in Section 5.3.3.

Since the DANTOC maximizes the stability region independently of the plasma configuration and takes account of the limitations of the FRFA, it is proposed to use the DANTOC controller for all the JET's operating configurations.

5.2 Setup of the controller for the JET Tokamak

A schematic diagram of the proposed control scheme is shown in Figure 5.1.

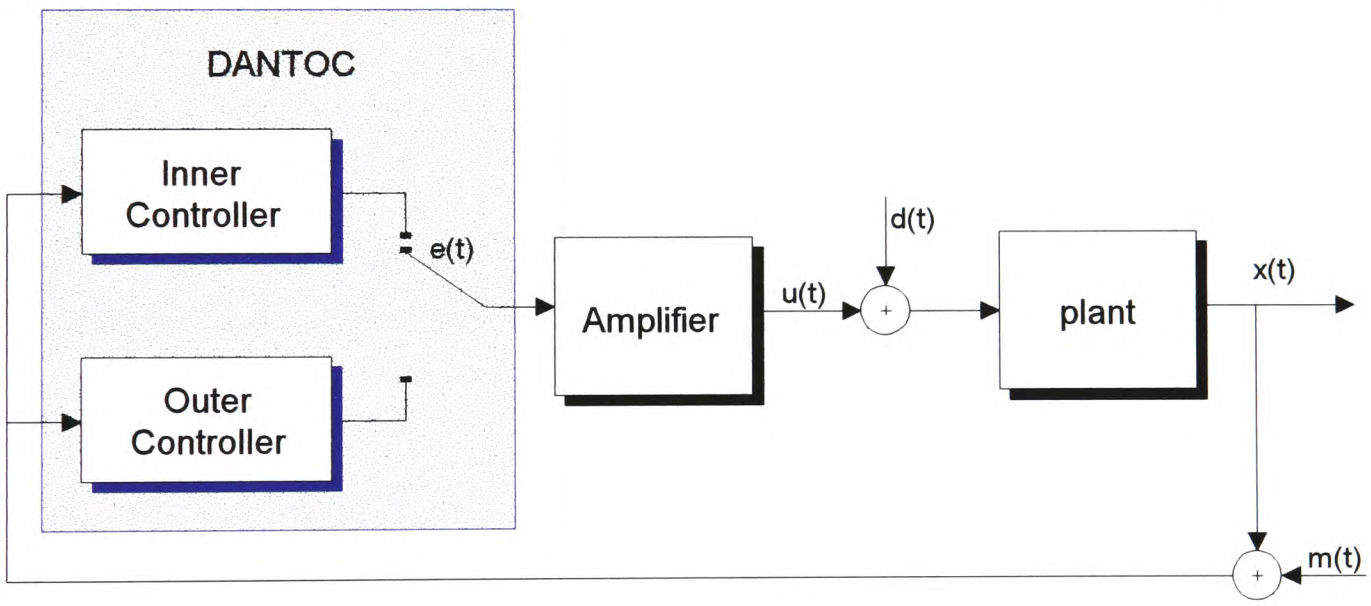


Figure 5.1: Proposed control scheme for JET tokamak.

A number of simulations were executed to tune the DANTOC parameters following the procedures given in the Section 4.3.1 and 4.3.2. As a result, the following set of parameters were found to be the most suitable for the JET Tokamak:

$$\begin{aligned} &\bullet \text{ Inner control region:} \quad \Omega_{in} = \left\{ \mathbf{x} \in \mathbf{R}^3 : \frac{\dot{z}_p^2}{(0.904)^2} + \frac{I_{FRFA}^2}{(173.27)^2} + \frac{x_i^2}{(173.27)^2} \leq 1 \right\}. \\ &\bullet \text{ Adaptation rates:} \quad \epsilon_r = 50 \text{ and } \epsilon_s = 1 \\ &\bullet \text{ Adaptation delay:} \quad \tau_s = 2 \cdot 10^{-3}\,[s] \end{aligned} \tag{5.1}$$

For the design of DANTOC, it is assumed that the highest instability growth rate is $\gamma_p^{\max} = 1000\,[s^{-1}]$.

For the inner control region the present $P + PI$ controller is used with parameters $P_v =$

$0.68\,[ms^{-1}]$, $P_i = 2 \cdot 10^{-3}\,[A]$ and $T_i = 0.5 \cdot 10^{3}\,[A^{-1}s^{-1}]$.

The inner control region for the JET Tokamak is derived from equation (4.3) and is given by

$$\Omega_{in} = \left\{ \mathbf{x} \in \mathbf{R}^3 : \sqrt{\frac{\dot{z}_p^2}{t_{11}^2} + \frac{I_{FRFA}^2}{t_{22}^2} + \frac{x_i^2}{t_{33}^2}} \leq \frac{u_o}{\rho \max(t_{11}, t_{22}, t_{33}) \sqrt{(k_1^2 + k_2^2 + k_3^2)\, K_a}} \right\}, \quad (5.2)$$

where x_i is the state variable associated with the integral part of the PI controller, u_o is the selected level of saturation, k_1, k_2 and k_3 are the equivalent gains of the feedback controller, ρ is given by equation (4.6) and the scaling matrix $\mathbf{T}$ is selected so that the level of measurement noise $\bar{m}_{600}$ is within Ω_{in}. For a typical JET experiment it is observed that

$$\bar{m}_{600}^{I_{FRFA}} \leq 100\,[A]$$
$$\bar{m}_{600}^{\dot{z}_p} \simeq 0.8\,[ms^{-1}]\,.$$

The $P + PI$ linear control algorithm is equivalent to a PID controller applied to the model given by equation (2.61). The equivalent controller is then expressed as

$$sk_1 + k_2 + \frac{k_3}{s}$$

where the equivalent parameters are: $k_1 = P_v = 0.68\,[ms^{-1}]$, $k_2 = \frac{A''_{pp}}{\acute{L}_{ap}} P_i = 0.38\,[m]$ and $k_3 = \frac{A''_{pp}}{\acute{L}_{ap}} \frac{1}{T_i} = 0.38\,[ms]$. The sampling frequency of the digital controller is $20 \cdot 10^3\,[Hz]$. Applying the design criteria given in Section 4.3.1 and assuming that the level of saturation is fixed at $u_o = 5000$, the values of $\bar{m}_{600}^{I_{FRFA}}$ and $\bar{m}_{600}^{\dot{z}_p}$ are inside the inner control region selecting $t_{11} = 1$, $t_{22} = \frac{A''_{pp}}{\acute{L}_{ap}}$ and $t_{33} = \frac{A''_{pp}}{\acute{L}_{ap}}$. Substituting the value of t_{11}, t_{22}, t_{33}, $u_o = 5000$, $K_a = 10000\,[V]$, and $\rho = 1.27$ into equation (5.2) and simplifying it, the inner control region given in the standard set is then obtained.

The values of the adaptation rates are calculated using equations (4.32) and (4.33). Recalling that $\gamma_p^{\max} = 1000\,[s^{-1}]$, $\gamma_n = 1.5\,[s^{-1}]$ and $\tau_{tot} = 300 \cdot 10^{-6}\,[s]$, from equation (4.31) the values of $q_s^{\max} \simeq 30$ is derived. The value of $q_r^{\max} \simeq 1000$ is obtained graphically as described in Section 4.3.2. A series of simulations have shown that reasonable values of iteration steps, N_r and N_s, are 20 and 30 respectively. The adaptation rates are obtained by substituting the values of $q_s^{\max}$, $q_r^{\max}$, N_s, N_r and γ_n into equations (4.32) and (4.33).

The adaptation delay τ_s is the average observed ELM's duration, $\bar{\tau}_{ELM} = 2 \cdot 10^{-3}\,[s]$, which was determined by analysis of the JET experimental data (see for example Figure 2.8).

5.3 Closed loop simulations using the proposed controller

The following test cases are simulated to validate the DANTOC design and compare the performance to the present vertical stabilization control system:

Section 5.3.1: Response to arbitrary initial conditions.

Section 5.3.2: Response to large disturbances (ELMs) and measurement noise (ELMs and 600 $[Hz]$) and comparison with present controller.

Section 5.3.3: Effect of the current limit constraint.

Section 5.3.4: Effect of asymmetric plasma configurations having different up/down growth rates.

In all the simulations the growth rate γ_p is set to 200 $[s^{-1}]$ (except in Section 5.3.4 where it varies from $\gamma_p = 200\,[s^{-1}]$ to $\gamma_p = 1000\,[s^{-1}]$) and the plasma current I_p to $3 \cdot 10^6\,[A]$. The DANTOC parameters are given by equation (5.1) and the FRFA current limiter is set so that $I^{\max}_{FRFA} = 2450\,[A]$.

5.3.1 Response to generic initial conditions

In these simulations the response to arbitrary initial conditions is analysed. The recovery from the initial conditions

$$\begin{aligned} z_p &= 6.4 \cdot 10^{-2}\,[m] \\ \dot{z}_p &= -3.0\left[ms^{-1}\right]. \end{aligned}$$

is presented in Figure 5.2. The results show that the DANTOC is able to drive the state trajectory close to the pseudo-sliding boundary locus. In this way the state trajectory is kept inside the region $\Omega_{\max}$. The adaptations of the switching hyperplanes gradually increase the speed of the closed loop dynamics so that a near minimum time response is obtained.

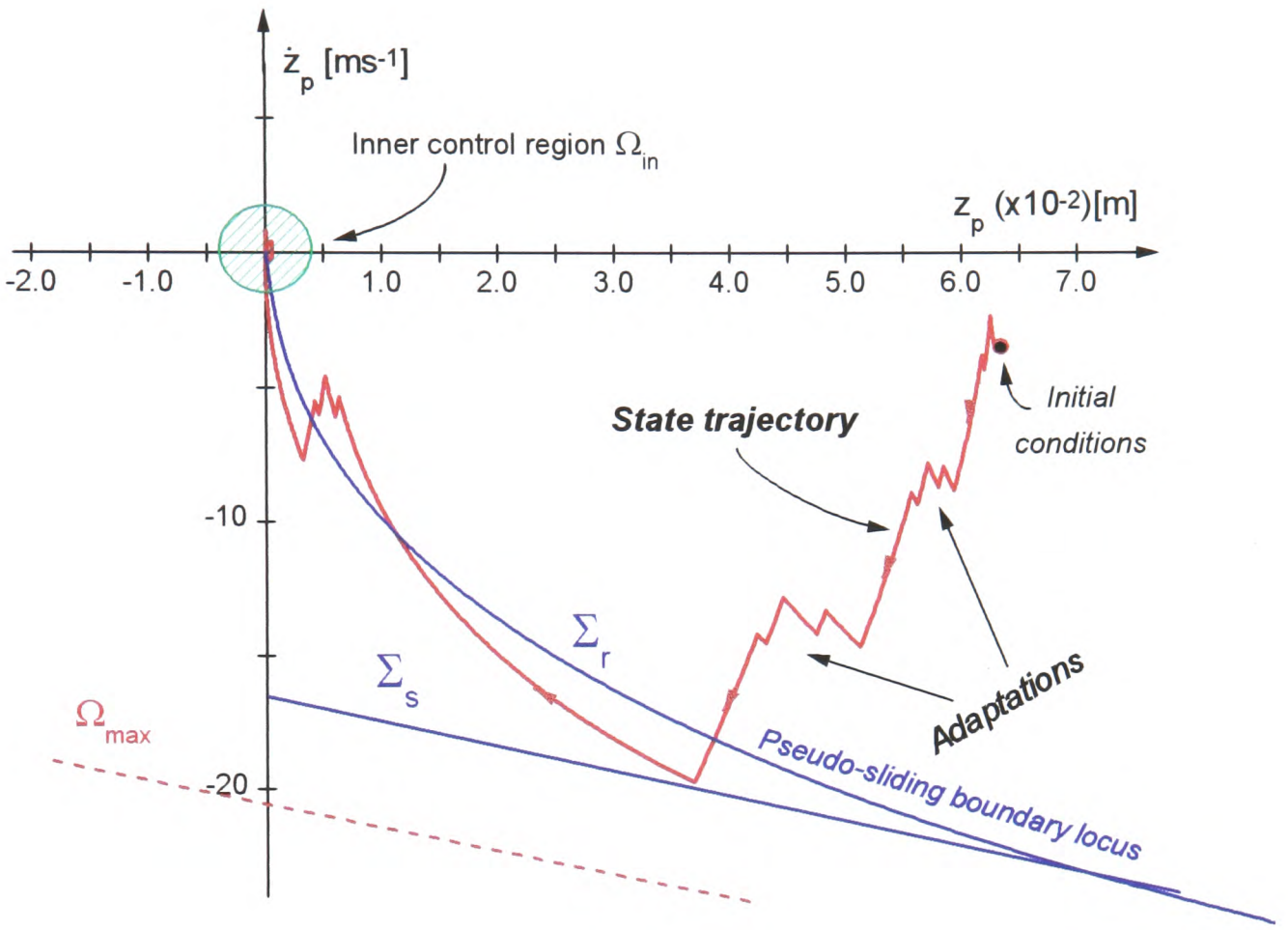


Figure 5.2: Simulation of the JET Tokamak vertical stabilization system using the DANTOC: phase-plane diagram of the response to arbitrary initial conditions.

In Figure 5.3 the time behaviour of the variables is shown. The switching rate of the FRFA amplifier is an indicator of the adaptation. The FRFA current is also quickly reduced once the state trajectory reaches the pseudo-sliding boundary locus. From this simulation it is concluded that the DANTOC performs as the theoretical analysis predicted.

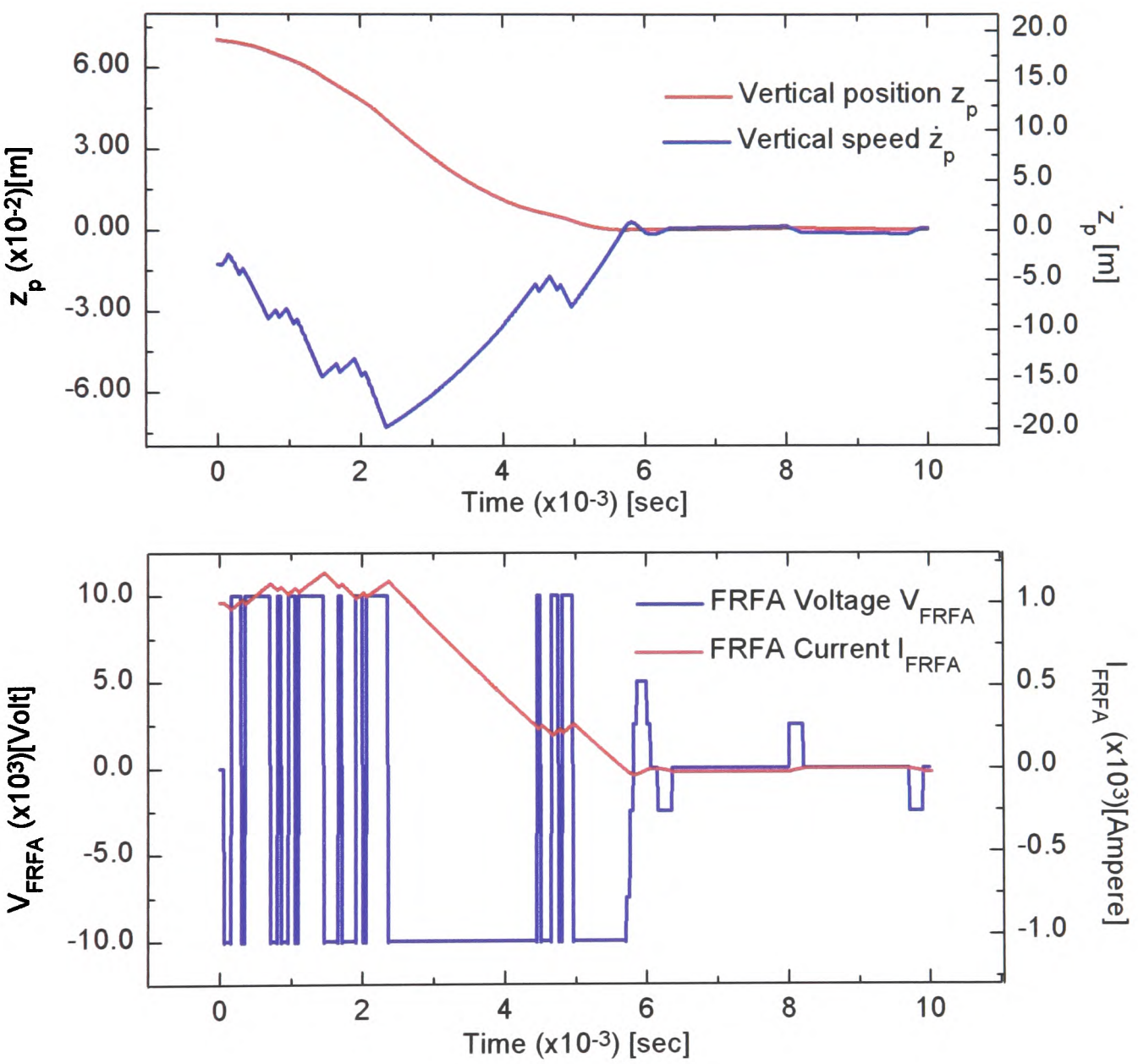
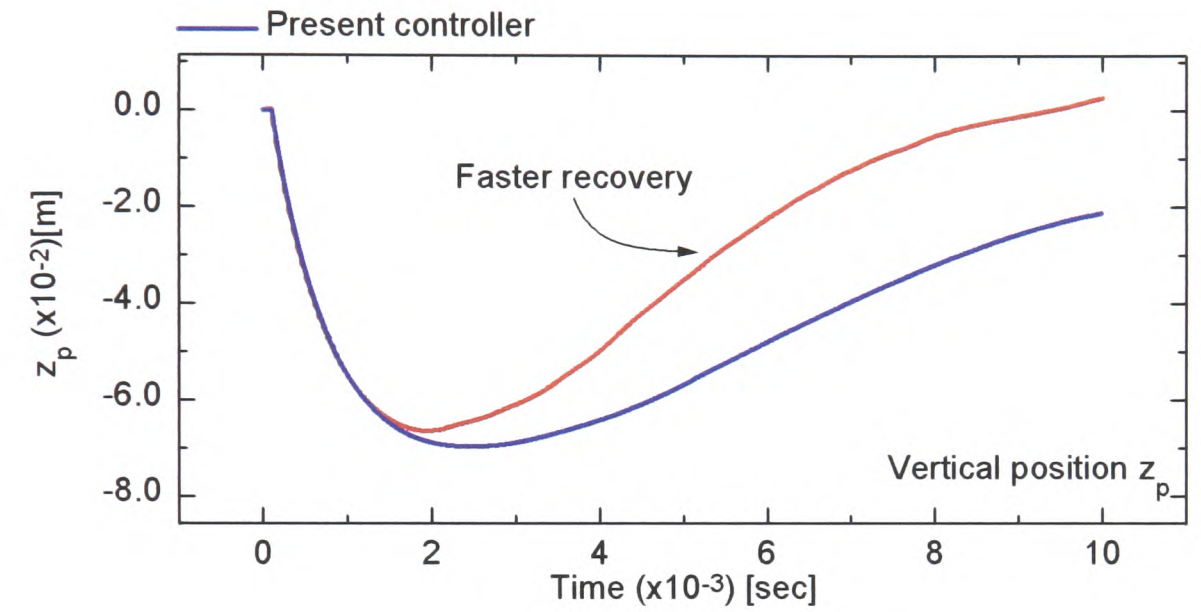


Figure 5.3: Simulation of the JET Tokamak vertical stabilization system using the DANTOC: time evolution of the response to generic initial conditions.

5.3.2 Response to large disturbances (ELMs) and measurement noise (ELMs and $600Hz$) - Comparison with the JET present controller

The response to large disturbances and measurement noise is examined in the following simulations. The results of the simulations using the DANTOC are also compared to the simulations using the present JET vertical stabilization controller.

In the first set of simulations the disturbance is assumed to be a large ELM described by equation (2.43) where $\tau_1 = 4 \cdot 10^{-3}\,[s]$, $\tau_2 = 0.5 \cdot 10^{-3}\,[s]$, $\tau_3 = 0$ and $\bar{d}_{600} = 8$. This is equivalent to a destabilizing force of about $50 \cdot 10^3\,[N]$. As it can be seen in Figure 5.4 a faster recovery can be achieved when using the DANTOC in contrast to the slower recovery associated with the present controller. The above also applies with respect to the FRFA current shown in Figure 5.5. The present controller design is based on a high value of γ_p to guarantee stability margins. However this causes a slower closed loop response. The DANTOC, on the other hand, adapts the switching hyperplanes to achieve high performance with respect to the actual value of γ_p. Therefore the closed loop response is faster. The only disadvantage of using the DANTOC is a temporary increase in the switching rate of the FRFA.



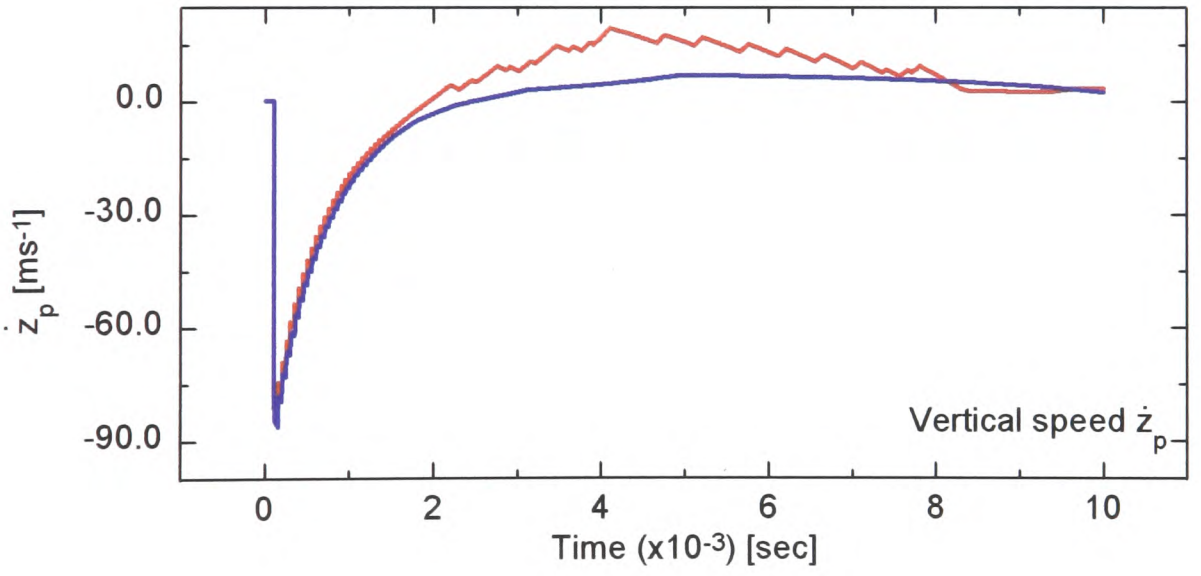
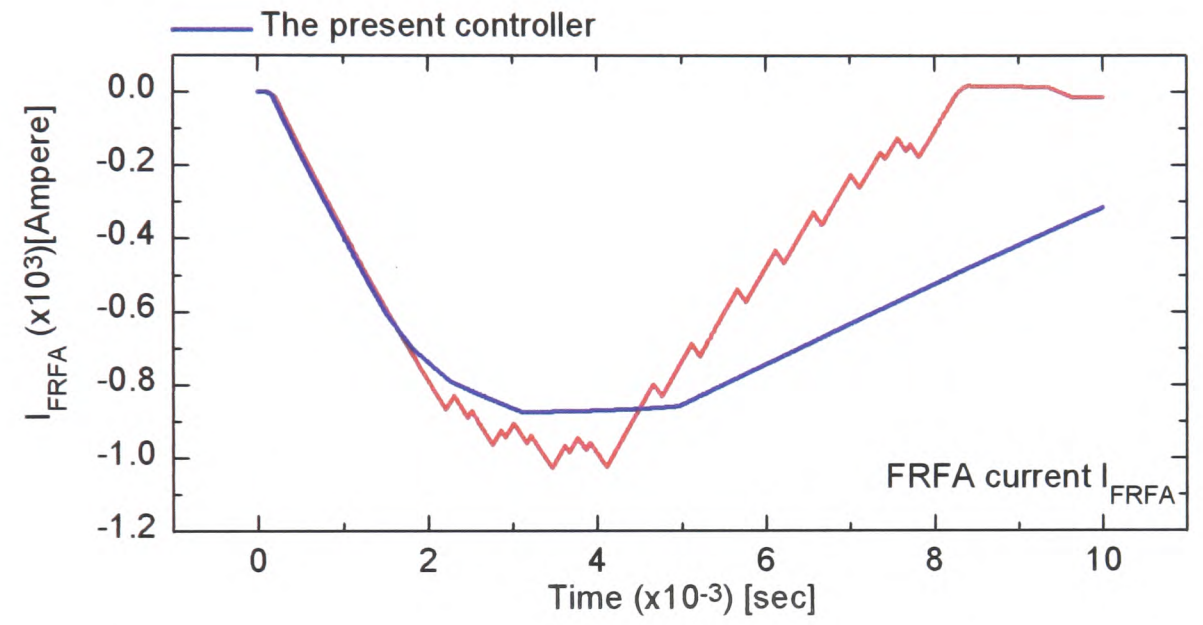


Figure 5.4: Comparison between the simulations of the JET vertical stabilization system using the DANTOC and using the present JET vertical stabilization controller (vertical position and speed): Response to large disturbances (ELMs).



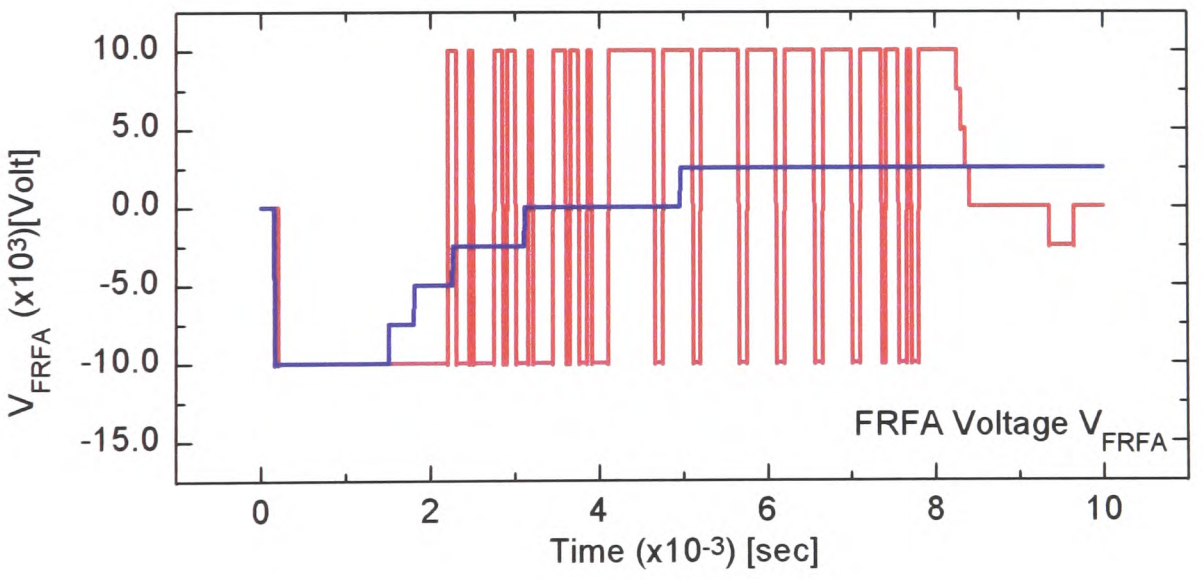


Figure 5.5: Comparison between the simulations of the JET vertical stabilization system using the DANTOC and using the present JET vertical stabilization controller (FRFA voltage and current): Response to large disturbances (ELMs).

In the following set of simulations a large ELM and a thyristor noise signal is added to the measurement of the plasma vertical speed and a thyristor noise signal is added to the measurement of the plasma vertical position. The ELM is assumed to have the same characteristics as the one in the previous simulations while the thyristor noise on the vertical position and speed signals are assumed to be

$$\begin{aligned} m_{600}^{\dot{z}_p}(t) &= \sin(2\pi 600t) + 0.5\sin(2\pi 1200t) + 0.1\sin(2\pi 1800t)\left[ms^{-1}\right] \\ m_{600}^{z_p}(t) &= \left[\sin(2\pi 600t) + 0.5\sin(2\pi 1200t) + 0.1\sin(2\pi 1800t)\right]\cdot 10^{-3}\,[m] \end{aligned}$$

respectively. In the Figure 5.6 it can be seen that the ELM saturates the measurement. The effect of the large ELM causes the vertical position controlled by the present JET controller to exceed both the FRFA current limit and, ultimately, the stability limits. As a consequence control is lost. The DANTOC succeeds in maintaining the state variables inside both of the above limits and the plasma enters the inner control region Ω_{in}. The effect of the thyristor

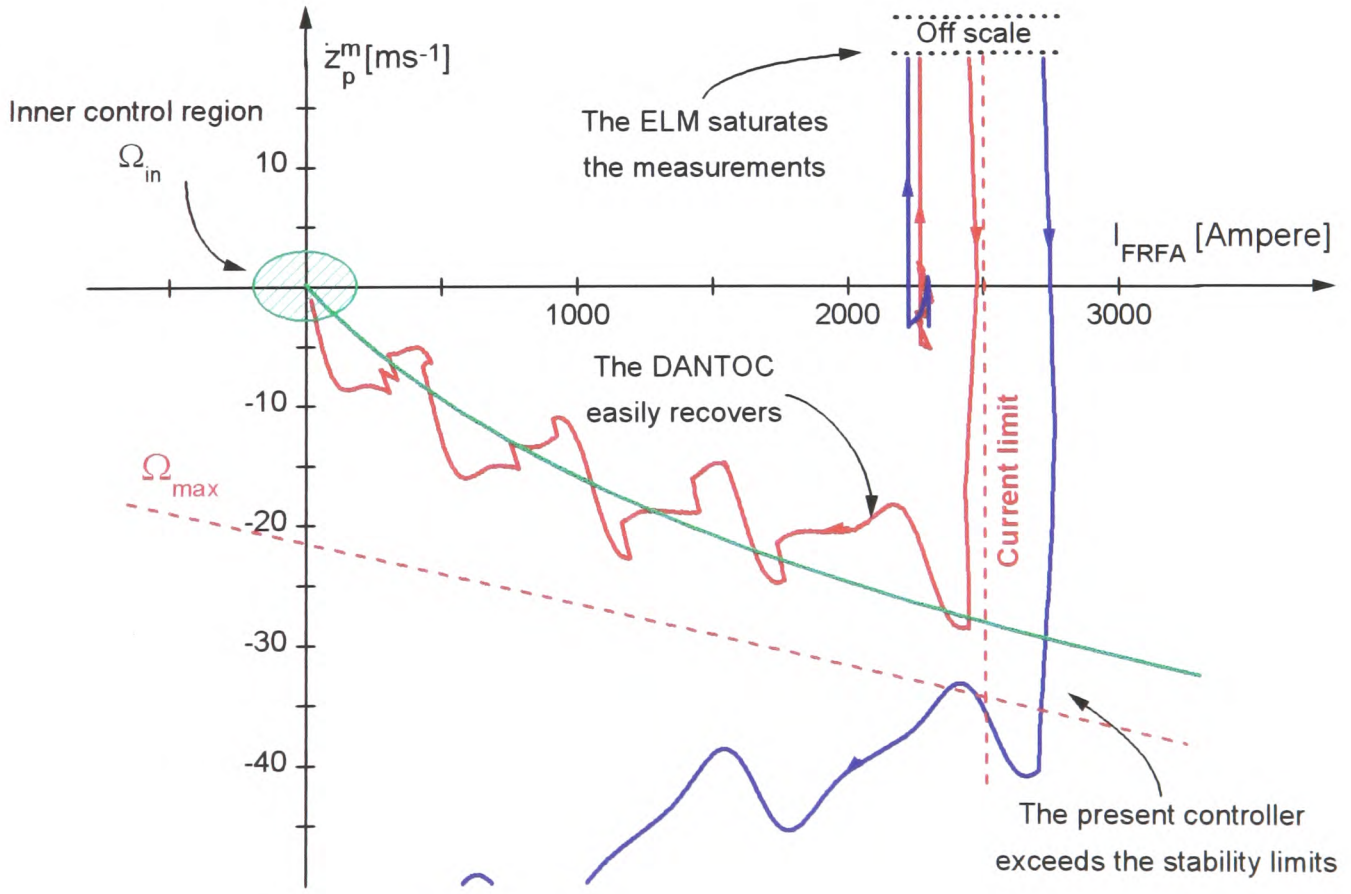


Figure 5.6: Comparison between the simulations of the JET vertical stabilization system using the DANTOC and using the present JET vertical stabilization controller (Phase-plane diagram): Response to measurement noise.

noise is clearly visible in Figure 5.6 and Figure 5.7. The noise does not prevent the DANTOC from adapting to the pseudo-sliding boundary locus. The effect of the FRFA current limiter

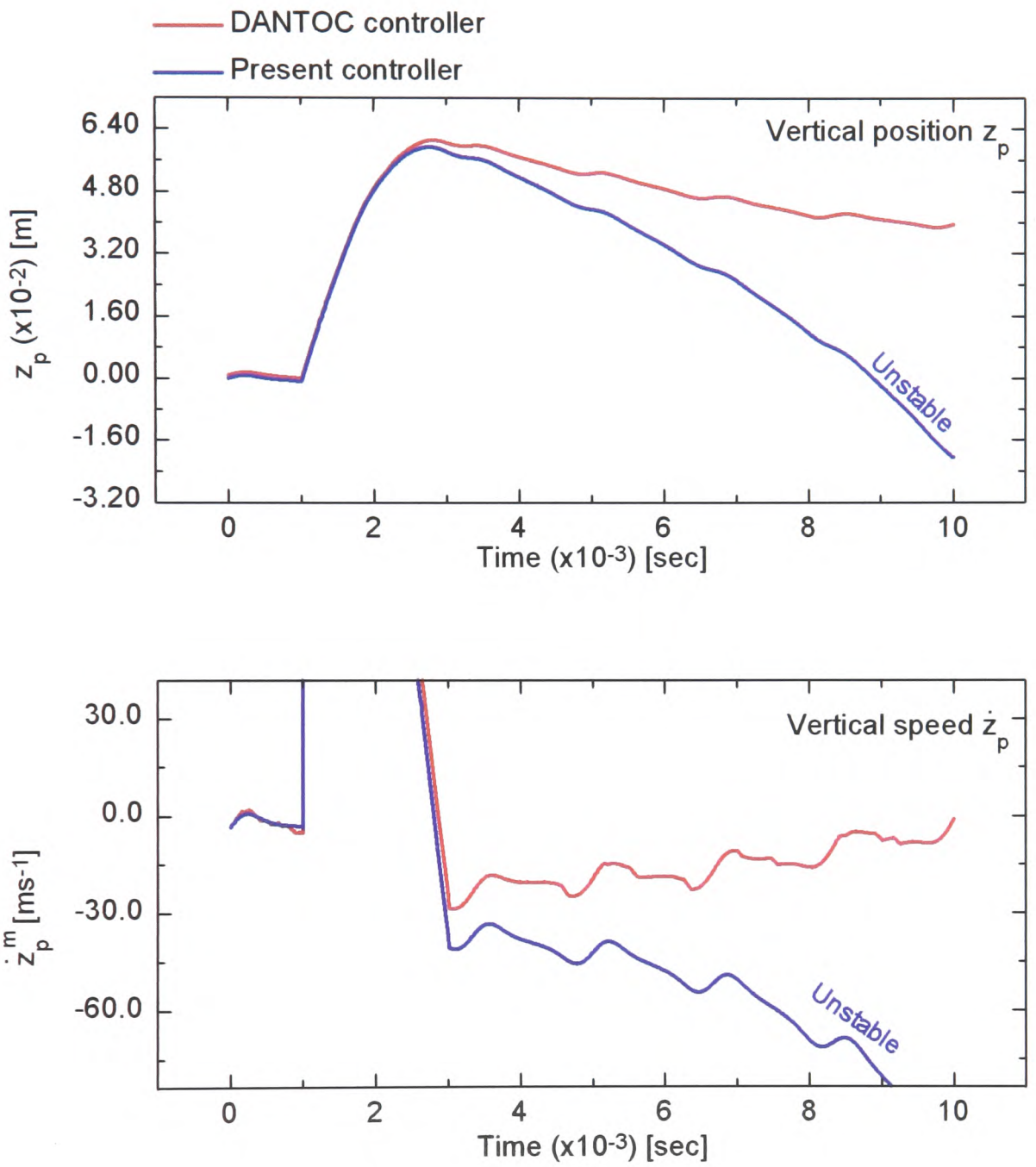
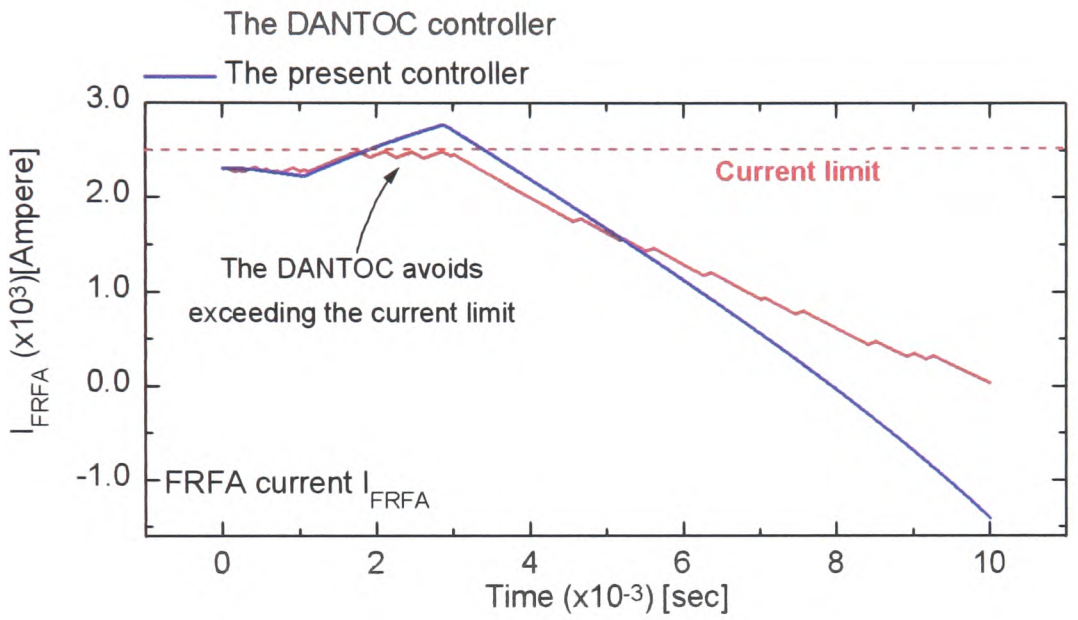


Figure 5.7: Comparison between the simulations of the JET vertical stabilization system using the DANTOC and using the present JET vertical stabilization controller (Vertical position and speed): Response to measurement noise.

can be clearly seen in Figure 5.8.

It is concluded that a good noise rejection is achieved both with respect to the noise induced by ELMs and to that induced by the thyristor power supplies.



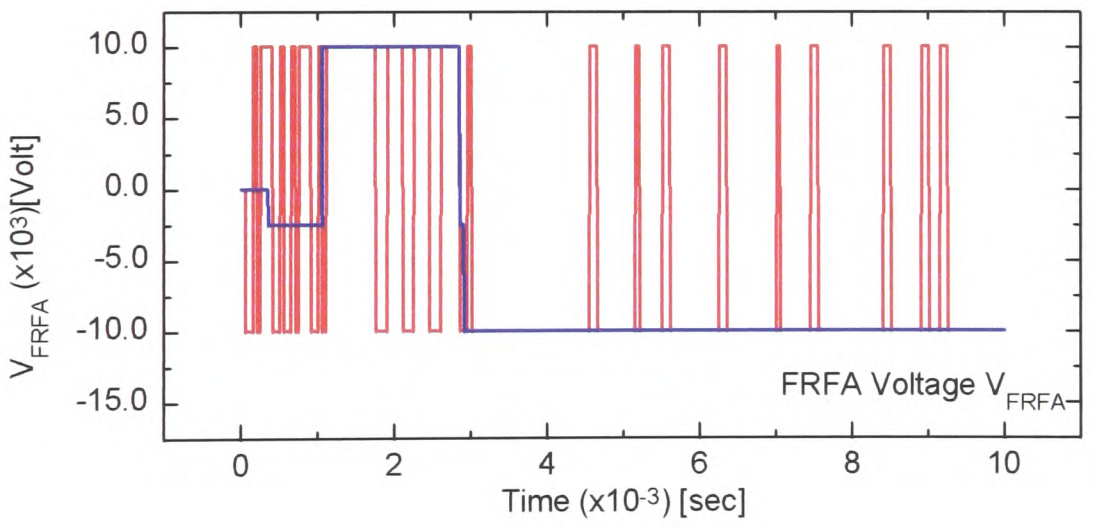


Figure 5.8: Comparison between the simulations of the JET vertical stabilization system using the DANTOC and using the present JET vertical stabilization controller (FRFA voltage and current): Response to measurement noise.

5.3.3 Effect of the current limit constraint

The effect of the FRFA current limiter is examined in the following simulation which assumes a set of initial conditions close to the current limit,

$$\begin{aligned} I_{FRFA} &= 2400\,[A] \\ \dot{z}_p &= -3.0\left[ms^{-1}\right]. \end{aligned}$$

As it can be seen in Figure 5.9, the results show that the DANTOC avoids exceeding both the FRFA current and the stability limits while maintaining a fast closed loop response. The state trajectory moves along the current limits until the pseudo-sliding boundary locus is intercepted. After then the state trajectory moves towards the inner control region Ω_{in}.

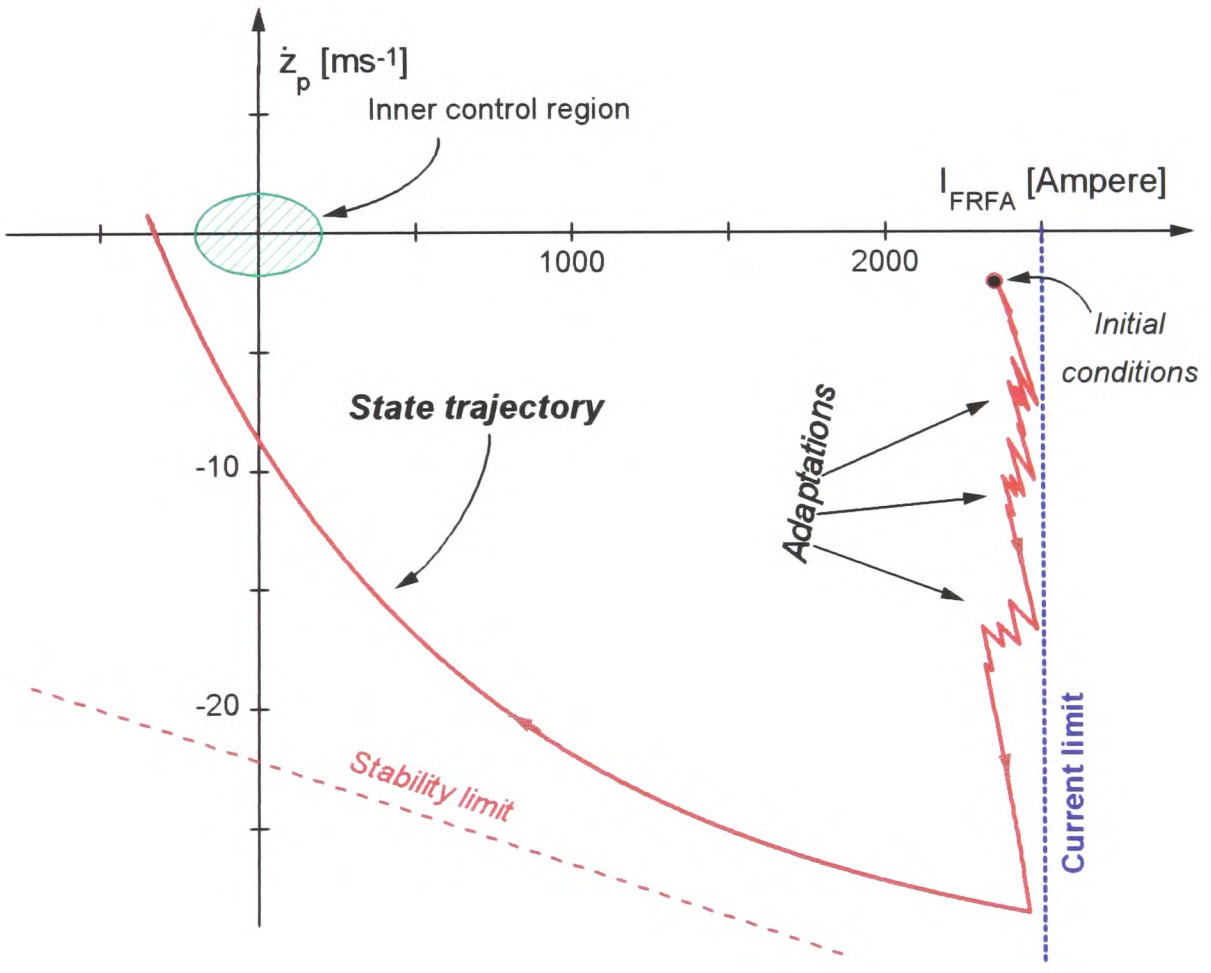


Figure 5.9: Simulation of the JET Tokamak vertical stabilization system using the DANTOC: phase-plane diagram of the response to initial conditions close to the FRFA current limit.

The effect of the FRFA current limiter can be seen in Figure 5.10 where the time behaviour of the variables is shown.

It is concluded that the FRFA current limiter is effective in limiting the FRFA current.

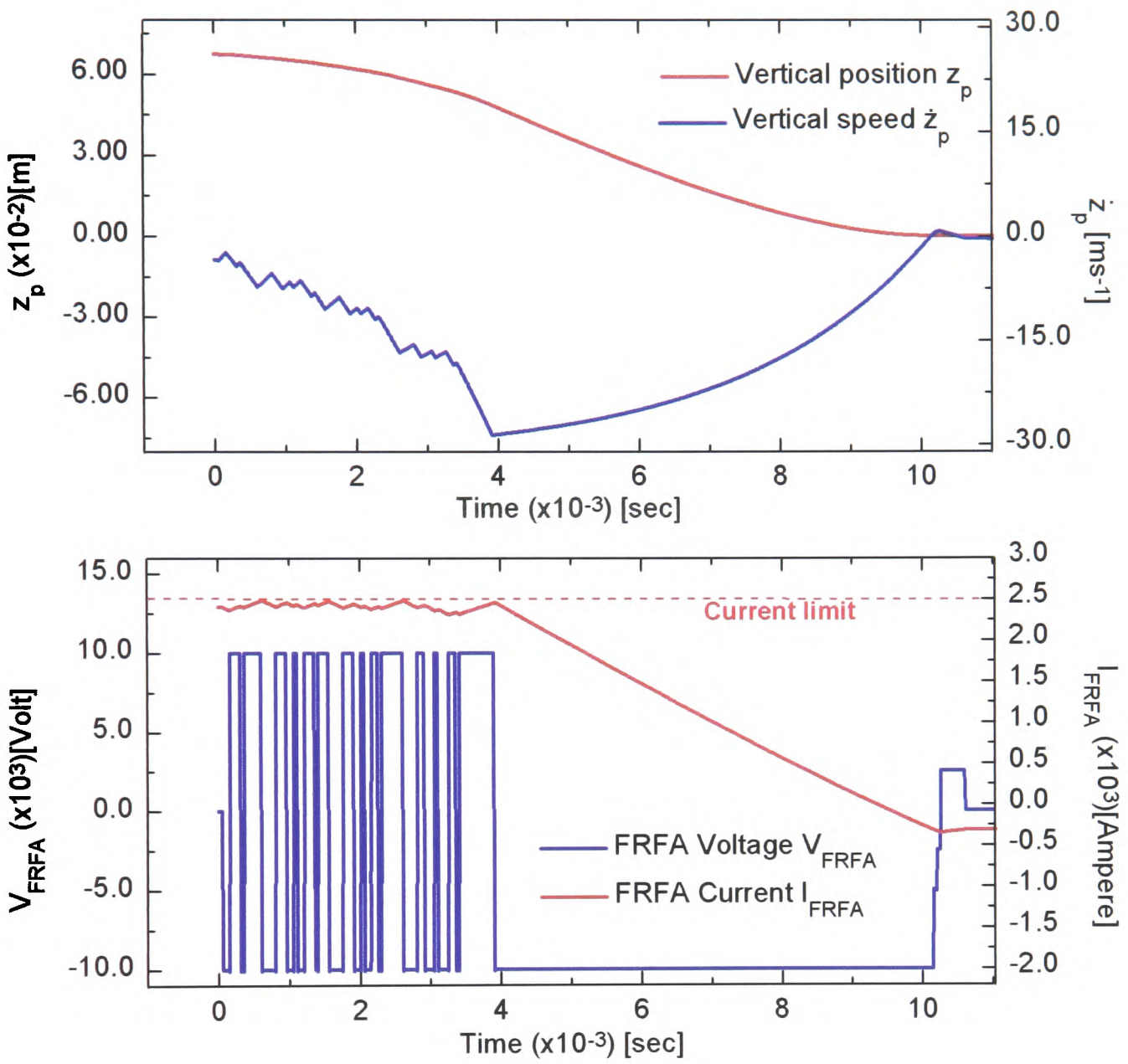


Figure 5.10: Simulation of the JET Tokamak vertical stabilization system using the DANTOC: time evolution of the response to initial conditions close to the FRFA current limit.

At the same time the controller does not slow down the closed loop response. By avoiding the overcurrent trips while controlling the plasma vertical position allows to coordinate a reduction of the plasma current before a disruption occurs. In this way the DANTOC could effectively reduce the effect of disruptions.

5.3.4 Effect of asymmetric plasma configurations having different up/down growth rates

As it has been observed in Section 2.2, in an up/down asymmetric plasma configuration the plasma vertical position has a different up/down growth rate. The response of an up/down asymmetric plasma configuration is examined in the following simulation. During the upward movement the plasma growth rate is $\gamma_p = 1000\,[s^{-1}]$ and during the downward movement is $\gamma_p = 200\,[s^{-1}]$. The recovery from the initial conditions

$$\begin{aligned} z_p &= \pm 0.015\,[m] \\ \dot{z}_p &= \mp 5.0\left[ms^{-1}\right] \end{aligned}$$

is presented in Figure 5.11. The results show that the DANTOC is able to identify the pseudo-sliding boundary locus without prior knowledge of the plant parameter and is robust to the plant parameters variations. It is concluded that the DANTOC can produce minimum time closed loop performance for different plasma growth rates.

5.4 Concluding remarks

The DANTOC has been tested via simulation for the JET Tokamak and the results show the great potential provided by this new controller.

The results of the simulations demonstrate that the DANTOC could be used to control the JET Tokamak plasma vertical position. As shown in Section 5.3.3, additional constraints can be added to the DANTOC algorithm. This has been shown in the case of the FRFA current limit. In fact the DANTOC avoids overcurrent trips while controlling the vertical position movement. In case of an emergency, a reduction of the plasma current could be requested and the effect of an imminent disruption reduced.

The result of the simulations also demonstrate the improvement to the performance resulting from the adaptation strategy and the increased stability range, allowing operation with more elongated plasmas. From the comparison between the DANTOC and the present linear controller it has been demonstrated that the DANTOC performs better therefore it

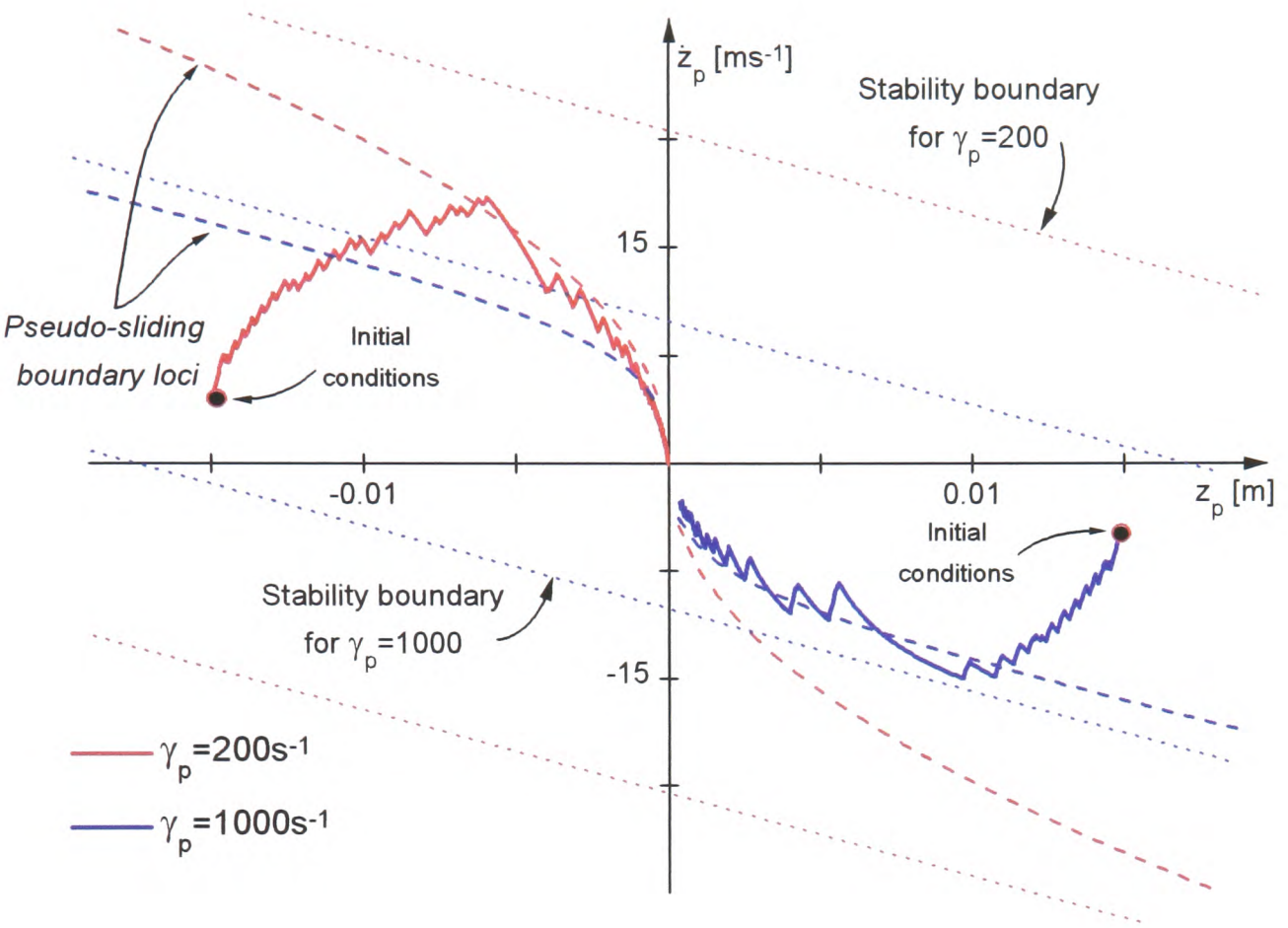


Figure 5.11: Example of the DANTOC with an up/down asymmetric plasma. A different up/down growth rate is used: $\gamma_p = 200s^{-1}$ for a downward movement and $\gamma_p = 1000s^{-1}$ for an upward movement.

is concluded that the DANTOC represents a much better solution than the present linear controller.

Chapter 6

Experimental testing of the controller on the COMPASS-D tokamak

6.1 Introduction

The feasibility of the DANTOC is demonstrated experimentally on a small tokamak (COMPASS-D) which is capable of withstanding high vertical disruptions. In order to make the vertical position control system on COMPASS-D similar to JET some modifications to the former are required. The COMPASS-D standard system configuration, described in Section A.4 of Appendix A, was modified to include a new switched power amplifier and a new digital control system (see schematic diagram in Figure 6.1). The new configuration allows the results to be extrapolated to other tokamaks using switched power supplies, like JET and ITER (for which switched power supplies have been proposed [Zama92]). However there are some differences between the JET and the COMPASS-D control systems that make COMPASS-D more difficult to control. The basic differences are:

- The switched power supply on COMPASS-D has a time delay larger than on JET.
- Growth rates γ_p in COMPASS-D (up to 2500 $[s^{-1}]$) are typically larger than in JET (up to 750 $[s^{-1}]$).
- COMPASS-D is smaller in size than JET and therefore the ratio of vertical position to growth rate γ_p is smaller.

The experiments were first reproduced using a simulation program which includes all of the system components. Using the simulations it is possible to predict the plasma vertical

position and tune the controller parameters. However experiments on the real system are required to test the sensitivity of the controller to parameter changes and to real disturbances, and to confirm the simulation results. Once the results of the simulations have been shown to be consistent with the experimental results it is possible to use the simulations to design new experiments before they are performed.

The experiments presented in this Chapter are divided into five groups:

Section 6.2: Tests to assess the correct hardware/software implementation and control parameter settings.

Section 6.3: Tests to assess the sensitivity of the closed loop behaviour to the choice of the controller parameters.

Section 6.4: Tests to investigate the effect of ELMs disturbances.

Section 6.5: Tests to examine the sensitivity to measurement noise.

Section 6.6: Tests to validate the predicted stability region.

The feasibility of the DANTOC is validated using different plasma configurations and scenarios. The parameters of the DANTOC are fine tuned by changing the algorithm parameters and comparing the experimental data with the simulated data. All the experiments have a Single Null Divertor (SND) plasma configuration which is described in Section A.2 of Appendix A.

The Integral Absolute Error (IAE) performance index and the Total Average Power Dissipation (TAPD) are used to give a quantitative evaluation of the controller performance. The IAE is defined as the integral of the absolute value of the difference between the reference input and the controlled output value. For the plasma vertical position this is defined as

$$P_{IAE} = \frac{1}{T}\int_0^T \left| z_p(t) - z_p^{ref}(t) \right| dt \tag{6.1}$$

and is measured in meters. The TAPD is defined as the sum of the average switching power loss P_s and the average power dissipated when the switching device is closed P_{on} (see Chapter 2 in [Mohan89]). The TAPD is defined as follows:

$$P_T = P_s + P_{on} = \frac{1}{T}\sum_{i=1}^{N_{sw}} \int_0^{T_c} V_{ps}(t)\, I_{ps}(t)\, dt + \frac{1}{T}\sum_{i=1}^{N_{on}} \int_0^{T_{on}} V_{on}(t)\, I_{ps}(t)\, dt \tag{6.2}$$

where T is period of observation, N_{sw} is the number of switches during the period of observation, T_c is the crossover interval (it is assumed for simplicity that the turn-on and the

turn-off crossover interval are the same: for a Gate Turn-Off thyristors (GTO) these are typically $10 \cdot 10^{-6}\,[s]$), V_{ps} is the power supply output voltage, I_{ps} is the power supply output current, $V_{on} \simeq 1\,[V]$ is the voltage drop across the closed GTO, N_{on} is the number of times the power supply output voltage is not zero during the period of observation and T_{on} is the interval when the power supply output voltage is not zero.

Note that z_p^e shown in all the following diagrams is the deviation from the equilibrium position.

6.2 Experimental setup of the COMPASS-D control system

Usually the COMPASS-D vertical position is controlled by an analogue P+D controller and the control signal is sent to a linear power amplifier (FAx) (see Section A.4 of Appendix A). In order to make the vertical position control system on COMPASS-D similar to the one on JET some modifications are required. In particular, the new controller is implemented on

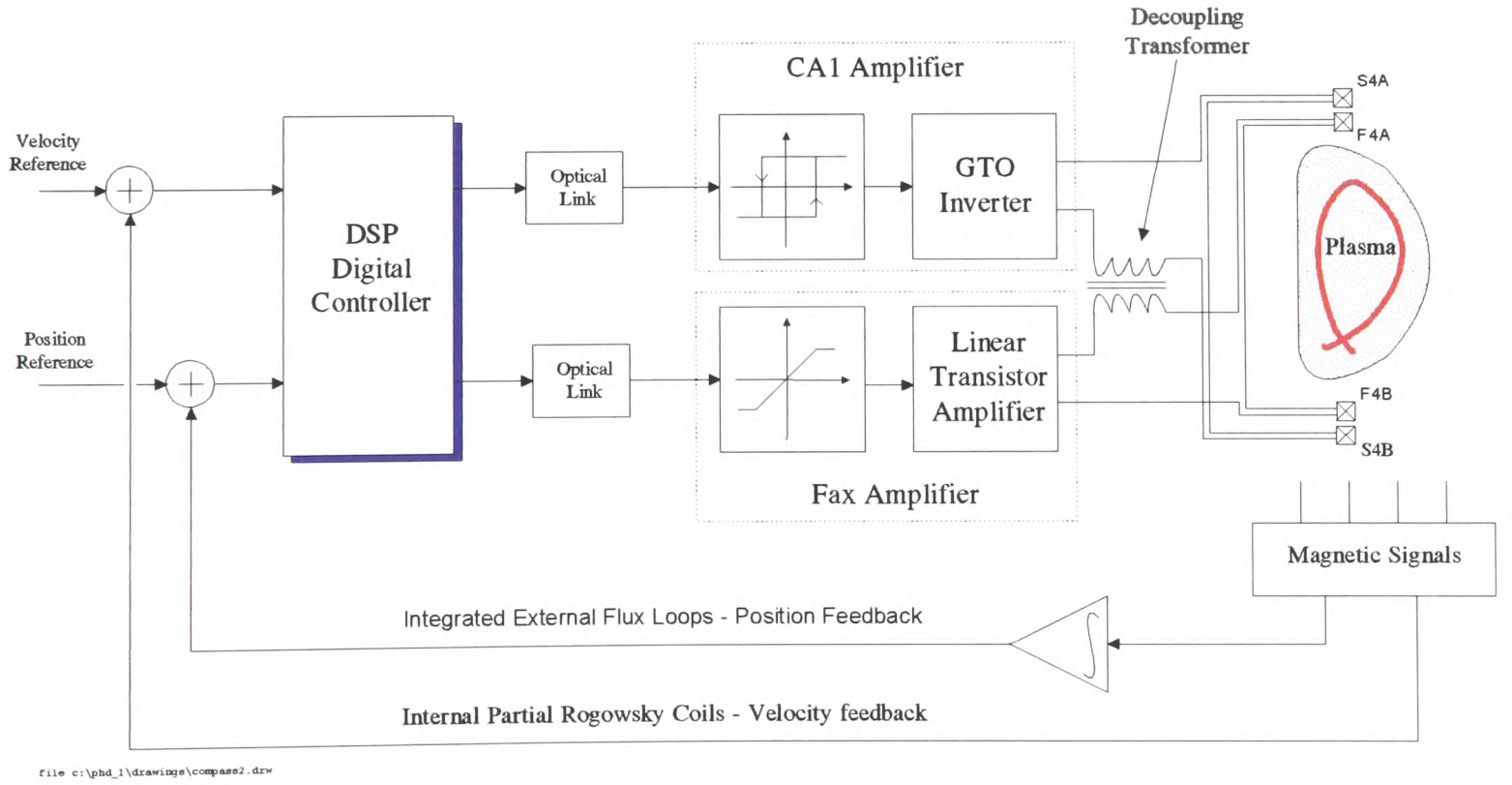


Figure 6.1: Schematic diagram of the COMPASS-D modified vertical position control system.

a Digital Signal Processor (DSP) which drives both the linear power amplifier FAx and a new switched power amplifier (CA1). Figure 6.1 shows a schematic diagram of the modified vertical position control system. The two amplifiers feed two sets of control coils through a decoupling transformer so that the current flowing in one coil will not induce any current in

the other. Experiment #17508 was performed to verify the actual decoupling. A reference voltage waveform drives the CA1 current I_{CA1} flowing into the S4A-S4B coils. The reference voltage for the FAx amplifier is set to zero so that, with a perfect decoupling transformer, there should be no current I_{FAx} induced in the F4A-F4B coils. The result of the experiment is shown in Figure 6.2 and demonstrates good decoupling between the two sets of coils keeping the I_{FAx} current close to zero.

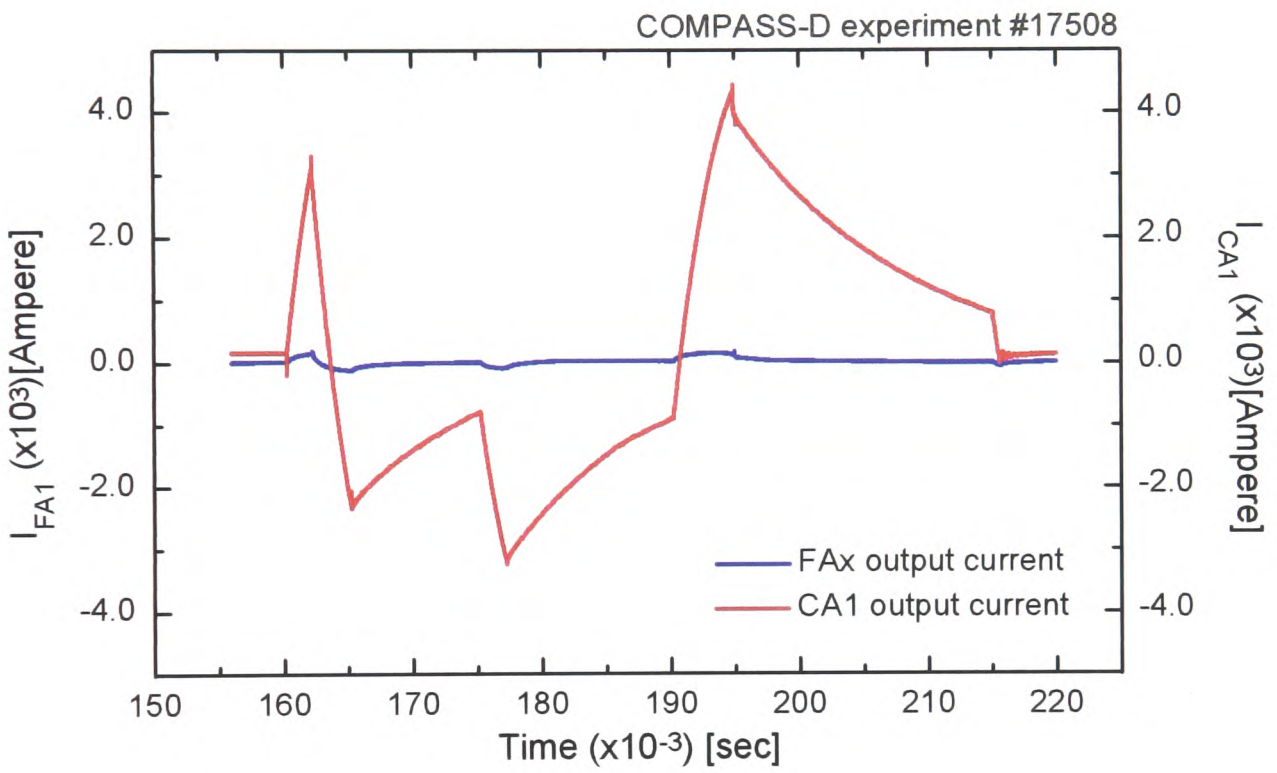


Figure 6.2: FAx - CA1 decoupling shot

The DSP is an *AT&T DSP32C* ($50MHz$, $32-bit$ floating point). There are two ADC input channels, sampled at $80 \cdot 10^3\,[Hz]$ with $16-bit$ resolution, and two DAC output channels with $16-bit$ resolution and $3 \cdot 10^{-6}\,[s]$ settling time. The ADC channels acquire the vertical position and speed feedback error. The DAC channels are used to control the FAx and CA1 amplifiers. Anti-aliasing Bessel filters with a $20 \cdot 10^3\,[Hz]$ bandwidth are used at the input channels. The total delay introduced by the DSP Digital Controller is approximately $30 \cdot 10^{-6}\,[s]$ which is one order of magnitude less than the delay introduced by the CA1 amplifier. The software running on the DSP implements the DANTOC using a discrete time version of COMPASS-D's analogue P+D controller in the inner region.

The use of simulations significantly reduced the time spent checking the correct status of the plant and, in particular, of the measurement system. For example the electrical connections between the digital controller and the amplifiers, the connection of the decoupling

transformer and the correct gains for conversion to engineering units in the DSP program were identified by comparing the simulation results with the experimental results.

The MATLAB package was used to simulate all of the system components including the model of the plasma vertical position derived in Section (2.2), the model for the disturbances derived in Section (2.4), the model of the power supplies derived in Section (2.5) and the control algorithm designed in Section (4.2). Since MATLAB allows 'C' language functions to be included in the simulations, the controller is implemented using the actual DSP software that implements the DANTOC. The simulations are therefore in very good agreement with the experiments. For example, in Figure 6.3 the vertical position/speed trajectory for experiment #18135 is compared to the results obtained from computer simulation.

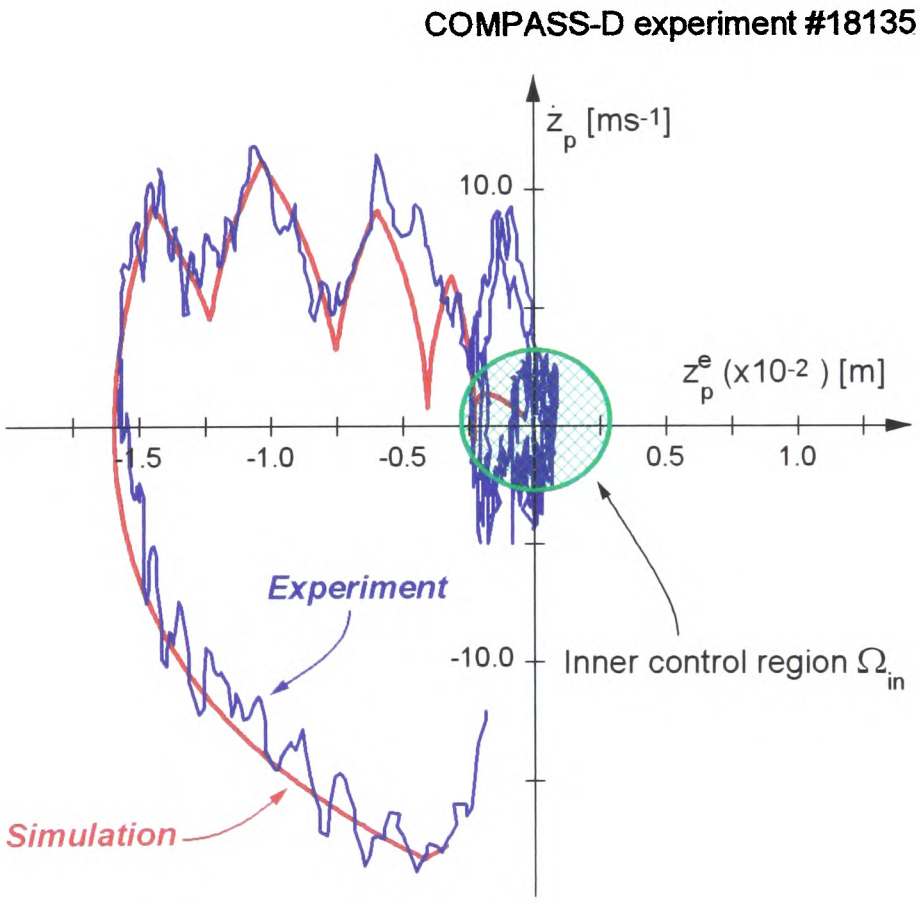


Figure 6.3: Comparison between the simulation results and the experiment #18135.

The simulations were also used to tune the controller parameters. For the inner control region the controller parameters were derived from COMPASS-D's analogue P+D controller and converted into engineering units as follows:

- Inner control region parameters: $P = 566.6\,[m]$ and $D = 0.95\,[ms^{-1}]$.

To tune the other DANTOC parameters a number of simulations were performed varying the parameters and following the criteria given in Sections 4.3.2 and 4.3.1. The following set of parameters was found to be the most suitable for the experiments on COMPASS-D:

$$\begin{aligned} &\bullet \text{ Adaptation rates:} && \epsilon_r = 100 \text{ and } \epsilon_s = 0.01 \\ &\bullet \text{ Adaptation delay:} && \tau_s = 2 \cdot 10^{-3}\,[s] \\ &\bullet \text{ Inner control region:} && \Omega_{in} = \left\{ (z_p, \dot{z}_p) : \frac{z_p^2}{(0.0035)^2} + \frac{\dot{z}_p^2}{(2.235)^2} \leq 1 \right\}. \end{aligned} \tag{6.3}$$

The values of the adaptation rates are calculated using equations (4.32) and (4.33) where the plant parameters where set to $\gamma_p^{\max} = 3000\,[s^{-1}]$, $\gamma_n = 100\,[s^{-1}]$ and $\tau_{tot} = 300 \cdot 10^{-6}\,[s]$, and the iteration step numbers N_r and N_s are both selected as 20, as evaluated from the simulations. The value of $q_r^{\max} \simeq 2000$ is derived from the intersection of the pseudo-sliding boundary locus Σ_r(for $\gamma_p^{\max}$) and Ω_{in}. The values of $q_s^{\max} \simeq 20$ is obtained by substituting the values of $\gamma_p^{\max}$, γ_n, K_1 and τ_{tot} into equation (4.31).

The adaptation delay is set to the duration of the longest observed ELMs, $\tau_{ELM}^{\max} = 2 \cdot 10^{-3}\,[s]$, which is determined by analysis of the COMPASS-D experimental data (see for example Figure 2.8).

A value for the level of measurement noise $\bar{m}_{600}$, which is obtained from experiments, is used to calculate the inner control region. On the COMPASS-D experiments it is observed that $\bar{m}_{600}^{z_p} \simeq 2.5 \cdot 10^{-3}[m]$ and $\bar{m}_{600}^{\dot{z}_p} \simeq 2.0[ms^{-1}]$. Applying the criteria given in Section 4.3.1 the inner control region is given by

$$\sqrt{\frac{z_p^2}{t_{11}^2} + \frac{\dot{z}_p^2}{t_{22}^2}} \leq \frac{u_o}{\rho \cdot \max(t_{11}, t_{22}) \cdot \sqrt{(P^2 + D^2)\,K_a^2}}$$

where $u_o = 60$, $K_a = 57.6\,[V]$, $t_{11} = 5 \cdot 10^{-6}$, $t_{22} = 2$ and $\rho = 558.1$ which is simplified into the inner control region of the standard set.

6.3 Tests to assess the sensitivity of the closed loop behaviour to the choice of the DANTOC parameters.

The aim of these tests is to assess the sensitivity of the closed loop behaviour to the choice of the DANTOC parameters. The tests have been performed to examine the following changes to the control parameters:

- Varying the adaptation rates (§ Section 6.3.1).
- Reducing the size of the inner control region (§ Section 6.3.2).
- Removing the resetting conditions (§ Section 6.3.3).

6.3.1 Varying the adaptation rates

The aim of these experiments is to show how the choice of the adaptation rates affects the closed loop system dynamics and the operation of the CA1 amplifier.

Three tests are executed where the vertical position reference signal z_p^{ref} is obtained by superimposing a sequence of five pulses of $1 \cdot 10^{-3}\,[s]$ duration and increasing amplitude ($0.8 \cdot 10^{-2}\,[m]$, $1.2 \cdot 10^{-2}\,[m]$, $1.6 \cdot 10^{-2}\,[m]$, $2.0 \cdot 10^{-2}\,[m]$ and $2.4 \cdot 10^{-2}\,[m]$ one every $10 \cdot 10^{-3}\,[s]$) on a position reference waveform with a constant value. The pulses produce a large plasma vertical displacement and make the adaptation control start. Experiment #18136 is executed using the standard set of DANTOC parameters given in equation (6.3); for experiment #18546, the adaptation rates are increased to $\epsilon_r = 300$ and $\epsilon_s = 0.03$, and, for experiment #18314, they are decreased to $\epsilon_r = 30$ and $\epsilon_s = 3 \cdot 10^{-3}$. The adaptation rates ($\epsilon_r$ and ϵ_s) are inversely proportional to the number of iterations (N_r and N_s) required to converge to the pseudo-sliding boundary locus (§ Section 4.3.2). Thus, when decreasing the adaptation rates, the number of iterations and, therefore, the switching activity of the CA1 amplifier increases as shown in Figure 6.4. The plasma vertical position is shown in Figure 6.5 for the three experiments. As expected increasing the adaptation rates results in faster closed loop dynamics and the IAE decreases ($P_{IAE}^{\#18546} = 2.7 \cdot 10^4\,[m]$, $P_{IAE}^{\#18136} = 3.2 \cdot 10^4\,[m]$ and $P_{IAE}^{\#18314} = 4.6 \cdot 10^4\,[m]$). The calculated TADP ($P_T^{\#18546} = 514\,[W]$, $P_T^{\#18136} = 825\,[W]$ and $P_T^{\#18314} = 1260\,[W]$) indicates that, if the adaptation rates are too small, the switching of the amplifier and, therefore the power dissipation, increases. On the other hand, if the adaptation rates are too high, the switching hyperplanes can move outside of the region

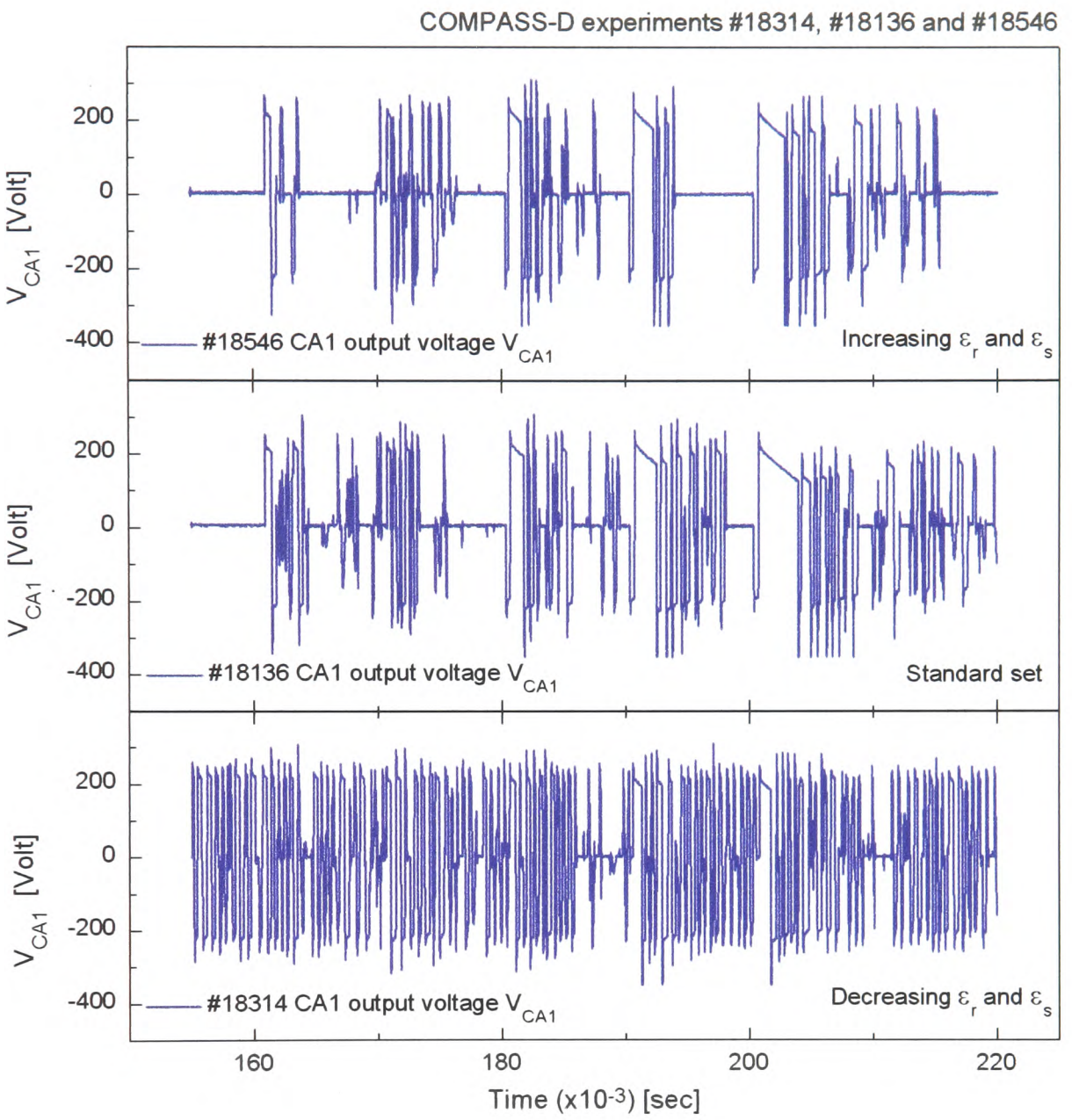


Figure 6.4: Experiments executed varying the adaptation rates: CA1 output voltage.

Ω_{max}. In practice, it may be necessary to fine tune the adaptation rates found in simulations. However the experimental results confirm that the original choice is appropriate in the case of COMPASS-D.

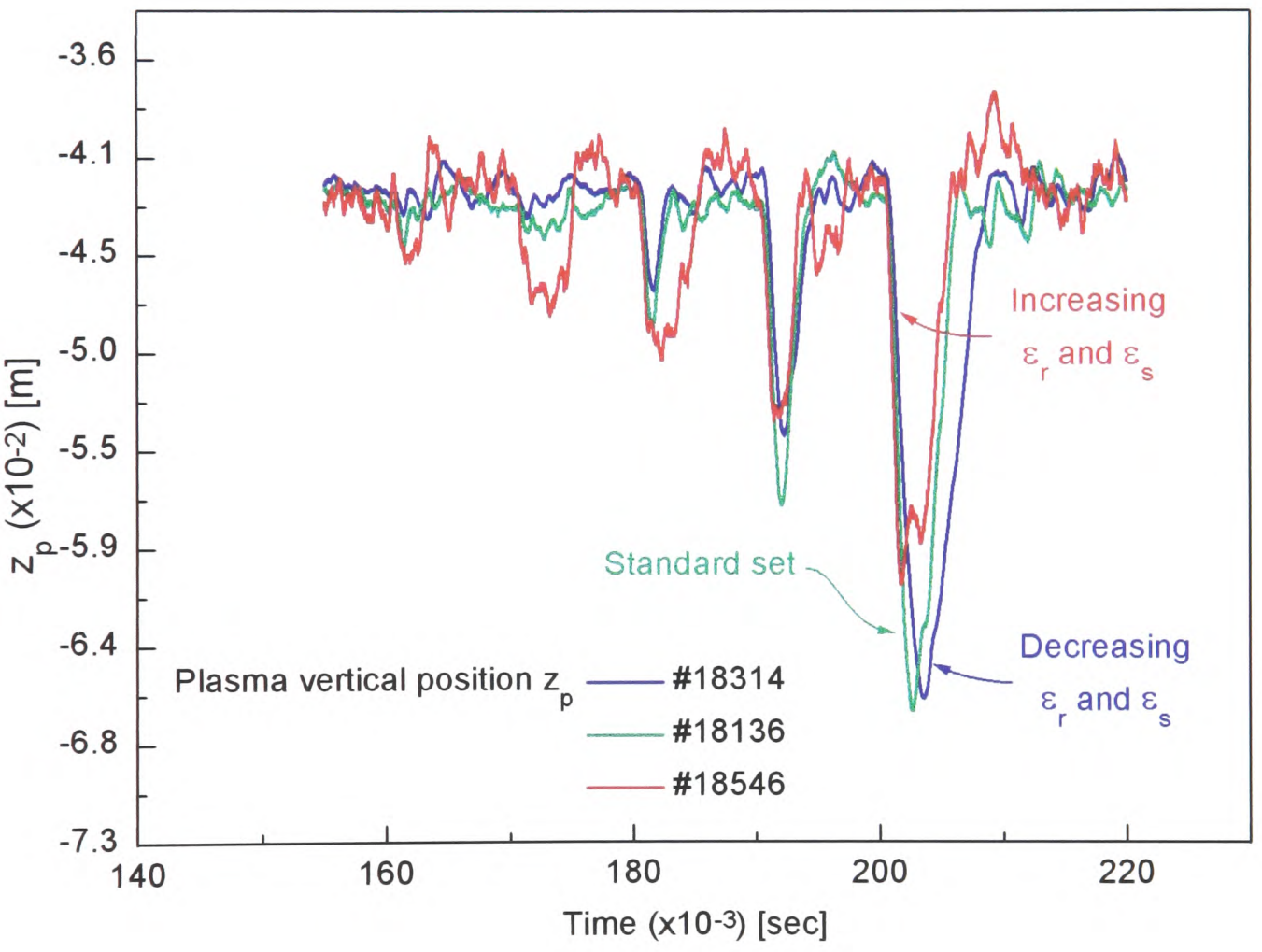


Figure 6.5: Experiments executed varying the adaptation rates: plasma vertical position z_p.

6.3.2 Reducing the size of the inner control region

The aim of the experiment is to test the sensitivity of the controller behaviour to the selection of the inner control region as a function of the $\bar{m}_{600}$ parameter. Two experiments (#17497 and #17500) with similar plasma current and elongation are performed. In both cases Ω_{in} is determined following the criteria described in Section 4.3.1. In the former $\bar{m}_{600}$ was estimated from previous experiments to be $2.5 \cdot 10^{-3}\,[m]$ (as for standard set (6.3)) while in the latter it is chosen equal to $1.7 \cdot 10^{-3}\,[m]$, that is lower than the actual measurement noise level. The resulting controller behaviours are compared by examining the phase-plane plots of the plasma vertical position/speed shown in Figure 6.6. After recovering from the perturbing

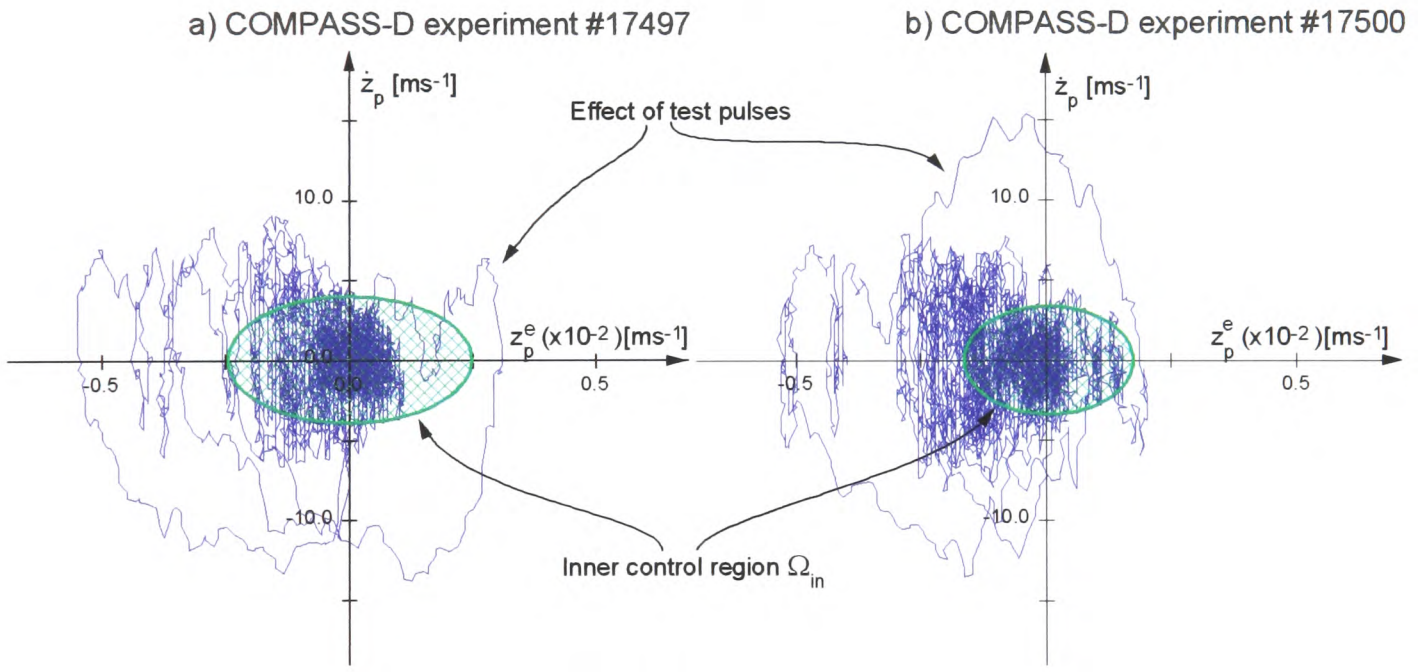


Figure 6.6: Phase-plane plot of the control response: a) using the correct estimate of $\bar{m}_{600}$, b) decreasing the estimate of $\bar{m}_{600}$ below the measurement noise level.

pulses, the state trajectory for experiment #17497 remains inside the inner region. For experiment #17500 the state spends more time outside the inner region, even when no test pulse is applied. As a consequence, the CA1 switching activity, shown in Figure 6.7, increases and so does the TADP ($P_T^{\#17497} = 820\,[W]$ and $P_T^{\#17500} = 1102\,[W]$). Another disadvantage is that the ELM's measurement noise rejection performance is reduced, as indicated by the IAE ($P_{IAE}^{\#17497} = 5.4 \cdot 10^3\,[m]$ and $P_{IAE}^{\#17500} = 6.8 \cdot 10^3\,[m]$), because the DANTOC is constantly enabled and the adaptation delay time may have elapsed. The results confirm that the system performance deteriorates when the selected $\bar{m}_{600}$ is lower than the measurement noise level.

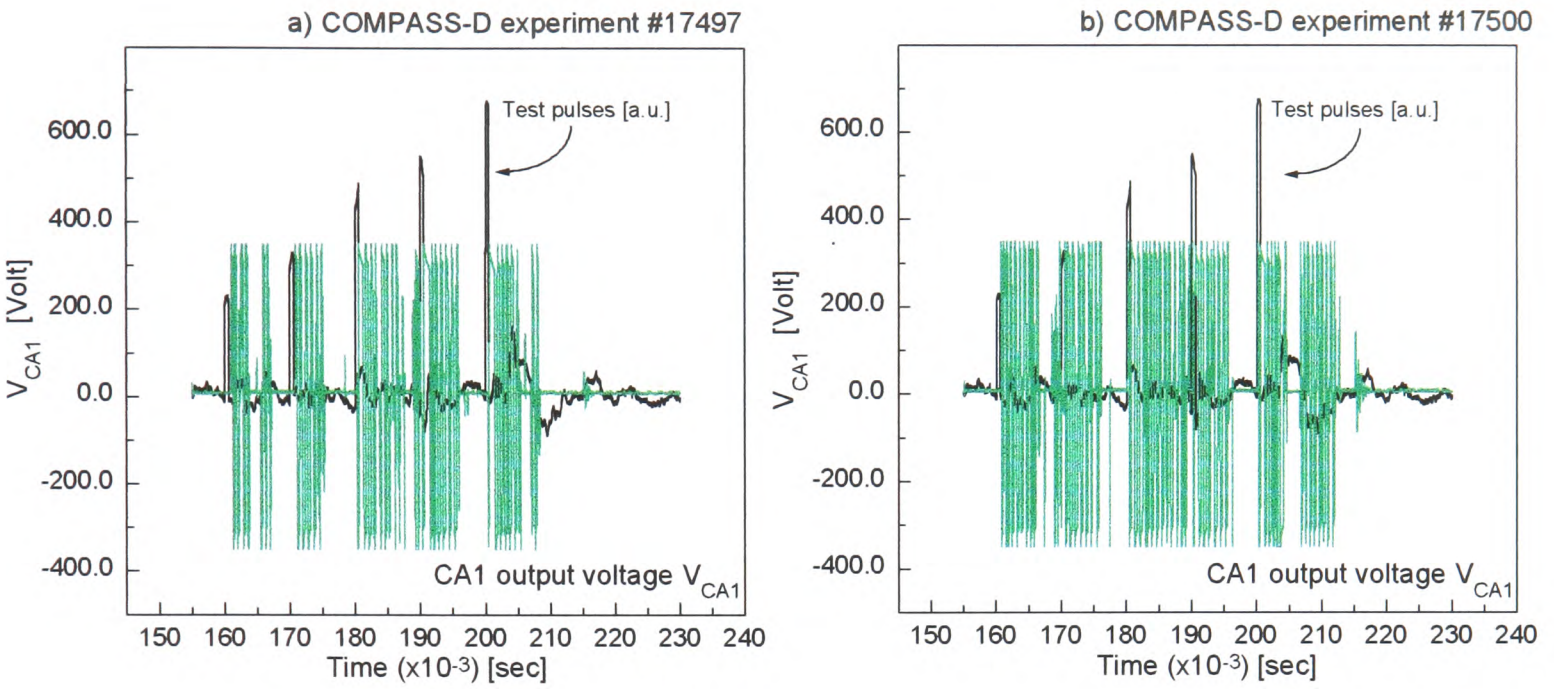


Figure 6.7: CA1 output voltage: a) using the correct estimate of $\bar{m}_{600}$, b) decreasing the estimate of $\bar{m}_{600}$ below the measurement noise level.

A comparison with a higher $\bar{m}_{600}$ could not be carried out because in this case the linear amplifier output voltage would have saturated.

6.3.3 Removing the resetting conditions

The aim of this experiment is to demonstrate that the resetting conditions defined in Section 4.2.3.1 are essential to ensure that the DANTOC is robust to plasma parameter variations and external disturbances, and to improve its performance.

The effect of eliminating the resetting conditions is examined by comparing experiment #18136 to experiment #18511. The former is performed using the standard set of DANTOC parameters given in equation (6.3) while the resetting conditions are removed in experiment #18511. In both experiments the vertical position reference signal described in Section 6.3.1 is used. The plasma vertical position and phase plane diagram for the two experiments are shown in Figure 6.8. Both experiments start from equilibrium conditions inside the inner region. When the first pulse pushes the trajectory outside Ω_{in}, the switching hyperplanes are updated in the same way. However, while the adaptation is always restarted from the initial switching hyperplanes with the resetting conditions , when the resetting conditions are removed, the adaptation re-starts from the switching hyperplanes prior to the state re-entering Ω_{in}. Thus the control is very poor and the plasma vertical position overshoots for the

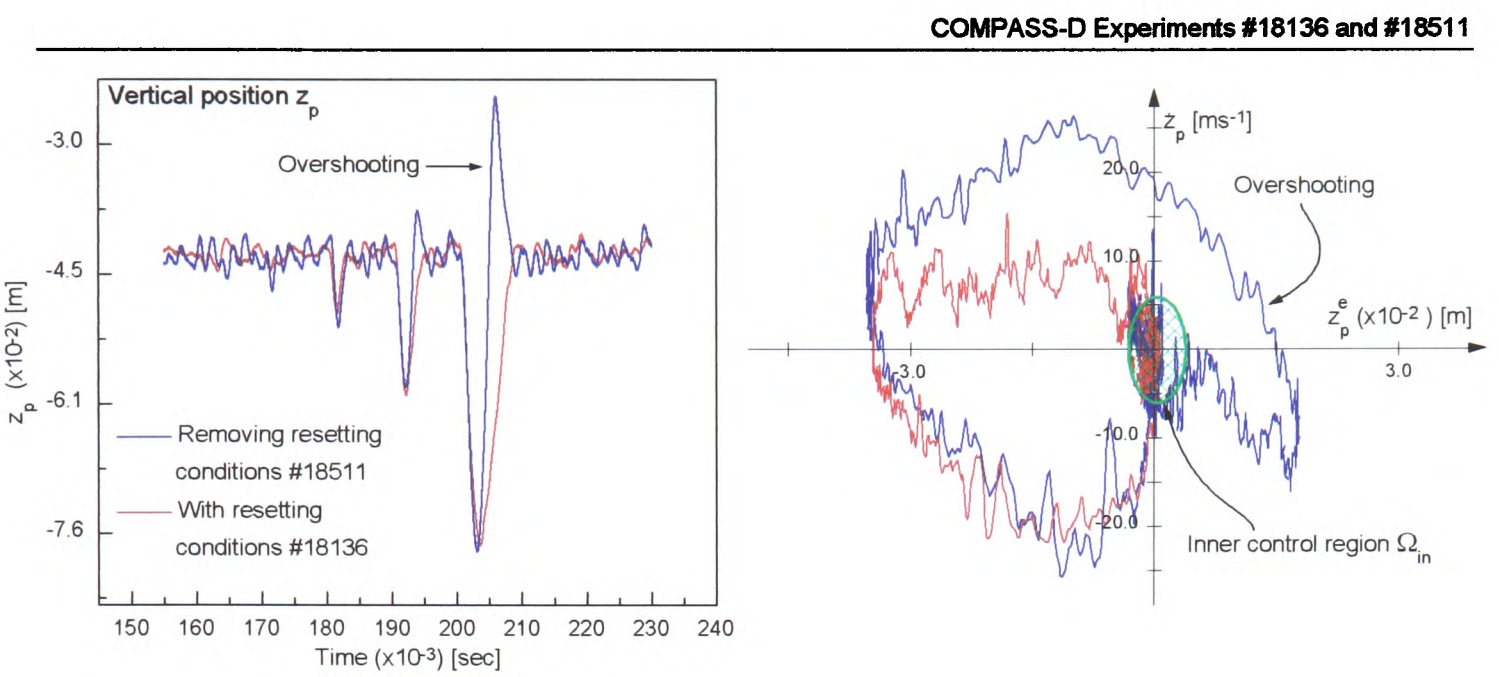


Figure 6.8: Experiment with no resetting conditions. Comparing the COMPASS-D experiments #18136 and #18511.

last two pulses. Furthermore, if the plasma characteristics change between two adaptation phases and, in particular, the elongation increases, the switching hyperplanes may move outside the region Ω_{max} and the control could be lost. It is concluded that the resetting conditions are necessary to make the controller robust to both plasma parameter variations and disturbances, as well as to improve the closed loop performance.

6.3.3.1 Effect of a reduction in the growth rate when removing the resetting conditions

The experiment #18509 is similar to #18511, except that the last two pulses on the position reference signal have been increased in amplitude. As happened during experiment #18511, the plasma position overshoots the desired position after the fourth pulse occurs (see Figure 6.9). However, due to the increased pulse amplitude, in this case the plasma does not recover before the last pulse is applied. The plasma vertical position is plotted against the time on the left hand side of Figure 6.9. The phase plane diagram is displayed on the right hand side. The black arrows represents the trajectory followed by the plasma after the 4^{th} pulse and the red arrows after the last. As a consequence of no resetting conditions, the plasma is bounced

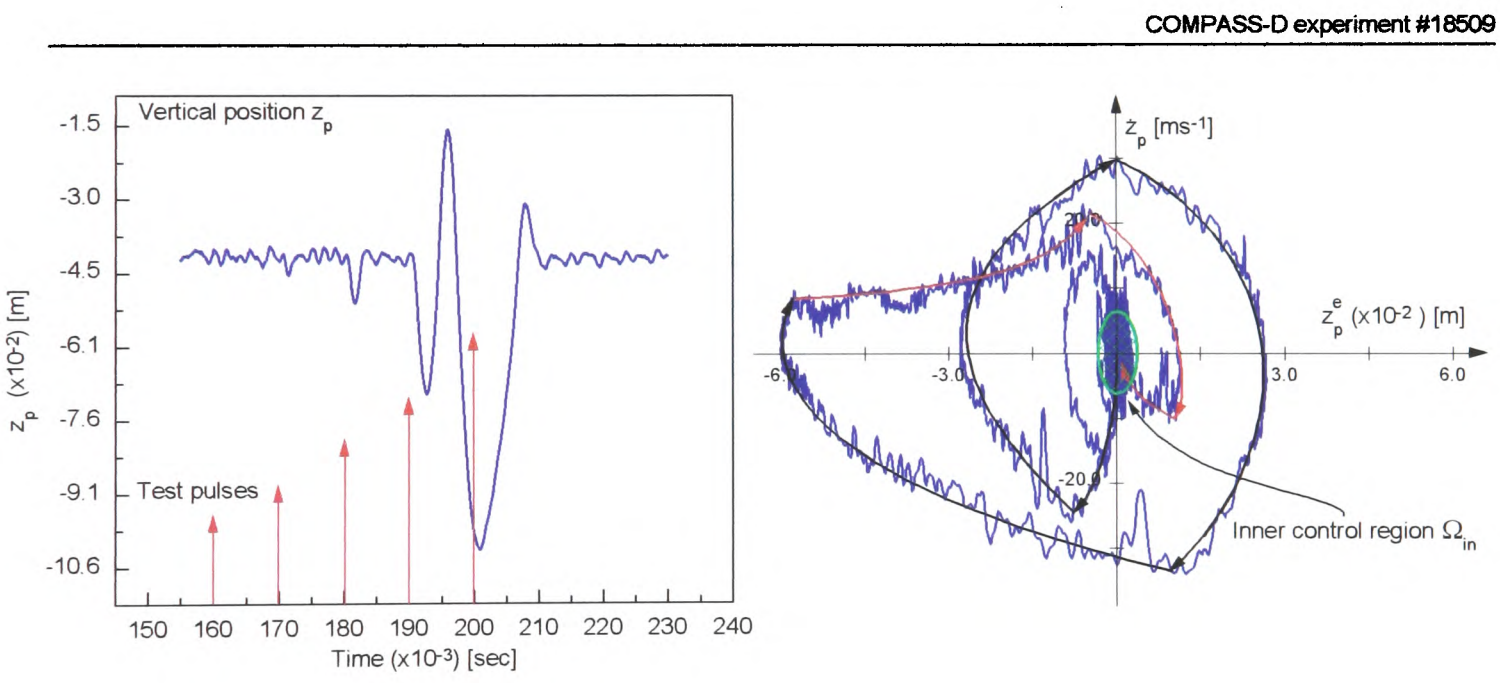


Figure 6.9: COMPASS-D experiment #18509 with no resetting conditions.

up and down in the vacuum vessel and the plasma growth rate γ_p decreases as indicated by the changes in the plasma shape shown in the plasma boundary reconstructions (Figure 6.10). Despite the large vertical excursion, control is not lost and the reference vertical position is restored. In fact , since $\Omega_{\mathbf{max}}|_{t>0.195} \subset \Omega_{\mathbf{max}}|_{t<0.195}$, the switching hyperplanes identified on the initial elongation will always be inside the region $\Omega_{\mathbf{max}}$. This shows that the controller is a maximum stabilizer with respect to a reduction in the growth rate (it satisfies the conditions of the Corollary 3.2.5).

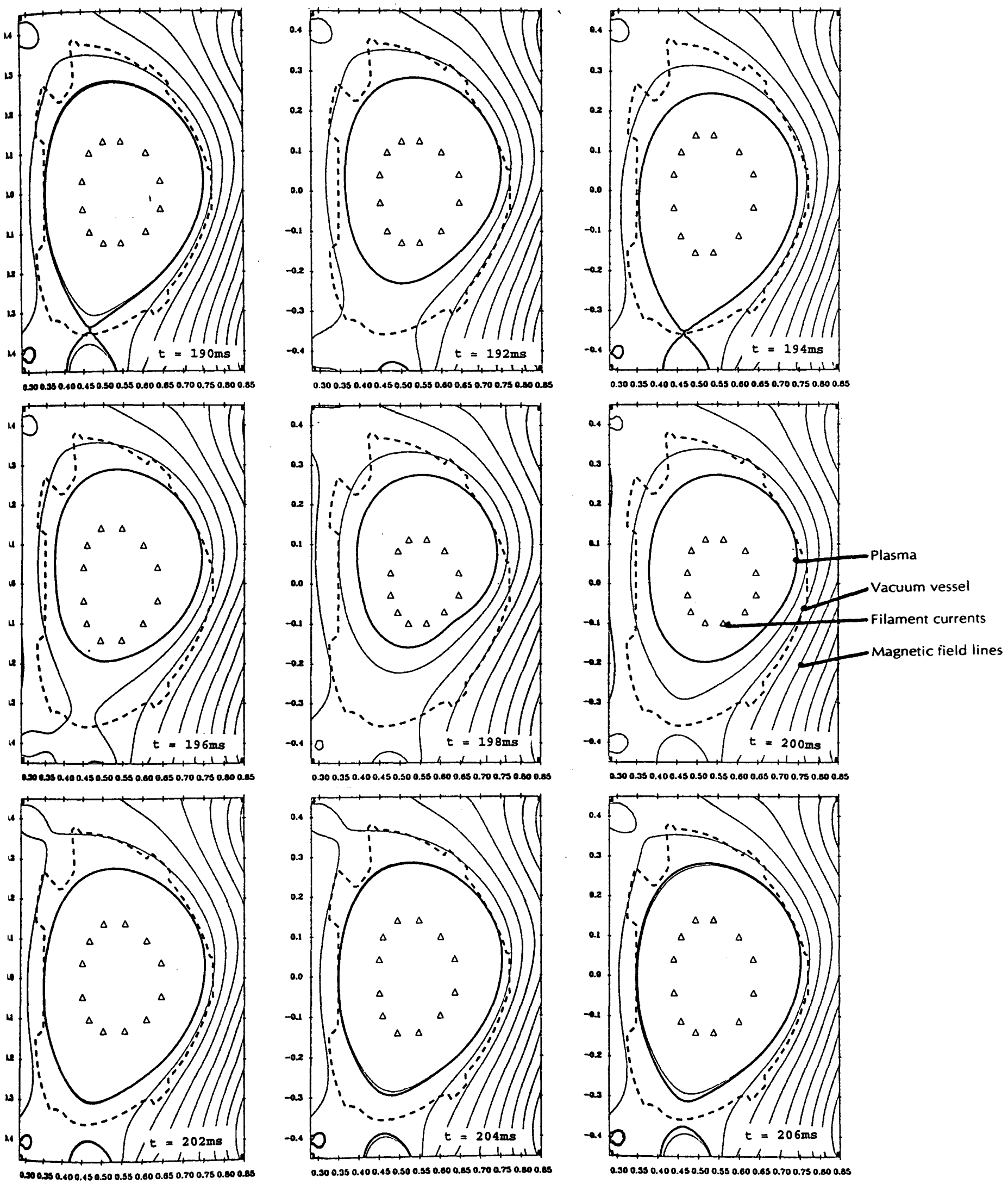


Figure 6.10: Plasma boundary reconstructions for experiment #18509

6.4 Tests to investigate the effect of ELMs on the plasma vertical position when using the DANTOC.

The aim of these tests is to investigate the effect of ELMs on the plasma vertical position when using the DANTOC. ELMs can sometimes trigger vertical instabilities. During a Vertical Displacement Event (VDE) the interaction between the plasma and the vacuum vessel generates electromagnetic forces which can be quite large in large tokamaks like JET [Noll89]. One way of reducing the effect of a VDE would be to counteract the plasma vertical displacement for as long as possible while the plasma current is reduced.

In order to generate ELMs, H-mode plasma configurations are used (see Section A.2 of Appendix A). In these experiments the plasma current is $I_p = 170 \cdot 10^3\,[A]$ and the growth rate $\gamma_p \simeq 2000\,[s^{-1}]$. The plasma vertical position reference signal is kept constant for all the above experiments. The comparison between different experiments is only qualitative because it is not possible to reproduce the same ELMs for different experiments.

6.4.1 The DANTOC behaviour in the presence of ELMs.

The aim of the test is to demonstrate the DANTOC's ability to control the plasma vertical position in the presence of ELMs. The DANTOC's standard set of parameters given in (6.3) is used. In experiment #17724 (Figure 6.11, H_α trace), after the L-H transition (see Section A.2 of Appendix A) at about $0.165\,[s]$ there is a sequence of large isolated ELMs until $0.196\,[s]$, followed by an ELM free period of $20 \cdot 10^{-3}\,[s]$ and a series of ELMs that have a large effect on the plasma vertical position z_p. Although the perturbation to the plasma vertical position is very small during the first sequence of ELMs, the induced noise alters the measured plasma speed in such a way that the controller could cause a large displacement in the plasma position. With the adaptation delay, the intervention of the controller is minimal demonstrating the virtue of the DANTOC in the case of small perturbations to the plasma position, as shown in Figure 6.11. The ELMs following the ELM free period result in a significant vertical position excursion. As shown in Figure 6.11 the results demonstrate that the DANTOC is able to maintain control in situations which have previously caused problems in JET and COMPASS-D [Morris95] [Ali-Arshad96]. In this experiment the value of the IAE is $P_{IAE}^{\#17724} = 8.18 \cdot 10^3\,[m]$.

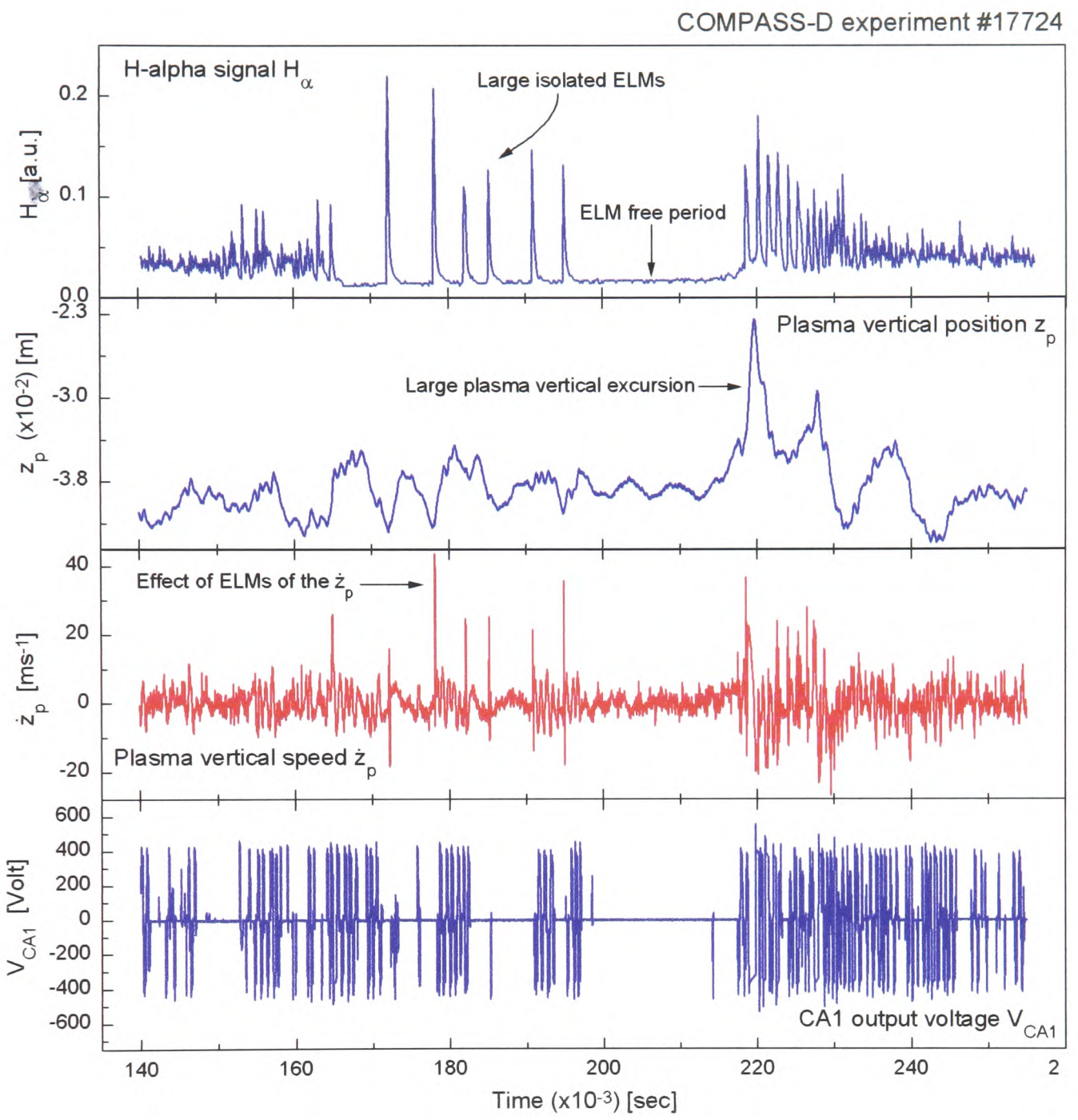


Figure 6.11: The effect of ELMs when the set of tuned DANTOC parameters is used.

6.4.2 Effect of increasing the adaptation delay

The aim of this test is to show how increasing the adaptation delay affects the controller performance in the presence of ELMs. In experiment #18537 the adaptation delay is increased from $\tau_s = 2 \cdot 10^{-3}\,[s]$ to $\tau_s = 5 \cdot 10^{-3}\,[s]$. The closed loop response slows down and therefore the effect of the measurement noise caused by an ELM is reduced. A drawback of increasing the adaptation delay is that, if the ELMs' amplitude is large and the repetition rate is too high, the plasma vertical displacement can gradually increase leading to a loss of control. It is difficult to show from the results that there are occasions when the effect of ELMs on the plasma vertical displacement is cumulative (see Figure 6.12). However in this experiment the

value of the IAE is $P_{IAE}^{\#18537} = 1.26 \cdot 10^4\,[m]$ indicating a decrease in performance compared to the previous experiment described in Section 6.4.1 where $\tau_s = 2 \cdot 10^{-3}\,[s]$.

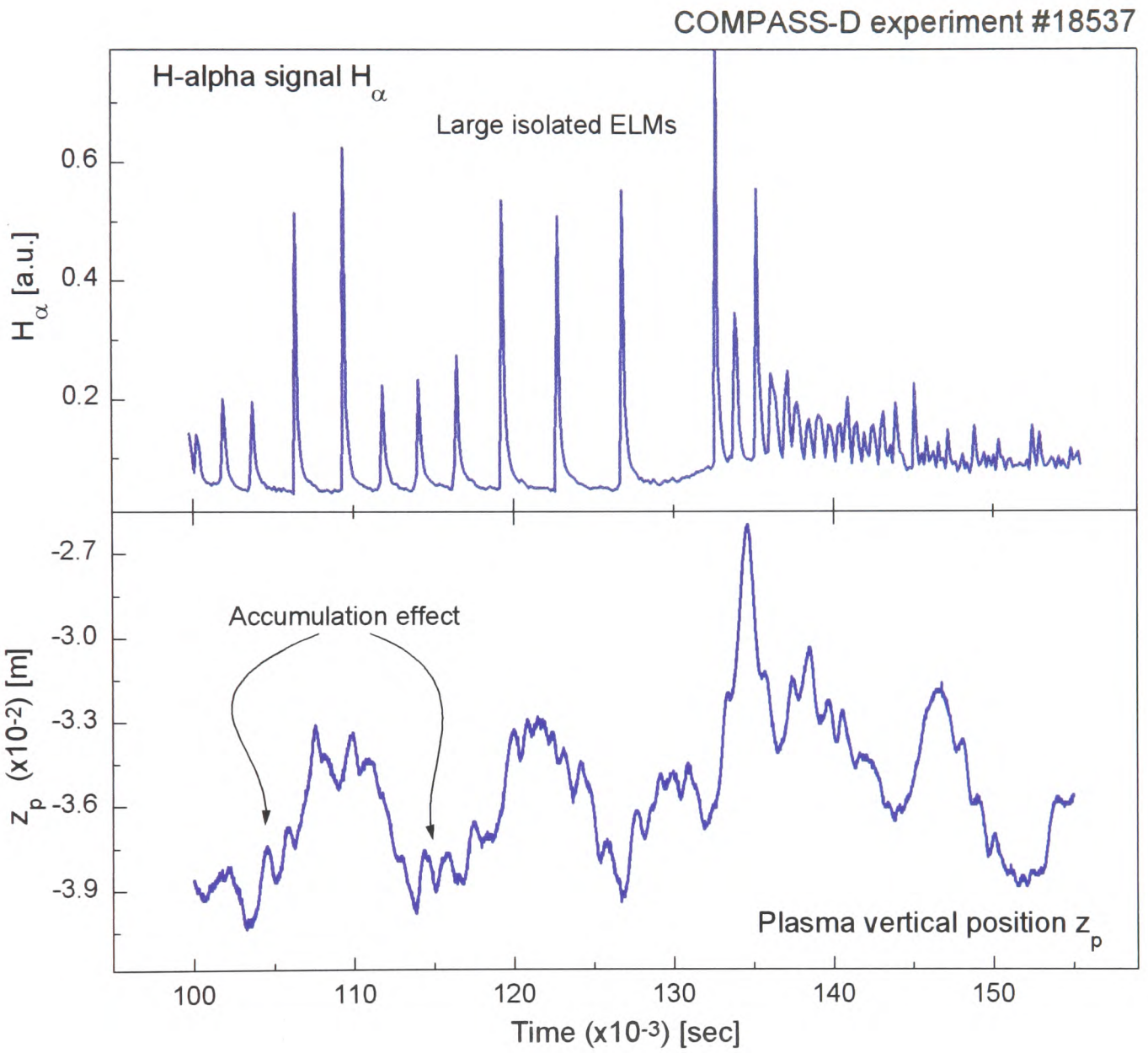


Figure 6.12: Effect of increasing the adaptation delay.

6.4.3 Effect of decreasing the adaptation delay

The aim of this test is to illustrate the effect of decreasing the adaptation delay on the controller performance in the presence of ELMs. In experiment #18531 there is no adaptation delay $\tau_s = 0$. The effect of decreasing the adaptation delay is to speed-up the closed loop response since the controller tries to eliminate displacements in the plasma position as fast as possible. However, if an ELM does not actually effect the plasma vertical position but only induces measurement noise, the controller will displace the plasma from its equilibrium position when action is not required (see Figure 6.13). The value of the IAE: $P_{IAE}^{\#18531} = 1.07 \cdot 10^4\,[m]$ is lower than for the case of increased adaptation delay, but higher than the IAE for the experiment where the adaptation delay is set to the correct value, as in Section 6.4.1. The results suggest that the adaptation delay plays a key role in rejecting the noise generated by the ELMs.

The results also show that the DANTOC operates correctly when the plasma configuration undergoes to an L to H-mode transition (around $0.110\,[s]$ in this experiment) and the equilibrium position of the plasma changes.

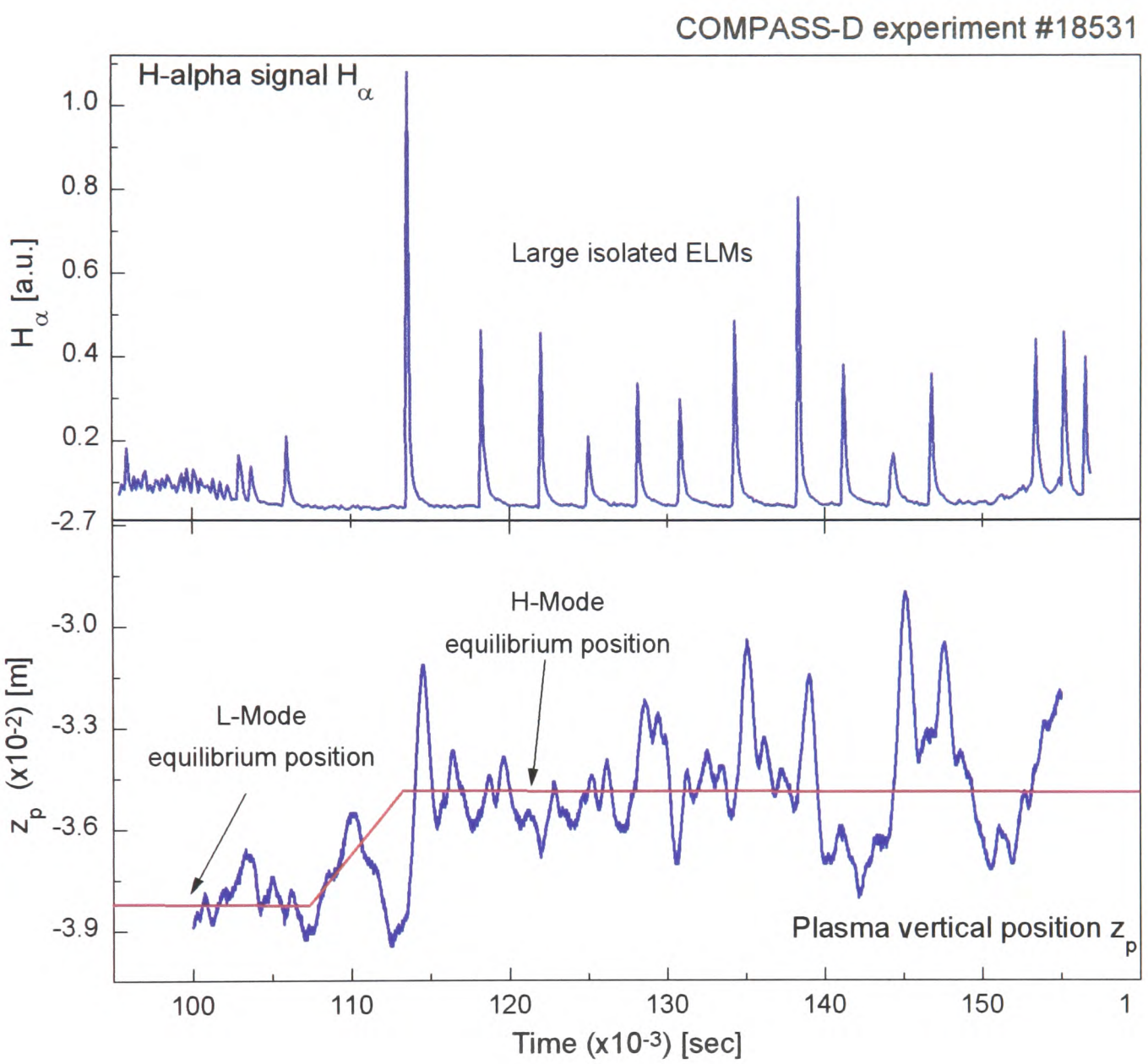


Figure 6.13: Effect of decreasing the adaptation delay.

6.4.4 Fixing the switching hyperplanes

The aim of the test is to investigate the effect of fixing the switching hyperplanes. The stability region and the performance are fixed if the switching hyperplanes remain unchanged (see Section 4.2). This may be desirable when the plant parameters do not vary but it could cause problems otherwise. In experiment #18541 the hyperplanes are fixed at values derived from the minimum time switching line for $\gamma_p = 2000\,[s^{-1}]$. In experiment #18542 the hyperplanes are updated by the DANTOC with the standard parameter set given in equation (6.3). The plasma vertical position z_p for the two experiments is shown in Figure 6.14 . The plasma position displacement due to ELMs is smaller during the experiment #18542, when there are larger ELMs, indicating that the DANTOC has a better noise and disturbance rejection capability. This observation is supported by the fact that the IAE for the second

experiment has a smaller value: $P_{IAE}^{\#18542} = 1.06 \cdot 10^4\,[m]$ and $P_{IAE}^{\#18541} = 1.32 \cdot 10^4\,[m]$.

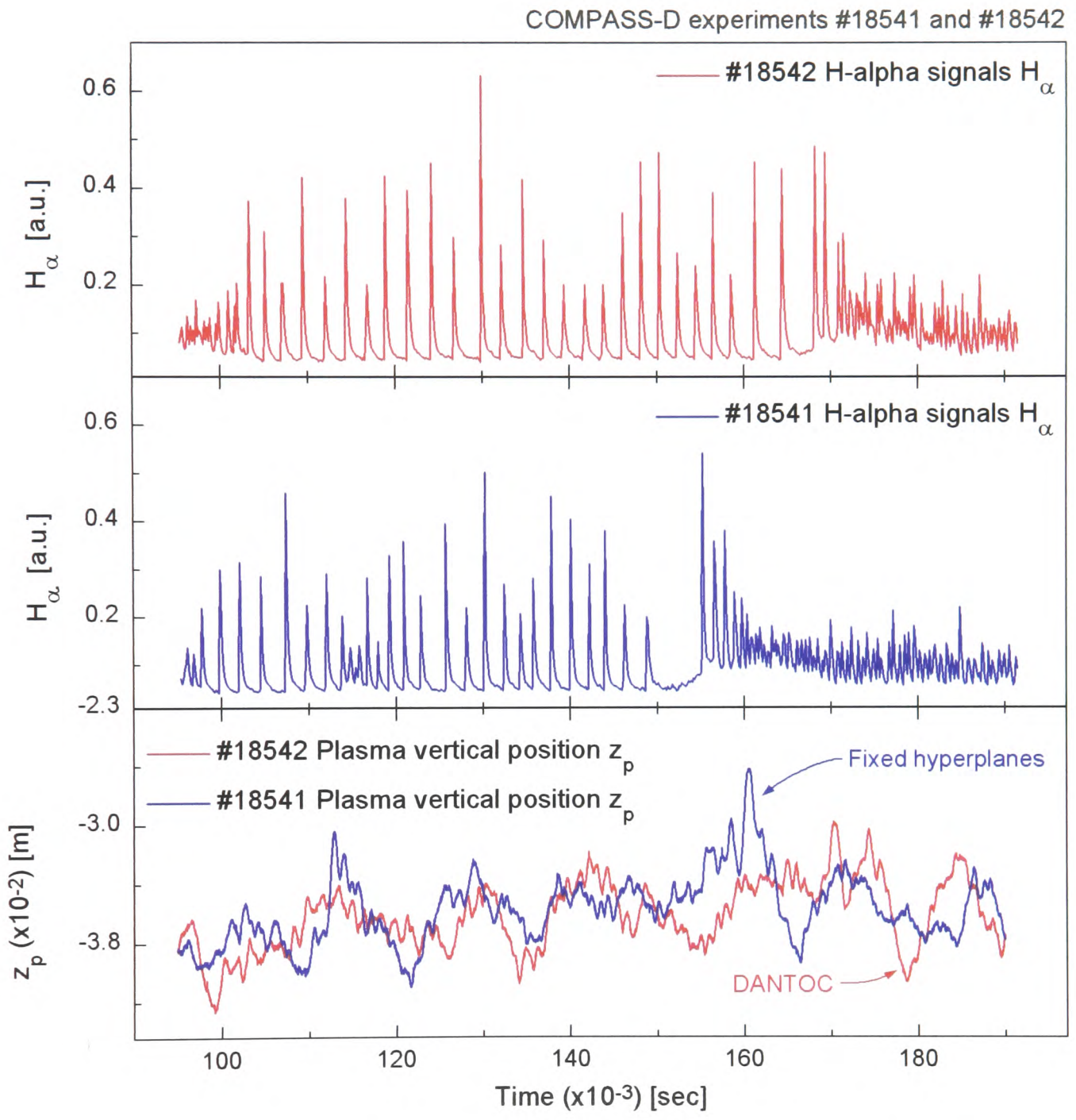


Figure 6.14: Experiment fixing the switching hyperplane.

6.5 Tests to examine the sensitivity to measurement noise.

The aim of these tests is to demonstrate that the DANTOC is able to reject the measurement noise caused by ELMs. During fusion experiments, the plasma vertical position reference signal has a slow rate of change ($\sim 0.5\,[ms^{-1}]$). It has been observed that the disturbances caused by ELMs results in spikes on the speed measurements (see Section 2.6.3). In the following experiments these disturbances are emulated by a sequence of short pulses added to the reference position signal. The use of known perturbations on the position reference signal allows systematic analysis because of the reproducibility of the experiments, which is very difficult in the case of real random perturbations. The tests are performed by introducing five short pulses every $10 \cdot 10^{-3}\,[s]$ of $500 \cdot 10^{-6}\,[s]$ duration and increasing amplitude and comparing the response of these perturbations when using the DANTOC and the standard analogue controller. Ideally with a perfect noise rejection the plasma vertical position should not deviate from the unperturbed set point. The DANTOC is used in experiment #17496 and the standard analogue controller in experiment #17479. The plasma current is $143{\cdot}10^3\,[A]$ and the growth rate $\gamma_p \simeq 1000\ [s^{-1}]$ in both of these cases. In these experiments the amplitude of the test pulses is set to $0.15 \cdot 10^{-2}\,[m]$, $0.3 \cdot 10^{-2}\,[m]$, $0.45 \cdot 10^{-2}\,[m]$, $0.6 \cdot 10^{-2}\,[m]$ and $0.75 \cdot 10^{-2}\,[m]$ respectively. The plasma vertical position and the plasma vertical position reference are shown in Figure 6.15. It is clear that the vertical position is less affected by the perturbation when the DANTOC is used. Indeed, the IAEs for the two experiments are

$$P_{IAE}^{\#17496} = 4.03 \cdot 10^3\,[m] \text{ and } P_{IAE}^{\#17479} = 6.70 \cdot 10^3\,[m]$$

indicate a net improvement in the noise rejection when the DANTOC is used.

The results confirm the DANTOC reduces the sensitivity to the measurement noise generated by ELMs with respect to the COMPASS-D linear analogue controller.

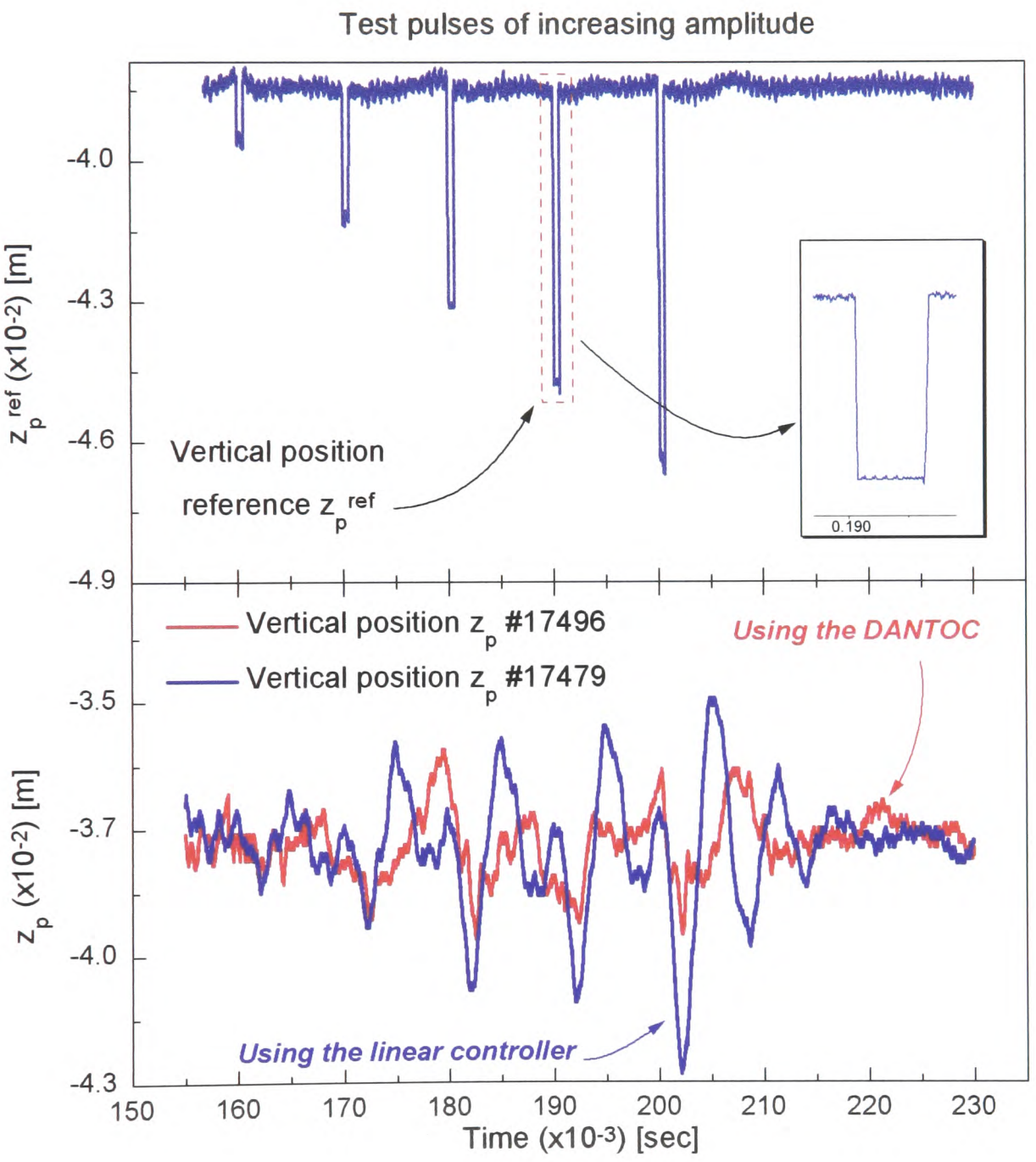


Figure 6.15: Comparison between the DANTOC (#17496) and the COMPASS-D's linear analogue controller (#17479).

6.6 Tests to validate the predicted stability region

The aim of this test is to validate the predicted stability regions $\Omega_{\max}$ and Ω_{sl} calculated using Theorem 3.2.2 and the results in Section 3.3.3. Two sets of experiments are performed.

In the first set (experiments #17480 and #17497) the amplitude of the test pulses used in the previous tests (see Section 6.5) is increased. The DANTOC is used in experiment #17497 and the standard analogue controller in experiment #17480. The plasma current is $143 \cdot 10^3\,[A]$ and the growth rate $\gamma_p \simeq 1000\,[s^{-1}]$ in both cases. The results from the experiments are presented in Figure 6.16. It can be seen that for a sufficiently large pulse the analogue controller loses control, while the DANTOC is still able to control the plasma vertical position by avoiding excursion outside the region $\Omega_{\max}$. This is a clear demonstration of the superior control capability of the DANTOC with respect to the standard analogue controller. Figure 6.17 shows the phase plane diagram of the speed versus position for the experiment #17480. The expected stability region Ω_{sl} for the case of a linear saturating controller is calculated using the procedure described in Section 3.3.3 and the maximum obtainable stability region $\Omega_{\max}$ is calculated using Theorem 3.2.2. The experimental results confirm the theoretical prediction. The system becomes unstable when the third pulse pushes the system state outside the calculated Ω_{sl}. The phase plane diagram for experiment #17497 is displayed in Figure 6.18. In this case the DANTOC keeps the position and speed inside the region $\Omega_{\max}$. It should be noted that the system configuration including the DANTOC has a larger maximum stability region $\Omega_{\max}$. But, even taking this into account, the DANTOC would have maintained the control because when the analogue controller loses control the state trajectory is still inside $\Omega_{\max}$.

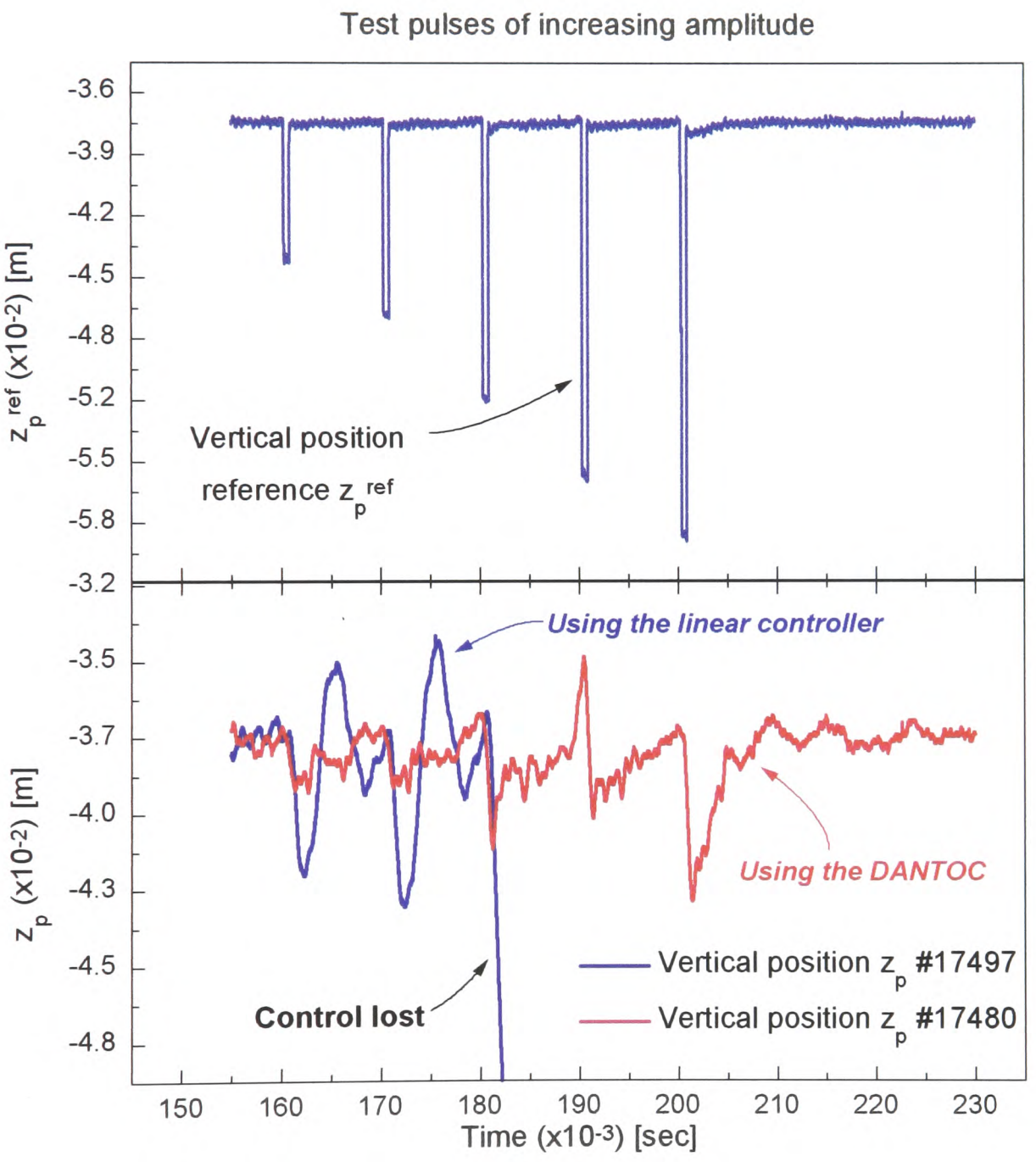


Figure 6.16: Comparison between the DANTOC (#17497) and the COMPASS-D's linear analogue controller (#17480).

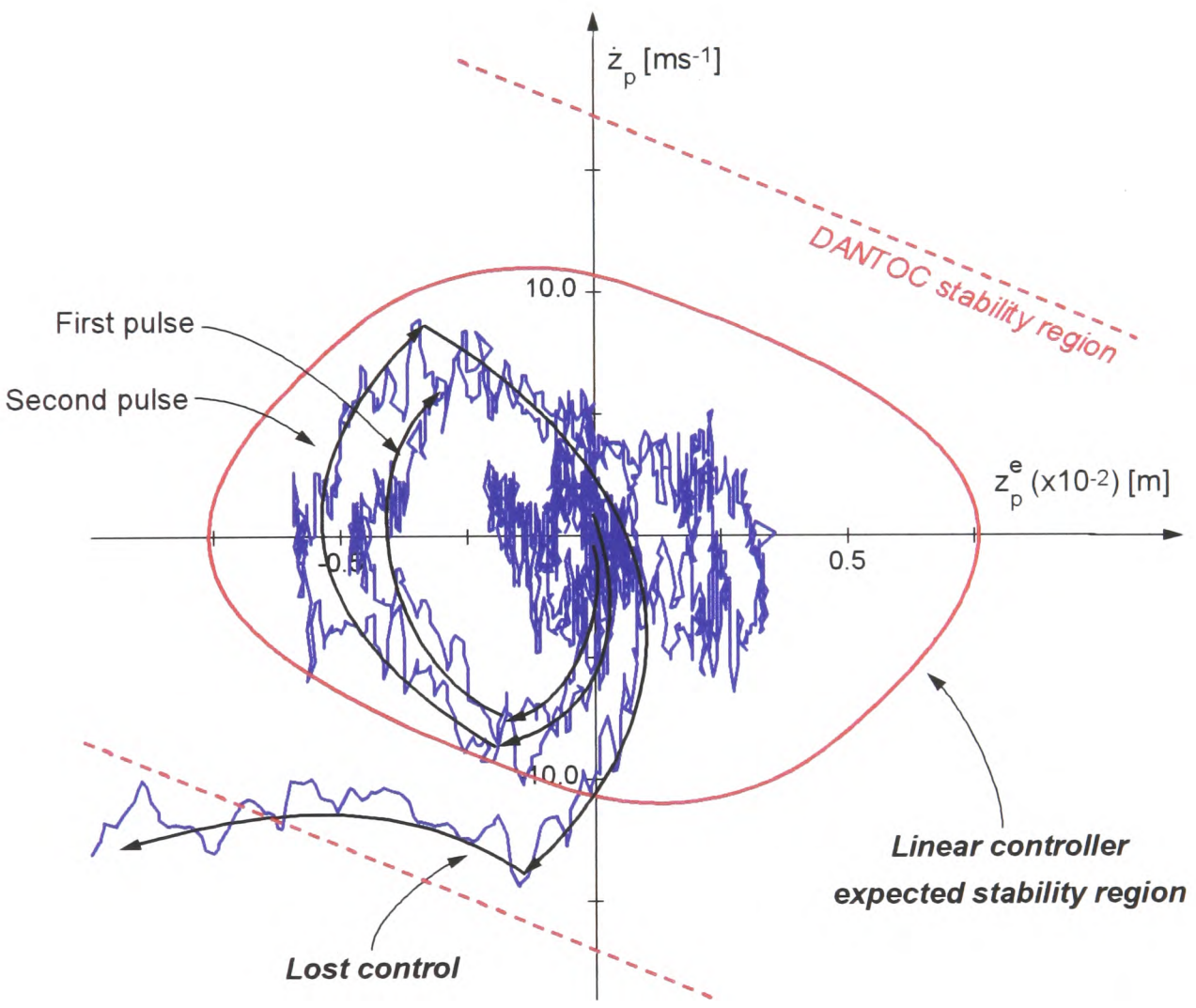


Figure 6.17: The expected stability region of experiment #17480 is displayed on the phase-plane diagram when using the P+D controller.

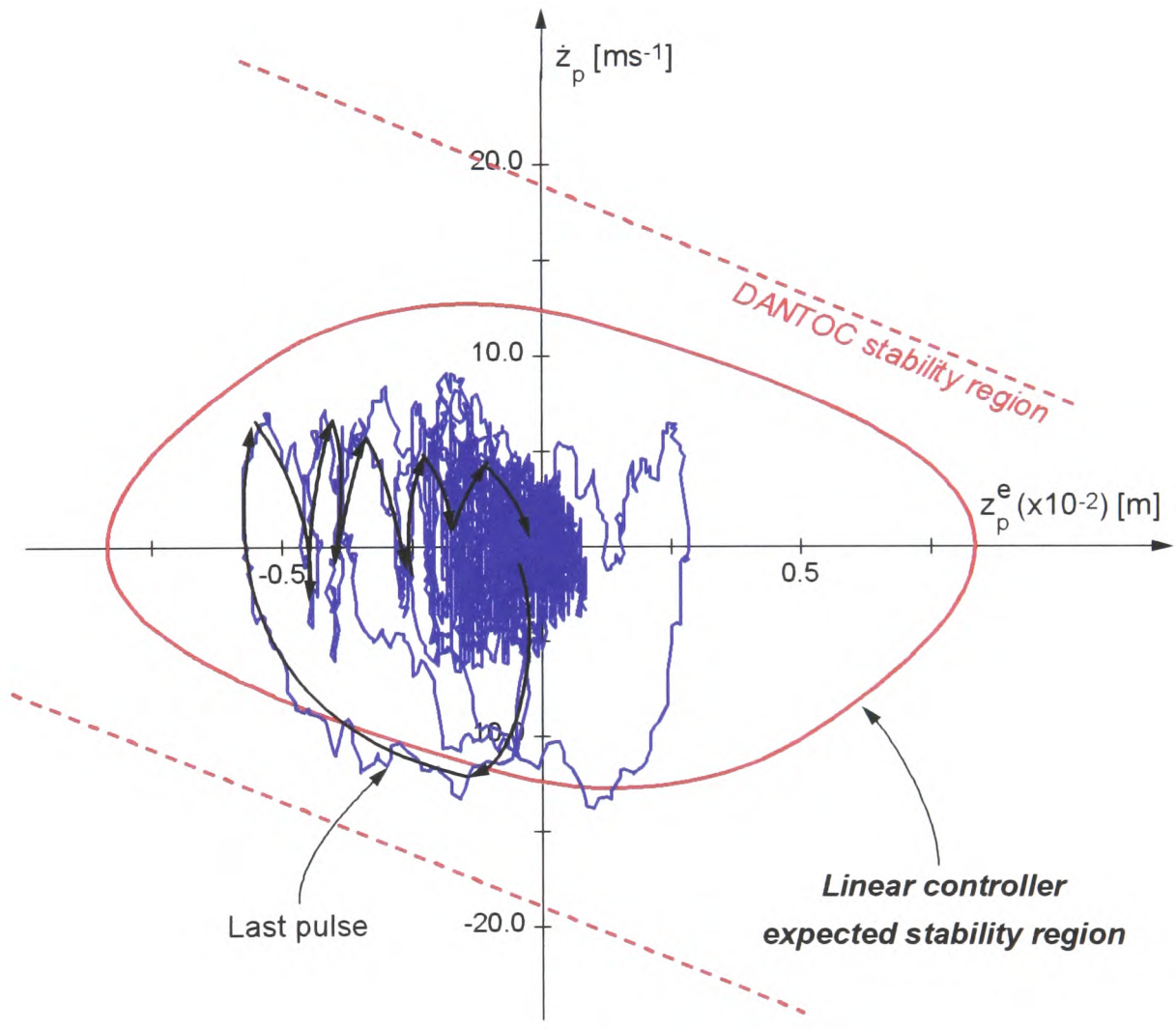


Figure 6.18: Phase-plane diagram when using the DANTOC (pulse #17497) also showing the stability region.

During the second set of experiments the plasma growth rate γ_p is increased until the plasma disrupts. The growth rate γ_p is measured at the time of the disruption and the corresponding stability region $\Omega_{\max}$ is calculated. The growth rate is raised by increasing the plasma elongation which is proportional to the ratio between the shaping current I_{sh} and the plasma current I_p. In experiment #18524 the elongation is increased by ramping-up the shaping current I_{sh} from $7000\,[A]$ to $8500\,[A]$ as shown in Figure 6.19. The plasma current is held constant at $I_p \simeq 170 \cdot 10^3\,[A]$ from $0.1\,[s]$ to the end of the test. The growth rate γ_p rises from $1000\,[s^{-1}]$ to $3000\,[s^{-1}]$ before the plasma disrupts due to the occurrence of a large ELM. In Figure 6.20 the phase-plane diagram of the state trajectory is shown. The circles corresponds to two different times also marked in Figure 6.19. The predicted stability region $\Omega_{\max}$ for the value of $\gamma_p = 1000\,[s^{-1}]$ is shown in green. As the shaping current increases the growth rate increases and the maximum stability region moves inwards towards the red lines representing the $\Omega_{\max}$ for the value of $\gamma_p = 3000\,[s^{-1}]$. As long as the state trajectory is confined inside the predicted $\Omega_{\max}$ the system is stable but at time $t_2 = 243 \cdot 10^{-3}\,[s]$ when $\gamma_p = 3000\,[s^{-1}]$, the ELM is sufficient to displace the plasma outside the region $\Omega_{\max}$. From that time onwards the system becomes unstable. Since the plasma disrupts only when the state trajectory exits the predicted stability region it can be concluded that Theorem 3.2.2 provides a good prediction of $\Omega_{\max}$. In addition, it can be seen that, despite the increasing elongation, the DANTOC's performance does not deteriorate even though ELMs are observed throughout the test. Furthermore, the fact that the loss of control happens when the state trajectory exits the region $\Omega_{\max}$, and not before, gives a good indication that the stability region obtained by the DANTOC is very close to $\Omega_{\max}$.

It is important to note that, even during a Vertical Disruption Event, the DANTOC operates correctly. In fact it tries to counteract the vertical movement until the plasma disrupts. In this way the stresses caused by the disruption are minimized. Since the maximum growth rates γ_p obtained on COMPASS-D with the standard linear controller are less than $2500\,[s^{-1}]$, the results demonstrate that the DANTOC is capable of increasing the plasma operating region, by allowing more elongated plasmas to be controlled, and confirms the theoretical result given in Section 4.2.

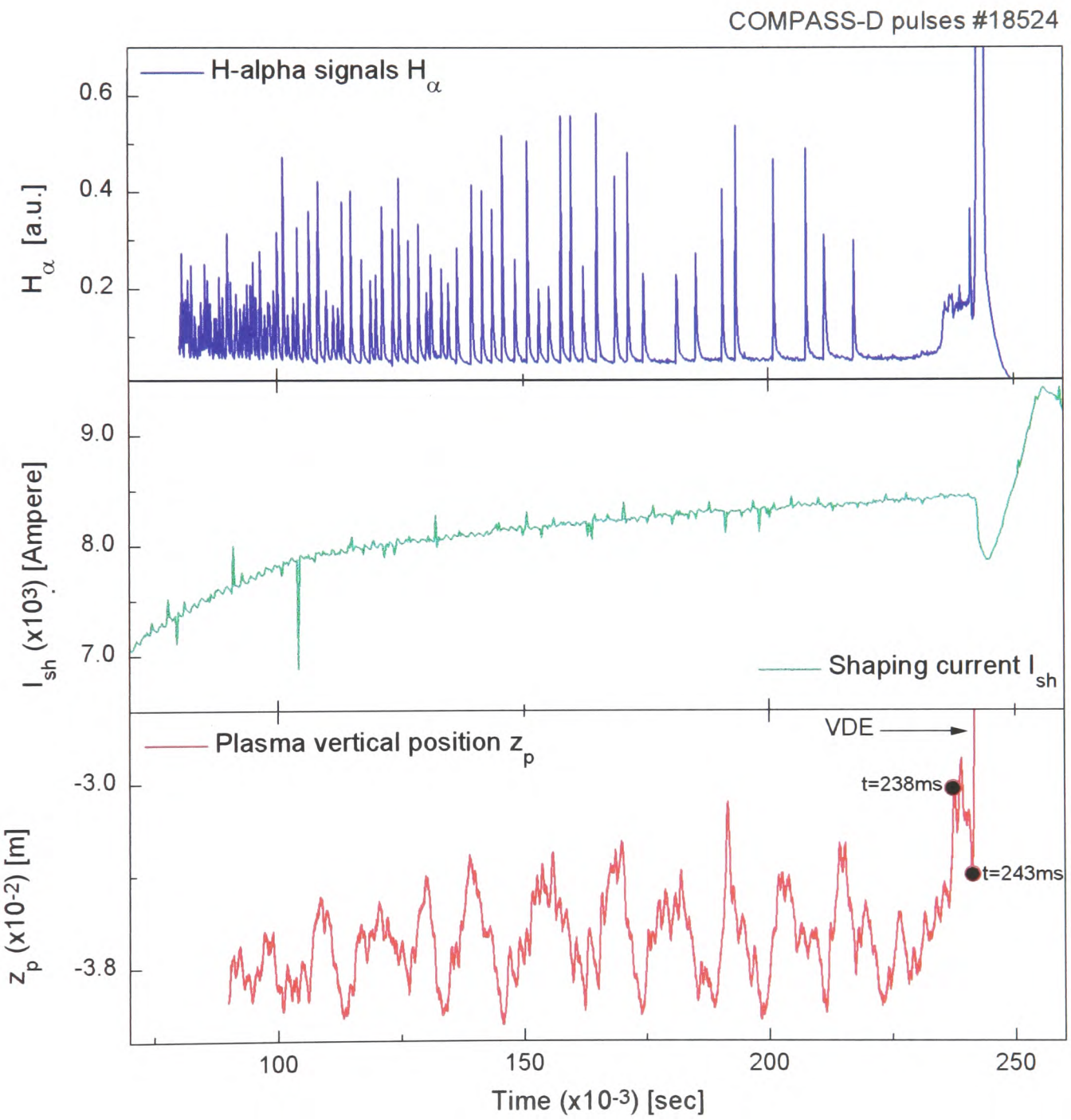


Figure 6.19: COMPASS-D experiment #18524 showing the control response during a gradual increase to the elongation of the plasma: time evolution.

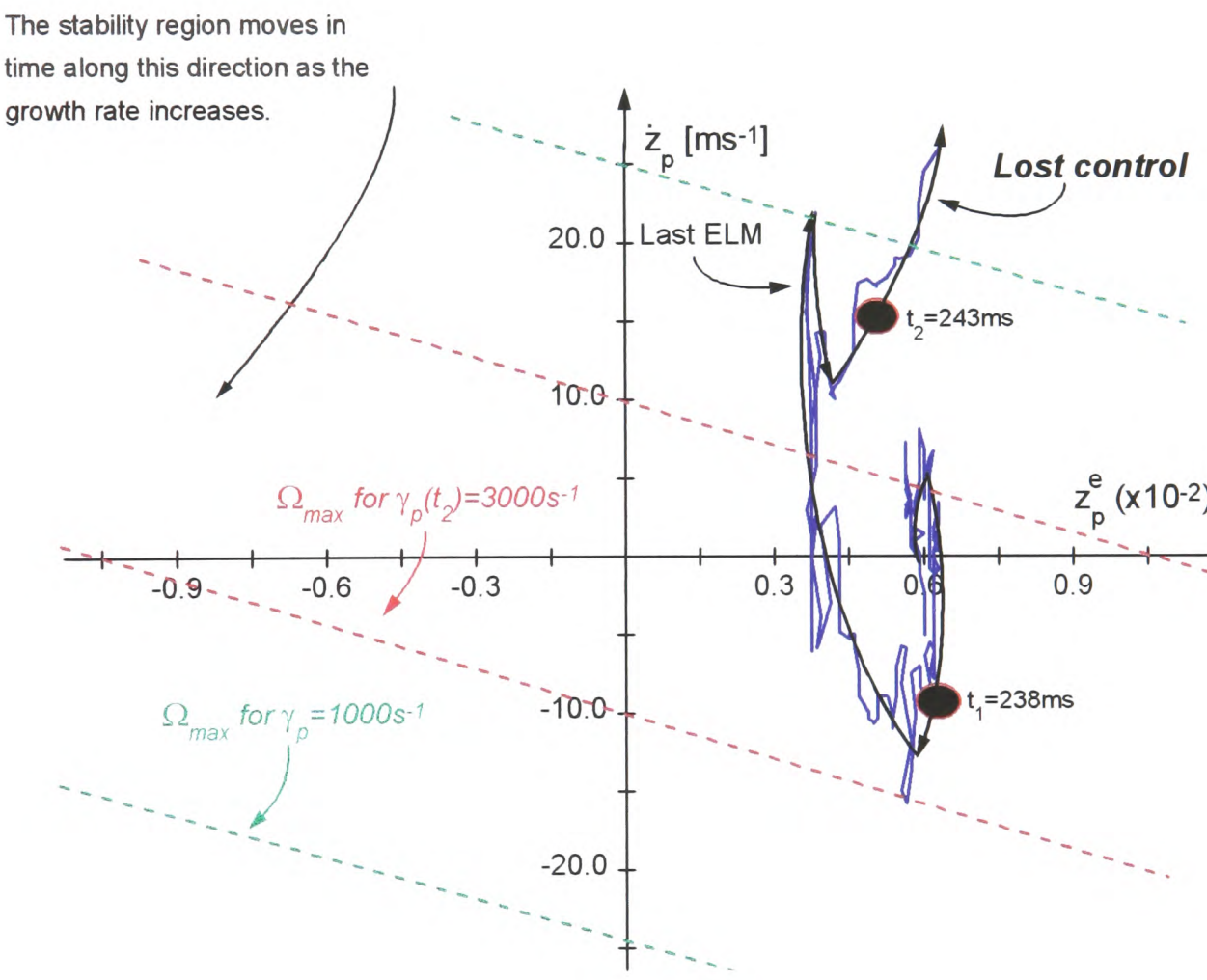


Figure 6.20: COMPASS-D experiment #18524 showing the control response during a gradual increase to the elongation of the plasma: phase-plane diagram.

6.7 Concluding remarks

Over 100 experiments have been performed on COMPASS-D that demonstrate DANTOC's ability to successfully control the vertical position of the plasma. H-mode plasma configurations have been used and the vertical plasma position has been controlled despite the presence of large ELMs.

The simplicity of the DANTOC meant that on-line implementation did not necessitate any special hardware or software and therefore the controller could be implemented quite easily on any other Tokamak such as JET.

The results of the experiments demonstrate the improvement to the performance resulting from the adaptation strategy and show that the stability range is increased, allowing operation with more elongated plasmas. They also indicate that the use of the adaptation delay reduces the effect of ELMs on the plasma vertical position.

It has been shown that both a reduction and an increase in the adaptation delay with respect to the duration of the longest observed ELM $\tau_{ELM}^{\max}$ appear to degrade the performance. This is an indication that ELMs displace the plasma position and induce noise on the measurement at the same time. Therefore it is concluded that the use of the adaptation delay limits the controller intervention to minimize the effect of ELMs, either if they move the plasma or if the induce only measurement noise. Good rejection of the $600Hz$ measurement noise has been observed in all experiments.

It has been shown that the DANTOC can cope with the type of ELMs which seem to cause problems in JET and COMPASS-D as described in [Morris95] and [Ali-Arshad96].

The comparison between the DANTOC and the linear analogue controller confirms DANTOC's superior performance.

Chapter 7

Conclusions and future work

In this thesis a controller based on a new technique, Discrete Near-Time Optimal Control with time varying hyperplanes for Unstable systems, has been designed for stabilizing the plasma vertical position in a tokamak.

The main contributions have been:

- The derivation of a simplified model structure for the plasma vertical position including the disturbances, the measurement noise and the power supplies (Chapter 2).
- A method to determine the maximum obtainable stability region Ω_{max} of unstable systems subject to control limitations in the case of systems with one unstable pole (Chapter 3).
- The definition of, and hence the required conditions for, a maximum stabilizer controller that guarantees a closed loop stable system for all the states inside Ω_{max} (Chapter 3).
- A novel technique to determine the existence, the stability and the period of limit cycles for relay controlled systems (Chapter 3).
- Sufficient stability conditions for unstable systems using relay control with and without time delays, which are also necessary in the case of systems with one unstable pole (Chapter 3).
- A novel non-linear control technique based on discrete time Variable Structure Control theory and Minimum Time Control theory named Discrete Adaptive Near-Time Optimal Control (DANTOC) (Chapter 4).

- A novel non-linear vertical stabilization controller based on the DANTOC which is robust to plant parameter variations, the primary sources of disturbances (ELMs) and the $600Hz$ measurement noise from the thyristor power supplies.

- The experimental validation of the DANTOC on the COMPASS-D Tokamak (Chapter 6).

The main conclusions and avenues for future work are:

- The plasma vertical position model derived in Chapter 2 is sufficient to predict changes in the plasma vertical position in response to the control input and to the modelled disturbances.

  The simplified model structure has been quite sufficient to simulate the plasma vertical position as demonstrated by comparison with experimental data (Chapter 2 and 6). The effect of ELMs on the plasma vertical position has been successfully modelled. An avenue for future work is to extend the simple model analysis to other Tokamaks and, in particular, to ITER. In the latter case it would be particularly interesting to predict the effect of ELMs.

- The method to calculate the stability region, based on the maximum obtainable stability region $\Omega_{\max}$, gives an exact measure of the stability region for unstable systems subject to control limitations in the case of systems with one unstable pole.

  The method has been successfully used to predict the stability region of the plasma vertical position on COMPASS-D. However, measurement of the $\Omega_{\max}$ is given only for systems with one unstable pole.

- In alternative to classical methods to analyse limit cycles, the method derived in Chapter 3 gives an exact solution to the existence, the stability and the period of limit cycles for relay controlled systems in one context.

- The control algorithm designed in Chapter 4 (DANTOC) guarantees the largest obtainable stability region for different plasma configurations. The DANTOC has a larger stability region than any linear controller with fixed parameters that is not a maximum stabilizer. The DANTOC achieves good robustness with respect to plant parameter variations and ELMs. It also improves the $600Hz$ thyristor noise rejection, as observed both in the simulations of the JET vertical stabilization system and in the experiments

on COMPASS-D.

An avenue for future work is to design a plasma vertical position controller based on the DANTOC for ITER. In ITER the plasma vertical position dynamics are close to the shaping variables and therefore the controller should be included in a multivariable controller structure. Alternatively the DANTOC could be used as a protection control system when excessive deviations in the vertical position are detected and stronger action is required to avoid a disruption.

- The DANTOC represents a much better solution than existing conventional controllers for the control of the plasma vertical position for the new generation of Tokamaks.

  The DANTOC has been tested via simulation for the JET Tokamak and the results have demonstrated its great potential. However due to inherent dangers of vertical instabilities in JET and the very limited machine time available it was considered more appropriate to test the on-line implementation of the controller on COMPASS-D. The tests have demonstrated the feasibility of the DANTOC in controlling the plasma vertical position for different plasma configurations including high performance plasma configurations (H-mode configurations), revealing the ability of the DANTOC to adapt to different plasma parameters. The tests have also shown the improvement with respect to a simple P+D linear controller. The on-line implementation on COMPASS-D did not necessitate any special hardware or software because of the simplicity of the DANTOC algorithm. Future work should be undertaken to experimentally validate DANTOC on other Tokamaks. An on-line version for the JET Tokamak is now ready for implementation.

Appendix A

A brief introduction to Nuclear Fusion and Tokamaks

A.1 Principles of Nuclear Fusion

The basic principle of nuclear fusion is that the defect of mass resulting from the fusion of two light nuclei into a heavier and more stable nucleum is transformed into a large amount of energy. For a reactor, there are, in principle, several possible fusion reactions, but the one considered to be of practical interest involves the hydrogenic isotopes (H, D and T) and the light elements (Figure A.1):

$$ {}^{2}_{1}D + {}^{2}_{1}D \rightarrow {}^{3}_{2}He + n + 3.27MeV \tag{A.1} $$

$$ {}^{2}_{1}D + {}^{2}_{1}D \rightarrow {}^{3}_{1}T + p + 4.03MeV \tag{A.2} $$

$$ {}^{2}_{1}D + {}^{3}_{1}T \rightarrow {}^{4}_{2}He + n + 17.59MeV \tag{A.3} $$

$$ {}^{2}_{1}D + {}^{3}_{2}He \rightarrow {}^{4}_{2}He + p + 18.3MeV \tag{A.4} $$

Deuterium can be easily and cheaply obtained from water and tritium can be bred in a fusion reactor from the light metal lithium using the neutrons, produced by the fusion itself, to induce the fission reaction:

$$ {}^{6}_{3}Li + {}^{1}_{0}n \rightarrow {}^{3}_{1}T + {}^{4}_{2}He + 4.8Mev \tag{A.5} $$

$$^{7}_{3}Li + ^{1}_{0}n \rightarrow ^{3}_{1}T + ^{4}_{2}He + ^{1}_{0}n - 2.5Mev \tag{A.6}$$

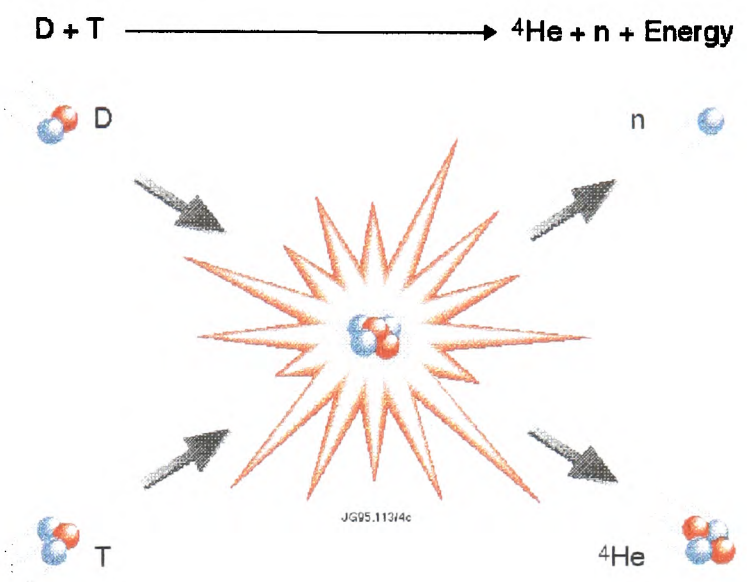


Figure A.1: The Deuterium (D) - Tritium (T) fusion reaction.

In order to have a sufficient high reaction rate, temperature of the order of $100 - 200 \cdot 10^6\,[^oC]$ $(10 - 20 \cdot 10^3\,[eV])$ are required [Wesson87]. In addition, in a reactor, the fuel density must be maintained at about $10^{20}\,[m^{-3}]$ at these temperatures for a sufficient period of time. At those temperature the fuel is in the plasma state, consisting of a mixture of charged particles (nuclei and electrons). In a reactor, there must be sufficient fuel present and the energy losses must be kept sufficiently low to ensure that more energy is released from the fusion reaction than is needed to heat the fuel and maintain the necessary temperature. These hot particles can be contained by gravitational forces, as in the sun, or by magnetic fields.

For magnetic confinement, the effectiveness of the magnetic field in containing plasma and minimising thermal losses can be measured by the time taken for the plasma to cool down after the source of heat is removed (this is called energy confinement time τ_E). Thus a fusion reactor must produce high temperature plasmas of sufficient density that can be contained for long enough to generate a net output of power. This condition can be expressed by the inequality

$$n_{ion} \cdot \tau_E \cdot T_{ion} \geq 5 \cdot 10^{25} \left[m^{-3} seV\right] \tag{A.7}$$

where n_{ion} is the plasma ion density and T_{ion} is the ion temperature. Typically, for magnetic

confinement concepts, this requires:

- Central ion temperature: $T_{ion} \sim 10 - 20 \cdot 10^3 \, [eV]$
- Central ion density: $n_{ion} \sim 2 - 3 \cdot 10^{20} \, [m^{-3}]$
- Global energy confinement time: $\tau_E \sim 1 - 2 \, [s]$.

A.2 The Tokamak

The most effective method of magnetic confinement has proven to be the tokamak (Figure A.2). This is a device introduced in the late '60s in the ex Soviet Union by Sakharov and Tamm (the word is an acronym for the Russian TO*roidalnaya* KA*mera i* MA*gnitnaya* K*atushka* for toroidal chamber and magnetic coils) which has rapidly spread all over the world thanks to its relative technological simplicity and its high performance.

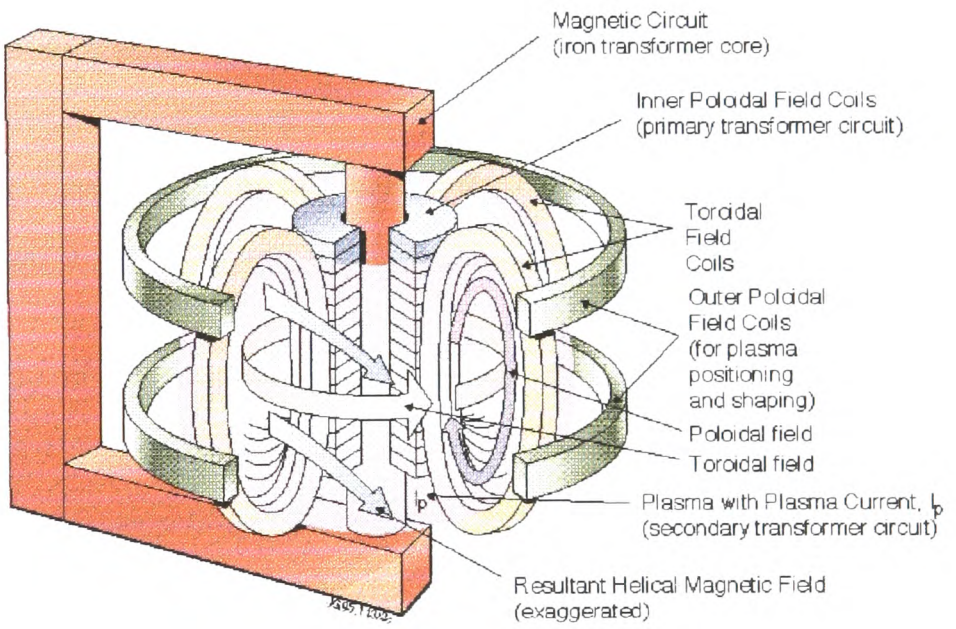


Figure A.2: The tokamak concept.

The magnetic field for the confinement is provided by the combination of a large field produced by the toroidal coils and by a smaller poloidal field associated with the plasma current. The plasma current is induced by the magnetic field variation generated by a current injected in the central solenoid (this acts as the primary winding of a transformer which gives a flux change through the torus and produces a toroidal electric field which drives the plasma current). The plasma current heats the plasma by Joule dissipation (ohmic heating). Since the plasma resistivity decays with temperature as $T^{-\frac{3}{2}}$, in order to reach the required temperature additional heating is needed. In Tokamaks radio-frequency heating and high

energy neutral beam injection are used [Bertolini91]. The position and the shape of the plasma cross-section is determined by magnetic fields generated by poloidal coils external to the plasma. The combination of these fields produces a helical magnetic field that contains the plasma (Figure A.3); the surfaces covered by such field are known as magnetic surfaces.

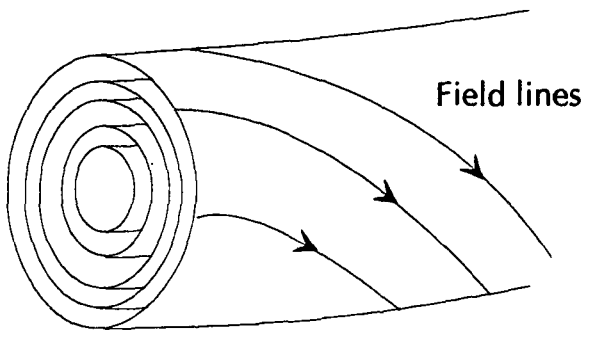


Figure A.3: Magnetic flux surfaces forming a set of nested toroids .

Under normal operating conditions the magnetic surfaces are nested inside each other surrounding a magnetic axis located at an 0-point. The edge of the plasma is defined by the last closed magnetic surface inside the vacuum vessel (separatrix).

At JET the magnetic field configuration can be of two types as shown in Figure A.4.

- *Limiter configuration:* in this configuration the magnetic null is outside the vacuum vessel and the separatrix position is determined by the intersection of the magnetic surface with a wall protuberance called limiter. Typically this configuration is up/down symmetric.

- *X-point configuration:* in this configuration one of the closed surfaces near the limiter is opened up so that it intersects with the vacuum vessel wall. In this configuration, the magnetic separatrix is moved to within the vacuum chamber. This so called X-point (or magnetic limiter) configuration can be operated with the two nulls of the separatrix within the vacuum chamber (**double** null divertor *DND*) or with only one inside (single null divertor *SND*). This configuration is **clearly not up/down** symmetric.

During X-point operation with low power additional heating, the plasma confinement is reduced relative to that obtained with ohmic heating. This mode is called low or *L-mode.* At high power additional heating the confinement is found to increase by up to a factor of 2 relative to that of L-mode and this mode is termed *H-mode.*

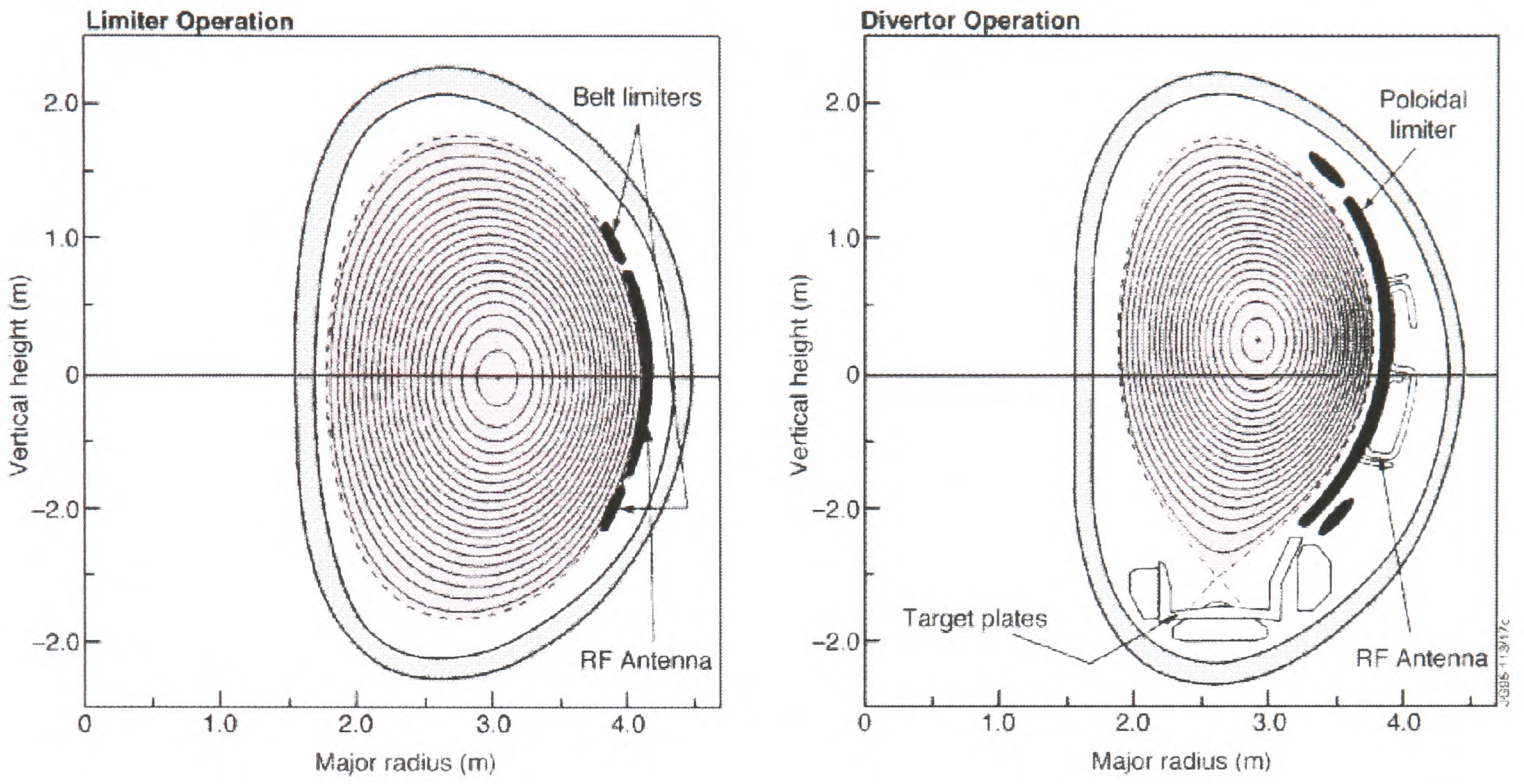


Figure A.4: Plasma operating modes.

During H-mode plasmas the so-called Edge Localized Modes (ELMs), an MHD instability occurring at the plasma edge, occur [Zohm96]. ELMs lead to a fast loss of energy and particles from the plasma edge in the order of milliseconds as it can be observed from the intensity of the H_α line emission. The H_α signal is the spectral line at the characteristic frequency of the photon emitted by the de-excitation of the hydrogenic atoms whose intensity is proportional to the number of hydrogenic atoms present in the plasma boundary.

Additional parameters of interest for tokamaks are:

- the safety factor q, which is a measure of the helicity of the field lines [Wesson87] and is defined as

$$q = \frac{number\,of\,toroidal\,turns}{number\,of\,poloidal\,turns} > 1. \tag{A.8}$$

  When q is a small rational number the plasma is specially sensitive to perturbation which may lead to a disruption due to an enhanced energy losses.

- the β-value, which is a measure the effectiveness with which the magnetic field confines the plasma; it is defined as

$$\beta = \frac{plasma\,pressure}{magnetic\,field\,pressure}.$$

This factor gives an estimate of the maximum plasma pressure which can be maintained by a given magnetic field for a given plasma current [Wesson87].

Tokamak plasmas with non-circular cross section exhibit significant performance improvements over plasmas with circular cross section. In fact it can be proved that the vertical elongation allows larger plasma currents to be carried for given values of magnetic field, major radius and minor radius, as well as producing larger values of β. Hence an increase in elongation leads to an increase in the maximum efficiency achievable [Wesson87].

Unfortunately, such plasmas are intrinsically vertical unstable and thus require a feedback control system to maintain plasma equilibrium.

A.3 The JET Tokamak

The schematic view of the JET Tokamak (Figure A.5) and the JET main parameters (table A.1) highlight the key features of the device [EAEC76][Hugue87][Bertolini87].

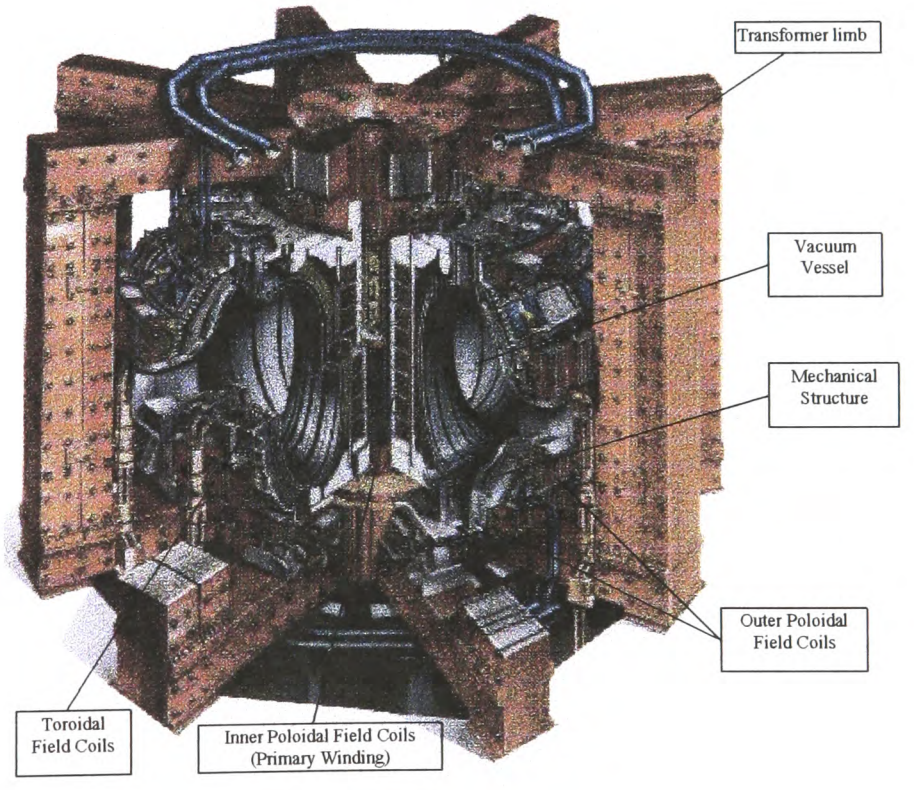


Figure A.5: The JET Machine.

- The vacuum vessel and the toroidal coils have an elongated (D-Shape) cross section, and this allows, with a proper poloidal field, the production of D-shape plasmas. The choice of the D-shape was originally made to reduce the mechanical stresses on the

JET Parameters		
Parameters	**Design Values**	**Achieved Values**
Major Radius (R)	2.96[m]	2.5-3.4[m]
Minor Radius (Horizontal) (a)	1.25[m]	0.8-1.2[m]
Minor Radius (Vertical) (b)	2.10[m]	0.8-1.2[m]
Toroidal Field (B_T)	3.45[T]	3.45[T]
Plasma Current (I_P)	4,8·10^6 [A]	7.0·10^6 [A]
NB Power	20·10^6 [W]	21·10^6 [W]
ICRH Power	15·10^6 [W]	22·10^6 [W]

Table A.1: Principal Parameters of JET

toroidal coils but it has proven to be the greatest asset of the JET design, allowing full use of the magnet volume with large plasma currents, to produce elongated plasma and so achieve the current performances [JETannual95].

- The tokamak transformer iron circuit improves the magnetic coupling between the primary winding and the secondary (plasma).

- The inconel vacuum vessel has a double wall. The temperature of the first wall (closer to the plasma) is controllable up to 350 [^oC] (see Figure A.6).

- The mechanical structure is a metallic shell (weighting 460 tonnes) that surrounds the Toroidal Field coils and supports them against strong lateral forces resulting from the interaction of the poloidal field with the current flowing in the TF coils (see Figure A.6).

- The core of the machine is made up by eight identical sections (octants), each comprising one eighth of the vacuum vessel, 4 toroidal coils and one eighth of the mechanical structure.

- The Toroidal Field (TF) Circuit:
  The TF coil system includes 32 magnets evenly spaced along the tokamak circumference, as it can be seen in Figure A.7. This high number of coils is needed in order to minimize the field ripple. The maximum generated field is, nominally, $B_T = 3.45\,[T]$ at the centre of the vacuum vessel.

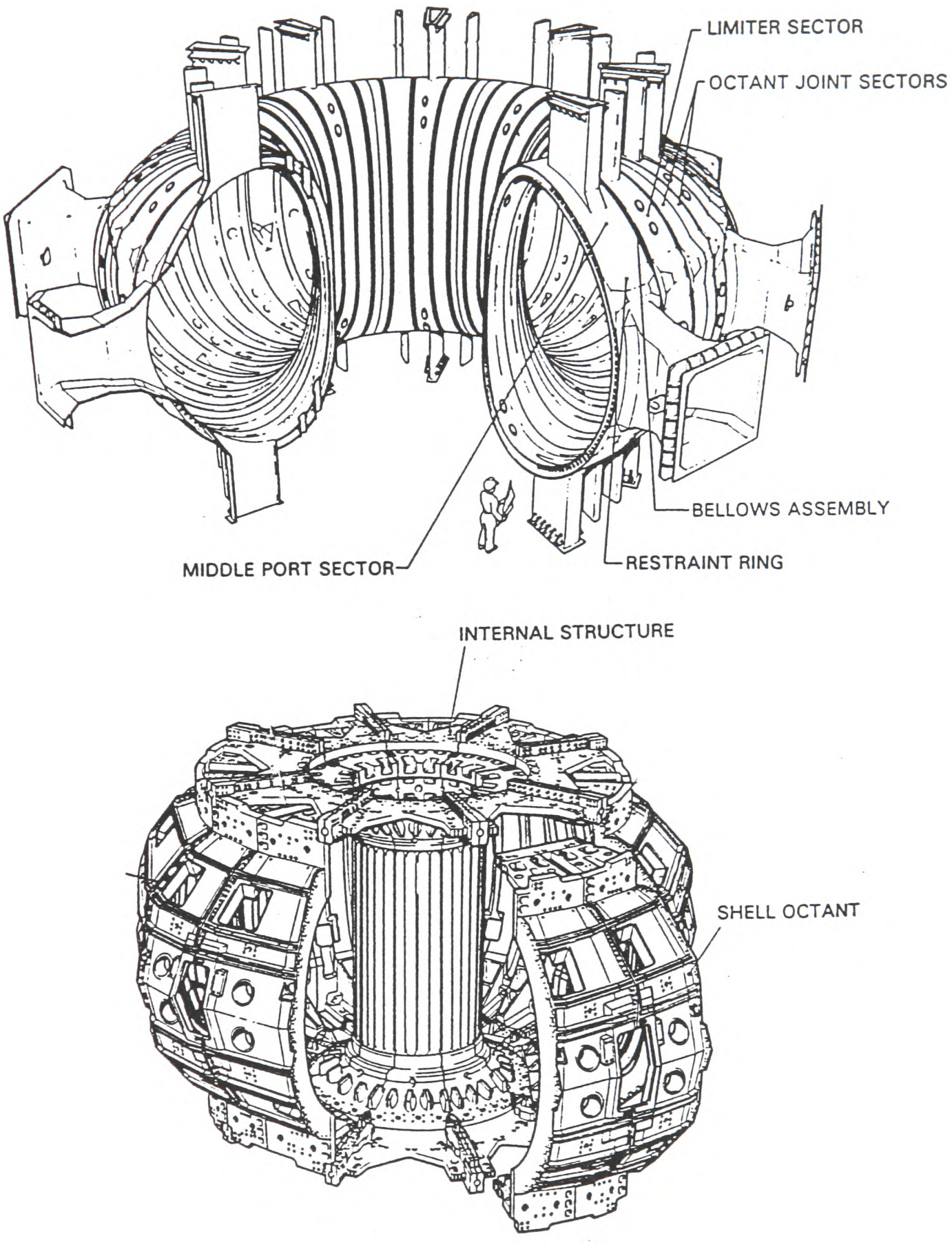


Figure A.6: JET tokamak vessel and mechanical structure

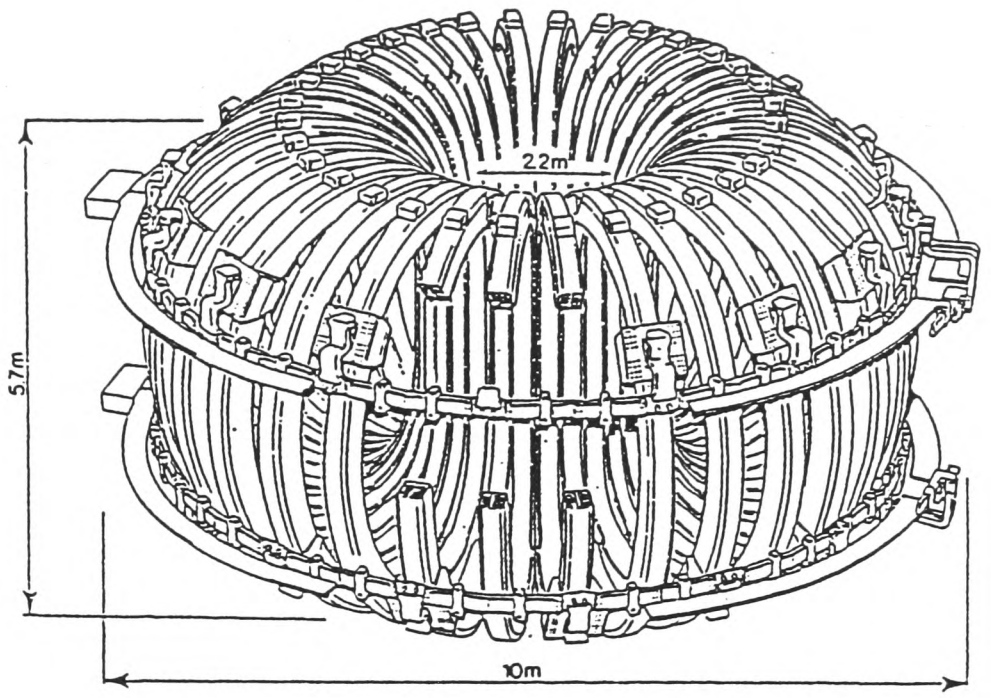


Figure A.7: TF coil system

- The Poloidal Field (PF) circuit:

  The PF coil system is composed by 4+4 coils (symmetric to the equatorial plane) and the new 4 divertor coils. The first one, usually named the PF coil system, are mounted outside the vacuum vessel while the divertor ones are inside as shown in Figure A.8 and Figure A.9. Each PF coil can be divided in turns and connected in series and in

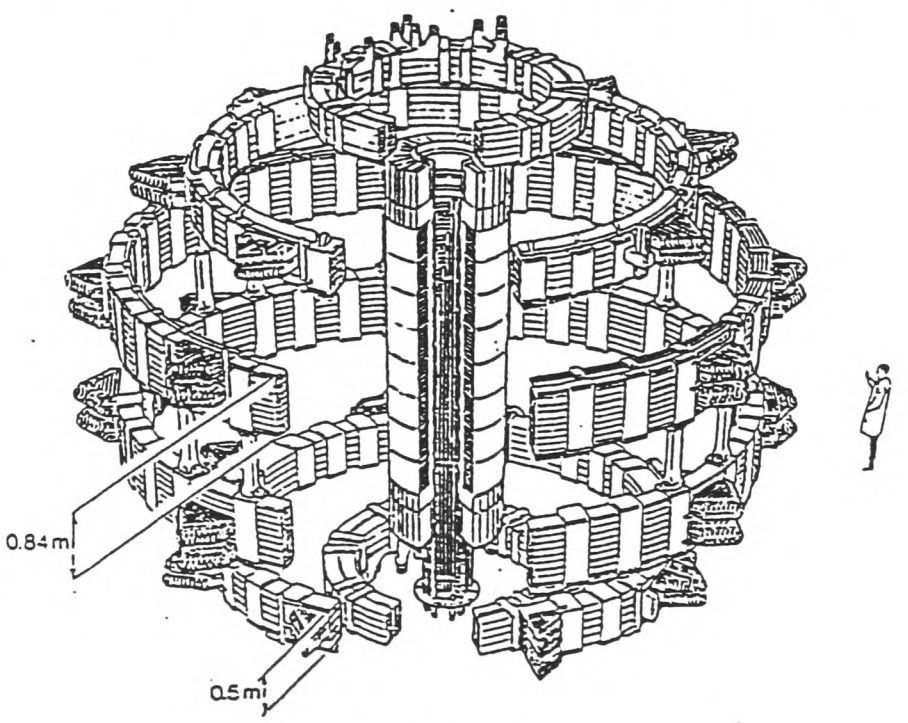


Figure A.8: PF coil system

parallel and independently fed so as to control the resulting magnetic configuration and the plasma current with maximum flexibility. A short description of each set of PF coils is given below.

1. The transformer circuit (coils P1_ and P3_ M) is the transformer's primary whose associated flux is tightly coupled to the iron core and is the e.m.f. source for the plasma current, that, in turn, is the energy source to sunstain the poloidal field and ohmically heat the plasma.
2. The vertical field circuit (coils P4_ V) generates the uniform vertical field essential for the MHD equilibrium; they are fed by two different amplifiers to generate an unbalanced current able to vertically move the plasma.
3. The shaping field circuit (coils P2_ and P3_ S) generates a quadrupolar field used to give the plasma its elongated shape. The P2s pull the plasma (having the same sign) while the P3s push it; the shaping is complemented by an additional current in the central part of the transformer coil (P1C) (fed by an additional power supply called PFX) and the small image current flowing in the polar shoes, which optimize the filling of the vacuum vessel D-section.
4. The radial field circuit (coils P2_ and P3_ R) generates the radial field whose purpose is to stabilize the vertical plasma position. This circuit is fed by the Fast Radial Field Amplifier.
5. The Divertor Coils consist of four freon-cooled copper coils installed inside the vacuum vessel (see Figure A.9). They are needed for the experiments in X-point configurations with the pumped divertor for the impurity control.

A complete list of the parameters of the PF circuit can be found in [Bertolini87].

The parameters for the simplified model of the plasma vertical position are derived from [Noll91a] and are summarized in table A.2.

A.3.1 Vertical position control system

The schematic diagram of the JET vertical position control system is given in Figure A.10. The plasma vertical speed feedback signal is derived by a combination of preprocessed magnetic signals, the measurement of the divertor current derivative and the plasma current and vertical position. These signals are digitally processed to obtain the measure of the plasma current centroid vertical speed $\dot{z}_p I_p$. The FRFA current feedback signal is measured by a hall-effect current transducer and is transmitted to the digital controller over an optical link. The DSP digital controller is implemented on a multiprocessor VME based system. The DSP

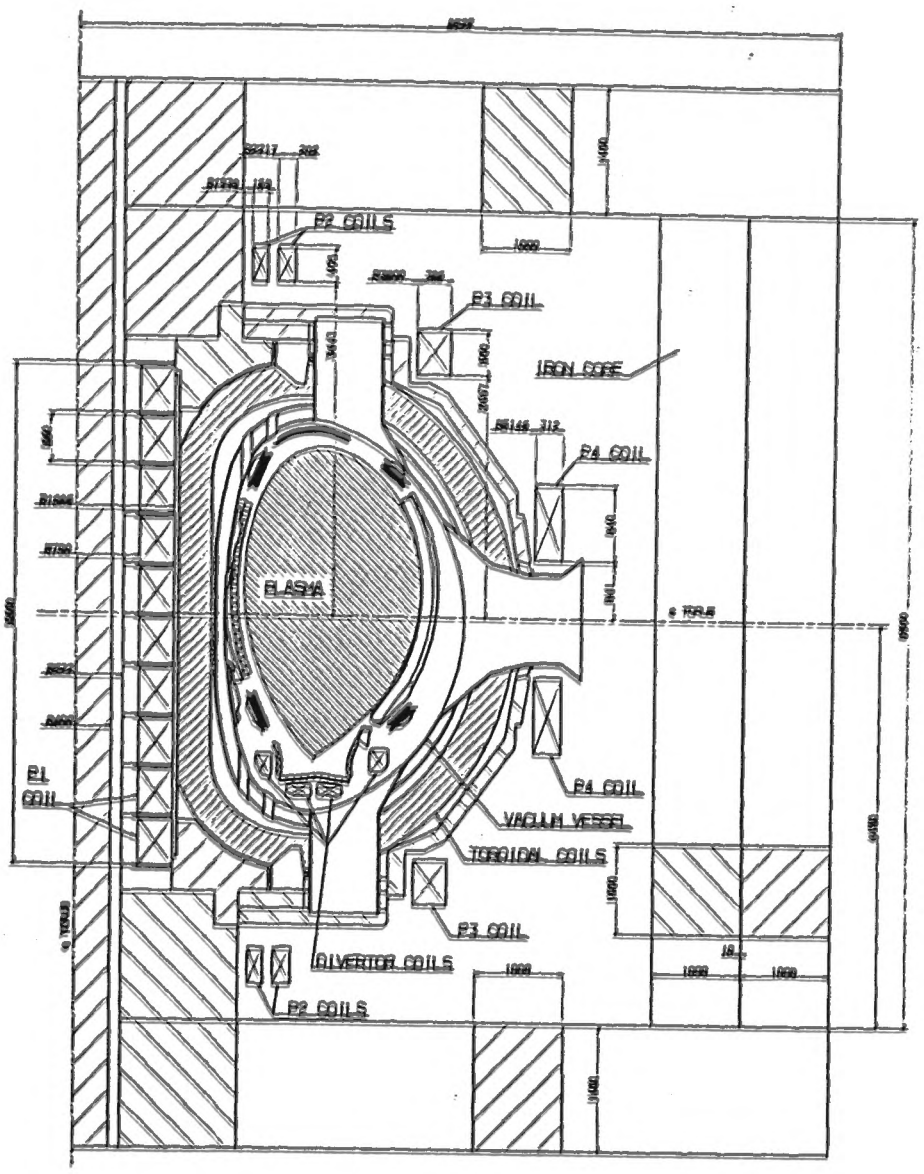


Figure A.9: Cross section of the PF System

processors are TMS320C40. The inputs are digitized at $20 \cdot 10^3\,[Hz]$ with $16-bits$ resolution. The digital to analogue converters have a $16-bits$ resolution and a $3 \cdot 10^{-6}\,[s]$ settling time. The total delay introduced by the DSP digital controller is less than $50 \cdot 10^{-6}\,[s]$.

The controller output is sent over an optical link to the FRFA amplifier. The FRFA is a high power GTO, four quadrant, H-bridge inverter.

The typical JET vertical stabilization control algorithm consists of a P controller on the speed loop and a P+I controller on the current loop such that the controller output is given by

$$V_z^* = P_D \dot{z}_p I_p + P_i I_a + \frac{1}{T_i} \int I_a dt.$$

Typical values of the controller parameters are: $P_D = 0.68\,[ms^{-1}]$, $P_i = 2 \cdot 10^{-3}\,[A]$ and $T_i = 0.5 \cdot 10^3\,[A^{-1}s^{-1}]$.

Parameter	Typical value	Description
L_{aa}	$\sim 42.5 \cdot 10^{-3}\,[H]$	Active coils self-inductance
$L_{av} = L_{va}$	$\sim 0.432 \cdot 10^{-3}\,[H]$	Mutual incuctance active/passive coils
L_{vv}	$\sim 0.012 \cdot 10^{-3}\,[H]$	Passive coils self-inductance
R_{aa}	$\sim 35.0 \cdot 10^{-3}\,[\Omega]$	Active coils resistance
R_{vv}	$\sim 2.56 \cdot 10^{-3}\,[\Omega]$	Passive coils resistance
$\acute{L}_{ap}$	$\sim 115.2 \cdot 10^{-6}\,[Hm^{-1}]$	Mutual change inductance between the active coils and the plasma displacement
$\acute{L}_{vp}$	$\sim 3.2 \cdot 10^{-6}\,[Hm^{-1}]$	Mutual change inductance between the passive coils and the plasma displacement
A''_{pp}	$0.4 \cdot 10^{-6}$ to $0.6 \cdot 10^{-6}$ $[Hm^{-2}]$	Normalized destabilizing force

Table A.2: List of parameters for the vertical position simplified model for JET

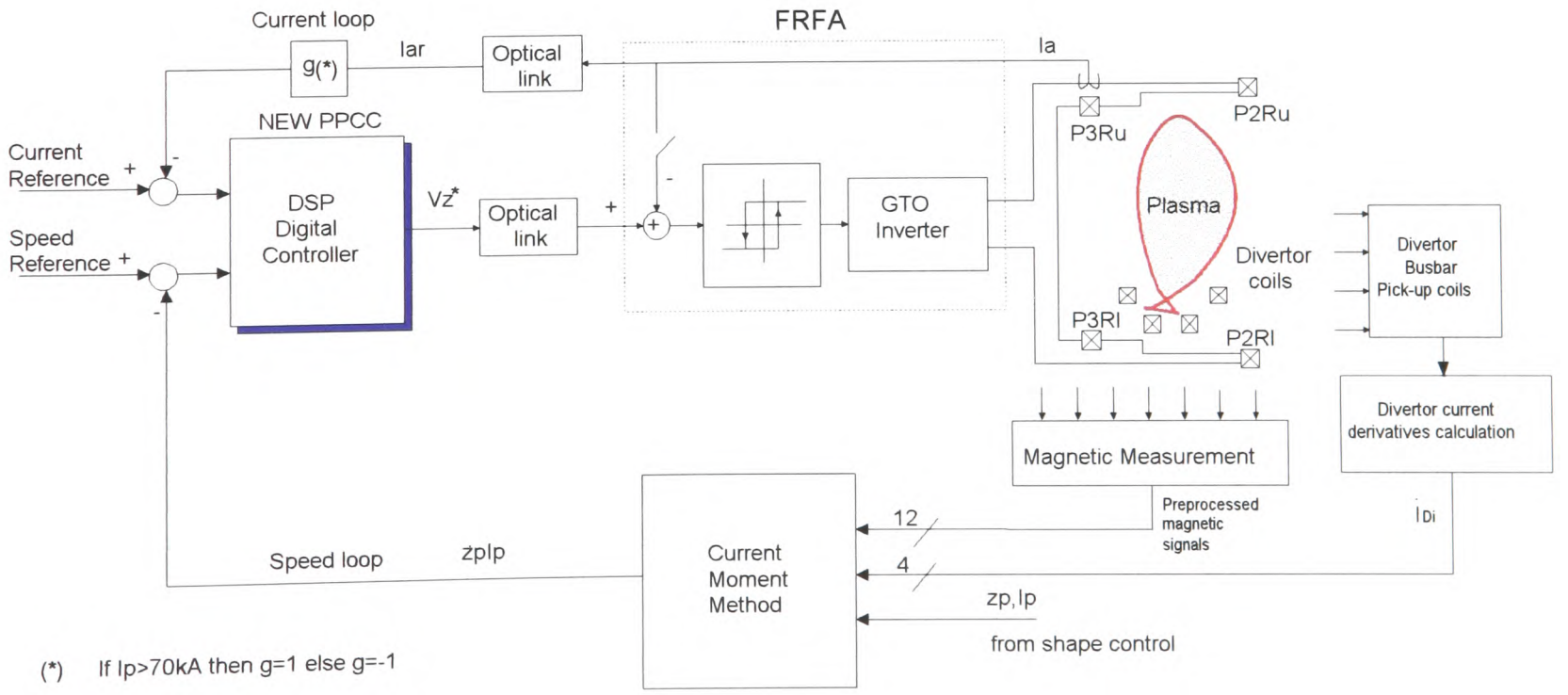


Figure A.10: Schematic diagram of the JET vertical stabilization system.

A.4 The COMPASS-D Tokamak

COMPASS-D is a small experimental tokamak at the Culham laboratory its main parameters are reported in Table A.3. Its main objective is to study plasma confinement and instability relevant to the design of future reactors. Since COMPASS-D is relatively small compared to JET it is much easier to implement new control ideas and try them without damaging the equipment with high stressing disruption. Different plasma configurations can be easily obtained by changing the shaping coil setup. By rearranging the control coils and the power supplies it is possible to emulate other tokamaks like JET.

COMPASS-D Parameters	
Parameter	**Value**
Major Radius (R)	$0.56\,[m]$
Minor Radius (Horizontal) (a)	$0.23\,[m]$
Minor Radius (Verical) (b)	$0.3\,[m]$
Toroidal Field (B_T)	$2.1\,[T]$
Plasma Current (I_p)	$400 \cdot 10^3\,[A]$

Table A.3: Principal parameters of COMPASS-D

A.4.1 Vertical position control system

The schematic diagram of the vertical position control system is given in Figure A.11. There are two sets of sensors: one inside and one outside the vacuum vessel. The first is used to measure the velocity of the plasma current centroid and the second, after analogue integration, is used to measure the position.

The external coils are subject to low pass filtering by the vacuum vessel at $\sim 1 \cdot 10^3\,[Hz]$ but, since they are integrated the effect is of no importance. [Vyas96] gives a clear description of these signals and in particular the scaling factors which are

$$\begin{aligned} z_p\,[m] &= 2.25 \cdot \int \dot{z}_{FL}\,[V] \\ \dot{z}_p\,[m] &= 0.582 \cdot \dot{z}_{IPR}\,[V] \end{aligned}$$

where z_p and $\dot{z}_p$ are respectively the position and velocity of the plasma current centroid,

$\dot{z}_{FL}$ is the signal measured by the external flux loop and $\dot{z}_{IPR}$ is the signal measured by the internal partial Rogowski coils.

The position and the velocity signals are multiplied by some predefined gain waveforms, $P(t)$ and $D(t)$, and the sum is the control signal. This is sent to a linear power amplifier via an optical link.

The power amplifier can be operated with one or two modules in series; each module is composed of a transistor amplifier rated at $\pm 50\,[V]$ and $\pm 5 \cdot 10^3\,[A]$ with a $6 \cdot 10^3\,[Hz]$ imposed bandwidth.

Typical values of the gains at the flat-top converted in engineering units are

$$\begin{aligned} P(t)|_{t_{flatop}} &= 566.6\,[m] \\ D(t)|_{t_{flatop}} &= 0.95\left[ms^{-1}\right] \end{aligned}$$

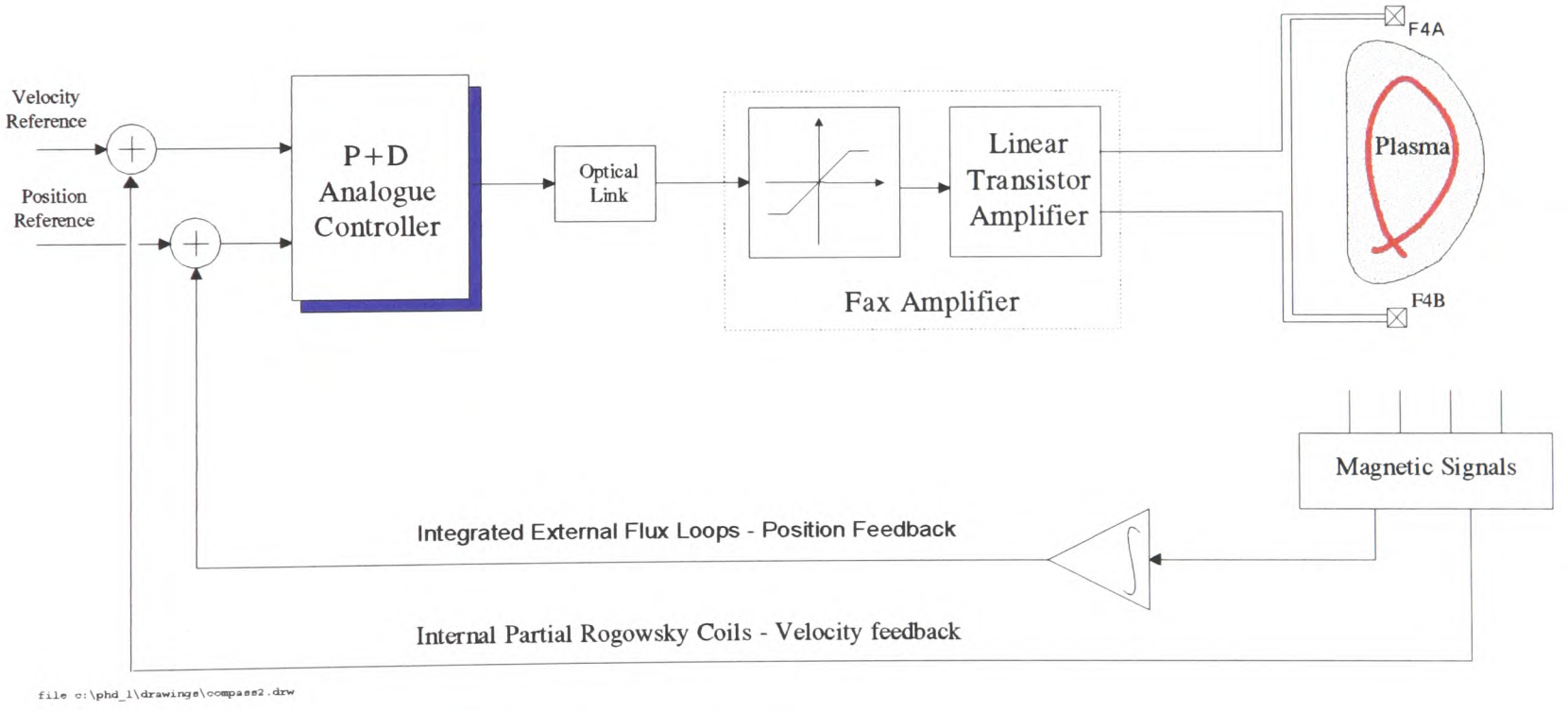


Figure A.11: Schematic diagram of the present COMPASS-D vertical stabilization system.

Appendix B

A brief introduction to Variable Structure Control and Minimum Time Control

B.1 Variable Structure Control review

The basic philosophy of the Variable Structure Control (VSC) is that the structure of the feedback control is altered as the state crosses discontinuity surfaces (hyperplanes) in the state space with the result that the resulting non-linear controller has certain desirable properties. The most important feature of VSC is its ability to achieve very robust control. In theory there are cases where invariant control systems result [Drazenovic69] (the term *invariant* means that the closed loop system is completely insensitive to parametric uncertainty and external disturbances). If the state variables move on an assigned switching hyperplane the system is said to be in *sliding mode.* The term *switching* is used to describe the fact that the system is switched from one structure to another as it crosses the hyperplane.

For example, consider a plant described by the following equations

$$\begin{bmatrix} \dot{x}_1 \\ \dot{x}_2 \end{bmatrix} = \begin{bmatrix} 0 & 1 \\ 0 & 0 \end{bmatrix} \begin{bmatrix} x_1 \\ x_2 \end{bmatrix} + \begin{bmatrix} 0 \\ 1 \end{bmatrix} u, \tag{B.1}$$

let the assigned hyperplane be

$$\sigma(x_1, x_2) = qx_1 + x_2 = 0 \tag{B.2}$$

and the VSC be a relay-type control law be given by

$$u = -u_o sgn\left[\sigma\left(x_1, x_2\right)\right]$$

where

$$sgn\left[\sigma\left(x_1, x_2\right)\right] = \begin{cases} 1 & \sigma > 0 \\ -1 & \sigma < 0 \end{cases}.$$

The block diagram of the closed loop system is shown in Figure B.1. A typical states tra-

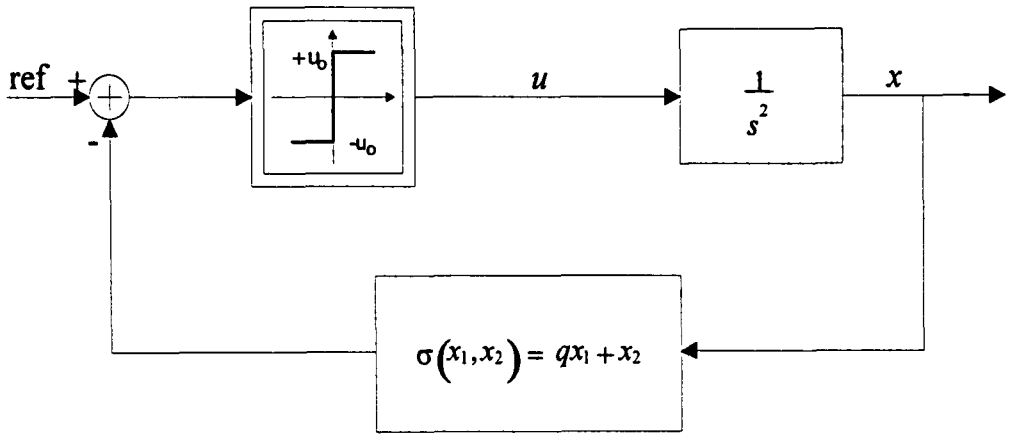


Figure B.1: Typical variable structure system with relay control law.

jectory is identified by a *reaching phase*, during which the states move towards the switching hyperplane, and a *sliding phase*, during which the states move on the switching hyperplane. One assumption for sliding motion is that the control can be switched infinitely fast. In practice there are various reasons why this cannot occur (e.g. the actuators' limitation and delays in the control action); therefore a typical high frequency *chattering* phenomenon about the switching hyperplane is observed. In Figure B.2 typical states trajectories are indicated on the phase-plane diagram. It is important to observe that during the sliding mode, by differentiating equation (B.2) and eliminating x_1 using equation (B.1), the equivalent system behaves as a 1^{st} order system defined by the equation

$$\dot{x}_2 + qx_2 = 0.$$

The design of a variable structure controller can be divided into two stages. The first is the design of a switching hyperplane so that the required dynamics during sliding mode are obtained. The second stage is the design of a switching control law to guarantee the existence

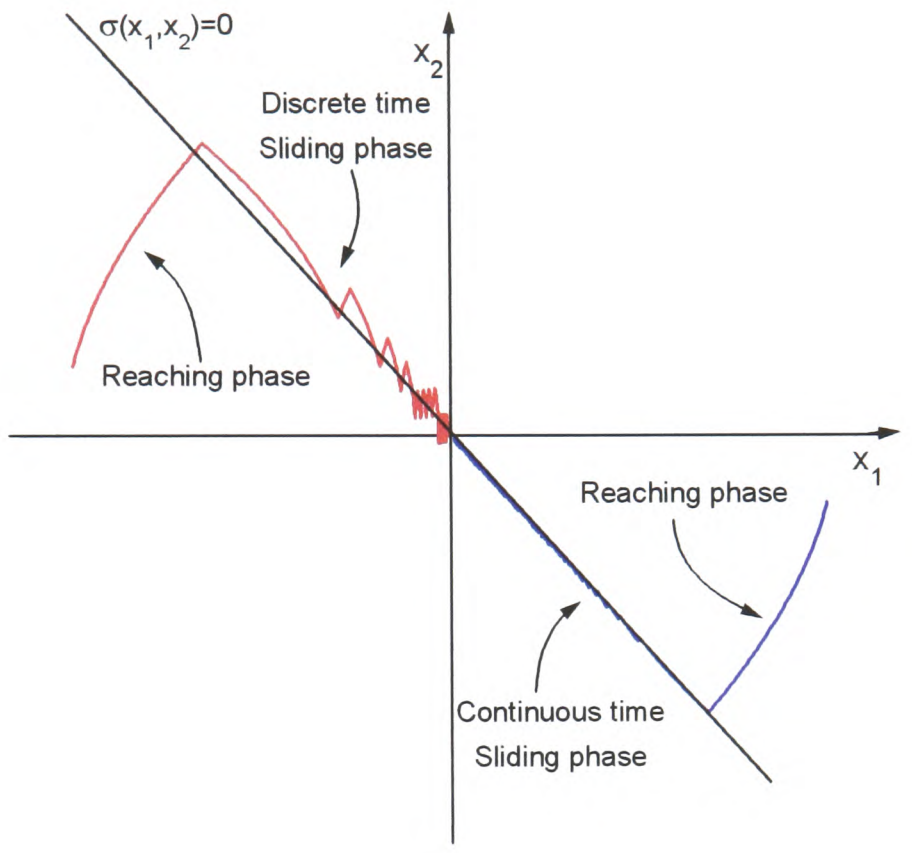


Figure B.2: Typical phase state trajectories.

and the reachability of a sliding mode. References to the more relevant works in the field of variable structure control are given in an excellent recent survey [Hung93]. The application of *discrete time* variable structure control is a relatively new field. [Milosavljevic85] pioneered the use of sliding modes in discrete time systems which he named *quasi-sliding mode.* However the mathematical definition of discrete-time sliding mode was introduced by [Drakunov89]: a system is said to be in sliding if the states are constrained to a manifold that is reached in finite time. Others give different definitions of discrete time sliding mode. [Gao95] defined a quasi-sliding mode as satisfying the following two conditions:

1. Once a trajectory has crossed the switching hyperplane the first time, it must cross the hyperplane again in every successive sampling period, resulting in a zigzag motion about the switching hyperplane

2. The size of each successive zigzagging step must be non-increasing and the trajectory must stay within a specified band.

Pseudo-sliding mode was defined by [Yu94b]. In his definition a system is in pseudo-sliding mode if in an open neighbourhood of the switching hyperplane $\sigma(k) = \sigma[\mathbf{x}(k)] = 0$

the condition

$$\nabla\sigma(k)\,\sigma(k) \leq 0 \tag{B.3}$$

holds, where $\nabla\sigma(k) = \sigma(k+1) - \sigma(k)$ and k indicates the sampling instant.

[Sarpturk87] showed that, if in an open neighbourhood of the switching hyperplane $\sigma(k) = \sigma[\mathbf{x}(k)] = 0$ the condition

$$|\sigma(k+1)| \leq |\sigma(k)| \tag{B.4}$$

was satisfied, then a system exhibited a stable pseudo-sliding mode. Different but equivalent definitions have been proposed by [Furuta90]

$$\sigma(k+1)^2 \leq \sigma(k)^2, \tag{B.5}$$

and [Sira-Ramirez91]

$$|\sigma(k)\,\sigma(k+1)| \leq \sigma(k)^2. \tag{B.6}$$

B.2 Minimum Time Control review

The minimum time control problem is a classical optimum control problem that can be solved using the Pontryagin minimum principle whose solution can be found in various textbooks (e.g. [Lewis92]). The solution of the problem of the minimum time control of vertical position of the plasma is presented. The problem can be stated as follows: given a system defined by the equations

$$\begin{cases} \dot{x}_1(t) = x_2(t) \\ \dot{x}_2(t) = \gamma_p\gamma_n x_1(t) + (\gamma_p - \gamma_n)\,x_2(t) + u(t) \end{cases} \tag{B.7}$$

with $\gamma_p > \gamma_n > 0$, $\tau > 0$ and the allowed control input to be constrained

$$|u(t)| \leq u_o, \tag{B.8}$$

find an allowable control $u(t)$ that transfers any initial condition

$$\begin{bmatrix} x_1(0) \\ x_2(0) \end{bmatrix} = \begin{bmatrix} x_{10} \\ x_{20} \end{bmatrix} \tag{B.9}$$

to the origin of the state space

$$\begin{bmatrix} x_1(T) \\ x_2(T) \end{bmatrix} = \begin{bmatrix} 0 \\ 0 \end{bmatrix} \tag{B.10}$$

such that the performance index

$$J(T) = \int_0^T dt \tag{B.11}$$

is minimized. First define an Hamiltonian function as

$$H(\mathbf{x}, \boldsymbol{\lambda}, u) = 1 + \boldsymbol{\lambda}^T \dot{\mathbf{x}} \tag{B.12}$$

where $\boldsymbol{\lambda}^T = \begin{bmatrix} \lambda_1 & \lambda_2 \end{bmatrix}$ is the vector of the costate variables. A necessary condition for $u(t)$ to minimize the objective function (B.11) is that $u(t)$ satisfies the following:

$$\begin{cases} \dot{x}_1(t) = \dfrac{\partial H}{\partial \lambda_1} = x_2(t) \\ \\ \dot{x}_2(t) = \dfrac{\partial H}{\partial \lambda_2} = \gamma_p \gamma_n x_1(t) + (\gamma_p - \gamma_n) x_2(t) + u(t) \end{cases} \tag{B.13}$$

$$\begin{cases} \dot{\lambda}_1(t) = -\dfrac{\partial H}{\partial x_1} = \gamma_p \gamma_n \lambda_2(t) \\ \\ \dot{\lambda}_2(t) = -\dfrac{\partial H}{\partial x_2} = \lambda_1(t) + (\gamma_p - \gamma_n) \lambda_2(t) \end{cases} \tag{B.14}$$

$$\min_{u(t)} H(\mathbf{x}, \boldsymbol{\lambda}, u) \ \forall t > 0 \tag{B.15}$$

Substituting equation (B.7) into equation (B.12), the Hamiltonian becomes

$$H(\mathbf{x}, \boldsymbol{\lambda}, u) = 1 + \lambda_1 x_2 + (\gamma_p - \gamma_n) \lambda_2 x_2 + \gamma_p \gamma_n \lambda_2 x_1 + \lambda_2 u. \tag{B.16}$$

Since equation (B.16) is linear in u the maximum values is obtained on the limit values $\pm u_o$. Therefore equation (B.16) is minimized by choosing

$$u(t) = -u_o sgn(\lambda_2). \tag{B.17}$$

The optimum control is a bang-bang (switching) control.

By observing that the optimal control has at most one change of sign (or switch) then

it is possible to determine λ_2 as function of x_1 and x_2. By calculating the state trajectories passing through the origin when the maximum control input is applied and eliminating the time, $\lambda_2(x_1, x_2)$ is given by

$$\lambda_2(x_1, x_2) = \gamma_p \ln\left[x_1 - \frac{\gamma_n x_2}{(\gamma_p + \gamma_n)}\right] - \gamma_n \ln\left[x_1 + \frac{\gamma_p x_2}{(\gamma_p + \gamma_n)}\right] - (\gamma_p + \gamma_n) \ln\left[\frac{\gamma_p \gamma_n}{u_o}\right]. \quad \text{(B.18)}$$

The (B.18) represents a non-linear time-optimum switching line.

Bibliography

[Ali-Arshad96] S. Ali-Arshad, et al., *Plasma Movement at ELMs in JET*, In Proc. 23^{rd} EPS Conference, Kiev, Ukraine, 24-28 June 1996,(also in JET-P(96)30).

[Al-Husari91] M. M. M. Al-Husari, et al., *Vertical Stabilisation of Tokamak Plasmas*, IEEE-Proc. of 30^{th} Conference on Decision and Control, 1991, pp. 1165-1169.

[Albanese89] R. Albanese, E. Coccorese, G. Rubinacci, *Plasma Modelling for the Control of Vertical Instabilities in Tokamaks*, Nuclear Fusion, 29, 1013 (1989)

[Albanese84] R. Albaneseet al, *Electromagnetic behaviour of teh national torus design: vertical stabilization*, Contribution to the INTOR Phase Two A, Part II Workshop, Rep. EUR-FU-BRU/XII-268/85/EDV1, CEC, Brussels (1984)

[Aikawa76] H. Aikawa, A. Ogata, Y. Suzuki, *Derivation of Plasma Displacement in a Tokamak from Magnetic Probe Signals*, Japan. J. Appl. Phys. Vol. 15 (1976), No. 10, pp. 2031-2032.

[Ambrosino84] G. Ambrosino, G. Celentano, F. Garofalo, *Variable structure model reference adaptive control systems*, Int. J. Control, 1984, Vol. 39, No. 6, pp. 1339-1349.

[Ambrosino88] G. Ambrosino, G. Celentano, E. Coccorese, F. Garofalo, *Controller design for plasma position and current control in NET*, Fusion Thechnology, Vol. 15, pp. 1670-1674, 1989.

[Atherton75] D. P. Atherton, *Non-linear Control Engineering*, London: Van Nostran Reinhold, 1975.

[Atherton82] D. P. Atherton, *Limit Cycles in Relay Systems*, Electronic Letters, Vol. 18, No. 21, pp992-993, 1982.

[Balasubramanian81] R. Balasubramanian, *Stability of limit cycles in feedback systems containing a relay*, IEE Proc., Pt. D, Vol. 128, No. 1, January 1981.

[Bartolini95] G. Bartolini, A. Ferrara, V. I. Utkin, *Adaptive Sliding Mode Control in Discrete-time Systems*, Automatica, Vol. 31, No. 5, pp. 769-773, 1995.

[Bertolini87] E. Bertolini, *JET Design, Construction and Performances*, Nuclear Fusion, pp13, 203, January 1987

[Bertolini91] E. Bertolini and the JET team, *The JET project*, Energia nucleare, Anno 8, No3, (1991)

[Bertolini95] E. Bertolini, et al., *Engineering Analysis of JET Operation*, In Proc. 16^{th} SOFE conference, Champaign, Illinois, USA, 1995.

[Bitsoris95] G. Bitsoris, M. Vassilaki, *Constrained Regulation of Linear Systems*, Automatica (1995), Vol. 31, No. 2, pp. 223-227.

[Blanchini90] F. Blanchini, *Feedback Control for Linear Time-Invariant Systems with State and Control Bounds in the Presence of Disturbances*, IEEE Transaction on Automatic Control (November 1990), Vol. 35, No. 11, pp. 1231-1234.

[Blanchini95] F. Blanchini, F. Mesquine, S. Miani, *Constrained stabilisation with an assigned initial condition set*, International Journal of Control (1995), Vol. 62, No 3, pp. 601-617.

[Browne90] M. Browne, L. Zheng, R. Fernandez, P Wellstead, *Self-tuning methods for plasma control applications*, In Proc. 16^{th} SOFT Conference, 1992.

[Bugart94] C. Bugart, S. Trourierch, M. Klai, *Continuous-time saturated feedback regualtors: theory and design*, Int. J. Systems Science, 1994, Vol. 25, No. 2, pp. 315-336.

[Burton88] J. A. Burton, A. S. I. Zinober, *Continuous self-adapting control using a smoothed variable structure controller*, Int. J. Systems Science, 1988, Vol. 19, No. 8, pp. 1515-1528.

[Chan94] C. Y. Chan, *Robust discrete-time sliding mode controller*, Systems & Control Letters, 1994, Vol. 23, pp. 371-374.

[Choi94a] H. H. Choi, M. J. Chung, *Estimation of the Asymptotic Stability Region of Uncertain Systems with Bounded Sliding Mode Controllers*, IEEE Transaction on Automatic Control (November 1994), Vol. 39, No. 11, pp. 2275-2278.

[Choi94b] Seung-Bok Choi, Dong-Won Park, *Moving Sliding Surfaces for Fast Tracking Control of Second-Order Dynamical Systems*, Journal of Dynamic Systems, Measurement and Control, Vol.116, pp. 154-158, March 1994.

[Choi93] Seung-Bok Choi,Chae-Cheon Cheong, Dong-Won Park, *Moving switching surfaces for robust control of second-order variable structure systems*, Int. J. of Control, 1993, Vol.58, No. 1, pp. 229-245.

[Core88] W. G. F. Core, P Noll, *Transverse magnetic field penetration through the JET toroidal coil and support structure*, JET Report, JET-R(88)03.

[Corless93] M. Corless, G. Leitman, *Bounded Controllers for Robust Exponential Convergence*, Journal of Optimization Theory and Applications (1993), Vol. 76, No. 1, pp. 1-12.

[Danbury94] R. N. Danbury, *Near time-optimal control of non-linear servomechanisms*, IEE Proc.-Control Theory Appl., Vol. 141, No. 3, May 1994.

[Drakunov89] S. V. Drakunov, V. I. Utkin, *On discrete-time sliding mode*, In Proc. IFAC Conf. on Nonlinear Control systems Design, Capri, Italy, 1989, pp. 273-278.

[Drazenovic69] B. Drazenovic, *The invariance conditions in variable structure systems*, Automatica, Vol. 5, pp. 287-295, 1969.

[Duchs92] D. F. Düchs, *Recent Step Toward a Controlled Thermonuclear Fusion Reactor with Results from the JET Tokamak Device*, JET-P(92)91

[EAEC76] European Atomic Energy Community, *The JET Project - Design Proposal. Commission of the European Communities*, 1976, EUR-5516-e

[Elghezawi83] O. M. E. El-Ghezawi, A. S. I. Zinober, S. A. Billings, *Analysis and design of variable structure systems using a geometric approach*, International Journal of Control (1983), Vol. 38, N° 3, pp. 657-671.

[Fielding96] S. J. Fielding et al., *ELM structure in the boundary plasma on COMPASS-D*, to be published in J. Nuclear Materials 96/97.

[Flugge-Lotz68] *Discontinuous Automatic Control*, Princeton University Press, Princeton, USA, 1953.

[Furuta90] K. Furuta, *Sliding mode control of a discrete system*, Systems & Control Letters (1990), Vol. 14, pp. 145-152.

[Gao95] W. Gao, *Discrete-Time Variable Structure Control Systems*, IEEE Transaction on Automatic Control (April 1995), Vol. 42, No. 2, pp. 117-122.

[Garribba88] M. Garribba, *Controllo della Posizione Verticale del Plasma nell'Esperimento JET*, Universitá degli studi di Padova, Tesi di Laurea,1988 (available in English).

[Garribba93] M. Garribba, R. Litunovsky, P. Noll, S. Puppin, *The New Control Scheme for the JET Plasma Position and Current Control System*,In Proc. 15^{th} SOFE conference, Hyannis, Mass, USA, 1993.

[Garribba94] M. Garribba, M.L. Browne, D. J. Campbell, Z. Hudson, R. Litunovsky, V. Marchese, F. Milani, J. Mills, P. Noll, S. Puppin, F. Sartori, L. Scibile, A. Tanga, I. Young, *First Operational Experience with the new Plasma Position and Current Control System of JET*, In Proc. 18^{th} SOFT conference, Karlsruhe, Germany,22-26 August, (1994).

[Gibson63] J. E. Gibson , *Nonlinear Automatic Control*, McGraw-Hill, 1963

[Glazos95] M. P. Glazos, S. H. Zak, *Practical stabilization of nonlinear/uncertain dynamic systems with bounded controllers*, Int. J. Control (1995), Vol. 62, No. 1, pp. 153-171.

[Gruber93] O. Gruber, et al., *Vertical Displacement Events and Halo Currents*, Plasma Physics of Controlled Fusion (1993), Vol. 35, pp. 191-198.

[Gutman86] **P. Gutman**, M. Cwikel, *Admissible Sets and Feedback Control of Discrete-Time Linear Dynamical Systems with Bounded Controls and States*, IEEE Transaction on Automatic Control (April 1986), Vol. AC-31, No. 4, pp. 373-376.

[Gutman87] P. Gutman, M. Cwikel, *An Algorithm to Find Maximal State Constraint Sets for Discrete_time Linear Dynamical Systems with Bounded Controls and States*, IEEE Transaction on Automatic Control (March 1987), Vol. AC-32, No. 3, pp. 251-254.

[Hugil74] J. Hugil, A Gibson, *Servo-Control of Plasma Position in Cleo-Tokamak*, Nuclear Fusion, Vol. 14, No. 5, pp. 611-619, 1974.

[**Hay92**] J. H. Hay et al, *Design and development of a* $\pm 2kV$ $\pm 10kA$ *high speed GTO switching amplifier for fast equilibrium control on COMPASS-D*, 17^{th} SOFT conference, Rome, Italy, 1992.

[Hoffmann86] F. Hoffmann, F. B. Marcus, A. D. Turnbull, *Axisymmetric Stability of Highly-Elongated Tokamak Plasma - A new Method and Initial Results*, Plasma Phys. Controlled Nulc. Fusion, 28, 705 (1986)

[Hugue87] M. Hugue, et al., *The JET Machine: Design, Construction and Operation of the Major Systems*, Fusion Technology, 13, 43, January 1987

[Hui93] S. Hui, S. H. Zak, **Robust** ***Output*** *Feedback Stabilization of Uncertain Dynamical* ***Systems*** *with Bounded Controllers*, Int. Journal of Robust and Nonl;inear Control (1993), Vol. 3, pp. 115-132.

[Humphreys93] D. A. Humphreys, I. H. Hutchinson, *Axisymmetric Magnetic Control Design in Tokamak using Perturbed Equilibrium Plasma Response Modelling*, Fusion Technology, Vol. 23, March 1993

[Hung93] J. Y. Hung, W. Gao, J. C. Hung, *Variable Structure Control: A Survey*, IEEE Transaction on Industrial Electronic (February 1993), Vol.40, N^o. 1, pp. 2-22.

[Hutchinson89] I. H. Hutchinson, Simplified models of axisymmetric magnetohydrodynamic instabilities, Nuclear Fusion, Vol. 29, No. 12, pp. 2107-2113, (1989).

[ITER95] *Technical basis for the ITER interim design report, cost review and safety analisys*, In ITER EDA documentation series, No. 7, July 12 1995

[Kamenetskiy96] V. A. Kamenetskiy, *Construction of a Constrained Stabilizind Feedback by Lyapunov Functions*, In Proc. 13th IFAC World Congress, San Francisco, USA, 1996, (2b-04 6) pp. 139-144.

[Keen93] B. E. Keen, M. L. Watkins, *Present State of Nuclear Fusion Research and Prospects for the Future*, JET document JET-P(93)67

[Kouvaritakis96] B. Kouvaritakis, J. R. Gossner, J. A. Rossiter, *A Priori Stability Conditions for an Arbitrary Number of Unstable Poles*, Automatica, Vol. 32, No. 10, pp. 1441-1446, 1996.

[Jardin82] S. C. Jardin, D. A. Larrabee, *Feedback Stabilization of Rigid Axisimmetric Modes in Tokamaks*, Nuclear Fusion, Vol. 22, No. 8, pp. 1095-1098, (1982).

[JETannual95] JET annual report 1995

[Lazarus90] E. A. Lazarus, J. B. Lister, G. H. Neilson, *Control of the Vertical Instability in Tokamaks*, Nuclear Fusion, Vol. 30, No. 1, pp. 111-141, (1990)

[Ledwich95] G. Ledwich, *Linear switching controller convergence*, IEE Proc.-Control Theory Appl. (July 1995), Vol. 142, No. 4, pp. 329-334.

[Lee95] A. W. Lee, J. K. Hedrick, *Some new results on closed-loop stability in the presence of control saturation*, Int. J. Control (1995), Vol. 62, No. 3, pp. 619-631.

[Leuer89] J. A. Leuer, *Passive Vertical Stability in the Next Generation Tokamaks*, Fusion Thechnology, Vol. 15, March 1989.

[Lewis92] F. L. Lewis, *Applied Optimal Control & Estimation*, Prentice-Hall, 1992.

[Lingertat95] J. Lingertat, et al., *The Effect of ELMs on the Plasma Edge of JET*, In Proc. 22^{rd} EPS Conference, Bournemouth, UK, 3-7 July 1995,(also in JET-P(95)31).

[Lister90] J. B. Lister et al., Experimental Study of the Vertical Stability of High Decay Index Plasmas in the DIII-D Tokamak, Nuclear Fusion, Vol. 30, No. 11, pp. 2349-2366, (1990).

[Lin96] Z. Lin, A. A. Stoorvogel, A. Saberi, *Output Regulation for Linear Systems Subject to Input Saturation*, Automatica (1996), Vol. 32, No. 1, pp. 29-47.

[Lin95] Z. Lin, A Saberi, *Semi-global exponential stabilization of linear discrete-time systems subject ot input saturation via linear feedback*, Systems & Control Letters (1995), Vol. 24, pp. 125-132.

[Lin93] Z. Lin, A Saberi, *Semi-global exponential stabilization of linear systems subject ot input saturation via linear feedbacks*, Systems & Control Letters (1993), Vol. 21, pp. 225-239.

[Liu95] J. Liu, *Using decomposition approach to estimate the stable regions of variable structure control for linear time-invariant system with bounded control variables*, Int. J. Systems Science (1995), Vol. 26, No. 9, pp. 1687-1699.

[Ljung87] L. Ljung, *System **identification**:theory for the user*, PTR Prentice Hall, 1987

[Madani-Esfahani90] S. M. Madani-Esfahani, M. Hached, S. H. Zak, *Estimation of Sliding Mode Domain of Uncertain Variable Structure Systems with Bounded Controllers*, IEEE Transaction on Automatic Control (April 1990), Vol. 35, No. 4, pp. 446-449.

[Maciejowski89] J. M. Maciejowski, *Multivariable Feedback Design*, Addison-Wesley, 1989.

[MATLAB] MATLAB® ver. 4.2 (1994), The MathWorks Inc., Natick, Massachusetts

[MAXFEA] Equilibrium code developed by P. Barabaschi for JET and still undocumented.

[Megretski96] **A. Megretski**, *L_2 BIBO Output Feedback Stabilization with Saturated Control*, In Proc. 13^{th} IFAC World Congress, San Francisco, USA, 1996, (2a-18 2) pp. 435-440.

[Milani92] F. Milani, *Misure per il sistema di controllo nell'esperimento JET*, Universitá degli studi di Padova, Tesi di Laurea,1992 (available in English).

[Milosavljevic85] D. Milosavljevic, *General conditions for the existence of a quasisliding mode on the switching hyperplane in discrete variable structure systems*, Automat. Remote Contr., Vol. 46, pp. 307-314, 1985.

[Mohan89] N. Mohan, T. M. Undeland, W. P. Robbins, *POWER ELECTRONICS: Converters, Applications and Design*, John Wiley & Sons, 1989.

[Mondino92] P.L. Mondino **et al.**, *The new Fast Radial Field Amplifier for the Control of the Plasma Vertical Position in JET*,In Proc. 17^{th} SOFT Conference, 1992.

[Mori87] M. Mori et al., *Stability Limit of Feedback Control of Vertical Plasma Position in the JFT-2M Tokamak*, Nuclear Fusion, Vol. 27, No. 5, pp. 725-734, 1987.

[Morris95] A. W. Morris et al., Disruptions, *Vertical Instabilities and Halo Currents in COMPASS-D*, Proceedings of the 22^{nd} European Physical **Society Conference on Controlled** Fusion and Plasma Physics, **Bournemouth**, 3^{rd}-7^{th} July 1995, Vol. 19C, Part III, pp. 49-52, 1995.

[Munchmeyer95] Hans-Christian Münchemeyer, *Aspects of Plasma Vertical Stability Control in the JET Tokamak Fusion Reactor*, Universität Hannover-Jet Joint Undertaking, Diplomarbeit, October 1995

[Moriyama85] S. Moriyama et al., *Analysis of Optimal Feedback Control of Vertical Plasma Position in a Tokamak System*, Japanese Journal of of Applied Physics (July 1985), Vol. 24, No. 7, pp. 849-855.

[Nagayama84] Y. Nagayama et al., *Feedback Control of Vertical Plasma Position in Non-Circular Tokamak TNT-A*, Nuclear Fusion, Vol. 24, No. 10, pp. 1243-1249, 1984.

[Newman91] W. S. Newman, K Souccar, *Robust, Near Time-Optimal Control of Nonlinear Second-Order Systems: Theory and Experiments*, Journal of Dynamic Systems, Measurement and control (September 1991), Vol.113, pp. 363-370.

[Noll86] P. Noll et al., *Stabilization of Vertical Position and Control of Plasma Shape in JET*, Fusion Technology, Vol. 10, pp. 33-40, 1986.

[Noll89] P. Noll, *Vertical Stabilisation: growth rate and transfer function.* JET memo 23/10/1989.

[Noll90] P. Noll, Bonnicelli, M. Garribba, *Vertical Instabilities in JET*, 17^{th} EPS Conference on Controlled Fusion and Plasma Heating, Amsterdam, June 1990.

[Noll91a] P. Noll, *A Simplified Model of the Stabilisation System*, JET Document, JDN/G(91)025.

[Noll91b] P. Noll, *Negative Effect of the Mechanical Shell*, JET Memo 7/2/91.

[Noll95a] P. Noll, *Recovery from an Initial Plasma Displacement*, JET Memo 07/04/1995.

[Noll95b] P. Noll, *Transfer Functions with Double Wall Vessel*, JET Memo, 4/5/95.

[Noll96] P. Noll, et al., *Present Understanding of Electromagnetic Behaviour during Disruptions in JET*, In Proc. 19^{th} SOFT Conference, Lisbone, Portugal, 16-20 September 1996.

[Ogata77] A.Ogata, H.Aikawa, Y.Suzuki, *Accuracy of Plasma Displacement Measurement in a Tokamak Using Magnetic Probes*, Japan. J. Appl. Phys. Vol. 16 (1977), No. 1, pp. 185-186.

[Pease65] M. C. Pease, *Methods of Matrix Algebra*, Mathematics in science and engineering, Academic Press, New York and London, 1965

[Pieper93] J. K. Pieper, B. W. Surgenor, *Discrete sliding control of a coupled-drives apparatus with optimal sliding surface and switching gain*, IEE Proc.-Control Theory Appl., Vol. 140, No. 2, March 1993.

[Portone92] A. Portone, *Controllability of NET Plasmas after Loss of Beta Events*, In Proc. 17^{th} SOFT Conference, 1992.

[PROTEUS] R. Albanese, J. Blum, O. de Barbieri, *Numerical Studies of the Next European Torus via PROTEUS Code*, Proc. of XII Conference on Numerical Simulation of Plasmas, S. Francisco 1987.

[Rossiter95] J. A. Rossiter, B. Kouvaritakis, J. R. Gossner, *Feasibility and Stability Results for Contrained Stable Generalized Predictive Control*, Automatica, Vol. 31, No. 6, pp. 863-877, 1995.

[Sarpturk87] S. Z. Sarpturk, Y. Istefanopulos, O. Kaynak, *On the Stability of Discrete-Time Sliding Mode Control Systems*, IEEE Transaction on Automatic Control (October 1987), Vol. AC-32, No. 10, pp. 930-932.

[Scibile92] L. Scibile, *Un Sistema di Stabilizzazione Verticale del Plasma per la Configurazione a Divertore del JET*, Universitá degli studi di Napoli, Tesi di Laurea,1992 (available in English).

[Seron95] M. M. Seron, G. C. Goodwin, S. F. Graebe, *Control system design issues for Unstable linear systems with saturated inputs*, IEE Proc.-Control Theory Appl. (July 1995), Vol. 142, No. 4, pp. 335-344.

[Sira-Ramirez91] H. Sira-Ramírez, *Nonlinear discrete variable structure systems in quasi-sliding mode*, International Journal of Control (1991), Vol. 54, No. 5, pp. 1171-1187.

[Spurgeon91] S. K. Spurgeon, *Sliding mode control design for uncertain systems*, 30^{th} Conf. on Decision and Control, Brighton, UK, 1991,pp. 2136-2141.

[Spurgeon92] S. K. Spurgeon, *Hyperplane design techniques for discrete-time variable structure contro systems*, International Journal of Control (1992), Vol. 55, No. 2, pp. 445-456.

[Su93] Wu-Chung Su, S. V. Drakunov, Ü. Özgüner, *Implementation of Variable Structure Control for Sampled-Data Systems*, In Proc. 3^{rd} Robust Control via Variable Structure and Lyapunov Techniques, Benevento, Italy, 1994, pp. 166-173.

[Summers92] D. Summers, Z. Y. Wu, G. C. W. Sabin, *State Estimation of Linear Dynamical Systems under Bounded Control*, Journal of Optimization Theory and Applications (February 1992), Vol. 72, No. 2, pp. 299-318.

[Tinios93] G Tinios et al., *Model Reduction for Axisymmetric Tokamak Control*, Fusion Technology, Vol. 24, pp. 355-365, December 1993.

[Tsypkin] YA. Z. Tsypkin, *Relay control Systems*, Cambridge University Press, Cambridge, 1984.

[Tomabechi91] K. Tomabechi et al, *ITER Conceptual design*, Nuclear Fusion, Vol. 31, No6 (1991)

[Utkin77] V. I. Utkin, *Variable Structure Systems with Sliding Mode*, IEEE Transaction on Automatic Control (April 1977), Vol.AC-22, N^o. 2, pp. 212-222.

[Vassilaki88] M. Vassilaki, J. C. Hennet, G. Bitsoris, *Feedback control of linear discrete-time systems under state and control constraints*, Int. J. Control (1988), Vol. 47, No. 6, pp. 1727-1735.

[Vyas96] P. Vyas, *Plasma Vertical Position Control in the Compass-D Tokamak*, Ph.D thesis, Oxford University, 1996.

[Yu94a] X. Yu, G. Ledwich, H. Sira-Ramírez, *Adaptive Switching Control for the Stabilisation of a Power System*, In Proc. 3^{rd} Robust Control via

Variable Structure and Lyapunov Techniques, Benevento, Italy, 1994, pp. 336-341.

[Yu94b] X. Yu, *Digital variable structure control with pseudo-sliding control*, in *Variable Structure and Lyapunov Control*, (Chapter 7), Ed. A. S. I. Zinober, Spring-Verlag, London.

[Ward92] D. J. Ward, S. C. Jardin, *Effect of the Plasma Deformability on the Feedback Stabilization of Axisymmetric Modes in Tokamaks Plasmas,* Nuclear Fusion, Vol. 32, No. 6, pp. 973-994, (1992).

[Wesson87] J. Wesson, *Tokamaks*, O.U.P., 1987.

[Wesson89] J. A. Wesson et al., *Disruptions in JET*, Nuclear Fusion, Vol. 29, No 4, pp. 641-666, (1989).

[Zakharov73] L. E. Zakharov, V.D.Shafranov, *Equilibrium of toroidal plasma with no circular cross section*, Sov. Phys. Tech. Vol. 18 (1973), pp. 151-156.

[Zama92] G. Zama, A. Portone, *Simulation of the Power Supply System for the Plasma Vertical Position Control in NET/ITER*, In Proc. 17^{th} SOFT Conference, 1992.

[Zhao95] Y. Zhao, S. Jayasuriya, *Stabilizability of Unstable Linear Plants Under Bounded Control*, Journal of Dynamic Systems, Measurement and control (March 1995), Vol.117, pp. 63-73.

[Zheng93] G. L. Zheng, P. E. Wellstead, M. L. Browne, *Self-tuning control studies pf the plasma vertical position problem*, Fusion Technology, Vol. 23, July (1993).

[Zinober75] A. S. I. Zinober, *Adaptive relay control of second-order systems*, Int. J. Control, 1975, Vol.21, No1

[Zinober80] A. S. I. Zinober, *Self-adaptive near-optimal control of diffusion equations*, IEE Proc.-Control Theory Appl., Vol. 127, No. 6, November 1980.

[Zohm96] H. Zohm, *Edge localized modes (ELMs)*, Plasma Phys. Control. Fusion, Vol. 38, pp. 105 128, (1996).